Gigante, Fabio Antonio (2016) *Time- and frequency-domain turbulent flow analysis of wind turbine unsteady aerodynamics.* PhD thesis.

Time- and Frequency-Domain Turbulent Flow Analysis of Wind Turbine Unsteady Aerodynamics

By
Fabio Antonio Gigante

Thesis submitted for the degree of Doctor of Philosophy
at the University of Glasgow

School of Engineering
University of Glasgow
James Watt Building South
University Avenue, G12 8QQ, Glasgow, UK

September 2015

Abstract

The main objective of the research work presented in this thesis is the development of a single aerodynamic CFD code for the analysis of complex turbulent flow unsteady aerodynamics such as those encountered in horizontal and vertical axis wind turbines. The finite volume parallel CFD Optimized Structured multi-block Algorithm (COSA) research code solves the Navier-Stokes equations on structured multi-block grids and models turbulence effects with Menter's shear stress transport turbulence model. The novel algorithmic contribution of this research is the successful development of a Harmonic Balance (HB) solver which can reduce the run-time required to compute nonlinear periodic flow fields with respect to the conventional time-domain (TD) approach. The thesis also presents a semi-implicit integration based on LU factorisation and a successfully LAPACK libraries integration to massively improve the computational efficiency of the integration of the HB RANS equations and the turbulence model of Menter. The main computational results of this research are for two low-speed renewable energy applications. The former application is a turbulent unsteady flow analysis of a Vertical Axis Wind Turbine (VAWT) working in a low-speed turbulent regime for a wide range of operating conditions. The test case is first solved using the COSA TD turbulent solver to analyse and discuss in great detail the unsteady aerodynamic phenomena occurring in all regimes of this complex device. During the turbine rotation there is a generation of blade vortex shedding and wakes all around the rotor which interacts with the blades itself on the returning side. The most important features of the investigated devices were captured with CFD. In addition, a series of investigations have been conducted to analyse the effects of computational domain refinement, number of time steps per revolution and distance of the farfield boundary from the rotor centre on prediction accuracy. The solution of the turbulent flow solver is validated by comparing torque and power coefficients with experimental data and numerical solutions obtained with a state-of-the-art time-domain of commercial package regularly used by the industry and the Academia worldwide. A detailed selection of results is presented, dealing with the various investigated issues. Afterwards, the COSA HB turbulent solver is used to solve the problem and compare the HB resolution and speed-ups with the TD results. The main motivation for analysing this problem is to highlight the predictive capabilities and the numerical robustness of the developed turbulent HB flow solver for complex realistic problems with a strong nonlinearity and to shed more light on the complex physics of this renewable energy device. The latter application regards the turbulent unsteady flow analysis of Horizontal Axis Wind Turbine (HAWT) blade sections in yawed wind regime. The TD and HB turbulent flow analysis of a 164 m-diameter wind turbine rotor is performed. CFD represents an accurate design tool to get a better understanding of the physical behaviour of the flow field past wind turbine rotors and the importance of accurate design is increased as the machines tend to become larger. A study at 30% and at 85% blade section is carried out, allowing the analysis of the unsteady forces acting on two different blade sections. The aim of these analyses is to assess the computational benefits achievable by using the HB method for a common nonlinear flow problem and also to further demonstrate the predictive capabilities of the developed CFD system. The turbulent HB solutions highlight that is possible to obtain an accurate analysis as its TD counterparts can do. Moreover, the results highlight that the turbulent HB solver can compute the hysteresis force cycles of the turbine blade more than 10 times faster than the TD approach. The purpose of proving the turbulent COSA HB capabilities for studying the flow field of wind turbines rotor has been fully achieved and this research represent one of the first turbulent HB RANS applications to the analysis of periodic horizontal axis wind turbine flows, and the first application to vertical axis wind turbine flows.

Keywords: Reynolds-Average Navier-Stokes equations, harmonic balance, horizontal axis wind turbine, vertical axis wind turbine.

Acknowledgements

I wish to acknowledge my supervisor Dr. M. Sergio Campobasso, who has supervised my research project during the years of my Ph.D. He has an amazing knowledge on the computational fluid dynamic field and during our meetings he always provided me helpful suggestions. His guidance has been essential to overcome the issues encountered during my research studies. I would like to acknowledge my examiners Dr. Manosh Paul, Dr. Andrea Da Ronch (University of Southampton) and convener Dr. Richard Green, for reading my thesis and providing advice which improved the quality of my work. I would also like to acknowledge my colleagues for their help and for the time we spent together. I wish to express my sincere thanks to my parents who always support my decisions, to my sisters, my grandmother and all my family for their encouragements. A special thanks to my fiance, for her love, support and understanding during the difficult periods of my Ph.D.

Contents

List of Figures

List of Tables

Nomenclature

Latin symbols

a	Induction factor
A	Rotor area
c	Aerofoil chord
CD_ω	Cross-diffusion term
C_d	Drag coefficient
C_l	Lift coefficient
C_m	Pitching moment coefficient
C_p	Power coefficient
C_T	Torque coefficient
C_x	Horizontal force coefficient
C_y	Vertical force coefficient
C_{F_N}	Sectional normal force
C_{F_T}	Sectional tangential force
c_f	Skin friction coefficient
c_p	Pressure coefficient
D	Rotor diameter
dF_D	Incremental drag force
dF_L	Incremental lift force
dm	Mass element
dR	Radial length
dS	Surface element
dV	Volume element
D_k	Destruction terms of k

D_ω	Destruction terms of ω
d_w	Distance from the wall
E	Total energy
$\widehat{\mathbf{E}}_c$	$x-$component of $\widehat{\boldsymbol{\Phi}}_c$
$\widehat{\mathbf{E}}_d$	$x-$component of $\widehat{\boldsymbol{\Phi}}_d$
f	Face fluxes
F	Forcing term
F_N	Normal force
F_T	Tangential force
$\widehat{\mathbf{F}}_c$	$y-$component of $\widehat{\boldsymbol{\Phi}}_c$
$\widehat{\mathbf{F}}_d$	$y-$component of $\widehat{\boldsymbol{\Phi}}_d$
h	Height
h_0	Motion amplitude
H	Total enthalpy per unit mass
k	Turbulent kinetic energy
K	Reduced frequency
k_T	Thermal conductivity
k_U	Flux Jacobian
I	Turbulence intensity
l	Runge-Kutta cycle counter
l_T	Turbulence length scale
L	Characteristic length of the obstacle
$\dot{m}$	Mass flow rate
m	Runge-Kutta stage index
M_∞	Freestream Mach number
N	Number of physical time steps
N_b	Number of blades
N_{be}	Number of blade elements
N_H	Number of complex harmonics
$\boldsymbol{n}$	Normal unit vector
n_x	$x-$component of $\boldsymbol{n}$

n_y	$y-$components of $\boldsymbol{n}$
p	Static pressure
P	Power
P_k	Production terms of k
P_ω	Production terms of ω
p_w	Pressure to the wall
$\boldsymbol{q}$	Heat flux vector
q_x	$x-$component of $\boldsymbol{q}$
q_y	$y-$component of $\boldsymbol{q}$
$\widehat{\mathbf{Q}}$	Unknown flow variables array
R	Rotor radius
R_k	Residual of the k equation
R_ω	Residual of the ω equation
$\widehat{\mathbf{R}}_g$	Residual vector
Re	Reynolds number
s	Wind shear exponent
S	Surface
$\widehat{\mathbf{S}}$	Source term
$\underline{S}$	Strain rate tensor
$S(t)$	Time-varying boundary
S_{ij}^*	Mean strain rate tensor
S_k	Source term of k
S_ω	Source term of ω
T	Static temperature
$\boldsymbol{u}$	Flow velocity vector
$u_{i(j)}$	Components of the flow velocity vector
u_τ	Friction velocity
$\widehat{\mathbf{U}}$	Conservative flow variable array
V	Volume
v_b	Velocity of the boundary S
V_{cell}	Cells volume

V_∞	Freestream wind speed
$x_{i(j)}$	Components of the position vector
W	Relative wind speed
y^+	Non-dimensional wall distance
z	Weibull scale factor

Greek symbols

α	Angle of attack
α_m	Runge-Kutta coefficient
β	Pitch angle
δ	Yaw angle
δ_{ij}	Kronecker Delta function
Δt	Time-step size
$\Delta \tau$	Pseudo-time-step
ϵ	Weibull shape factor
γ_p	Twist angle
λ	Tip speed ratio
μ	Dynamic viscosity
μ_T	Turbulent eddy viscosity
ν	Kinematic viscosity
ν_T	Turbulent kinematic viscosity
ν_w	Kinematic viscosity at the wall
ω	Specific dissipation rate
Ω	Angular velocity
$\widehat{\Omega}$	Modulus of the vorticity
$\widehat{\boldsymbol{\Phi}}_c$	Convective flux vector
$\widehat{\boldsymbol{\Phi}}_d$	Diffusive flux vector
ϕ	Inflow angle
ρ	Air density
σ	Wind turbine solidity
$\underline{\tau}$	Molecular stress tensor

τ_{ij}^{F}	Reynolds stress tensor
θ	Azimuth angle

Abbreviations

AoA	Angle of attack
ALE	Arbitrary Lagrangian Eulerian
BEMT	Blade element momentum theory
CFD	Computational Fluid Dynamics
CV	Control volume
CFL	Courant Friedrichs Lewy
DES	Detached Eddy Simulation
DTS	Dual-time stepping
FAS	Full Approximation Scheme
FD	Frequency-Domain
FDM	Finite Difference Method
FEM	Finite Element Method
FERK	Fully Explicit Runge-Kutta
FVM	Finite Volume Method
HAWT	Horizontal axis wind turbine
HB	Harmonic Balance
HDHB	High Dimensional Harmonic Balance
IRS	Implicit Residual Smoothing
LES	Large Eddy Simulation
LHS	Left-hand side
LTS	Local-time stepping
MG	Multigrid
MPI	Message Passaging Interface
N_H	Number of harmonics
NS	Navier-Stokes
ODE	Ordinary Differential Equations
PDE	Partial Differential Equation

PIRK	Point-Implicit Runge-Kutta
PV	Photovoltaic
RANS	Reynolds Averaged Navier-Stokes
RHS	Right-hand side
RPM	Revolutions per minute
RK	Runge-Kutta
S-A	Spalart-Allmaras
SST	Shear Stress Transport
SIRK	Semi-Implict Runge-Kutta
TD	Time-Domain
URANS	Unsteady Reynolds Averaged Navier-Stokes
VAWT	Vertical axis wind turbine
VTM	Vorticity Transport model

Chapter 1

Introduction

1.1 Renewable energy

Renewable energy is the term used to describe any energy resource that is naturally regenerated over a short time scale and derived directly from the sun (such as thermal and photovoltaic), indirectly from the sun (such as wind, hydropower, and photosynthetic energy stored in biomass), or from other natural movements and mechanisms of the environment (such as geothermal and tidal energy). Throughout history, these sources have been harnessed and used to provide energy. Today's technological advancements have developed more efficient means of harnessing and using renewable energy sources, and these sources are gaining increasing popularity. They offer alternatives to nonrenewable energy sources such as oil, coal and natural gas. Existing renewable energy installations are making significant contributions to energy supply, and research activities are demonstrating the far-reaching impact that a greater reliance on renewable energy sources could have. Renewable energy provided an estimated 19% of global final energy consumption in 2013, and continued to grow strongly in 2014 and 2015 [9]. Of this total share, traditional biomass, which currently is used primarily for cooking and heating in remote and rural areas of developing countries, accounted for about 9%, and modern renewables (geothermal, solar, hydropower, wind, biofuels, etc.) increased their share to approximately 10%. Modern renewable energy is being used increasingly in four distinct areas: power generation, heating and cooling, transport fuels, and rural/off-grid energy services. The breakdown of modern renewables, as a share of total final energy use in 2013, was as follows: hydropower generated an estimated 3.8%; other renewable power sources comprised 1.2%; heat energy accounted for approximately 4.2%; and transport biofuels provided about 0.8% (See Fig. 1.1).

During the years 2009 through 2013, installed capacity as well as output of most renewable energy technologies grew at rapid rates, particularly in the power sector (Fig. 1.2). Over this period, solar photovoltaics (PV) experienced the fastest capacity growth rates of any energy technology, while wind saw the largest power capacity added of any renewable technology. In Europe, a growing number of countries has reduced financial support renewables at a rate that exceeds the decline in technology costs. Such actions have been driven, in part, by the ongoing economic crisis in some member states, by related electricity over-capacity, and by rising competition with fossil fuels. Policy uncertainty has increased the cost of capital making it more difficult to finance projects.

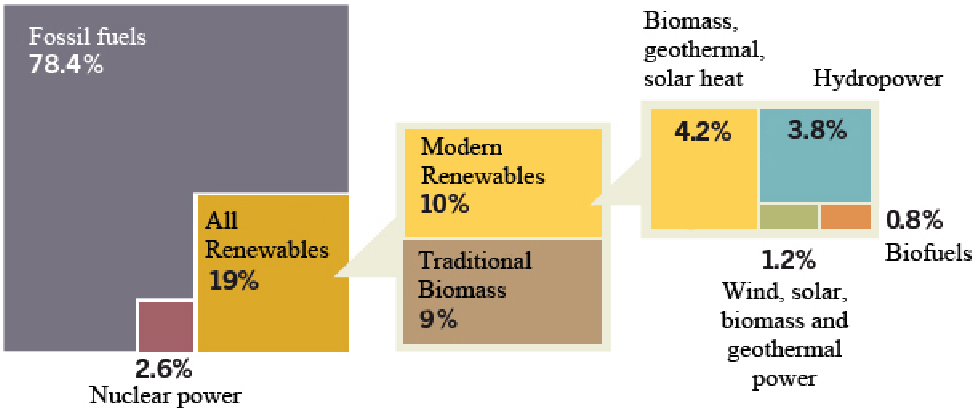

Figure 1.1: Estimated Renewable Energy Share of Global Final Energy Consumption, 2012 [9]

Overall, renewables saw a number of significant and positive developments during the last years. At the moment, wind power is increasing more quickly into Africa and Latin America and solar thermal power into Middle East and North Africa region and to South Africa. The solar PV continues to spread in the world, with most capacity on-grid but also significant increases in off-grid markets in developing countries. Such developments highlight that renewables are no longer dependent upon a small number of countries. United Kingdom produces more than 20% of its electricity from onshore and offshore wind farms, biomass power stations and hydropower systems [8]. To meet

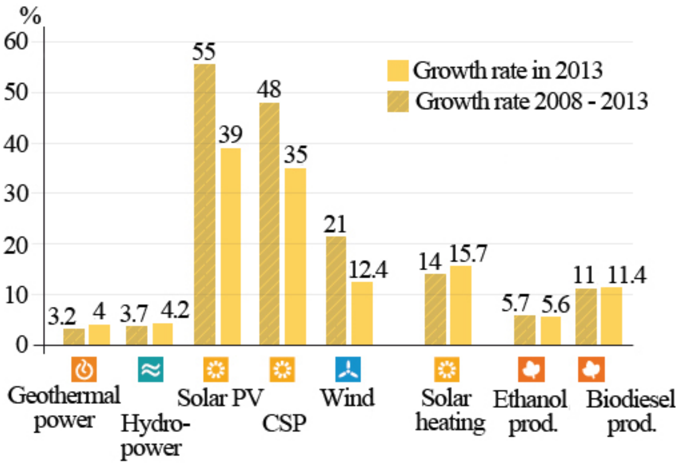

Figure 1.2: Average Annual Growth Rates of Renewable Energy Capacity and Biofuels Production, End-20082013 [9]

its EU goals, electricity generation from renewable sources needs to increase to above 30% by 2020. An increasing number of countries is aiding integration through improvements in grid management practices, system flexibility, and modifying existing grid infrastructure. Renewables have been aided by continuing progress in technologies, falling prices, and innovations. These developments are making renewable energy cheaper than new fossil and nuclear installations under many circumstances, and so more affordable for a broader range of consumers in many countries. In addition, there is increasing awareness of renewable energy technologies, and their potential to help meet rapidly rising energy demand, while also creating jobs, accelerating economic development, reducing local air pollution, and reducing carbon emissions. Moreover, renewable energy can expand access to modern energy services in developing countries, both rapidly and cost effectively. To achieve a variety of energy security and sustainability goals, growing numbers of cities, states, and regions around the world are trying to transition to a higher percentage renewable energy in individual sectors or economy-wide, and many have already achieved their targets. Many renewable industries saw a rapid increase in worldwide demand for construction and engineering, consulting, equipment maintenance, and operations services. Innovative financing mechanisms, such as crowd funding and risk-guarantee schemes, continued to expand and spread across China, Europe, and the United States.

1.2 Wind energy

Harnessing the energy of wind is one of the cleanest and most sustainable ways to generate electricity. Wind energy has been used for millennia for several applications. The use of wind energy to generate electricity on a commercial scale became possible only in the 1970s as a result of technical advances and government support [51]. Different wind energy technologies are available across a range of applications, but the largest contribution on energy production come from large grid-connected horizontal axis wind turbines, deployed either on land ("onshore") or in sea- or freshwater ("offshore"). Wind energy offers significant potential for near-term (2020) and long-term (2050). The wind power capacity installed by the end of 2009 satisfied roughly 1.8% of worldwide electricity demand, and the contribution could grow to in excess of 20% by 2050. Moreover, though average wind speeds vary considerably by location, ample technical potential exists in most regions of the world to enable significant wind energy deployment. In some areas with good wind resources, the cost of wind energy is already competitive with current energy market prices. However, in most regions of the world, policy measures are still required to ensure rapid deployment. Wind energy is the fastest growing source of electricity in the world, thanks to its many benefits and significantly reduced costs.

1.2.1 History of wind power

From the sailing ships of the ancient Greeks, to the grain mills of pre-industrial Holland, to the latest high-tech wind turbines rising over the Minnesota prairie, humans have used the power of the wind for many years [6]. In the United States, first applications on wind energy were developed between 1870 and 1930, when thousands of farmers across the country used wind to pump water. Small electric wind turbines were used in rural areas and prototypes of larger machines were built in the 1940s. In Europe, Denmark was the first country to use the wind for generation of electricity. The Danes were using a 23 m diameter wind turbine in 1890. By 1910, several hundred units with capacities of 5 to 25 kW were in operation in Denmark. In the following years, in all the world, were built larger wind turbines. The largest one was a 1250 kW machine and it was built before the late 1970's. The concept of this machine started in 1934 when an engineer, Palmer C. Putnam, began to look at wind electric generators to reduce the cost of electricity. The Smith-Putnam machine had two blades rotor with a diameter of 53 m and a tower length of 34 m. The blade pitch (the angle at which the blade passes through the air) was adjustable to maintain a constant rotor speed of 28.7 r/min. The rotor turned an AC synchronous generator that produced 1250 kW of electrical power. The project was very successful from a technical point of view but the economics did not justify building more machines at that time because appeared too expensive (more Smith-Putnam machines could be built for 190\$/installed kW). Oil and coal fired generation could be bought in 1945 for 125\$/installed kW. This difference was too large to justify the production of new machines, so the project was stopped. Anyway, the technical results of the Smith-Putnam wind turbine caused the engineer Percy H. Thomas, to spend many years in a detailed analysis of wind power electric generation. Thomas used economic data from the Smith-Putnam machine and concluded that even larger machines were necessary for economic viability. He designed two large machines, one was 6500 kW and the other was 7500 kW in size. Thomas estimated the capital costs for his machine at 75\$ per installed kW but the low investment was not enough to capture the investors interest and the project was later cancelled. Several countries continued research on wind energy for a longer period of time. Denmark built their Gedser wind turbine in 1957. This machine produced 200 kW in a 15 m/s wind. It was connected to the Danish public power system and produced approximately 400,000 kWh per year. The installation cost of this system was approximately 250\$/kW. Dr. Ulrich Hutter of Germany built a 100 kW machine in 1957. It reached its rated power output at a substantially lower wind speed compared with the Danish machine mentioned earlier. This machine used lightweight, 35 m diameter fiberglass blades with a simple pipe tower. The blade pitch would change at higher wind speeds to keep the propeller angular velocity constant. Dr. Hutter obtained over 4000 hours of full rated power operation over the next 11 years, a substantial amount for an experimental machine. This allowed important contributions to the design of larger wind turbines to be made. After a period of stagnation, the interest in wind power reborn. Research by the U.S. Department of Energy (DOE) in the 1970s focused on large turbine designs, with funding going to major aerospace manufacturers. While the 2- and 3-MW machines proved mostly unsuccessful at the time, they provided basic research on blade design and engineering principles. The modern wind era began in California in the 1980s. Between 1981 and 1986 were installed 15,000 medium-sized turbines. Pushed by the high cost of fossil fuels, a moratorium on nuclear power, and concern about environmental degradation, the state provided tax incentives to promote wind power. These, combined with federal tax incentives, helped the wind industry take off. In the early 1990s, improvements in technology resulting in increased turbine reliability and lower costs of production provided another boost for wind development. In Europe, wind has had more consistent long-term support. As a result, European countries are currently capable of meeting more of their electricity demands through wind power with much less land area and resource potential. Denmark, for example, already meets about 30 percent of its electricity demand from wind power. Wind generation also accounts for about 17 percent of the national power needs in Portugal, 13 percent in Ireland, and 11 percent in Germany [6].

1.2.2 The wind resource

The wind speed frequency distribution plays a significant role in the power generation cost. The power output of a wind turbine depends from the cube of wind speed. Therefore, higher-speed winds are more easily and inexpensively captured. Wind speeds are divided into seven classes [68], the first class is the lowest speed and the last is the highest. Wind turbines operate between cut-in and cut-out speed. If the wind is lower than cut-in speed, the turbines will not be able to turn, and if higher than cut-out, they shut down to avoid being damaged. Wind speeds in classes three (6.7 - 7.4 m/s) and above are typically needed to economically generate power. Ideally, a wind turbine should be matched to the speed and frequency of the resource to maximize power production. Several factors can affect wind speed, for example wind speed increases as the height from the ground increases. If wind speed at 10 meters off the ground is 7 m/s, it will be about 10 m/s at a height of 100 m. Thus, in order to generate more power, the rotors of the newest wind turbines can reach heights up to 130 m.

But the wind does not blow consistently all the time. The “capacity factor” is the term used to describe the actual mean power a turbine actually produces over a period of time divided by the amount of power it could have produced if it had run at its full rated capacity over that time period. A more precise measurement of output is the “specific yield” which measures the annual energy output per square meter of area swept by the turbine blades as they rotate. Overall, wind turbines capture between 20% and 40% of the energy in the wind. So at a site with average wind speeds of 7

m/s, a typical turbine will produce about 1,100 kWh per square meter of area per year. If the turbine has blades that are 50 m long, for a total swept area of 7,854 m^2, the power output will be about 8,600,000 kWh for the year. Increasing the blade length, the swept area increases and a significant effect on the amount of power output of the wind turbine can be achieved.

1.2.3 Estimation of potential wind resource

The global technical potential for wind energy is related to the status of the technology and assumptions made regarding other constraints to wind energy development. However, several global wind resource assessments have demonstrated that the world's technical potential exceeds current global electricity production [51]. According to some estimates, the technical potential for onshore wind energy is 180 EJ/yr (50,000 TWh/yr). Other estimates of the global technical potential for wind energy that consider relatively more development constraints range from a low of 70 EJ/yr (19,400 TWh/yr) (onshore only) to a high of 450 EJ/yr (125,000 TWh/yr) (on- and near-shore) [51]. This range corresponds to about one to six times global electricity production, and may understate the technical potential due to several of the studies relying on outdated assumptions and the exclusion of offshore wind energy. Estimates of the technical potential for offshore wind energy alone range from 15 EJ/yr to 130 EJ/yr (4,000 to 37,000 TWh/yr). Global climate change may alter the geographic distribution and the annual variability of the wind resource and the quality of the wind resource. Moreover, the occurrence of extreme weather events may impact wind turbine design and operation. Research to date suggests that it is unlikely that multi-year annual mean wind speeds will change during the present century even if research in this field is nascent and additional study is warranted.

The process to generate electricity from the wind requires the conversion of the kinetic energy of moving air into electrical energy, and the engineering challenge for the wind energy industry is to design cost-effective wind turbines and power plants to perform this conversion. There are several wind turbine configurations, but commercially available turbines are primarily horizontal axis machines with three blades positioned upwind of the tower. In order to reduce the cost of wind energy, typical wind turbine sizes have grown significantly (Fig. 1.3), with the largest fraction of onshore wind turbines installed from 2012 to 2015 having a rated capacity of 3 to 5 MW. These onshore wind turbines typically stand on 100- to 130-m towers, with rotors diameter of 80 to 130 m. Commercial machines with larger rotor diameters and tower heights are under development. Offshore wind energy technology is less mature than onshore due to higher investment costs. However, considerable interest in offshore wind energy exists in many countries. The main motivations to develop offshore wind energy are to provide access to additional wind resources in areas where onshore wind energy development is constrained by limited technical potential, the ability to use higher-quality wind resources located at sea and even larger wind turbines, and the ability to build larger power plants than onshore. As experience is gained, water depths are expected to increase and more exposed locations with higher winds will be utilised. Wind energy technology specifically for offshore applications may become more prevalent as the offshore market expands, and it is expected that larger turbines in the 5 to 10 MW range may come to dominate this segment.

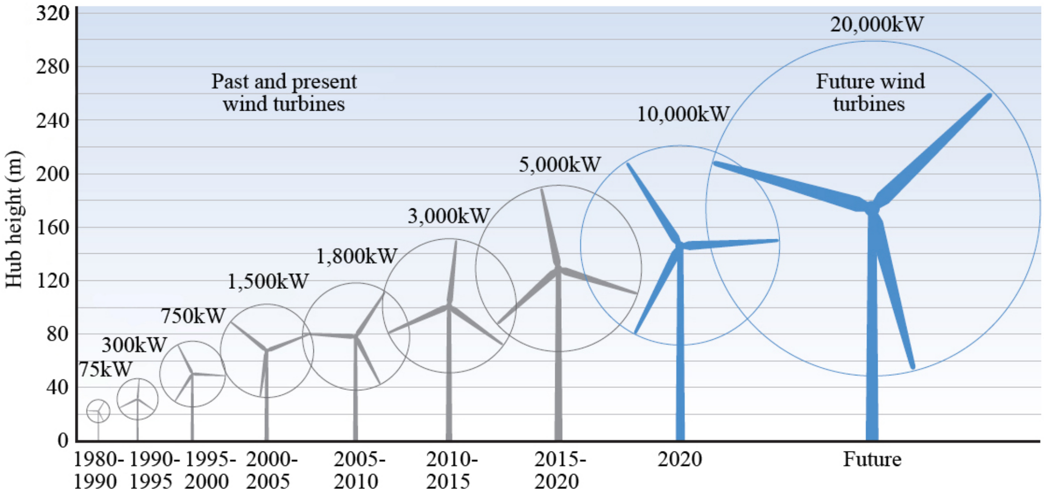

Figure 1.3: Growth in size of typical commercial wind turbines

1.2.4 Global origins

The original source of the energy contained in the Earth's wind resource is the sun. Global winds are caused by pressure differences across the Earth's surface due to the irregular heating of the earth by solar radiation which is greater at the equator than at the poles. The variation in incoming energy sets up convective cells in the lower layers of the atmosphere [95]. In a simple flow model, air rises at the equator and sinks at the poles. This circulation of the air that results from irregular heating is greatly influenced by the effects of the rotation of the earth (at a speed of about 1670 km/h at the equator, decreasing to zero at the poles) [95]. In addition, seasonal variations in the distribution of solar energy produce variations in the circulation. The spatial variations in heat transfer to the atmosphere create variations in the atmospheric pressure field that cause air to move from high to low pressure. The pressure gradient force in the vertical direction is usually cancelled by the downward gravitational force. Thus, the winds blow predominantly in the horizontal plane, responding to horizontal pressure gradients. In addition to the pressure gradient and gravitational forces, inertia of the air, the Earth's rotation, and friction with the Earth's surface (resulting in turbulence), affect the atmospheric winds. The influence of each of these forces on atmospheric wind systems differs depending on the scale of motion considered. The variability of the wind varies geographically and temporally, so it persists over a wide range of scales, both in space and time. The importance of this is amplified by the cubic relationship to available energy. On a large scale, spatial variability describes the fact that there are several climatic regions in the world. These regions are characterised by different latitude, which affects the amount of insolation [32]. Within each climatic region, there is a great variation on a smaller scale, caused by proportions of land and sea, size of land masses and presence of mountains or plains for example. Also the type of vegetation have a significant influence because its effects on the absorption or reflection of solar radiation affect surface temperatures and humidity. More locally, the topography has a major effect on the wind climate. More wind is experienced on the tops of hills and mountains than in sheltered valleys. More locally still, wind velocities are significantly reduced by obstacles such as trees or buildings.

At a given location, temporal variability on a large scale means that the amount of wind may vary from one year to the next, with even larger scale variations over periods of decades or more. These long-term variations are not well understood, and may compromise the accuracy of predictions of the economic viability of particular wind-farm projects. On time-scales shorter than a year, seasonal variations are much more predictable, but often not more than a few days ahead [32]. These variations are associated with the passage of weather systems. On these time-scales, the predictability of the wind is important for integrating large amounts of wind power into the electricity network, to allow the other generating plant supplying the network to be organized appropriately.

1.2.5 Statistical distribution of wind speed

Wind speed is a stochastic quantity. The most common density function used to represent wind speed is Weibull, whose probability density function $pd(V_\infty)$ is:

$$pd(V_\infty) = (\epsilon/z)(V_\infty/z)^{\epsilon-1}e^{-(V_\infty/z)^\epsilon} \ , \quad V_\infty > 0 \tag{1.1}$$

where V_∞ is the wind speed, ϵ is the shape factor, and z is the scale factor. As the names suggest, ϵ determines the shape of the curve and z determines the scale of the curve. (Fig. 1.4)

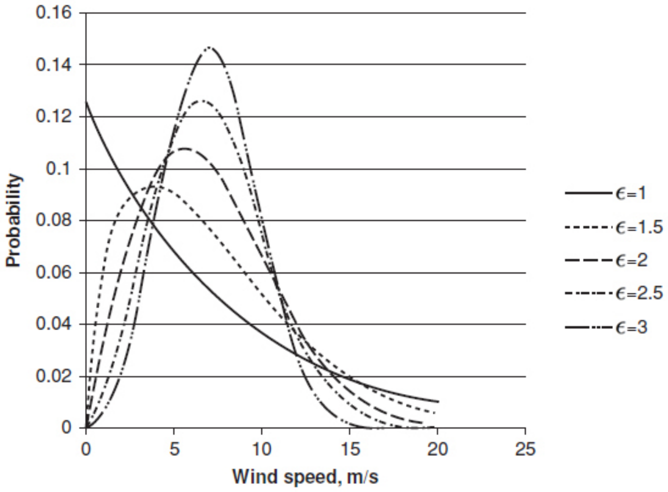

Figure 1.4: Weibull probability density function for $z = 8\ m/s$ [114]

As a convention when speaking about Weibull density function, wind speed V_∞ is the 10-min average. In a wind measurement campaign, for each 10-min interval the average wind speed and standard deviation are recorded. The Weibull probability density function is a model that represents the 10-min average wind speed. This assumes that over the 10-min interval the wind conditions are stationary. However, not all wind measurements are at 10-min intervals, therefore, it is important to mention the time interval when a reference is made to wind speed density function. Instead of a probability density function that represents the fraction of time wind speed is at V_∞, it is sometimes customary to speak in terms of hours in a year. That is, $pd(V_\infty)$ is multiplied by 8760 (number of hours in a year) (see Fig. 1.5). For instance, the area under the curve between 5 and 10 m/s represents the total number of hours in a year the wind speed is likely to be in that wind speed range. An example of Weibull distribution in terms of number of hours is seen in Fig. 1.5.

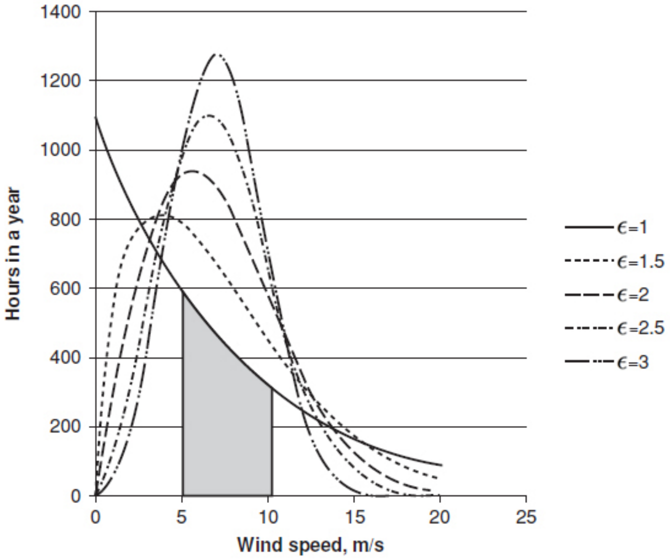

Figure 1.5: The Weibull probability density function expressed in hours per year [114]

Note that the Weibull distribution is defined only for positive value of wind speed. The other properties of the Weibull for different value of ϵ are:

- $\epsilon = 1$, the Weibull distribution becomes an exponential distribution.
- $\epsilon = 2$, the Weibull distribution becomes a Rayleigh distribution (Fig. 1.6).
- $\epsilon > 3$, the Weibull distribution approaches a Gaussian distribution.

Empirically, it has been observed that wind speed in most locations is a Weibull distribution. Furthermore, the value of ϵ is approximately 2 for most wind sites. In order to understand the impact of statistical distribution of wind speed on power generation, consider the impact on power density. Power density is defined as:

$$PD = \frac{Power}{Area} = \frac{1}{2}\rho V_\infty^3 \left[\frac{W}{m^2}\right] \tag{1.2}$$

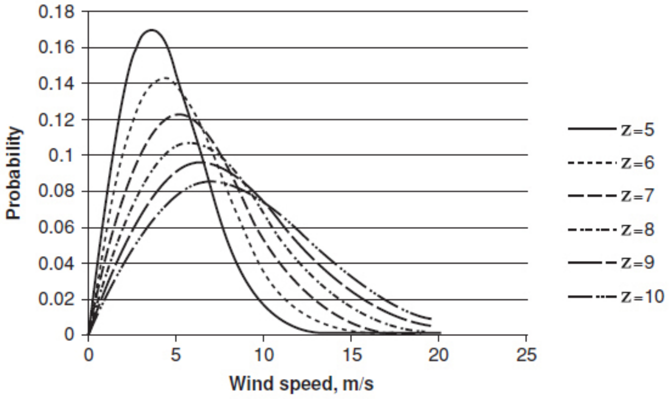

Figure 1.6: Weibull probability density function for $\epsilon = 2$ and different values of z [114]

If the statistical distribution of wind is ignored and it is assumed that there is no variation in wind speed, then the annual power density is incorrectly computed. However, if the energy density is computed correctly while taking into account probability density of wind speed, then the annual power density numbers are very different.

$$PD = \int_0^\infty \frac{1}{2}\rho V_\infty^3 pd(V_\infty)dV_\infty \tag{1.3}$$

where $pd(V_\infty)$ is the Weibull probability density function in Eq. (1.1).

1.3 Wind turbine

A wind turbine is a device that converts kinetic energy from the wind into electrical power. The smallest turbines are used for applications such as battery charging for auxiliary power for boats or caravans or to power traffic warning signs. Slightly larger turbines can be used for making contributions to a domestic power supply while selling unused power back to the utility supplier via the electrical grid. Arrays of large turbines, known as wind farms, are becoming an increasingly important source of renewable energy and are used by many countries as part of a strategy to reduce their reliance on fossil fuels. Wind turbines can be classified in a first approximation according to their rotor axis orientation and the type of aerodynamic forces used to take energy from wind.

1.3.1 Horizontal axis wind turbines

Horizontal axis wind turbines (HAWTs), such as those shown in Fig. 1.7, are the most common type of wind turbines in use today. In fact all grid connected commercial wind turbines are today designed with propeller-type rotors mounted on a horizontal axis on the top of a tower. In contrast to the mode of operation of the vertical axis turbines, the horizontal axis turbines need to be aligned with the direction of the wind, thereby allowing the wind to flow parallel to the axis of rotation.

Figure 1.7: Three-bladed upwind turbines [7]

A first HAWT distinction is made between upwind and downwind rotors. Upwind rotors face the wind in front of the vertical tower and have the advantage to avoid the tower shadow effect. This type of rotors need a yaw mechanism to keep the rotor axis aligned with the direction of the wind. Downwind rotors counterpart are placed on the lee side of the tower. A great disadvantage in this design is the fluctuations in the wind power due to the rotor passing through the wind shade of the tower which gives rise to more fatigue loads. Theoretically, downwind rotors can work without a yaw mechanism, the rotor and the nacelle can follow the wind passively [95]. This may, however, induce to a power cables twist when the rotor has been yawing passively in the same direction for a long time. For large wind turbines, it is rather difficult to use slip rings or mechanical collectors to avoid this problem. The vast majority of wind turbines in operation today have upwind rotors.

The three-bladed concept is the most common concept for modern wind turbines [49]. A turbine with an upwind rotor, an asynchronous generator and an active yaw system is usually referred to as the Danish concept. Relative to the three-bladed rotor, the two and one-bladed concepts have the advantage of representing a possible saving in relation to the cost and weight of the rotor. However, the use of fewer rotor blades implies that a higher rotational speed or a larger chord is needed to yield the same energy output as a three-bladed turbine of a similar size. The use of one or two blades will also result in more fluctuating loads because of the variation of the inertia, depending on the blades being in horizontal or vertical position and on the variation of wind speed when the blade is pointing upward and downward. Therefore, the two and one-bladed concepts usually have so-called teetering hubs, implying that they have the rotor hinged to the main shaft. This design allows the rotor to teeter in order to eliminate some of the unbalanced loads. One-bladed wind turbines are less widespread than two-bladed turbines. This is due to the fact that they, in addition to a higher rotational speed, more noise and visual intrusion problems, need a counterweight to balance the rotor blade.

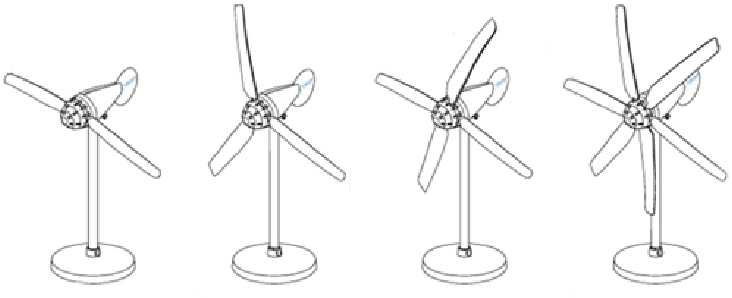

Figure 1.8: Example of multi blades wind turbines

Wind turbines are designed to produce electricity as cheaply as possible. For this purpose, wind turbines are designed to yield a rated power output at wind speeds around 13 m/s. In case of stronger winds, it is necessary to waste part of the excess energy to avoid damage on the wind turbine. Thus, the wind turbine needs a power control which is divided into two regimes with different concepts:

- power optimisation for low wind speeds
- power limitation for high wind speeds

These regimes are separated by the wind speed at which the rated power output is achieved, typically about 13 m/s. Basically, there are three approaches to power control:

- stall control
- pitch control
- active stall control

Stall-controlled wind turbines have their rotor blades at a fixed angle. The stall phenomenon is used to limit the power output when the wind speed becomes too high. This is achieved by designing the geometry of the rotor blade in such a way that flow separation is created on the downwind side of the blade when the wind speed exceeds some chosen critical value. Stall control of wind turbines requires correct trimming of the rotor blades and correct setting of the blade angle relative to the rotor plane. A drawback of this method is the lower efficiency at low wind speeds. Pitch-controlled wind turbines have blades that can be pitched out of the wind to an angle where the blade chord is parallel to the wind direction [106]. When the power output becomes too high, the blades are pitched slightly out of the wind to reduce the produced power. The blades are pitched back again once the wind speed drops. To optimise the power output at all wind speeds, the pitch control requires a design that ensures that the blades are pitched at the exact angle required. Pitch control of wind turbines is only used in conjunction with variable rotor speed. An advantage of this type of control is that the mean value of the power output is kept close to the rated power of the generator at high wind speeds. A disadvantage is the complexity due to the pitch mechanism and high power fluctuations at high wind speeds. Active stall-controlled turbines resemble pitch-controlled turbines by having pitchable blades [150]. At low wind speeds, active stall turbines will operate like pitch-controlled turbines. At high wind speeds, they will pitch the blades in the opposite direction of what a pitch-controlled turbine would do and force the blades into stall. This enables a rather accurate control of the power output, and makes it possible to run the turbine at the rated power at all high wind speeds.

A constant rotor speed has the same rotational speed while the wind turbine is generating energy; they do not need power electronics to adapt to grid frequency which makes them cheaper. A stall-regulated wind turbine falls into this category as it maintains constant RPM once the rated rotational speed is achieved. A variable speed rotor tries to achieve the optimum rotational speed for each wind speed, maintaining constant the optimum tip speed ratio will ensure optimum efficiency at different airspeeds. From a structural point of view, letting the rotor change its speed reduces the load supported by the wind turbine in presence of gusts or sudden starts.

A wind turbine tower is the main structure which supports rotor, power transmission and control systems. A successful structural design of the tower should ensure efficient, safe and economic design of the whole wind turbine system. It should provide easy access for maintenance of the rotor components and sub-components, and easy transportation and installation. Moreover, the tower raises the wind turbine so that its blades safely clear the ground and it can reach the stronger winds at higher altitude. There are many types of wind towers on the market today. They vary in size and structure and are designed to support wind turbines of different size and output.

- Guyed tower: a guyed tower is one which is held in place with guy wires. The tower itself is often just a long steel pole. There are usually three or four guy lines which run from the top of the tower to the ground and hold the tower in place. Guyed towers are often the cheapest type of wind tower and are often an excellent choice for a small residential scale wind turbine.

- Guyed tilt-up tower: this is a type of guyed tower which has a pivot joint at the base of the tower so one can easily raise the tower initially or lower it to do maintenance on the turbine later. As with all guyed towers, one needs to have a large space for the guy wires and for the tower.

- Freestanding lattice tower: this type of tower is made of steel or aluminium lattice work. Because this type of tower cannot be laid down it will usually include a built-in ladder so that someone can climb the tower to do maintenance on the turbine. The latticed frame includes many structural supports and so is usually extremely sturdy and holds up well in high winds. Latticed towers have the advantage that they take up less space but usually cost more than guyed towers because they use more steel [42].

- Freestanding tubular tower: this tower is constructed as a large tube. On most of the larger towers of this type there is a ladder inside of the tube so that a worker can climb the tower to do maintenance on the turbine. Most large commercial scale turbines use this design. As the commercial wind industry has grown, tubular towers for turbines in the 3 MW to 5 MW range have become quite large and tall.
- Floating tower: a floating wind tower is an offshore wind turbine mounted on a floating structure. In most cases the wind turbines are held in place by wires or chains attached to weights on the ocean floor. One advantage of mounting turbines at sea is that the wind is strong and not disrupted by any terrain features.

1.3.2 Vertical axis wind turbines

Vertical axis wind turbines (VAWTs) have been developed in parallel with HAWTs, but with less financial support and less interest. The engineer S.J. Savonius invented the Savonius turbine in 1922, (see left of Fig. 1.10) [112]. In 1931, Georges Darrieus patented his idea to have a VAWT with straight blades, (see middle and right Fig. 1.10) [46].

During the 1970s and 1980s vertical axis machines came back into focus when both Canada and the United States built several prototypes of Darrieus turbines. The prototypes proved to be quite efficient and reliable [112]. According to a report from Sandia National Laboratories in the USA, the VAWTs fell victims to the poor wind energy market in the USA [58]. In the 1980s the American company FloWind commercialised the Darrieus turbine and built several wind farms with Darrieus turbines [136]. The machines worked efficiently but had problems with fatigue of the blades, which were designed to flex [111]. The Eole, a 96 m tall Darrieus turbine built in 1986, was the largest VAWT ever built with a rated maximum power of 3.8 MW [41]. The machine was shut down in 1993 due to failure of the bottom bearing. The straight-bladed VAWT was also an invention included in the Darrieus patent [46]. This turbine is usually referred to as the straight-bladed Darrieus turbine or the H-rotor, but has also been called giromill or cycloturbine (different concepts of the same invention) (see

Figure 1.9: Example of vertical axis wind turbine [10]

right Fig. 1.10). In the United Kingdom, the H-rotor was investigated by a research team led by Peter Musgrove [112,107,103]. The biggest H-rotor built in the UK was a 500 kW machine, which was designed in 1989 [97]. In the 1990s, the German company Heidelberg Motor GmbH worked with development of H-rotors and they built several 300 kW prototypes [148].

VAWTs may have either drag-driven or lift-driven rotors. The Savonius rotor is the most common drag-driven VAWT. It has been used for water pumping and other high-torque applications. An advantage of Savonius rotor turbines is that they can be relatively inexpensive to build. In practice, being a drag-driven machine, they have intrinsically low power coefficients. In addition, they have a solidity approaching 1.0, so they are very heavy relative to the power that they produce. When VAWT have been used for electrical power generation they have nearly always used lift-driven rotors

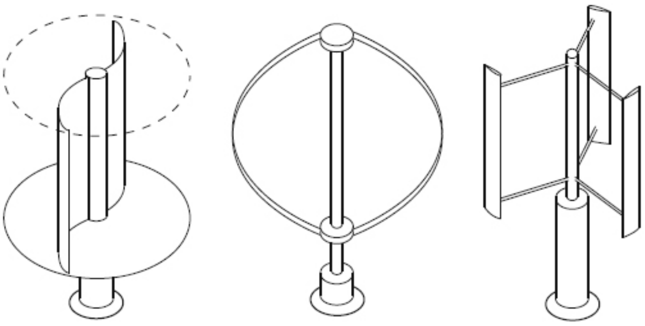

Figure 1.10: Savonius rotor (left), Darrieus turbine (middle) and H-rotor (right) [124]

(Darrieus rotor type). Some rotors with straight blades have incorporated a pitching mechanism, but most lift-driven vertical axis turbines have fixed pitch blades. Thus, power limitation at high winds is accomplished by stalling.

Compared to HAWT, the vertical rotational axis of a VAWT allows the generator to be located at the bottom of the tower. This makes installation, operation and maintenance much easier. The tower can be lighter since the nacelle is excluded, which reduces structural loads and problems with erecting the tower [30]. The generator design can be focused on efficiency, cost and minimising maintenance, as the size of the generator is not a problem. The control system can also be located at ground level to facilitate access [123]. Direct drive here denotes a solution where the turbine is directly connected to the rotor of the generator. By using a direct drive generator, the gearbox is excluded from the system. A gearbox is often associated with breakdown and need of maintenance [22]. Furthermore, a direct drive system is much more efficient than a generator with a gearbox, since the gearbox is a source of losses comparable to the losses in the generator. The overall system, when excluding a gearbox, is simpler and it is easier to install. Since a direct drive machine is more bulky and has a larger diameter than a generator that includes a gearbox [57], the advantage of using a vertical axis turbine is that the generator is placed on the ground and the size is not an issue.

Other differences between HAWT and VAWT is that the blades of a HAWT have to be self-supporting since they are only attached at the root while the blades of an VAWT are supported by radial arms, which usually are attached to the centre of the blades. However, the arms add extra structure and mass to the turbine. The blades of a H-rotor, for example, are much easier to manufacture than the blades of a HAWT.

The blades of the latter have different shape along the length of the blade and the blades might also be twisted. The blade area is often larger for an H-rotor than for a HAWT with the same rated power. Mass production of H-rotor blades would imply low production costs since their shape makes them easy to fabricate in large numbers compared to HAWTs [30]. The VAWTs are normally placed on top of a high tower, just as the HAWT, in order to reach higher and less turbulent winds. Guy wires could be used to support the shaft of a turbine since it gives a more robust construction. The blade of a HAWT is subject to a gravity-induced reversing stress at the root of the blade, which is not the case for VAWT blades [102, 128]. This is believed to be the main limitation for increasing the size for HAWTs. Furthermore, HAWTs have relatively constant torque over the rotor period of revolution. VAWTs have an inherent torque ripple [30]. The torque ripple is caused by the continuously changing angle of attack between the blades and the apparent wind. The torque ripple can affect the fatigue life of the drive train components as well as the output power quality [119]. By increasing the number of blades to three or more, the torque ripple is decreased substantially [13]. Furthermore, the problem with torque ripple is decreased when the turbine is operated at variable speed. The aerodynamic forces on the blades caused by the changing angle of attack will also cause a cyclic aerodynamic stress on the blades.

The trend in wind power development is the increasing of the size of the turbines. Steven Peace, director of the company Eurowind Developments Ltd., believes in multi-megawatt VAWTs [111, 96], which was suggested by Musgrove 20 years ago [107]. They both claim that HAWTs have reached their maximum size and that the size will not be of economic benefit anymore. The reason for this is the cyclically reversing gravity loads on the blades, which increases with an increasing turbine size. For VAWTs there are no such limit and therefore VAWTs are a good replacement for the HAWTs as the size of the turbines are expected to continue increasing. On the other hand, Riegler finds the biggest value in small VAWTs [120]. He claims that HAWTs are so economical they might be hard to beat when it comes to big turbines, but that small VAWTs can play their role in areas where HAWTs do not work that well for example in mountain areas or in regions with extremely strong and gusty winds, for instance roof tops.

1.4 Wind turbine aerodynamics

Wind turbine power production depends on the interaction between the rotor and the wind. As reported before, the wind may be considered to be a combination of the mean wind and turbulent fluctuations about that mean flow. Periodic aerodynamic forces caused by wind shear, off-axis winds, and randomly fluctuating forces induced by turbulence and dynamic effects are the source of fatigue loads and are a factor in the peak loads experienced by a wind turbine. Horizontal and vertical axis wind turbine designs use aerofoils to transform the kinetic energy in the wind into useful energy. The classical analysis of the wind turbine was originally developed by Betz and Glauert [60] in the 1930s. Subsequently, the theory was expanded and adapted for solution by digital computers [156, 157, 47].

1.4.1 Horizontal axis machines

A simple model, generally attributed to Betz, can be used to determine the power from an ideal turbine rotor, the thrust of the wind on the ideal rotor, and the effect of the rotor operation on the local wind field. The analysis assumes a control volume, in which the control volume boundaries are the surface of a stream tube and two cross-sections of the stream tube. The only flow is across the ends of the stream tube. The turbine is represented by a uniform “actuator disc” which creates a discontinuity of pressure in the stream tube of air flowing through it. Assuming that the affected mass of air remains separate from the air which does not pass through the rotor disc and does not slow down, a boundary surface can be drawn containing the affected air mass, and this boundary can be extended upstream as well as downstream forming a long stream-tube. No air flows across the boundary and so the mass flow rate of the air flowing along the stream-tube will be the same for all stream-wise positions along the stream-tube. Since fluid compressibility effects can be ignored due to the low air speed, the cross-sectional area of the stream-tube must expand to accommodate the slower moving air (Fig. 1.11). Although kinetic energy is extracted from the airflow, a sudden step change in velocity is neither possible nor desirable because of the enormous accelerations and forces this would require. Pressure energy can be extracted in a step-like manner, however, and all wind turbines, whatever their design, operate in this way. The presence of the turbine causes the approaching air, upstream, to gradually slow down so that when the air

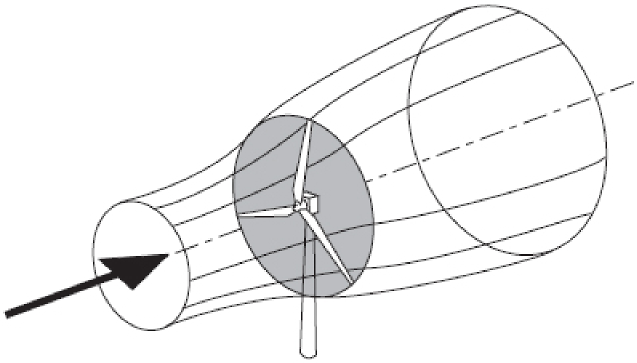

Figure 1.11: Energy extracting stream-tube of a wind turbine [32].

arrives at the rotor disc its velocity is already lower than the freestream wind speed. The stream-tube expands as a result of the deceleration and, because no work has yet been done on or by the air, its static pressure rises to absorb the decrease in kinetic energy. As the air passes through the rotor disc, there is a drop in static pressure such that, on leaving, the air is below the atmospheric pressure level. The air then proceeds downstream with reduced speed and static pressure. Far downstream, the static pressure will return to the atmospheric level. The rise in static pressure is at the expense of the kinetic energy and so causes a further deceleration of the wind. Thus, between the far upstream and far downstream conditions, no change in static pressure exists but there is a reduction in kinetic energy. According to Betz's law, no turbine can capture more than 59.3% of the kinetic energy in wind (see *Appendix A* for details). Modern large wind turbines achieve peak values of power coefficient C_p between 0.45 and 0.50 [32] about between 75% and 85% of the theoretically possible maximum.

The HAWT blades use aerofoils to develop mechanical power. The width and the length of the blade are functions of the desired aerodynamic performance, the maximum desired rotor power and the assumed aerofoil properties. From blade element analysis [78] it is possible to express the forces acting on the blade as function of lift and drag coefficients and the angle of attack. Generally, lift and drag coefficients of an aerofoil are generated by the pressure variations over the aerofoil surface and the friction between the air and the aerofoil. Dividing the blade into N_{be} elements (with radial length dR), one can represents the forces on a specific section, which are characteristics of the aerofoil shape of the blade. As shown from Fig. 1.12, incremental lift dF_L is the force perpendicular to the direction of a relative wind W and incremental drag force dF_D is parallel to the direction of a relative wind [78].

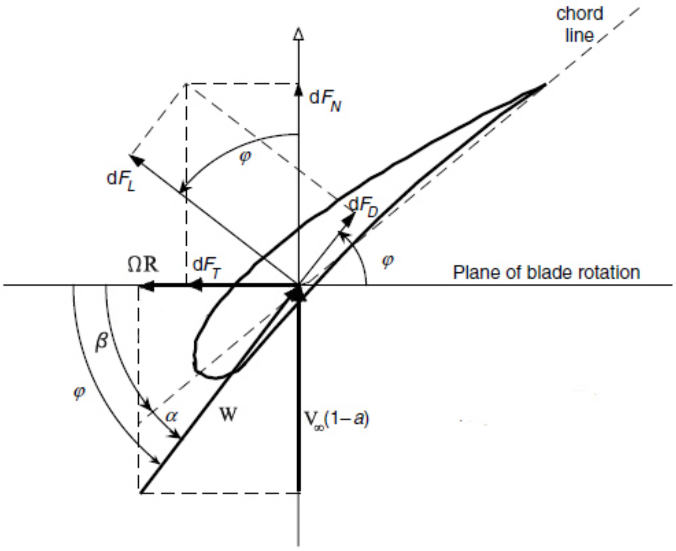

Figure 1.12: Forces acting on a blade section of HAWT [95]

Lift and drag can be split into components parallel and perpendicular to the direction of freestream wind speed $V_\infty(1-a)$ (where a is the induction factor defined as the fractional decrease in wind velocity between the freestream and the rotor plane) to give the incremental force dF_N and dF_T. dF_N is the force normal to the rotor plane and contributes to the thrust, while dF_T is tangential to the rotor plane and creates useful torque. Other important parameters showed in Fig. 1.12, are the pitch angle β, which is the angle between the chord line of the blade and the plane of rotation, the angle of attack α between the chord line of the blade and the relative wind or the effective direction of air flow and ϕ that is the angle of the relative wind. The blade section velocity at distance R from the hub is ΩR, where Ω is the angular velocity.

1.4.2 Vertical axis machines

By the nature of the aerodynamics of the rotor of VAWTs, the structural loads on the blades vary greatly during the rotation. Such loads contribute to high fatigue damage, and require that the blades and joints themselves have a very long cycle life. In addition, the vertical axis turbines do not lend themselves to being supported by a separate, tall tower. This means that a large fraction of the rotor tends to be located close to the ground in a region of relatively low wind. Productivity may then be less than that of a horizontal axis machine of equivalent rated power, but on a taller tower.

Taking into account a straight-blade Darrieus rotor, a single blade of this machine is illustrated in Fig. 1.13. In the figure the blade is shown rotating in the counter-clockwise direction, and the wind is seen impinging on the rotor from left to right. As is typical in VAWT, the aerofoil is symmetric. The blade is oriented so that the chord line is perpendicular to the radius of the circle of rotation. The radius R defining the angular position of the blade forms an angle of θ with the wind direction. As shown in Fig. 1.13, V_∞ denotes the absolute wind velocity vector which is defined as the vector sum of the relative velocity and the entrainment velocity ΩR. The entrainment velocity vector due to the rotation is tangential to the circle of rotation, and thus parallel to the chord line of the aerofoil. The velocity vector $V_\infty(1-a)$ denotes the wind velocity near the blade. An induction factor, a, accounts for the deceleration in the wind as it passes through the rotor. By Pythagoras's Theorem, one can find the wind velocity relative to the blade element (W). It is illustrates in Fig. 1.14 and it is defined as:

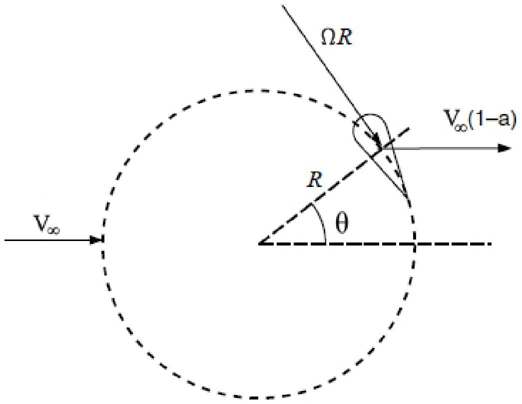

Figure 1.13: Schematic view of a vertical axis wind turbine [95]

$$W^2 = \{\Omega R + (1-a)V_\infty \sin(\theta)\}^2 + \{(1-a)V_\infty \cos(\theta)\}^2 \tag{1.4}$$

Equation (1.4) can be rewritten as:

$$\frac{W}{V_\infty} = \sqrt{\{\lambda + (1-a)\sin(\theta)\}^2 + \{(1-a)\cos(\theta)\}^2} \tag{1.5}$$

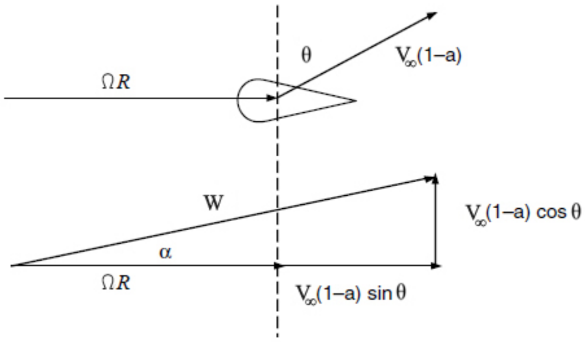

Figure 1.14: Velocity triangles of a VAWT blade section.

where:

$$\lambda = \frac{\Omega R}{V_\infty} \tag{1.6}$$

The symbol λ denotes the tip speed ratio. Note that at high λ, the second term under the square root becomes small, so that:

$$\frac{W}{V_\infty} \approx \lambda + (1-a)\sin(\theta) \tag{1.7}$$

The λ is of vital importance in the design of wind turbine generators. If the rotor of the wind turbine turns too slowly, most of the wind will pass undisturbed through the gap between the rotor blades. Alternatively if the rotor turns too quickly, the blurring blades will appear like a solid wall to the wind. Therefore, wind turbines are designed with optimal tip speed ratios to extract as much power out of the wind as possible. Different types of turbine have completely different optimal tip speed ratio values, for example a Darrieus wind turbine which generates aerodynamic lift has an high λ, but a Savonius wind turbine which is also a VAWT but drag driven, has a λ less than 1.

Since the chord is perpendicular to the radius of the circle, an angle of attack (α) is defined as:

$$\alpha = \tan^{-1}\left[\frac{(1-a)\cos(\theta)}{\lambda + (1-a)\sin(\theta)}\right] \tag{1.8}$$

The VAWTs have an inherent unsteady aerodynamic behaviour due to the variation of angle of attack with azimuthal position. The maximum values of α during a complete revolution decrease as the λ increases. The phenomenon of dynamic stall is then an intrinsic effect of the operation of VAWTs at low λ, having a significant impact on power production. More details on vertical axis machines aerodynamics are reported in *Chapter 5*.

1.5 Navier-Stokes analysis of periodic wind turbine flows

Periodic wind turbine flow problems are often represented as nonlinear dynamical systems. The complexity of the unsteady aerodynamics of wind turbine devices make them too intricate to solve analytically, so they must be analysed experimentally or using Computational Fluid Dynamics (CFD) through numerical simulations.

CFD is based on the Navier-Stokes (NS) equations which are the fundamental governing equations of fluid dynamics: continuity, momentum and energy equations. Most NS CFD analyses of wind turbines aerodynamics are based on the so-called Reynolds Averaged Navier-Stokes (RANS) approach, whereby the time-dependent NS equations are averaged on the time- and length-scales of turbulence. This yields the RANS equations, a system of partial differential equations (PDEs) formally similar to the steady NS equations, and differing from them primarily because of the presence of the Reynolds stresses, accounting in an averaged manner for the effects of turbulence. Different approaches exist for calculating the components of the Reynolds stress tensor, the tensor required for the local calculation of the components of the "turbulent" stress vector. The most widely used turbulence closure approach consists of assuming that the Reynolds stress tensor depends linearly on the strain tensor through a space-dependent scalar called turbulent or eddy viscosity, and solving one or two additional PDEs yielding the eddy viscosity. Popular examples include the $k - \omega$ Shear Stress Model (SST) [101] requiring the solution of two additional equations for the turbulence closure, and the one equation $Spalart - Allmaras$ model [138].

The traditional approach for solving nonlinear dynamical systems begins with a spatial discretisation of the governing equations, followed by a temporal discretisation. In case of time-periodic flows the solution is time-marched from an initial state until a user-given final time. A drawback of using time-marching methods for time-periodic problems is that they include a transient response in the solution. So, time marching approach can become inefficient when several periods have to be simulated before a fully developed periodic solution is achieved. In order to reach the periodic solution in a short time and accelerate the wind turbine unsteady flow analysis, the harmonic balance

(HB) technology can be applied. It is a frequency-domain (FD) method introduced by Hall et. al [65] who first showed the run-time reduction compared to the time-domain approach, for the case of turbomachinery flows. This technology has also been applied to the prediction of the periodic flow associated with flutter and forced response of turbomachinery blades [140, 149], and various vibratory motion modes of aircraft configurations [44, 130, 158]. For this type of applications, the HB NS approach for the calculation of periodic flows can lead to a reduction of the wallclock time varying between one and two orders of magnitude with respect to conventional TD NS analyses.

In this thesis the HB approach was used for the first time on wind energy applications and has been demonstrated that the HB approach is a computationally efficient alternative to time marching method [36].

1.6 Motivation, objectives and overview of the thesis

The main topics of the research work reported in this thesis were to develop, assess and validate a novel frequency-domain method and modelling technology to improve the computational efficiency of the RANS model-based analysis of unsteady complex systems, where fluids play a significant role. Moreover the work aimed to demonstrate the accuracy and the effectiveness of the developed technologies by using the new RANS framework to investigate turbulent unsteady flow past horizontal and vertical axis wind turbines rotors.

The objectives associated to the algorithmic work concerned the development of a turbulent RANS SST harmonic balance solver for the rapid solution of periodic flows, the integration of LAPACK libraries to massively improve the computational efficiency of a semi-implicit approach to the integration of the HB RANS equations [36] and the assessment of the RANS-based analysis of wind turbines periodic flows achieved by using the harmonic balance rather than the conventional time-domain approach.

The thesis presents several elements of novelty like a high dimensional harmonic balance approach to solve several turbulent unsteady flows past some renewable energy devices like horizontal axis wind turbine sections in yawed wind condition and vertical-axis wind turbines for a wide range of tip speed ratios, highlighting a very good agreement with time-domain results. On the modelling side, the thesis reports some important parametric analysis on the numerical set-up like the sensibility to the farfield boundary distance, sensibility to mesh and temporal refinement and sensibility to the characteristic turbulent variables of the SST turbulence model.

Chapter 2 gives an explanation on wind turbines unsteady environment like dynamic stall, atmospheric turbulence, wind shear, misalignment of the rotor to the incoming wind, tower shadow and wake/blade interactions. The *Chapter 3* reports in great detail the time-domain formulation of the compressible RANS and SST turbulence model equations and the cell-centred finite volume space discretisation. It shows the iterative solver used to solve iteratively the steady and time-domain RANS equations and it also mentioned the methods used for the space discretisation of the convective fluxes, the diffusive fluxes and the source terms of the SST turbulence model. *Chapter 4* presents the classical formulation of the harmonic balance method for finding the periodic solution of systems of ordinary differential equations, and the so-called high-dimensional formulation of the harmonic balance method, which is a variant of the former formulation better suited to the numerical solution of the Navier-Stokes equations. The chapter also reports a description of the optimisation performed on the point-implicit numerical integration of the HB RANS and SST equations, incorporating the lower-upper factorisation of the LAPACK package in the considered CFD solver. *Chapter 5* focuses on the time-domain analysis of a Darrieus rotor, including the computational set-up, the space and time-refinement sensitivity analyses, assessment of the sensitivity of the computed solution varying farfield boundary distances and validation of the predictive flow capabilities of the CFD research code used in this thesis. A detailed aerodynamic analysis is reported to show the behaviour of a VAWTs in all operating conditions (from low to high tip speed ratios). Time-domain analyses on a HAWT in yawed wind conditions is reported in *Chapter 6*. Two different aerodynamics analyses are shown for inboard and outboard blade sections of a 164 m diameter machine in terms of unsteady forces acting on the blades. An explanation of the yawed wind modelling and the computational set-up is also reported. *Chapter 7* presents the HB acceleration of wind turbines unsteady flows analyses for vertical and horizontal axis wind machines, showing the flow predictive capabilities of the HB approach, the accuracy and the computational performances. The main motivation of these analyses is to assess the computational benefits achievable by using the HB solution of the RANS and SST equations rather than the conventional TD solution, and also to further demonstrate the predictive capabilities of the developed CFD system. The conclusions of the thesis and future work are provided in *Chapter 8*.

1.7 Conclusion

An overview of the existing renewable energy installations and the contribution to the global energy supply has been presented in this chapter. Today, wind power is the fastest growing source and the most economically competitive energy compared to other renewables because the cost of wind turbines is getting cheaper thanks to the technology advancement and government incentives. Typical wind turbines used to generate electricity are horizontal axis rotors with three blades mounted on a tubular tower. The installation of VAWTs is increasing rapidly thanks to the several advantages over HAWTs for wind energy capture. The aerodynamic design of these machines is a challenging task, since reliable quantitative estimates and sound understanding of the aforementioned unsteady aerodynamic phenomena is required to obtain the power output as a function of the wind and turbine speeds. A discussion on the different types of horizontal and vertical axis wind turbines, control systems, rotor towers and blades aerodynamics has been reported.

Chapter 2

Wind turbine unsteady flows

2.1 Unsteadiness in horizontal axis machines

There are several unsteady aerodynamic phenomena which have a large impact on HAWTs operation. The turbulent wind conditions cause rapid changes in speed and direction over the rotor disc. These changes cause blade vibrations, fluctuating aerodynamic forces and material fatigue. Additionally, the effects of tower shadow, dynamic stall and yawed wind, change turbine operation in unexpected ways. Several experimental measurements performed in wind tunnels and several studies based on analytical models and CFD approaches have been done during the years. An overview of the research works on horizontal axis machines is reported in the next subsections.

2.1.1 Tower shadow

Tower shadow is a phenomenon that occurs in downwind rotors (Fig. 2.1). It refers to the wind speed deficit behind a tower caused by the tower obstruction. The blades will encounter the tower shadow once per revolution, causing a rapid drop in power and vibrations in the turbine structure. As can be expected a downwind turbine rotor will give larger and more fluctuating tower interferences than its upwind counterpart. Many studies [64, 92, 59] over the recent years have tried to describe the tower shadow impact on the blade fatigue loading. They have considered several tower geometries and used several approaches like wake models, CFD simulations and model scale experiments.

Reiso et al. [118] conducted an experiment run in the wind tunnel at the Norwegian University of Science and Technology to determine the wind forces that act on a rotor

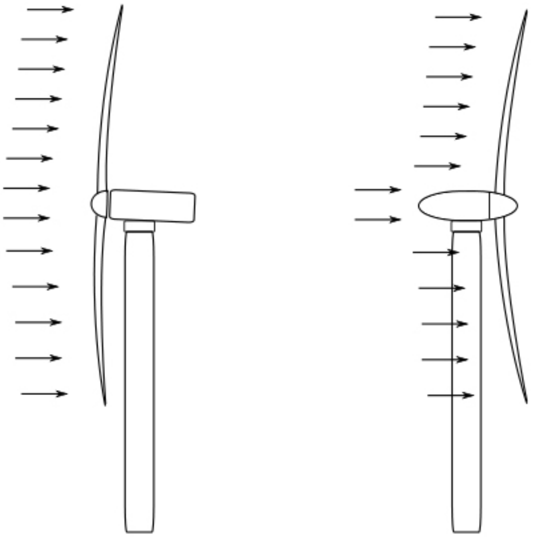

Figure 2.1: Upwind rotor (left), downwind rotor (right)

mounted on the downwind side of the tower. The experiment was carried out using both a model for a tubular and truss tower (Fig. 2.2). The towers were scaled down from

Figure 2.2: Tubular and truss tower (left and right, respectively).

the NREL Offshore 5-MW Reference Turbine [80]. Both scaled tower heights were 762 mm. Both towers were placed at a distance from the measuring-point corresponding to the distance between the tower and rotor plane (the rotor turbine was not considered in the experiment). Measurements referred to a freestream wind speed equal to 11.4 m/s and freestream turbulence level in the tunnel of 0.4%. A hot-wire anemometer was used to measure the mean and turbulent wind velocity at the centreline behind the tower, and at several positions on the right side of the tower (see Fig. 2.3). The truss tower was tested in two positions, 0 degrees and 45 degrees towards the wind direction. From the experimental results, the largest mean velocity deficit behind the towers was found at the centreline of the tubular tower, showing a minimum wind velocity of 4.6 m/s. The truss tower showed multiple velocity deficits, originating from the different truss members across the tower region, but smaller compared to the tubular tower. These deficits behind the towers corresponded to a reduction of the freestream wind velocity of the 60%, 44% and 31% for the tubular tower, truss at 45^o and truss at 0^o angle towers respectively. This conclusion highlight that truss tower results advantageous for downwind rotor configuration.

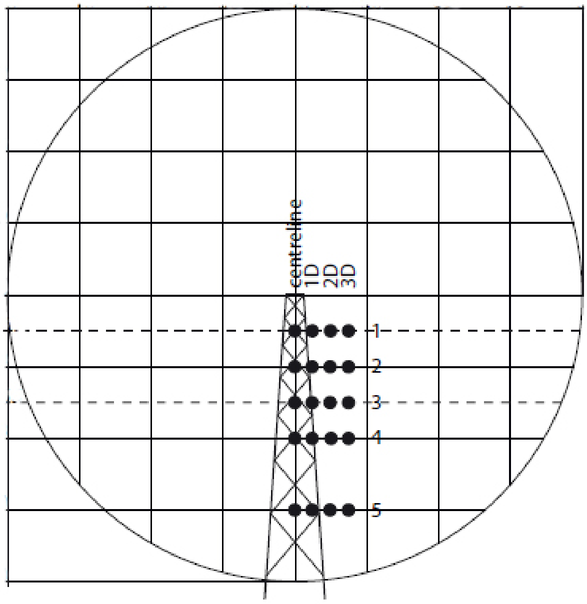

Figure 2.3: Measurement points behind the towers in the rotor plane. $D = 2.5$ cm is tubular tower diameter [118]

Hagen et al. [64] presented a study on numerical analysis of turbulent flow past two dimensional (2D) cross sections of both a monopile and a truss tower. Moreover, the tower shadow models of Powles [113], Blevins [28] and Schlichting [126] were compared with numerical results. The numerical model was implemented in the commercial software ANSYS FLUENT. An approximation adopted was the bidimensionality of the model. The truss tower was represented by four main cylinders and an intersection between the main cylinders was represented by eight additional smaller cylinders. For the monopile, the geometry was represented as a single cylinder. In both cases the computational domain was rectangular. The top and bottom side of the domain were implemented with periodic boundaries while the outflow boundary was implemented with the reference pressure of one atmosphere. The inflow boundary was implemented with a freestream velocity of 12 m/s, which represented a typical rated wind speed for offshore wind turbines. The turbulence parameters were specified by turbulence intensity of 10% and length scale of 1 m. Using the RANS coupled to the $k-\omega$ SST turbulence model, the CFD approach was able to reproduce the main properties of the flow regime and the results were in excellent accordance with the literature [152]. The comparison of the three steady parametric wake models results (Powles [113], Blevins [28] and Schlichtings [126]) with the CFD results, highlighted that the velocity profile behind the monopile tower was predicted fairly well from all three wake models, but they did not predict very well the velocity profiles behind the truss tower. The deficit of the steady wake models to accurately predict the flow behind truss towers was due to the fact that those models do not account for the interacting effects between the truss tower members. A tower shadow model able to predict all features of a flow field behind a multi-member tower is difficult to realise because their simplifications try to generalise a complex flow situation, for example when several wakes from different members interact to each other, thus the CFD is a good approach to accurately predict the tower shadow effect.

As seen from the study of Reiso et al. [118], the tower shadow effect and the cyclic fatigue loading on the downwind rotor could be reduced using a truss tower instead of the traditional tubular tower. Moreover, according to Long and Moe [92], a truss tower can save up to 50% of the material compared to a tubular tower. This estimate is for an upwind rotor configuration. For a downwind rotor configuration the material savings could be even more if the blades are specially designed.

2.1.2 Dynamic stall

The components of a wind turbine, such as generators and blades, are frequently subjected to variable dynamic loading. A source of fatigue derives from the cyclic load due to the blade weight, that affects the turbines during their entire life. Another source of fatigue is related to aerodynamic unsteadiness that vary all the time like dynamic stall. Dynamic stall is a nonlinear aerodynamic effect that occurs when the angle of attack (AoA) exceeds the static stall limit, and when the AoA keeps changing. Such effect at the blade surface is not easy to predict and affect turbine operations. A dynamic stall model is necessary to predict peak and fatigue loads on the blade. If the dynamic stall affect smaller regions of the blade, the latter can achieve a longer operational life with less maintenance operations. Currently, the impulsive loading introduced by dynamic stall aerodynamic models can amplify, or have little effect on the resulting structural loads [121]. Fully appreciate the three-dimensional aerodynamic response of a turbine rotor is very complex. One needs to consider multiple effects like blade geometry, pitch, turbine architecture, wind magnitude and local angle of attack. For downwind turbines there are additional complexity like tower shadow effect which occurs when the wake from the tower intersects the rotor plane downstream. As the blade crosses the tower shadow, the wake velocity deficit change the value of the AoA until the blade moves out of the wake. This variation of the AoA due to the tower shadow effect can also induce dynamic stall events [121].

Choudhry et al. [43] proposed an analytical model in order to relate rapidly changing of wind speeds and directions to the dynamic variations in blade section angle of attack. The model validation using the HAWT described by Schreck et al. [127] was also reported in [43]. The case study used for the prediction of dynamic stall occurrence along a wind turbine blade was performed using a theoretical wind turbine with a rotor diameter of 15 m, a tower height of 10 m, a constant chord length of 3 m and a rotational speed of 30 RPM. Two types of blade aerofoils were considered, S809 and NACA0012. Using ambient wind conditions as wind speed, yaw angle and rates of change of these parameters as input of the analytical model, the authors observed that the model was able to predict the regions of the wind turbine blade affected by dynamic stall. The authors observed that the aerofoil type had a large effect on dynamic stall, indeed, the NACA0012 aerofoil was more resistant to dynamic stall compared to the

S809 aerofoil. In other words, considering the same input wind conditions, it was observed that approximately 90% of the S809 blade was affected by dynamic stall against 70% of the blade for the NACA0012.

2.1.3 Yawed wind

A wind turbine in operation will not always experience wind perpendicular to the rotor plane. It is impossible to have a wind turbine axis permanently aligned toward the wind direction, and hence, the flow is often yawed. Without any yaw control, the turbines would constantly operate in large yaw errors (Fig. 2.4).

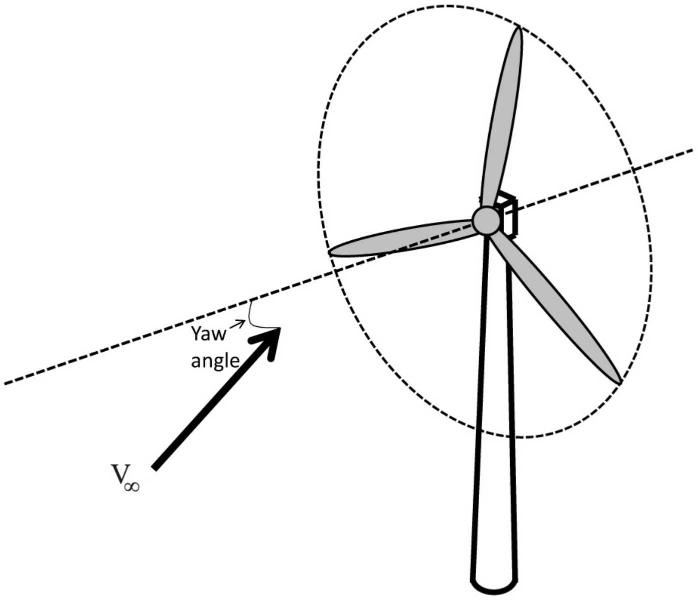

Figure 2.4: HAWT in yaw condition [91]

Under these conditions the power extracted from the wind decreases. To avoid this phenomenon the wind turbines have a yaw control which tracks the direction of the wind and rotates the nacelle to achieve the realignment. Even if controlling action is not instantaneous, both large and small HAWTs rarely operates in large yaw, and therefore are not likely to experience too much dynamic stall due to yaw, except in cases when the yaw control system is faulty. Several research works have been performed to investigate the flow around the blades of a HAWT operating in yawed condition [48, 147] .

An investigation of the performance characteristics and near wake of a three-bladed upwind rotor type in yawed condition was proposed by Adaramola et al. [12]. The experiments were performed in a low-speed wind tunnel. The turbine rotor had a blade chord length of 82 mm at the rotor root and 26 mm at the tip, the rotor diameter was 900 mm and its height on the ground plane was 820 mm. The performance measurements were conducted for various yaw angles (δ), freestream wind speed of about 10 m/s, and for λ from 0 to 12. From the performance characteristics of the turbine in yawed condition was shown that the effects of yaw angle on the performance were quite large. The power coefficient at non-yawed condition (when the wind is perpendicular to the rotor plane of the turbine, $\delta = 0^o$) was similar to the expected power curve characteristics for the wind turbine considered. Increasing the yaw angle ($\delta > 0^o$) the maximum achievable power coefficient reduced as reduced the total swept area and less power was extracted from the wind. The maximum λ for which positive power was obtained, was about 11.6 for the wind turbine examined for $\delta = 0^o$ and this value decreased as the yaw angle increased. The power loss was found about 4% when the yaw angle was less than 10^o, and over 30% when the yaw angle was greater than 30^o. The effect of yaw on the torque coefficient was also analysed in [12]. The torque was measured directly on the rotor shaft and the authors highlighted that increasing the yaw angle, there was a general reduction in the total torque coefficient of the wind turbine.

2.1.4 Wind shear

HAWT are also influenced by periodical loads due to wind shear. These loads could cause fatigue of the blades [95]. The friction of the moving air masses against the Earth's surface decelerates the wind speed from a constant value at great altitude to zero at ground (Boundary Layer Effect) [67]. Wind shear effect is important for modern wind turbine machines because with the increasing of the turbine size (some rotors of 8 MW HAWT can reach a diameter of 160 m), the rotor plane is affected by different wind speeds at different heights (see Fig. 2.5). The wind shear effect is described by the shear exponent s obtained from the assumption of a power law profile:

$$V_{h_2} = V_{h_1} \left(\frac{h_2}{h_1} \right)^s \tag{2.1}$$

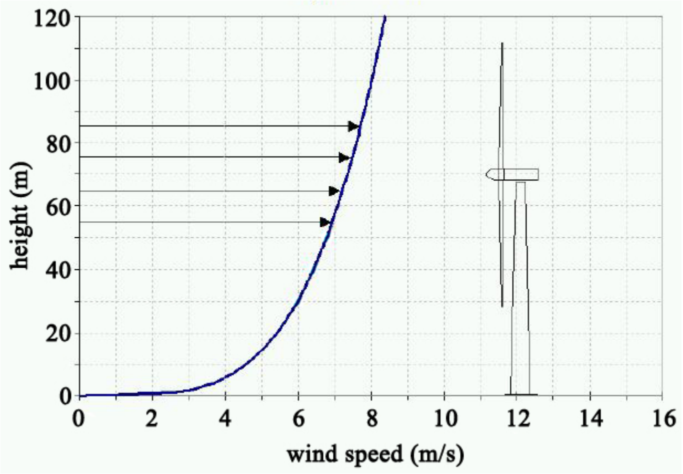

Figure 2.5: Example of wind shear for $s = 0.25$ [11]

where V_{h_2} is the wind speed at height h_2 and V_{h_1} is the wind speed at height h_1. Usually the wind velocity V_{h_1} is the speed measured at 10 m above the ground. The wind shear exponent s varies with the characteristics of the terrain, assuming values that vary from 0.1 for the open water case to 0.30 for terrains with hills and mountains.

Wind turbine power performance is affected by wind shear. The assumption that the wind velocity at hub height is representative of the entire swept area, leads to inconsistencies in power curve measurements. This is true especially for large wind turbines, as shown in Elliott et al. [55] and Sumner et al. [141]. Some studies showed that the power production decreases with increasing shear. One of those is the study presented by Honrubia et al. [70]. To evaluate the influence of wind shear on wind turbine performance, the authors conducted wind speed measurements at different heights. In the past, wind data were measured and evaluated from a meteorological point of view [67], but they did not provide much detailed informations about wind shear. So, the wind speed at hub height was the input parameter for power curve assessment. This approach could be adopted for smaller wind turbines, but for modern multi-MW machines the wind speed at hub height is not sufficient to estimate accurately the power curve. The investigation proposed by Honrubia [70] considered a multimegawatt wind turbine (for confidentiality reasons, the authors did not show informations regarding the physical parameters of the turbine). After a wind speed measurement at height that varies between lower and higher rotor tip, an equivalent wind speed was computed weighing the wind speed recorded at different heights over the rotor swept area according to the area covered by each measurement point. A relatively large variation in terms of power curve was observed between the power computed using the equivalent wind speed which accounts the shear effect and the power computed using the wind speed measured only at hub height. The results showed that the power curve obtained accounting the wind shear was slightly lower than the one obtained considering the wind speed at the hub height and this difference increased with the increasing of the shear exponents s.

2.2 Unsteadiness in vertical axis machines

The unsteady aerodynamics phenomena which characterise VAWTs make these devices extremely attractive to be analysed. Effects such as dynamic stall and blade/wake interactions occur during the operation of these machines. During the recent years, several analyses of VAWT aerodynamics are based on RANS CFD approach [94, 122]. Danao et al. [45] used the incompressible solver of FLUENT for the 2D investigation into the effects of wind fluctuations on the time-dependent power output of a three-blade Darrieus turbine. A transitional $k - \omega$ SST model was used for the turbulence closure. The validation study reported in the article highlighted a very good agreement between RANS results and flow measurements obtained with particle image velocimetry. The same computational set-up was used by Biswas et al. [24] to assess the effects of twisted trailing edges on the aerodynamic performance of a two-blade Darrieus rotor with NACA0012 aerofoils in low-Reynolds number flows. An overview of aerodynamic influences impacting vertical axis wind turbine operation is reported in the next subsections.

2.2.1 Blade rotation

From the λ equation ($\lambda = \Omega \cdot R/V_\infty$) one can easily compute the rotational speed Ω (R is the rotor radius and V_∞ is the freestream wind velocity). For a constant V_∞ the rotational speed increases with the increase of the λ.

Cao et al. [40] performed a numerical analysis to investigate the influence of the rotational speed on the aerodynamic performance of a VAWT. Two dimensional CFD simulations were carried out using FLUENT. The turbine analysed was a three blades

H-type VAWT with aerofoil blade section of NACA0018, chord length of 0.1 m and diameter of 0.9 m. The computational grid was composed by sliding interface, thus, an internal region around the rotor was able to rotate and an external region was fixed (see Fig. 2.6). Three different working conditions were simulated according to different rotational speeds: 50, 100 and 150 RPM. Wake velocity distributions behind the rotor and turbulent kinetic energy distributions were analysed. From the analyses results the authors showed that different rotational speeds affect mainly the rotor wakes generated during the turbine operation. Higher rotational speed corresponded to the larger reduction of the wake's velocity which restored gradually away from the rotor. In addition it was observed a larger turbulent kinetic energy near the trailing edge of the blades, for the highest rotational speeds. It indicates that a high level of turbulence due to complex unsteady behaviour of the turbine is generated for 150 RPM and the distribution of turbulent kinetic energy behind the rotor decreased with the decreasing of the rotational speed.

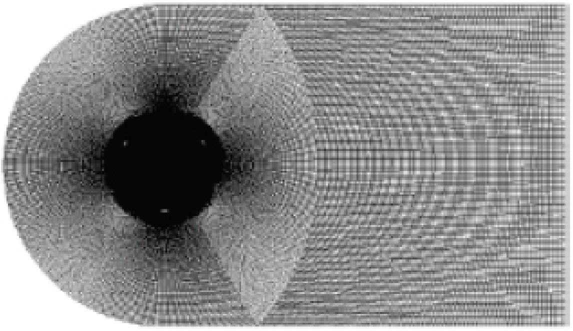

Figure 2.6: 2D computational grid of an H-type VAWT [40]

The tip speed ratio is an important parameter for wind turbine. The optimum λ depends on the number of blades of wind turbine rotor. A lower number of blades is characteristic of wind turbine that needs to run faster to extract maximum power from the wind. If the λ is too low, the wind turbine will tend to slow and/or stall. If the λ is too high, the turbine will spin very fast through turbulent air, power will not be optimally extracted from the wind, and the wind turbine will be highly stressed. A study conducted by Raciti Castelli et al. [115] showed the variation of the maximum power coefficient depending from the number of blades and the angular speeds. The numerical analysis in [115] was conducted to analyse the behaviour of a three, four and five bladed Darreius VAWT. The tested model had a rotor diameter of 1.03 m, chord length of 0.0858 m and the aerofoil blade section NACA0025. A rectangular domain was used with an inlet boundary condition on the left side with a constant velocity profile of 9 m/s, an outlet boundary on the right side with pressure outlet setting and two symmetry boundary conditions on the top and bottom side. The authors showed that taking as reference the power coefficient of a three-bladed configuration, a 5% performance decreases for the four-bladed, and a 15% performance decreases for the five-bladed configuration. In addition, they showed that the value of the λ to achieve the maximum power coefficient increases with the decreasing of the number of blades. A similar analysis was performed for a Savonius type VAWT by Mohmoud et al. [93].

2.2.2 Dynamic stall

The phenomenon of dynamic stall in a VAWT is a characteristic effect of the operation of a VAWT. The variation of AoA of the blade during the rotor revolution, can exceeds the aerofoil's stalling angle and lead to a stalled flow on the blade. This is particularly important at low tip speed ratios because the performance are highly important for the start-up behaviour.

The dynamic stall analysis of a 2D model of the middle section of a single bladed VAWT was presented by Ferreira et al. [131]. The geometry of the model was a 2D representation of a single blade Darrieus turbine tested in a wind tunnel in a previous work of Ferreira [132]. The rotor was characterised by a NACA0015 aerofoil blade with chord of 0.05 m and diameter of 0.4 m. The authors decided to use a single blade turbine to reduce the flow complexity, reducing the amount of wake/blades interactions inside the rotor space. The 2D simulations were performed for $\lambda = 2$ with a frestream wind speed of 7.5 m/s. In this work four different turbulence models were used, two URANS ($S - A$ [138] and $k - \epsilon$ [154]) and two *large eddy* models (Detached Eddy Simulation (DES) and Large Eddy Simulation (LES)). The simulations results were validated against the experimental measurements [132] for $\lambda = 2$. The results demonstrate the influence of different turbulence models on the accuracy of the prediction of dynamic stall development on a VAWT. The comparison of the vorticity contours near the aerofoil between numerical and experimental results highlighted that the $S-A$ and $k - \epsilon$ models underestimate the generation of vorticity at the leading edge and they did not predict very well the roll-up of the trailing edge shed vorticity. Using LES, the results showed an improvement, even if the location of the vorticity shed at the leading edge covers a larger area than what was observed in the experimental results. The authors found the results closest to experiments using DES which was able to predict the generation and shedding of vorticity. Although LES and DES models presented a better flow resolution, their disadvantage was the higher computational cost, due to the required very high spatial and temporal resolution with respect to the URANS approaches. So, this still severely hinders the use of LES and DES technologies for large scale VAWT parametric investigations and design. DES model, as implemented in FLUENT [16], use an hybrid method of LES and URANS, where the wall region is modelled with a URANS model and the outer region with LES. But also in this case, the design process became too computationally expensive. In addition, in the paper of Ferreira [131], it was performed the VAWT validation for a very low λ, where the dynamic stall is very common. If one considers a complete design process of a wind turbine, a wide range of tip speed ratios is considered, and for higher λ the RANS approach based on one- and two-equation turbulence models yields acceptable accuracy (assessed by comparisons with experimental data) with a much lower computational cost than large eddy models.

In order to understand the physics involved during dynamic stall, Nobile et al. [109] presented a 2D analysis of a Darrieus wind turbine. The rotor was characterised by three blades and a central mast. The aerofoil blade analysed was a NACA0018. The numerical simulations were performed by the CFD software ANSYS CFX 12.0. The authors analysed three turbulence models: $k-\epsilon$ model, the standard $k-\omega$ model and the SST (Shear Stress Transport) model. The simulations were performed for several λ and validated against experimental measurements available in literature. The results highlighted a strong instability due to dynamic stall, particularly for low tip speed ratios. In addition, the authors observed the development of upstream wakes that after crossing the rotor interacted with the downstream blades. Also the presence of a central mast generated wakes that affected the flow downstream. Several hysteresis loops reported in [109] show the development of the dynamic stall. Moreover, from the comparison between the three turbulence models used, they observed that the SST method showed a good agreement with the experimental data obtained by Ferreira et al. [134] and Wang et al. [151] than the $k-\omega$ and $k-\epsilon$ model. The SST turbulence model was able to accurately predict the generation of vortices at the leading and trailing edges respectively. (Fig. 2.7).

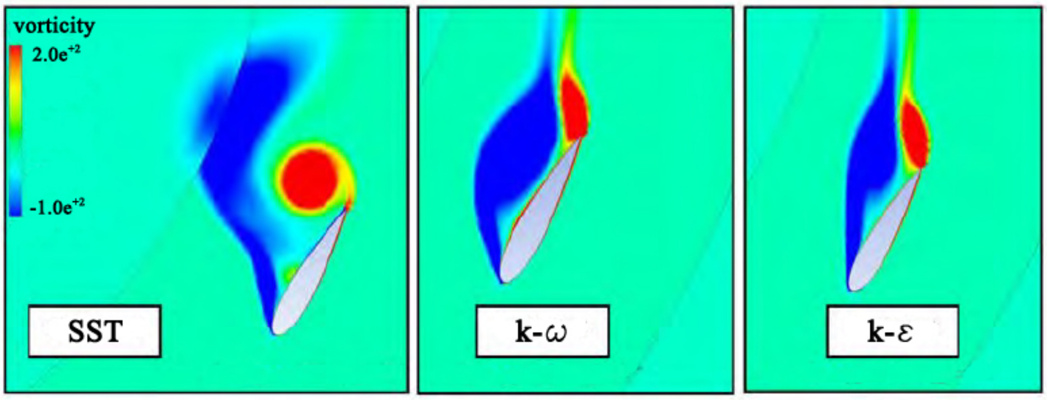

Figure 2.7: Vorticity field for azimuth angle $\theta = 120^o$ for the three turbulence model analysed [109]

2.2.3 Blade/wake interaction

The complexity of a VAWT results in blade/vortex interaction at the downwind passage of the blade between the blade and the shed vorticity that is generated at the upwind passage.

A 2D CFD computation of a single-bladed VAWT turbine using a NACA0015 aerofoil was performed by Allet et al. [14]. A turbulent solver based on a stream function-vorticity formulation was used with two turbulence models. The authors observed that even if the amplitudes of the oscillations of the AoA on the blade was significantly smaller when the turbine operated at high λ, the interactions between the blade and their own wake, influenced more greatly the aerodynamic loading on the blade with respect to lower λ. It happened because at higher λ, the wake developed by the blade convected downstream relatively slowly if compared to the rotational speed of the rotor, so each blade crossed its own wake in each subsequent revolution. The interaction between blade and wake is considered one of the most important problem in the numerical modelling of the aerodynamics of VAWTs because these interactions are very difficult to simulate with a good accuracy. Using a CFD approach, to correctly modelled the wake inside the entire rotor diameter a finer computational mesh is needed in order to avoid numerical dissipation.

A three-dimensional numerical analysis of a Darrieus rotor was proposed by Scheurich et al. [125]. The VAWT investigated was a two straight blades rotor, with NACA0012 aerofoil section, chord length of 9.14 cm and operating at $\lambda = 5$. This turbine rotor was studied experimentally in [139], where the variation of the blade loads with azimuth angle was measured. The rotor aerodynamic performance and wake dynamics reported in [125], were simulated using a particular Vorticity Transport Model (VTM) [31]. An important feature of the VTM was its ability to predict quite well the evolution of the turbine wake. The VTM allowed to use a grid with different level of cells density in order to reduce the computational cost of the simulations. Thus, in a rectangular computational domain adopted, coarser grids were used moving from the turbine centre to the outflow boundary. Normal and tangential forces acting on the blades were predicted for an aerofoil section at the mid-span of the blades and showed a good agreement with experimental measurements reported in [139]. However, the authors highlighted some discrepancies when the blades were immediately downstream of the rotor. In this region blade/wake interactions occurred and a significant effect on the distribution of aerodynamic loading on the blades was observed. The discrepancies caused by these interactions, generated oscillations of the angle of attack beyond the static stall leading to dynamic stall near the blades. So, the authors showed that also for $\lambda = 5$ considered in this study, the effects of dynamic stall (that should be considered to be small for that λ due to smaller variation of the AoA) induced by the blade/wake interaction was still evident.

2.3 Conclusion

A literature review of some important research works on wind turbine unsteady flows has been presented. The studies have showed the analysis of unsteadiness affecting horizontal and vertical axis wind turbines, like tower shadow, dynamic stall, yawed wind condition, wind shear and blade/wake interaction, using analytical models, experimental measurement and CFD approaches. The research works reported in the chapter have highlighted several aspects of the analysis of wind turbines and they have demonstrated that the CFD RANS approach coupled to a $k-\omega$ SST model is able to reproduce the main properties of the flow regime in a reasonable computational time and the results are in good accordance with the literature. It has also been shown that although LES and DES models presented a better flow resolution, their disadvantage is the higher computational cost, due to the required very high spatial and temporal resolution with respect to the RANS approaches. This severely hinders the use of LES and DES technologies for HAWT and VAWT parametric investigations and design.

Chapter 3

Numerical solution of steady and time-domain Reynolds-averaged Navier-Stokes equations

Computational Fluid Dynamics (CFD) is the technique that studies systems involving fluid flow, heat transfer and phenomena like chemical reaction by means of numerical simulation. The technique is very powerful and can be applied to a large number of applications.

In the wind energy field, this technique has become increasingly important. Several advantages are achieved by a CFD approach:

- CFD is faster and cheaper than traditional approaches based on physical model tests. An assessment of different solutions can be done in the early phase of the design process, in order to fit with the requested tasks.
- Full-size analyses are hard to perform for large systems, like modern horizontal axis wind turbines. CFD studies are a favourable choice since they provide more reliable results than BEM-based aerodynamic and aeroelastic analyses.
- An important quality of CFD are the detailed solutions allowed by the recent techniques, even for time-dependent flows and complex systems.
- Algorithmic improvements enable a much faster solution, which is needed for using CFD for complex realistic problems. Modelling improvements, such as better turbulence modelling, are instead needed for getting more reliable results.

In this chapter, the formulation of the Navier-Stokes equations is reported. In addition, a complete description of the compressible density-based structured multi-block finite volume CFD code used in this research has been reported, like the two-equations $k-\omega$ shear stress transport turbulence model by Menter to take into account the turbulence effects, the space discretisation method and the integration method used to solve steady and time-domain flow problems.

3.1 Navier-Stokes equations

The milestones of computational fluid dynamics are the fundamental governing equations of fluid dynamics: the mass, momentum and energy equations [69]. They are the mathematical statements of three fundamental physical principles upon which all of fluid dynamics is based:

- the total mass of any system is conserved, so it is neither created nor destroyed, the system is closed from any external transfers of matter;
- the variation of momentum is caused by the overall force acting on a mass element. It derives from Newton's second law ($F = ma$). In 2D problems, the momentum conservation results in two scalar equations, one for each direction.
- the total energy of a system remains constant over time. It corresponds to the first law of thermodynamics.

In fluid dynamics, the expression $Navier - Stokes$ equations refers to a system of N_{pde} nonlinear partial differential equations (PDEs) obtained by imposing the governing equations over a control volume (CV). The CV is an imaginary surface enclosing a volume of interest. Once the CV and its boundary are established, the various forms of energy crossing the boundary with the fluid can be treated with NS equations to solve fluid problems. The NS equations can be written in the differential form if applied at a point or in the integral form if applied to an extended region. Consider a general flow field as represented by the streamlines of Fig. 3.1. Let us imagine a closed volume drawn within a finite region of the flow. This volume defines a control volume, V, and a control surface, S, is defined as the closed surface which bounds the volume. The figure also depicts a surface element dS and its normal unit vector $\boldsymbol{n}$. In 2D problems

V is a surface and S is a curve. The mass element dm is enclosed by an infinitesimal volume dV and it is equal to ρdV where ρ is the density.

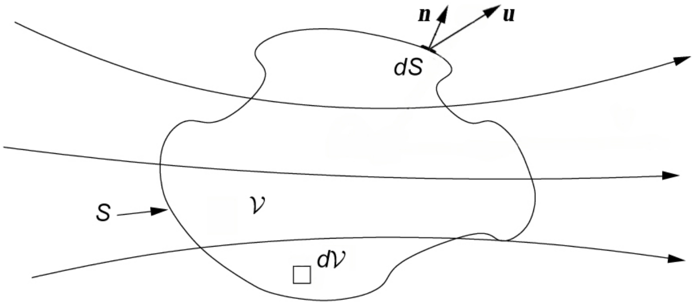

Figure 3.1: Fixed Control Volume

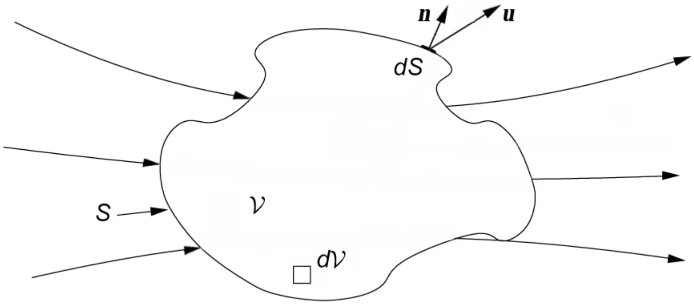

Figure 3.2: Moving Control Volume

The CV may be fixed in space with the fluid moving through it (Fig. 3.1), or it may be moving with the fluid (Fig. 3.2) such that the same fluid particles are always inside it. In either case, the CV is a reasonably large finite region of the flow. The expression of the integral form of the NS equations that one directly obtain applying the fundamental physical principles to a finite CV depends on whether this CV is fixed or not.

3.1.1 Continuity equation

Consider the model of a finite control volume fixed in space, as sketched in Fig. 3.1. In this case it is said that the "Eulerian approach" is used. At a point on the control surface, let $\boldsymbol{u}$ denote the flow velocity vector and dS the elemental surface. Also let

dV be an infinitesimal volume inside the finite control volume. Applied to this control volume, our fundamental physical principle that mass is conserved means that the net mass flow out of CV through surface S is equal to the time rate of change of mass inside the CV. The continuity equation can be expressed as:

$$\oint_S \rho(\boldsymbol{u} \cdot \boldsymbol{n}) dS = -\frac{\partial}{\partial t} \int_V \rho dV \tag{3.1}$$

Note that by convention, $\boldsymbol{n}$ always points in a direction out of the control volume. Hence, when $\boldsymbol{u}$ also points out of the CV (as shown in Fig. 3.1), the product $\rho(\boldsymbol{u} \cdot \boldsymbol{n})dS$ is positive and the mass flow is physically leaving the control volume. In turn, when $\boldsymbol{n}$ points into the control volume, $\rho(\boldsymbol{u} \cdot \boldsymbol{n})dS$ is negative and the mass flow is physically entering the CV.

3.1.2 Momentum equation

The momentum equation is based on Newton's second law. This can be expressed as:

$$\frac{d}{dt}(mV) = F \tag{3.2}$$

The left hand side of the Eq. (3.2) represents the rate of change of the flow momentum in the CV and it can be written as:

$$\frac{d}{dt}(mV) = \frac{\partial}{\partial t} \int_V \rho \boldsymbol{u} dV + \oint_S \rho \boldsymbol{u}(\boldsymbol{u} \cdot \boldsymbol{n}) dS \tag{3.3}$$

where $\frac{\partial}{\partial t} \int_V \rho \boldsymbol{u} dV$ is the time rate of change due to unsteady flow fluctuation of the momentum of fluid in the elemental volume dV at any instant inside the CV, while $\oint_S \rho \boldsymbol{u}(\boldsymbol{u} \cdot \boldsymbol{n}) dS$ is the net flow of momentum through S. The right hand side of Eq. (3.2) is the summation of all surface forces (shear and pressure forces) acting on the CV. The shear stresses are defined by the following equation:

$$\oint_S \underline{\tau} \cdot \boldsymbol{n} dS \tag{3.4}$$

where $\underline{\tau}$ denotes the molecular stress tensor. This tensor depends on the divergence of the flow velocity vector $\boldsymbol{u}$ and the strain rate tensor $\underline{S}$. For a Newtonian fluid, the expression of stress tensor is:

$$\tau_{ij} = 2\mu \left[S_{ij} - \frac{1}{3} \frac{\partial u_k}{\partial x_k} \delta_{ij} \right] \ , \quad S_{ij} = \frac{1}{2} \left[\frac{\partial u_i}{\partial x_j} + \frac{\partial u_j}{\partial x_i} \right] \tag{3.5}$$

where μ is the molecular dynamic viscosity, $u_{i(j)}$ are the Cartesian components of the flow velocity vector $\boldsymbol{u}$, δ_{ij} is the Kronecker Delta Function and $x_{i(j)}$ are the components of the position vector $\boldsymbol{x}$. The total pressure force over the entire control surface is expressed as:

$$-\oint_S p\boldsymbol{n}dS \tag{3.6}$$

where the negative sign indicates that the force is in the direction opposite to dS. Hence, the momentum conservation equation is defined as:

$$\frac{\partial}{\partial t}\int_V \rho\boldsymbol{u}dV + \oint_S \rho\boldsymbol{u}(\boldsymbol{u}\cdot\boldsymbol{n})dS = -\oint_S p\boldsymbol{n}dS + \oint_S \underline{\tau}\cdot\boldsymbol{n}dS \tag{3.7}$$

3.1.3 Energy equation

The law of conservation of energy states that “energy can neither be created nor destroyed, it can only change its form”. Consider the CV shown in Fig. 3.1 as the thermodynamic system. Any form of energy to the system, changes the amount of total energy, which is the sum of the internal energy (equal to the sum of the amount of heat added to the system and the work done on the system from the surrounding) and the kinetic energy of the system. The expression of the conservation of energy in integral form is:

$$\frac{\partial}{\partial t}\int_V \rho E dV + \oint_S \rho E(\boldsymbol{u}\cdot\boldsymbol{n})dS = \oint_S (\underline{\tau}\cdot\boldsymbol{u})\cdot\boldsymbol{n}dS - \oint_S p(\boldsymbol{u}\cdot\boldsymbol{n})dS - \oint_S \boldsymbol{q}\cdot\boldsymbol{n}dS \tag{3.8}$$

The left hand side of Eq. (3.8) is the sum of the rate of change of the internal energy and the net rate of flow of total energy across control surface. The total energy E is expressed as:

$$E = e + \frac{u_i u_i}{2} \tag{3.9}$$

The right hand side of Eq. (3.8) is the sum of the amount of heat added to the CV and the work done on the CV. The term $\oint_S(\underline{\tau}\cdot\boldsymbol{u})\cdot\boldsymbol{n}dS$ represents the work done on the fluid across the surface by the shear stress $\underline{\tau}$ on the control surface. The second term on the right hand side is the work done on the fluid passing through dS with velocity $\boldsymbol{u}$ by the pressure force $-pdS$. The term $-\oint_S \boldsymbol{q}\cdot\boldsymbol{n}dS$ is the rate of heat energy transfer through the control volume.

3.1.4 Eulerian formulation of the Navier-Stokes equations

Grouping the governing equations exposed in the preceding subsections, the 2D NS equations can be defined as:

$$\frac{\partial}{\partial t}\left(\int_V \widehat{\mathbf{U}} dV\right) + \oint_S (\widehat{\mathbf{\Phi}}_c - \widehat{\mathbf{\Phi}}_d) dS = 0 \tag{3.10}$$

The array $\widehat{\mathbf{U}}$ is the array of the conservative flow variable and it is defined as:

$$\widehat{\mathbf{U}} = \begin{bmatrix} \rho \\ \rho u_x \\ \rho u_y \\ \rho E \end{bmatrix}$$

The generalised convective flux vector $\widehat{\mathbf{\Phi}}_c$ is:

$$\widehat{\mathbf{\Phi}}_c = \widehat{\mathbf{E}}_c n_x + \widehat{\mathbf{F}}_c n_y \tag{3.11}$$

where $\widehat{\mathbf{E}}_c$ and $\widehat{\mathbf{F}}_c$ are the $x-$ and $y-$ components of $\widehat{\mathbf{\Phi}}_c$ and are respectively:

$$\widehat{\mathbf{E}}_c = \begin{bmatrix} \rho u_x \\ \rho u_x^2 + p \\ \rho u_x u_y \\ \rho u_x H \end{bmatrix}, \qquad \widehat{\mathbf{F}}_c = \begin{bmatrix} \rho u_y \\ \rho u_y u_x \\ \rho u_y^2 + p \\ \rho u_y H \end{bmatrix}$$

The symbol p denotes the static pressure and the symbol H denotes the total enthalpy per unit mass, the expression of which is:

$$H = h + \frac{u_i u_i}{2}, \qquad h = c_p T, \qquad H = E + \frac{p}{\rho} \tag{3.12}$$

The generalised diffusive flux vector $\widehat{\mathbf{\Phi}}_d$ is:

$$\widehat{\mathbf{\Phi}}_d = \widehat{\mathbf{E}}_d n_x + \widehat{\mathbf{F}}_d n_y \tag{3.13}$$

where $\widehat{\mathbf{E}}_d$ and $\widehat{\mathbf{F}}_d$ are the $x-$ and $y-$ components of $\widehat{\mathbf{\Phi}}_d$ and are respectively:

$$\widehat{\mathbf{E}}_d = \begin{bmatrix} 0 \\ \tau_{xx} \\ \tau_{xy} \\ u_x \tau_{xx} + u_y \tau_{xy} - q_x \end{bmatrix}, \qquad \widehat{\mathbf{F}}_d = \begin{bmatrix} 0 \\ \tau_{xy} \\ \tau_{yy} \\ u_x \tau_{xy} + u_y \tau_{yy} - q_y \end{bmatrix}$$

The scalars q_x and q_y are the Cartesian components of the heat flux vector $\boldsymbol{q} = -k_T \nabla T$, where k_T is the thermal conductivity and T is the static temperature. The scalars τ_{xx}, τ_{xy} and τ_{yy} are the Cartesian components of the stress tensor $\underline{\tau}$.

In cases with moving bodies involved, the Eulerian formulation has to be generalised to include body motion. The so-called *Arbitrary Lagrangian Eulerian* (ALE) formulation allows to the CV to move with a speed different from that of the fluid. Denoting by $V(t)$ a time-varying control volume and with $S(t)$ a time-varying boundary, the ALE integral form of the 2D NS equations is defined as:

$$\frac{\partial}{\partial t}\left(\int_{V(t)} \widehat{\mathbf{U}} dV\right) + \oint_{S(t)} (\widehat{\mathbf{\Phi}}_c - \widehat{\mathbf{\Phi}}_d) dS = 0 \tag{3.14}$$

The generalised diffusive flux vector $\widehat{\mathbf{\Phi}}_d$ is unchanged in the ALE formulation. The generalised convective flux vector $\widehat{\mathbf{\Phi}}_c$ is instead defined as:

$$\widehat{\mathbf{\Phi}}_c = \widehat{\mathbf{E}}_c n_x + \widehat{\mathbf{F}}_c n_y - v_b \widehat{\mathbf{U}} \tag{3.15}$$

The vector v_b is the velocity of the boundary S and the flux term $-v_b\widehat{\mathbf{U}}$ is its contribution to the overall flux balance, which is nonzero only in the case of unsteady problems with moving boundaries.

3.2 Turbulence modelling

For 2D laminar flows the number of PDEs is equal to 4 because the momentum equation has only two scalar components. In the case of turbulent flows, the effects of turbulence are often taken into account by averaging the NS equations on the time-scales of turbulence. This process leads to the so-called Reynolds-averaged NavierStokes (RANS) equations and the appearance in these equations of the Reynolds stress tensor. Making use of the Boussinesq approximation [25], this tensor depends mainly on the product of the strain rate tensor and a turbulent or eddy viscosity. Boussinesq approximation states that the momentum transfer caused by turbulent eddies can be modelled with an eddy viscosity. The Boussinesq assumption assumes that the Reynolds stress tensor, τ_{ij}^F, is proportional to the mean strain rate tensor S_{ij}^*, and can be written in the following way:

$$\tau_{ij}^F = 2\mu_T \left(S_{ij}^* - \frac{1}{3}\frac{\partial \tilde{u_k}}{\partial x_k}\delta_{ij}\right) - \frac{2}{3}\rho k \delta_{ij} \tag{3.16}$$

where μ_T is the turbulent eddy viscosity, ρ is the density and δ_{ij} is the Kronecker Delta Function.

In this research, to take into account the turbulence effect, the two-equations $k-\omega$ shear stress transport (SST) turbulence model by Menter were used [101]. It is a two-equation eddy-viscosity model. The eddy viscosity is computed from the two transported variables (turbulent kinetic energy (k) and specific dissipation rate (ω)) in each cell of the grid to represent the turbulent properties of the flow. For this reason, the simulations of two-dimensional turbulent flows presented in this thesis require the solution of a system of six PDEs, namely four RANS PDEs, one PDE describing the convection, diffusion, creation and destruction of the turbulent kinetic energy k and one describing the evolution of the specific dissipation rate ω. The $k-\omega$ SST model is an extension of the original $k-\omega$ model introduced by Wilcox [155] (*Appendix B*). The shear stress transport (SST) formulation combines the use of a $k-\omega$ formulation and the $k-\epsilon$ model [79]. This combination is preferred because the $k-\omega$ formulation is fairly accurate in the boundary layers, while the $k-\epsilon$ formulation is good on the farfield boundaries because it is less sensitive to the freestream turbulence data and enhance the behaviour in adverse pressure gradients and separating flow.

3.2.1 Menter's shear stress transport model

The basic equations of Menter [101] for the turbulent kinetic energy k and the specific dissipation ω are:

$$\frac{\partial}{\partial t}(\rho k) + \frac{\partial}{\partial x_j}(\rho u_j k) = \tau_{ij}^F \frac{\partial u_i}{\partial x_j} - \beta^* \rho \omega k + \frac{\partial}{\partial x_j}\left[(\mu + \sigma_k \mu_T)\frac{\partial k}{\partial x_j}\right] \tag{3.17}$$

$$\frac{\partial}{\partial t}(\rho \omega) + \frac{\partial}{\partial x_j}(\rho u_j \omega) = \frac{\gamma \rho}{\mu_T}\tau_{ij}^F \frac{\partial u_i}{\partial x_j} - \beta \rho \omega^2 + \frac{\partial}{\partial x_j}\left[(\mu + \sigma_\omega \mu_T)\frac{\partial \omega}{\partial x_j}\right] + CD_\omega \tag{3.18}$$

The turbulent eddy viscosity is computed from:

$$\mu_T = \frac{\alpha_1 \rho k}{\max(\alpha_1 \omega, \widehat{\Omega} F_2)} \tag{3.19}$$

where α_1 is a constant, $\widehat{\Omega}$ is the modulus of the vorticity, F_2 (Eq. (3.20)) is a function of k, ω, the molecular kinematic viscosity ν and the distance from the wall d.

$$F_2 = \tanh(arg_2^2) \tag{3.20}$$

$$arg_2 = \max\left(\frac{2\sqrt{k}}{\beta^*\omega d}, \frac{500\mu}{\rho\omega d^2}\right) \tag{3.21}$$

In the Eq. (3.17) and (3.18), one can see the production terms of k and ω:

$$P_k = \tau_{ij}^F \frac{\partial u_i}{\partial x_j}, \qquad P_\omega = \frac{\gamma\rho}{\mu_T}\tau_{ij}^F \frac{\partial u_i}{\partial x_j} \tag{3.22}$$

which can be written in the form:

$$P_k = \mu_T P_d - \frac{2}{3}(\nabla\cdot\boldsymbol{u})\rho k \tag{3.23}$$

$$P_\omega = \gamma\rho P_d - \frac{\gamma\rho}{\mu_T}\frac{2}{3}(\nabla\cdot\boldsymbol{u})\rho k \tag{3.24}$$

where $P_d = 2\left(S^* - \frac{1}{3}\nabla\cdot\boldsymbol{u}\right)\nabla\boldsymbol{u}$ and $S^* = \frac{1}{2}(\nabla\cdot\boldsymbol{u} + \nabla\cdot\boldsymbol{u}')$. The destruction terms of the k and ω are defined as:

$$D_k = \beta^*\rho\omega k, \qquad D_\omega = \beta\rho\omega^2 \tag{3.25}$$

Only in the ω equation, there is an additional cross-diffusion term CD_ω defined as:

$$CD_\omega = 2\rho(1-F_1)\sigma_{\omega 2}\frac{1}{\omega}\frac{\partial k}{\partial x_j}\frac{\partial\omega}{\partial x_j} \tag{3.26}$$

where the function F_1 is:

$$F_1 = \tanh(arg_1^4) \tag{3.27}$$

$$arg_1 = \min\left[\max\left(\frac{\sqrt{k}}{\beta^*\omega d}, \frac{500\mu}{\rho\omega d^2}\right), \frac{4\rho\sigma_{\omega 2}k}{CD_\omega d^2}\right] \tag{3.28}$$

All production, destruction and cross-diffusion terms form the so-called source term S and they can be summarised as follow:

$$S_k = \mu_T P_d - \frac{2}{3}(\nabla\cdot\boldsymbol{u})\rho k - D_k \tag{3.29}$$

$$S_\omega = \gamma\rho P_d - \frac{2}{3}(\nabla\cdot\boldsymbol{u})\frac{\gamma\rho k}{\nu_T} - D_\omega + CD_\omega \tag{3.30}$$

where ν_T is the turbulent kinematic viscosity and the variables σ_k, σ_ω, γ, β^* and β are weighted averages of the constants of the standard $k-\omega$ model [155] and constants of the standard $k-\epsilon$ model [79] with weights F_1 and $(1-F_1)$, respectively. The symbol $\sigma_{\omega 2}$ is a constant of the standard $k-\epsilon$ model and the function F_1 shown by Eq. (3.27) depends on the local values of k, ω, ν, ρ, d, ∇k and $\nabla\omega$. It can be shown that the production term P_d is always positive. Thus the source term S_k of the k-equation has a term which is always positive (production term proportional to P_d), a term which is always negative (destruction term D_k) and a term which is positive or negative depending on the sign of $\nabla \cdot \boldsymbol{u}$. Similarly to S_k, the source term S_ω of the ω equation also has a term which is always positive (production term proportional to P_d), a term which is always negative (destruction term D_ω), and a term which is positive or negative depending on the sign of $\nabla \cdot \boldsymbol{u}$. The source term S_ω, however, features an additional cross-diffusion term CD_ω which can be positive or negative. The identification of positive and negative source terms is very important when using a semi-implicit multigrid integration of the equations of turbulence, due to the different numerical treatment to be adopted for positive and negative source terms [89, 87].

The terms $\frac{\partial}{\partial x_j}\left[(\mu + \sigma_k \mu_T)\frac{\partial k}{\partial x_j}\right]$ and $\frac{\partial}{\partial x_j}\left[(\mu + \sigma_\omega \mu_T)\frac{\partial \omega}{\partial x_j}\right]$ are instead the diffusion term of k (Eq. (3.17)) and ω (Eq. (3.18)). To complete the definition of the SST model, the turbulent coefficients have to be specified. In the SST model there are two sets of coefficients which are combined using the blending function $\Phi = F_1\Phi_1 + (1 - F_1)\Phi_2$. The sets of coefficients are defined in the Eq. (3.31) and Eq. (3.32)

$$set_1 : [\beta_1 \quad \sigma_{k1} \quad \sigma_{\omega 1} \quad \gamma_1] = [0.0750 \quad 0.85 \quad 0.500 \quad 0.55317] \tag{3.31}$$

$$set_2 : [\beta_2 \quad \sigma_{k2} \quad \sigma_{\omega 2} \quad \gamma_2] = [0.0828 \quad 1.00 \quad 0.856 \quad 0.44035] \tag{3.32}$$

The equations used to calculate the coefficients γ_1 and γ_2 are:

$$\gamma_1 = \frac{\beta_1}{\beta^*} - \frac{\sigma_{\omega 1} k_1^2}{\sqrt{\beta^*}}, \qquad \gamma_2 = \frac{\beta_2}{\beta^*} - \frac{\sigma_{\omega 2} k_1^2}{\sqrt{\beta^*}} \tag{3.33}$$

Other coefficients used in the SST model are $\beta^* = 0.09$, $k_1 = 0.41$ and $\alpha_1 = 0.31$.

The actual implementation of the source terms reported in Eq. (3.29) and (3.30), however, is often slightly different from these nominal definitions due to some numerical issues. As reported in a paper on the SST turbulence model of Menter [100], it is suggested to limit the production term P_k to eliminate the occurrence of spikes in the eddy viscosity due to numerical “wiggles” in the strain rate tensor, and to eliminate the unphysical build-up of eddy viscosity in the stagnation region of an aerofoil. The proposed limited value of the k production term is:

$$\tilde{P}_k = min(P_k, l_k \cdot D_k) \tag{3.34}$$

with $l_k = 20$. Several research and commercial codes extend the same limiter to the ω production term, adopting a limited value of:

$$P_\omega = \frac{\gamma\rho}{\mu_T}\tilde{P}_k \tag{3.35}$$

Although for relatively simple problems, the use of these limiters has a negligible impact on the computed solution [100], in this thesis has been found that the solutions of highly unsteady flow problems obtained by using the unlimited definitions of P_k and P_ω, and those obtained with limiters of the same type as those defined by Eq. (3.34) and (3.35) differ significantly.

3.3 Time-domain formulation of the governing equations

Time-dependent engineering problems can be treated using RANS which incorporates time-derivatives that take into account the variations in time associated to non-stationary flows. So, in this case one can use the so-called Unsteady Reynolds Average Navier-Stokes (URANS) equations. Given a moving control volume $V(t)$ with time-dependent boundary $S(t)$, the Arbitrary Lagrangian-Eulerian integral form of the system of the time-dependent RANS equations coupled to the two transport equation of the SST turbulence model are expressed as:

$$\frac{\partial}{\partial t}\int_{V(t)} \widehat{\mathbf{U}} dV + \oint_{S(t)} (\widehat{\mathbf{\Phi}}_c - \widehat{\mathbf{\Phi}}_d) dS - \int_{V(t)} \widehat{\mathbf{S}} dV = 0 \tag{3.36}$$

The array $\widehat{\mathbf{U}}$ of the conservative flow variables ρ, u_x, u_y, E, k and ω is defined as:

$$\widehat{\mathbf{U}} = \begin{bmatrix} \rho \\ \rho u_x \\ \rho u_y \\ \rho E \\ \rho k \\ \rho\omega \end{bmatrix}$$

The generalised convective flux vector $\widehat{\mathbf{\Phi}}_c$ is defined as:

$$\widehat{\mathbf{\Phi}}_c = \widehat{\mathbf{E}}_c n_x + \widehat{\mathbf{F}}_c n_y - v_b \widehat{\mathbf{U}} \tag{3.37}$$

where $\widehat{\mathbf{E}}_c$ and $\widehat{\mathbf{F}}_c$ are the $x-$ and $y-$ components of $\widehat{\mathbf{\Phi}}_c$ and are respectively:

$$\widehat{\mathbf{E}}_c = \begin{bmatrix} \rho u_x \\ \rho u_x^2 + p \\ \rho u_x u_y \\ \rho u_x H \\ \rho u_x k \\ \rho u_x \omega \end{bmatrix}, \qquad \widehat{\mathbf{F}}_c = \begin{bmatrix} \rho u_y \\ \rho u_y u_x \\ \rho u_y^2 + p \\ \rho u_y H \\ \rho u_y k \\ \rho u_y \omega \end{bmatrix}$$

The vector v_b is the velocity of the boundary S, and $-v_b\widehat{\mathbf{U}}$ is the flux term as seen in the preceding sections. The symbol p denotes the static pressure and the total enthalpy per unit mass H is defined by Eq. (3.12). The expression of the generalised diffusive flux vector $\widehat{\mathbf{\Phi}}_d$ is:

$$\widehat{\mathbf{\Phi}}_d = \widehat{\mathbf{E}}_d n_x + \widehat{\mathbf{F}}_d n_y \tag{3.38}$$

where the $x-$ and $y-$ components of $\widehat{\mathbf{\Phi}}_d$ are respectively:

$$\widehat{\mathbf{E}}_d = \begin{bmatrix} 0 \\ \tau_{xx} \\ \tau_{xy} \\ u_x\tau_{xx} + u_y\tau_{xy} + (\mu + \sigma_k\mu_T)\frac{\partial k}{\partial x} - q_x \\ (\mu + \sigma_k\mu_T)\frac{\partial k}{\partial x} \\ (\mu + \sigma_\omega\mu_T)\frac{\partial \omega}{\partial x} \end{bmatrix}$$

$$\widehat{\mathbf{F}}_d = \begin{bmatrix} 0 \\ \tau_{xy} \\ \tau_{yy} \\ u_x\tau_{xy} + u_y\tau_{yy} + (\mu + \sigma_k\mu_T)\frac{\partial k}{\partial y} - q_y \\ (\mu + \sigma_k\mu_T)\frac{\partial k}{\partial y} \\ (\mu + \sigma_\omega\mu_T)\frac{\partial \omega}{\partial y} \end{bmatrix}$$

where μ is the dynamic viscosity, μ_T is the turbulent viscosity defined by Eq. (3.19) and the variables σ_k and σ_ω are weighted averages of the constants of the standard $k - \omega$ model. The scalars q_x and q_y are the Cartesian components of the heat flux vector and the scalars τ_{xx}, τ_{xy} and τ_{yy} are the Cartesian components of the stress tensor $\underline{\tau}$, as seen before. The symbol $\widehat{\mathbf{S}}$ into Eq. (3.36) is the source term defined as:

$$\widehat{\mathbf{S}} = \begin{bmatrix} 0 \\ 0 \\ 0 \\ 0 \\ S_k \\ S_\omega \end{bmatrix}$$

where S_k and S_ω are defined by Eq. (3.29) and (3.30).

In this thesis, the CFD research code used to solve the RANS equations and the Menter's $k-\omega$ SST turbulent model [101] is called COSA. It is a compressible density-based structured multi-block finite volume code featuring a steady flow solver, a time-domain (TD) solver for the solution of general unsteady problems [38], and a harmonic balance solver (see *Chapter 4*) for the rapid solution of periodic flows [36]. The COSA development started in 2008 [2] and year after year its features have increased, achieving the implementation of novel advanced farfield boundary conditions (BCs) [33], a novel unsteady low-speed preconditioner [34, 39] to enable the CFD analysis of very low-speed flows as well as flows featuring both high- and low-speed regions, an HB solver for the rapid analysis of unsteady periodic flows [36], a LAPACK libraries integration to massively improved the computational efficiency of a semi-implicit approach to the integration of the HB RANS equations and a robust and accurate turbulence Shear Stress Transport (SST) model of Menter [38].

3.4 Space-discretisation

The RANS system and the two PDEs of the SST turbulence model have to be solved numerically. Solving them analytically is possible only in a few cases. Numerical solution of PDEs requires representing the continuous nature of the governing equations in a discrete form. A key step for the discretisation process is the subdivision of the domain into cells or elements (computational grid or mesh). The fundamental classifications of meshes are based upon the connectivity of a mesh or on the type of elements present.

- Structured meshes: they are characterised by regular connectivity that can be expressed as a two or three dimensional array. This restricts the element choices to quadrilaterals in 2D or hexahedra in 3D (Fig. 3.3). The vertices of the intersections define the grid vertices. Since the intersections can be easily numbered using a progressive sequence in each direction, the neighbours of each vertex, the edges sharing a common vertex and the volumes sharing a common vertex can be immediately defined, given the intrinsic topology of the structured meshes. Structured meshes are typically easier to compute with but may require more elements or worse-shaped elements.
- Unstructured meshes: they are characterised by irregular connectivity (Fig. 3.3). In 2D problems, they are usually (not always) made up of triangles, whereas in 3D problems, they are made up of tetrahedral. Unstructured meshes lack the inherent topology required to easily identify the neighbours of a given grid node, the edges sharing a common vertex and the volumes sharing a common vertex. These characteristics increase the complexity of unstructured CFD codes, such as the calculation of the convective fluxes. The typical motivation for accepting this kind of additional complexity of unstructured CFD codes is the ease by which unstructured grids can handle geometric complexities.
- Hybrid meshes: they are a mesh that contains structured portions and unstructured portions (Fig. 3.3).

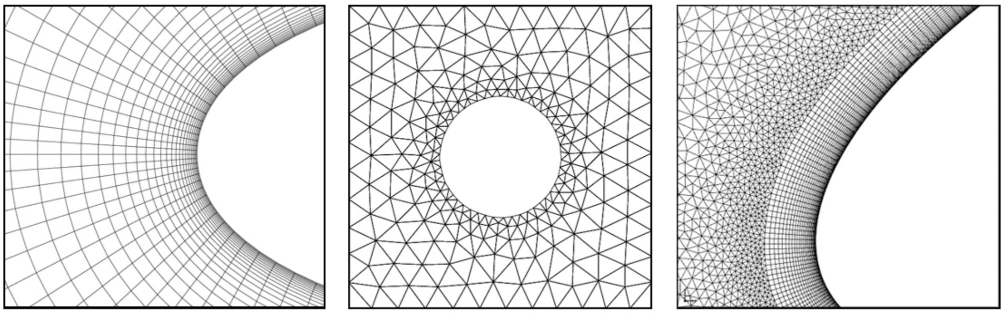

Figure 3.3: Example of structured (left), unstructured (center) and hybrid grid (right)

The research code COSA can handle 2D and 3D structured grids. In a structured grid the cells are arranged in an $i \times j$ (2D case) or $i \times j \times k$ (3D case) array where i, j, and k are known as the grid's dimensions. The term *structured* refers to the structure provided to the cells organization within that array such that a cell's neighbours are known implicitly. In other words, for a 2D case, the point at (i, j) has neighbours at (i+1, j), (i-1, j), (i, j+1) and (i, j-1) (Fig. 3.4). This structure contrasts with an unstructured mesh in which a connectivity table has to be maintained and queried to find any point's neighbours.

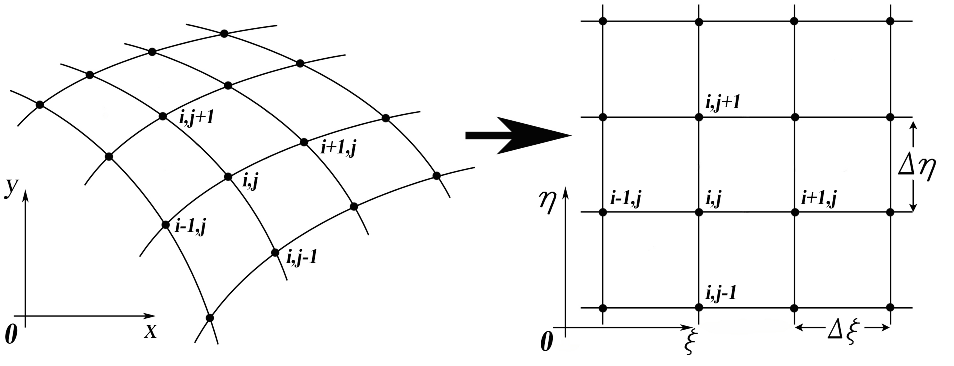

Figure 3.4: This schematic illustrates the mapping of a physical domain to a computational domain.

In fact, structure is the source of one of the benefits of structured grids in terms of computational performance, such as the calculation of the convective fluxes is simpler. Finding neighbours directly (via the structure) is much faster and uses less memory than having to look them up in a table. The use of structured grids implies that the distribution of boundary points has been performed in a manner such that dimensions (number of grid points) of opposite boundaries are identical. Domains (surface grids) will have four boundaries (edges) and blocks (volume grids) will have six boundaries (faces) [145, 82, 146]. Generating a computational grid requires the use of a grid generator which takes as input some information regarding the geometry of the boundaries of the physical domain, the geometry of any solid bodies inside the domain, minimum distances from selected wall boundaries, stretching factors, etc. Doing a good mesh is very important to have a good solution quality. Necessary conditions are that the mesh density should be high enough to capture all relevant flow features, the grid adjacent to the solid wall should be fine enough to resolve the boundary layer flow, the lines ending on wall boundaries need to be as orthogonal as possible to such boundaries, the grid lines must be as smooth as possible (i.e. their first derivatives should not have discontinuities) and all elements should be well shaped. One can make very simple grids using only one block, but for complex geometries it is impossible to have a good quality mesh using a single block grid. This problem, however, is easily overcome by using multi-block grids which offer better computational efficiency and more flexibility. Multi-block means that the grid topology can be made from multiple connected structured blocks. It gives to the user flexibility in the mesh design so that the highest quality can be achieved.

Once the computational grid has been generated, the governing equations must be expressed in discrete form at each point in the grid by using a particular discretisation approach like finite difference method (FDM), finite element method (FEM) or finite volume method (FVM).

3.4.1 Finite volume approach

The FVM is the technique used in the research code COSA [34, 38, 35, 74] by which the integral formulation of the conservation laws is discretised directly on the computational domain subdivided into a number of CVs. By the direct discretisation is possible to ensure that the basic quantities like mass, momentum and energy will also remain conserved at the discrete level. The local conservativity concerns also the numerical fluxes which are conserved from one discretisation cell to its neighbour. The FVM can handle any type of meshes, but the following analysis will refer only to structured grid configuration, in agreement with the code features. The discretisation of the convective fluxes of both the RANS and the SST equations is based on Van Leer's second order Monotone Upstream centred extrapolations (MUSCL) and Roe's flux difference splitting. The second order discretisation of all diffusive fluxes and the source terms is instead based on central finite-differencing [38].

As shown in the previous sections, the integral form of RANS and SST equations is defined by Eq. (3.39). Using the finite volume method to discretise the conservation laws, one needs to solve Eq. (3.39) in each control volume defined by the mesh.

$$\frac{\partial}{\partial t}\int_V \widehat{\mathbf{U}} dV + \oint_S (\widehat{\mathbf{\Phi}}_c - \widehat{\mathbf{\Phi}}_d) dS - \int_V \widehat{\mathbf{S}} dV = 0 \tag{3.39}$$

The term $\frac{\partial}{\partial t}\int_V \widehat{\mathbf{U}} dV$ and $\int_V \widehat{\mathbf{S}} dV$ require the integration over the CV and the term $\oint_S (\widehat{\mathbf{\Phi}}_c - \widehat{\mathbf{\Phi}}_d) dS$ represent the flux on the CV boundaries which can be replaced by the sum of the fluxes over each face of the CV. Applying the FVM, Eq. (3.39) can be written in the discrete form as:

$$\frac{\partial}{\partial t}(\widehat{\mathbf{U}}_{cell}V_{cell}) + \sum(\widehat{\mathbf{\Phi}}_c - \widehat{\mathbf{\Phi}}_d)_{cell}S - \widehat{\mathbf{S}}_{cell}V_{cell} = 0 \tag{3.40}$$

which can be viewed as a set of conservation laws applied to the control volumes. The first terms on the left hand side is the time variation of the averaged $\widehat{\mathbf{U}}$ in each cell. It requires the calculation of the cells volume V_{cell} that in the cell-centred scheme can be computed using the coordinates of each cell vertices (see Fig. 3.5). In this scheme the unknown flow field refers to the centre of the cells and the CVs match the cells themselves.

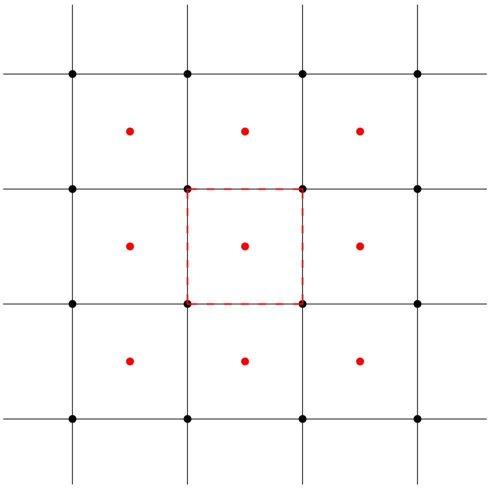

Figure 3.5: Cell-centred scheme. A grid cell highlighted with red dashed line

The second term on the left hand side of Eq. (3.40) represent the flux terms refers to all the external sides of the cell. The two-dimensional analytical expression of the convective fluxes through a cell face of area dS, can be derived from Eq. (3.36) and defined as:

$$\widehat{\mathbf{\Phi}}_c = (\widehat{\mathbf{\Phi}}_{c,f} \cdot \boldsymbol{n})dS = (\widehat{\mathbf{E}}_c n_x + \widehat{\mathbf{F}}_c n_y)dS \tag{3.41}$$

where n_x and n_y are, respectively, the x- and y- components of unit vector $\boldsymbol{n}$. To calculate the fluxes $\widehat{\mathbf{\Phi}}_c$, the flow state $\widehat{\mathbf{U}}$ has to be extrapolated from the cell centres to the left and right sides of the CV faces. Considering a flow state $\widehat{\mathbf{U}}_i$ of a $i-th$ cell of the grid, the MUSCL extrapolation [86] approximates the convective flux from the left and right, with a combination of backward and forward extrapolations using only the informations from one side of the flux. The flow state on the interface $i + \frac{1}{2}$ can be written as:

$$\widehat{\mathbf{U}}^{L}_{i+\frac{1}{2}} = \widehat{\mathbf{U}}_{i} + \frac{\widehat{\mathbf{U}}_{i} - \widehat{\mathbf{U}}_{i-1}}{2} \tag{3.42}$$

$$\widehat{\mathbf{U}}^{R}_{i+\frac{1}{2}} = \widehat{\mathbf{U}}_{i+1} - \frac{\widehat{\mathbf{U}}_{i+2} - \widehat{\mathbf{U}}_{i+1}}{2} \tag{3.43}$$

Such approximation forms the basis of the *linear upwind method.* To avoid discontinuities or sharp changes in the solution, flux limiters have been applied to Eq. (3.42) and (3.43). After calculating the flow state $\widehat{\mathbf{U}}$ at the cell faces, the convective fluxes described by Eq. (3.41) can be computed using the *flux difference splitting* method [104] as defined by Eq. (3.44):

$$\widehat{\mathbf{\Phi}}_{c} = \frac{1}{2}\left[\widehat{\mathbf{\Phi}}_{c,f}(\widehat{\mathbf{U}}^{L}) + \widehat{\mathbf{\Phi}}_{c,f}(\widehat{\mathbf{U}}^{R}) - |k_u|\delta\widehat{\mathbf{U}}\right] \tag{3.44}$$

where the subscript f denote the face fluxes and the superscript L and R denote flow states extrapolated from the left and right side of the considered grid cell. The term $|k_u|\delta\widehat{\mathbf{U}}$ represent the numerical dissipation and depends on the flow state discontinuity across the cell face. $\delta\widehat{\mathbf{U}}$ is defined as the difference between the flow state on the right side and on the left side, while k_U represent the generalised flux Jacobian evaluated at the considered face defined as:

$$k_U = \frac{\partial\widehat{\mathbf{\Phi}}_{c}}{\partial\widehat{\mathbf{U}}} = \left(\frac{\partial\widehat{\mathbf{E}}_{c}}{\partial\widehat{\mathbf{U}}}n_x + \frac{\partial\widehat{\mathbf{F}}_{c}}{\partial\widehat{\mathbf{U}}}n_y\right) \tag{3.45}$$

where the terms $\frac{\partial\widehat{\mathbf{E}}_{c}}{\partial\widehat{\mathbf{U}}}$ and $\frac{\partial\widehat{\mathbf{F}}_{c}}{\partial\widehat{\mathbf{U}}}$ denote the flux Jacobian in the x- and y- fluxes respectively.

Regarding the discretisation of the diffusive fluxes $\widehat{\mathbf{\Phi}}_{d}$, one needs to consider the flux balance of the viscous stresses on a CV on area S:

$$\oint_{S} \widehat{\tau} \cdot \boldsymbol{n} dS \tag{3.46}$$

The discretisation of the net flux of the viscous stress on the boundary of a cell (i, j) is given by the sum of the fluxes through the i and j surfaces, so the x- and y- components of the flux of the viscous stress are written as:

$$\begin{gathered}[(\widehat{\tau}_{xx}n_x + \widehat{\tau}_{xy}n_y)\Delta S]_{i+\frac{1}{2},j} + [(\widehat{\tau}_{xx}n_x + \widehat{\tau}_{xy}n_y)\Delta S]_{i,j+\frac{1}{2}} + \\ [(\widehat{\tau}_{xx}n_x + \widehat{\tau}_{xy}n_y)\Delta S]_{i-\frac{1}{2},j} + [(\widehat{\tau}_{xx}n_x + \widehat{\tau}_{xy}n_y)\Delta S]_{i,j-\frac{1}{2}}\end{gathered} \tag{3.47}$$

$$\begin{aligned}[(\widehat{\tau}_{xy}n_x + \widehat{\tau}_{yy}n_y)\Delta S]_{i+\frac{1}{2},j} + [(\widehat{\tau}_{xy}n_x + \widehat{\tau}_{yy}n_y)\Delta S]_{i,j+\frac{1}{2}} + \\ [(\widehat{\tau}_{xy}n_x + \widehat{\tau}_{yy}n_y)\Delta S]_{i-\frac{1}{2},j} + [(\widehat{\tau}_{xy}n_x + \widehat{\tau}_{yy}n_y)\Delta S]_{i,j-\frac{1}{2}}\end{aligned} \tag{3.48}$$

where $\widehat{\tau}_{xx}$, $\widehat{\tau}_{xy}$ and $\widehat{\tau}_{yy}$ are the components of the stress tensor which are computed on the four faces on the CV.

3.5 Solution of steady problems

In this research, the steady RANS and the two-turbulence equations are treated as a single set of strongly coupled equations and solved iteratively with the same four-stage Runge-Kutta (RK) smoother. Multigrid (MG) technique is adopted to achieve a faster convergence. For steady problems the time-derivative appearing in Eq. (3.36) vanishes, and space-discretising all remaining terms on a computational grid consisting of N_{cell} finite volumes leads to a system of nonlinear algebraic equations of the form:

$$\widehat{\mathbf{R}}_{\Phi}(\widehat{\mathbf{Q}}) = 0 \tag{3.49}$$

The entries of the array $\widehat{\mathbf{Q}}$ are the unknown flow variables at the N_{cell} cell centres, and the array $\widehat{\mathbf{Q}}$ is made up of N_{cell} subarrays each of which stores the N_{pde} flow unknowns at a particular cell center. The length of $\widehat{\mathbf{Q}}$ is therefore $(N_{pde} \times N_{cell})$. The array $\widehat{\mathbf{R}}_{\Phi}$ stores the cell residuals, and its structure is the same as that of $\widehat{\mathbf{Q}}$. For each cell, the N_{pde} residuals are obtained by adding the convective fluxes and the diffusive fluxes through all its faces, and, for the k and ω residuals, by also adding the associated source terms evaluated at the cell center, and given respectively by Eq. (3.29) and (3.30).

In COSA, the RANS and SST equations are solved with a time-marching algorithm using the so-called fully coupled approach [89, 87, 54], whereby the mean flow and the turbulence equations are solved simultaneously in the iterative process. This integration approach leads to significantly faster convergence rates than the loosely coupled method [88, 85], where the mean flow and turbulence equations are solved separately and often with different methods. The unknown flow vector $\widehat{\mathbf{Q}}$ is computed by solving iteratively Eq. (3.49). A fictitious time-derivative $(\partial\widehat{\mathbf{Q}}/\partial\tau)$ premultiplied by the cell volumes is added to the System (3.49), and it is then discretised with a four-stage Runge-Kutta scheme [21, 77, 135]. The numerical solution is thus marched in pseudo-time until the steady state is achieved. The convergence rate is enhanced by means of local time-stepping (LTS), variable-coefficient central implicit residual smoothing (IRS) [76, 26, 142, 27] and a full-approximation scheme (FAS) multigrid (MG) [50, 153] algorithm. The explicit RK iteration to solve RANS and $k-\omega$ SST equations is defined as:

$$\begin{aligned}
&\widehat{\mathbf{W}}^0 = \widehat{\mathbf{Q}}_l \\
&\widehat{\mathbf{W}}^m = \widehat{\mathbf{W}}^0 - \alpha_m \Delta\tau V^{-1} L_{IRS}[\widehat{\mathbf{R}}_\Phi(\widehat{\mathbf{W}}^{m-1}) + f_{MG}] \\
&\widehat{\mathbf{Q}}_{l+1} = \widehat{\mathbf{W}}^m
\end{aligned} \tag{3.50}$$

where $\Delta\tau$ is the local pseudo-time-step, l is the RK cycle counter, m is the RK stage index, and α_m is the m^{th} RK coefficient. L_{IRS} denotes the IRS operator, and f_{MG} is the MG forcing function. The diagonal matrix V stores the volumes of the grid cells and it is a block-diagonal matrix of size $(N_{cell} \times N_{cell})$ with each block being an identity matrix of size $(N_{pde} \times N_{pde})$ multiplied by the volume of the cell the block refers to.

When solving turbulent problems using a two-equation turbulence model, however, this explicit integration method has a very poor convergence rate, due to the operator stiffness caused by the large negative source terms of the turbulence model, such as $-D_k$, $-D_\omega$ and, when the velocity divergence is positive, $-\nabla \cdot \boldsymbol{u}$. To alleviate this problem, a semi-implicit integration strategy is adopted [89], whereby the negative source terms of the turbulence equations are treated implicitly within each RK stage. Adopting this approach, the semi-implicit turbulent smoother reads:

$$\begin{aligned}
&\widehat{\mathbf{W}}^0 = \widehat{\mathbf{Q}}_l \\
&(I + \alpha_m \Delta\tau A)\widehat{\mathbf{W}}^m = \\
&\qquad \widehat{\mathbf{W}}^0 + \alpha_m \Delta\tau A \widehat{\mathbf{W}}^{m-1} - \alpha_m \Delta\tau V^{-1} L_{IRS}[\widehat{\mathbf{R}}_\Phi(\widehat{\mathbf{W}}^{m-1}) + f_{MG}] \\
&\widehat{\mathbf{Q}}_{l+1} = \widehat{\mathbf{W}}^m
\end{aligned} \tag{3.51}$$

The matrix A is block-diagonal and has size $(N_{cell} \times N_{cell})$. The only nonzero elements of each $(N_{pde} \times N_{pde})$ block A_i on the diagonal of A are those of the bottom right (2×2) partition, and this occurrence results in the coupling of the update process of the turbulent variables. The matrix A is defined as:

$$A_i(5:6, 5:6) = A_{SST} = \begin{bmatrix} (\Delta^+ + \beta^*\omega) & \beta^* k \\ \frac{\gamma\Delta^+}{\nu_T} & 2\beta\omega \end{bmatrix} \tag{3.52}$$

in which $\Delta^+ = \max(0, \frac{2}{3}\nabla \cdot \boldsymbol{u})$, all variables are evaluated at the RK stage $m-1$, and the subscript i identifies the grid cell the matrix block refers to. The cross-diffusion term CD_ω can also be positive or negative depending on the local flow conditions, and therefore, when negative, it could be treated like Δ^+ in the semi-implicit integration. However, the treatment of the CD_ω term, introduce additional complexity in the algorithm design and a lower efficiency. For this reason, the integration of COSA treats the term CD_ω explicitly regardless of its sign. It should be noted that this term is absent in the standard $k-\omega$ model (see *Appendix B*). Another difference between the semi-implicit integration of the standard $k-\omega$ model and that of the SST model is that, in the former case, $\rho\omega$ can be updated independently of ρk. This is however not possible in the SST case, since $A_{SST}(2,1)$ is not zero. Hence, a (2×2) matrix inversion is required at each grid cell to update ρk and $\rho\omega$. The different turbulent variables update of the $k-\omega$ and SST models occurs because the expression of the turbulent viscosity of the former model is obtained by setting $F_2 = 0$ in Eq. (3.19). This operation results in the relationship $k/\nu_T = \omega$, which can be used to remove the dependence of the equation for updating $\rho\omega$ on k. By performing this substitution, the bottom right partition of each block of A becomes:

$$A_i(5:6, 5:6) = A_{k-\omega} = \begin{bmatrix} (\Delta^+ + \beta^*\omega) & \beta^* k \\ 0 & \gamma\Delta^+ + 2\beta\omega \end{bmatrix} \tag{3.53}$$

In general, when using the SST turbulence model, one would adopt Eq. (3.52) rather than Eq. (3.53). Numerical experiments, however, reveal that the results computed with either approach present fairly small differences for low-speed flows, such as those analysed in this thesis. For this reason all the results presented in this thesis are based on Eq. (3.53).

The turbulent COSA code adopts the strongly coupled integration method also for computing time-dependent problems, whereby the explicit multigrid integration is used to solve the unsteady RANS (URANS) equations coupled to the SST turbulence model. For such time-dependent problems, the turbulent multigrid solver also features a point-implicit treatment of certain terms arising from the discretisation of the physical time-derivatives. This approach is an extension of the stabilisation process reported by Melson et al. [99], and it enables the use of fairly high Courant Friedrichs Lewy (CFL) numbers, thus significantly reducing the number of multigrid cycles required to achieve a user-given reduction of the flow residuals.

3.6 Solution of time-dependent problems

General time-dependent flow problems are solved using the so-called dual-time-stepping (DTS) approach. The physical time-derivative of System (3.36) is discretised with a second order backward finite-difference. At each new physical time-level $n+1$, the sought flow solution is computed by solving the set of nonlinear algebraic equations resulting from the space- and time-discretisation of System (3.36) with the same integration method used for steady problems. The RK smoother (3.51) is used for computing the sought flow solution $\widehat{\mathbf{Q}}^{n+1}$ by solving the system of algebraic equations:

$$V\frac{\partial \widehat{\mathbf{Q}}^{n+1}}{\partial \tau} + \widehat{\mathbf{R}}_g(\widehat{\mathbf{Q}}^{n+1}) = 0 \tag{3.54}$$

where

$$\widehat{\mathbf{R}}_g(\widehat{\mathbf{Q}}^{n+1}) = \frac{3\widehat{\mathbf{Q}}^{n+1} - 4\widehat{\mathbf{Q}}^{n} + \widehat{\mathbf{Q}}^{n-1}}{2\Delta t}V + \widehat{\mathbf{R}}_\Phi(\widehat{\mathbf{Q}}^{n+1}) = 0 \tag{3.55}$$

In the Eq. (3.55), $\widehat{\mathbf{R}}_g$ denotes the residual vector which also includes the source terms associated with the discretisation of the physical time-derivative $\partial\widehat{\mathbf{U}}/\partial t$ of Eq. (3.36), and Δt indicates the user-given physical time-step. Also for time-dependent problems with moving bodies, the matrix V is independent of the physical time-level because in this study only rigid-body grid motion is considered.

The Eq. (3.54) represent a system of size ($N_{pde} \times N_{cell}$) ordinary differential equations and the flow state at time $n+1$ ($\widehat{\mathbf{Q}}^{n+1}$) is the unknown. $\widehat{\mathbf{Q}}^{n+1}$ is calculated by discretising the fictitious time-derivative using the RK scheme and marching the equations in pseudo-time until a steady state is achieved. Using the dual time stepping approach to the integration of time-dependent problem [75, 37], once the flow solution at the physical time-level $n+1$ has been computed, the array $\widehat{\mathbf{Q}}^{n}$ is copied to $\widehat{\mathbf{Q}}^{n-1}$ and the array $\widehat{Q}^{n+1}$ is copied to $\widehat{\mathbf{Q}}^{n}$ and the iterative process computes the new solution at new time-level. This procedure may become unstable when the physical time-step Δt is much smaller than the pseudo-time-step $\Delta\tau$ as reported in [18, 99].

The study solved the stability problem by treating implicitly the $\widehat{\mathbf{Q}}^{n+1}$ term of the physical time-derivative within the RK integration process. This strategy has also been implemented in the CFD code COSA for the fully coupled integration of the RANS and SST equations. The TD counterpart of the turbulent steady smoother (3.51) is:

$$\begin{aligned}
&\widehat{\mathbf{W}}^0 = \widehat{\mathbf{Q}}_l \\
&[I + \alpha_m(\beta_{TD} I + \Delta\tau A)]\,\widehat{\mathbf{W}}^m = \\
&\qquad \widehat{\mathbf{W}}^0 + \alpha_m(\beta_{TD} I + \Delta\tau A)\widehat{\mathbf{W}}^{m-1} - \alpha_m \Delta\tau V^{-1} L_{IRS}[\widehat{\mathbf{R}}_g(\widehat{\mathbf{W}}^{m-1}) + f_{MG}] \\
&\widehat{\mathbf{Q}}_{l+1} = \widehat{\mathbf{W}}^m
\end{aligned} \tag{3.56}$$

where $\beta_{TD} = 1.5\Delta\tau/\Delta t$, and $\widehat{\mathbf{Q}}_l$ is shorthand for $\widehat{\mathbf{Q}}_l^{n+1}$. The matrix multiplying $\widehat{\mathbf{W}}^m$ in Algorithm (3.56) is block-diagonal with N_{cell} blocks. In each $(N_{pde} \times N_{pde})$ block the top left (4×4) partition is proportional to the identity matrix through the coefficient $(1+\alpha_m\beta_{TD})$, the bottom right (2×2) partition is given by the sum of the (2×2) identity matrix multiplied by $(1+\alpha_m\beta_{TD})$ and a non-diagonal (2×2) matrix given by Eq. (3.52) or Eq. (3.53), depending on whether the exact or approximate update of $(\rho\omega)$ is used, and all other entries are zero. Similarly to the case of the integration of the steady equations, this structure of the matrix premultiplying $\widehat{\mathbf{W}}^m$ results in the coupling of the update process of the turbulent variables, whereas it still enables the four mean flow variables to be updated without any actual matrix inversion. Due to the fact that the $\widehat{\mathbf{Q}}^{n+1}$ term arising from the backward finite-difference of the physical time-derivative is evaluated at stage m, Algorithm (3.56) is said to be based a point-implicit Runge-Kutta (PIRK) integration of the time-dependent mean flow and turbulence equations. The standard fully explicit Runge-Kutta (FERK) integration method is retrieved by setting $\beta_{TD} = 0$ in this algorithm. Several numerical tests [38] have highlighted that the turbulent PIRK integration significantly improves the stability of the fully coupled integration, enabling stable pseudo-time-marching with larger CFL numbers than with the standard FERK integration. This yields significant reductions of run-times, due to the reduction of the overall number of MG cycles required to achieve a user-given reduction of the flow residuals.

3.7 Conclusion

The CFD research code COSA uses a time-marching method to solve time-dependent engineering flow problems. The fundamental governing equations of fluid dynamics coupled to the SST turbulence model of Menter have been presented in this chapter. The finite volume discretisation method used to represent the continuous nature of the governing equations in a discrete form and the integration method to solve the system of nonlinear algebric equations obtained from the discretisation approach have also been described. Moreover, an important approximation to the integration of the SST equations has been implemented and discussed. A drawback of using time-marching methods for solving periodic flow problems is the presence of a transient response in the solution, so, they become inefficient when several periods have to be simulated before a fully developed periodic solution is achieved. In order to reach the periodic solution in a shorter computational time, a frequency-domain CFD approach has been implemented and the details are presented in the *Chapter 4*.

Chapter 4

Numerical solution of Harmonic Balance Navier-Stokes equations

At present, the most of time-periodic flow problems are solved using traditional time-marching approaches where the flow solution is computed by solving the set of nonlinear algebraic equations resulting from the space- and time-discretisation of System (3.36) and time-marched from an initial state until a user-given final time. The downside to using time-marching methods for time-periodic problems is that they include a transient response in the solution. So, they become inefficient when several periods have to be simulated before a fully developed periodic solution is achieved. In many cases, only the steady-state solution is desired. In order to reach the periodic solution in a short time, the harmonic balance (HB) technology can be applied (Fig. 4.1). It is a nonlinear frequency-domain (FD) method computationally more efficient than time marching methods for unsteady flow problems, where the output response is periodic in time and described by one or more ordinary differential equations (ODE). Any computational cost associated with a transient response is completely avoided. The HB solution is represented as a truncated Fourier series retaining a user given number of complex harmonics, and the given time-domain problem is reformulated and solved in the frequency-domain using the solution approximation provided by the truncated Fourier series. The HB NS technology for the solution of unsteady periodic flows is one of the most promising FD NS methods. It was first introduced by Hall et al. [65], who first showed the run-time reduction compared to the TD approach, for the case of turbomachinery flows. In this thesis the HB approach was applied for the first

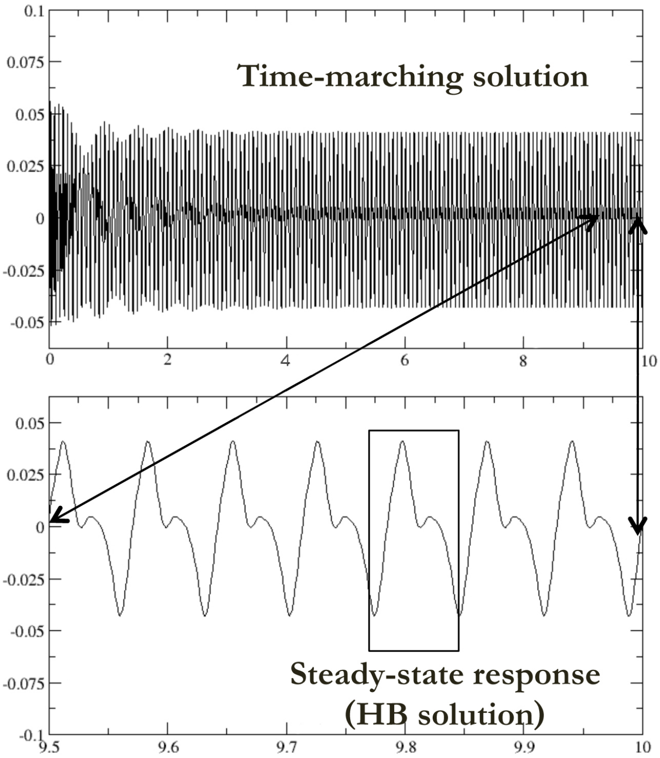

Figure 4.1: Time marching method against HB approach.

time to turbulent wind turbine aerodynamics and has been demonstrated that it can reduce the run-time of a CFD simulation by one or more order of magnitude with respect to the case in which the conventional TD is used. The CFD code COSA adopts the high dimensional harmonic balance (HDHB) formulation, which differs from the implementation of the classical HB. In this chapter it is provided the general definition of the HB solution process of a system of three ODEs. It is discussed to highlight the differences between the two mathematical HB implementations. A comparison of these two methods is provided and the HDHB formulation of the URANS and the turbulence model equations is presented.

4.1 Harmonic balance method

The harmonic balance method has been used for many years to analyse the behaviour of harmonic ordinary differential equations. The technique assumes that the solution may be represented as a truncated Fourier series with a predetermined number of harmonics. This form of the solution is substituted into the governing equations and after algebraic manipulations it is possible to collect the coefficients of every harmonic. The first formal presentation of the HB method is usually accredited to Kryloff and Bogoliuboff in the 1940s [83]. Throughout the years, many variants of HB technology have emerged. As a result, the technique has been applied to myriad of problems in several fields, especially nonlinear circuit analysis [17, 108] and nonlinear dynamics [23, 81, 98, 63]. A harmonic balance approach for modelling unsteady nonlinear flows in turbomachinery was proposed in 2002 by Hall et al. [65]. The analysis exploits the fact that many unsteady flows in turbomachinery are periodic in time. The authors represented the unsteady flow conservation variables by a Fourier series in time with spatially varying coefficients. This leads to a harmonic balance form of the Navier-Stokes equations, which can be solved efficiently as a system of coupled steady problems using conventional CFD methods. They found that increasing the terms of the Fourier series (harmonics), the solution improves. Inserting the Fourier representations into the original equations, yields a system of coupled partial differential equations and the unknowns are the Fourier coefficients. McMullen et al. [98] used a HB approach, involving a nonlinear frequency-domain method to investigate the flow around a cylinder and a pitching aerofoil. Also Ekici and Hall [53] developed a variant of the HB method that uses a mixed TD/FD approach to compute the unsteady aerodynamic response of multistage turbomachines to blade vibration and wake interaction.

Recently, a new formulation of the HB method has been developed by Thomas et al. [143] for deterministic dynamical system. The approach was suitable for high dimensional dynamical systems and for this characteristic was denoted as high dimensional harmonic balance (HDHB). In the HDHB approach the flow field variables are discretised in time and solved at $(2N_H + 1)$ equally spaced time-domain snapshots over the period instead of solving the Fourier coefficients directly. Working in terms of time-domain sub-time level solution variables avoids the harmonic balancing of the Fourier coefficient solution variables of the classical HB method. This makes the HDHB method very easy to formulate within the framework of an existing time marching nonlinear solver. The HB technology has also been applied to several studies [144, 62, 19, 66] like those to predict various vibratory motion modes of aircraft configurations [44, 130, 158] and to predict periodic flows associated with turbomachinery unsteady flows and aeroelasticity [140, 149].

On wind energy applications, a preliminary demonstration of the use of HB NS technology for yawed HAWT flows was reported in [34], which showed that also for this problem type, the wallclock time required for accurately predicting the time-dependent blade loads in laminar flow conditions is about 10 times smaller than that of the time-grid-independent TD analysis. This thesis presents the implementation and the successful application of a compressible turbulent HB NS solver to the prediction of HAWT flows in yaw condition [36] and also to the strongly nonlinear periodic flow problem associated with the aerodynamics of vertical axis wind turbines.

This is the first reported study on the use of the turbulent HB RANS technology for turbulent unsteady HAWT and VAWT aerodynamics. On the algorithmic and numerical sides, further elements of novelty are the extension of the fully coupled integration approach to the HB framework, the design and the implementation of a point-implicit approach to the integration of the turbulent HB equations enabling the use of a fewer MG cycles than the fully explicit approach to achieve solution convergence and the introduction of an approximation yielding a significant cost reduction of the fully coupled integration of the HB RANS and SST equations with negligible effects on the solution accuracy. Furthermore, it has been demonstrated that the wallclock time required to predict an unsteady flow solution using COSA HB solver depends from the particular test case and the operating condition analysed. For strongly nonlinear problems like VAWT, the HB wallclock time required to predict the unsteady flow solutions is about 5 times smaller than the TD analysis (see *Chapter 7*). In this case, COSA allows the user to use an efficient hybrid parallelisation that adopts a combination of MPI libraries to communicate between nodes and openMP libraries for communication inside each shared memory node, to take back the HB wallclock time to a factor of 10.

4.2 Harmonic balance integration of ODE system

The System (4.1) is an example of first order nonlinear system of ordinary differential equations. The unknowns of this system are denoted by x, y, z and F denotes the forcing term.

$$\begin{cases} \dot{x} = y - z^3 + 1 + Fsin(\omega t) \\ \dot{y} = 0.1z + 1 - y \cdot z \\ \dot{z} = 2x - z^2 + 0.5 \end{cases} \tag{4.1}$$

The System (4.1) represents in a simplified manner the structure of the governing equations implemented in a RANS code making use of differential two-equation turbulence models for the turbulent closure. The first equation can represent the RANS equations, the second and third equations can represent the k and ω equations of the turbulence model. *Appendix C* reports the Matlab script developed to solve the system of ODEs using the explicit and implicit method adopted by COSA as well as the Runge-Kutta time marching and the Matlab function FSOLVE. The aim of studying this system is to highlight the differences between the HB and HDHB integration.

4.2.1 Classical harmonic balance

For the derivation of the standard HB method, one begins by considering the solution of the System (4.1) to be of the form of a truncated Fourier series expansion:

$$x(t) = \widehat{x}_0 + \sum_{n=1}^{N_H} (\widehat{x}_{2n-1} \cos(n\omega t) + \widehat{x}_{2n} \sin(n\omega t)) \tag{4.2}$$

$$y(t) = \widehat{y}_0 + \sum_{n=1}^{N_H} (\widehat{y}_{2n-1} \cos(n\omega t) + \widehat{y}_{2n} \sin(n\omega t)) \tag{4.3}$$

$$z(t) = \widehat{z}_0 + \sum_{n=1}^{N_H} (\widehat{z}_{2n-1} \cos(n\omega t) + \widehat{z}_{2n} \sin(n\omega t)) \tag{4.4}$$

where ω is the known fundamental frequency of oscillation, $\widehat{x}_0$, $\widehat{y}_0$ and $\widehat{z}_0$ are the mean values of the sought periodic solutions, $\widehat{x}_{2n-1}$, $\widehat{x}_{2n}$, $\widehat{y}_{2n-1}$, $\widehat{y}_{2n}$, $\widehat{z}_{2n-1}$ and $\widehat{z}_{2n}$ for $(n = 1, 2, ..., N_H)$ are the real and imaginary parts of the N_H complex harmonics of each unknown complex harmonic component and N_H is the number of complex harmonics used in the truncated Fourier series expansion.

In the case of the ODE equations of the system considered, it is needed also the expression of the first time-derivative terms:

$$\dot{x}(t) = \sum_{n=1}^{N_H} (-n\omega \widehat{x}_{2n-1} \sin(n\omega t) + n\omega \widehat{x}_{2n} \cos(n\omega t)) \tag{4.5}$$

$$\dot{y}(t) = \sum_{n=1}^{N_H} (-n\omega \widehat{y}_{2n-1} \sin(n\omega t) + n\omega \widehat{y}_{2n} \cos(n\omega t)) \tag{4.6}$$

$$\dot{z}(t) = \sum_{n=1}^{N_H} (-n\omega \widehat{z}_{2n-1} \sin(n\omega t) + n\omega \widehat{z}_{2n} \cos(n\omega t)) \tag{4.7}$$

Considering the first ODE of the System (4.1), also the cubic nonlinear term must be expressed as truncated Fourier series:

$$(z(t))^3 = \widehat{r}_0 + \sum_{n=1}^{N_H} (\widehat{r}_{2n-1} \cos(n\omega t) + \widehat{r}_{2n} \sin(n\omega t)) \tag{4.8}$$

where $\widehat{r}_0$, $\widehat{r}_{2n-1}$ and $\widehat{r}_{2n}$ are the mean value, the real part of the n^{th} complex harmonic and the imaginary part of the n^{th} complex harmonic of the nonlinear cubic term respectively. The expressions of $\widehat{r}_0$, $\widehat{r}_{2n-1}$ and $\widehat{r}_{2n}$ are expressed as:

$$\widehat{r}_0 = \frac{1}{2\pi} \int_0^{2\pi} \left(\widehat{z}_0 + \sum_{n=1}^{N_H} (\widehat{z}_{2n-1} \cos(nt) + \widehat{z}_{2n} \sin(nt)) \right)^3 dt \tag{4.9}$$

$$\widehat{r}_{2n-1} = \frac{1}{\pi} \int_0^{2\pi} \left(\widehat{z}_0 + \sum_{n=1}^{N_H} (\widehat{z}_{2n-1} \cos(nt) + \widehat{z}_{2n} \sin(nt)) \right)^3 \cos(nt)\, dt \tag{4.10}$$

$$\widehat{r}_{2n} = \frac{1}{\pi} \int_0^{2\pi} \left(\widehat{z}_0 + \sum_{n=1}^{N_H} (\widehat{z}_{2n-1} \cos(nt) + \widehat{z}_{2n} \sin(nt)) \right)^3 \sin(nt)\, dt \tag{4.11}$$

Similar expressions can be defined for the nonlinear terms in the second and third equation of the System (4.1). The coefficients defined by Eq. (4.9), (4.10) and (4.11) are functions of the unknown coefficients $\widehat{z}_n$. Substituting the expressions (4.3), (4.5), and (4.8) into the first equation of System (4.1) and collecting terms associated with each harmonic $\cos(n\omega t)$ and $\sin(n\omega t)$ with $n = 0, 1, 2, ..., N_H$ yield $(2N_H + 1)$ algebraic equations for Fourier coefficients $\widehat{x}_n$, $\widehat{y}_n$ and $\widehat{z}_n$ $(n = 0, 1, 2, ..., N_H)$. Applying the same procedure for the second and third equation, each ODE is transformed into $(2N_H + 1)$ algebraic equations that yields the harmonic components of the truncated Fourier series representation of the sought periodic solutions.

The resulting system of algebraic equations can be written in vector form as:

$$\begin{cases} (\omega A)\widehat{\mathbf{Q}}_x - \widehat{\mathbf{Q}}_y + \widehat{\mathbf{R}}_{z^3} = \widehat{\mathbf{C}} + F\widehat{\mathbf{H}} \\ (\omega A)\widehat{\mathbf{Q}}_y - 0.1\widehat{\mathbf{Q}}_z + \widehat{\mathbf{R}}_{yz} = \widehat{\mathbf{C}} \\ (\omega A)\widehat{\mathbf{Q}}_z - 2\widehat{\mathbf{Q}}_x + \widehat{\mathbf{R}}_{z^2} = 0.5\widehat{\mathbf{C}} \end{cases} \tag{4.12}$$

where the arrays $\widehat{\mathbf{Q}}_x$, $\widehat{\mathbf{Q}}_y$ and $\widehat{\mathbf{Q}}_z$ are the unknowns arrays of length $(2N_H + 1)$ defined as:

$$\widehat{\mathbf{Q}}_x = \begin{bmatrix} \widehat{x}_0 \\ \widehat{x}_1 \\ \widehat{x}_2 \\ \vdots \\ \widehat{x}_{2N_H} \end{bmatrix}, \quad \widehat{\mathbf{Q}}_y = \begin{bmatrix} \widehat{y}_0 \\ \widehat{y}_1 \\ \widehat{y}_2 \\ \vdots \\ \widehat{y}_{2N_H} \end{bmatrix}, \quad \widehat{\mathbf{Q}}_z = \begin{bmatrix} \widehat{z}_0 \\ \widehat{z}_1 \\ \widehat{z}_2 \\ \vdots \\ \widehat{z}_{2N_H} \end{bmatrix}$$

The entries of the arrays $\widehat{\mathbf{R}}_{z^3}$, $\widehat{\mathbf{R}}_{yz}$ and $\widehat{\mathbf{R}}_{z^2}$ are the coefficients of the Fourier expansion of the nonlinear terms and have length $(2N_H + 1)$. They are defined as:

$$\widehat{\mathbf{R}}_{z^3} = \begin{bmatrix} \widehat{r}_{0_{z^3}} \\ \widehat{r}_{1_{z^3}} \\ \widehat{r}_{2_{z^3}} \\ \vdots \\ \widehat{r}_{2N_{H_{z^3}}} \end{bmatrix}, \quad \widehat{\mathbf{R}}_{yz} = \begin{bmatrix} \widehat{r}_{0_{yz}} \\ \widehat{r}_{1_{yz}} \\ \widehat{r}_{2_{yz}} \\ \vdots \\ \widehat{r}_{2N_{H_{yz}}} \end{bmatrix}, \quad \widehat{\mathbf{R}}_{z^2} = \begin{bmatrix} \widehat{r}_{0_{z^2}} \\ \widehat{r}_{1_{z^2}} \\ \widehat{r}_{2_{z^2}} \\ \vdots \\ \widehat{r}_{2N_{H_{z^2}}} \end{bmatrix}$$

The arrays $\widehat{\mathbf{H}}$ and $\widehat{\mathbf{C}}$ of length $(2N_H + 1)$ are expressed as:

$$\widehat{\mathbf{H}} = \begin{bmatrix} 0 \\ 0 \\ 1 \\ \vdots \\ 0 \end{bmatrix}, \quad \widehat{\mathbf{C}} = \begin{bmatrix} 1 \\ 0 \\ 0 \\ \vdots \\ 0 \end{bmatrix}$$

and the matrix A that is a block structure where only the diagonal blocks hold non-zero entries are expressed as:

$$A = \begin{bmatrix} 0 & & & & \\ & J_1 & & & \\ & & J_2 & & \\ & & & \cdots & \\ & & & & J_{N_H} \end{bmatrix}, \quad J_n = n \begin{bmatrix} 0 & 1 \\ -1 & 0 \end{bmatrix}, \quad n = 1, 2, ..., N_H$$

The block $(1, 1)$ of matrix A is a scalar 0, all the other diagonal blocks are 2×2. The overall dimension of matrix A is $(2N_H + 1) \times (2N_H + 1)$.

Solving System (4.12) requires analytical expressions of the nonlinear functions $\widehat{\mathbf{r}}_{i_{z^3}}$, $\widehat{\mathbf{r}}_{i_{yz}}$ and $\widehat{\mathbf{r}}_{i_{z^2}}$ $(i = 0, 1, 2, ..., 2N_H)$ in terms of the variables $\widehat{\mathbf{y}}_i$ and $\widehat{\mathbf{z}}_i$ $(i = 0, 1, 2, ..., 2N_H)$. When the nonlinearity in the governing equations is not a simple polynomial function of the solution variable, the expression of the nonlinear terms can be very complex to compute and the standard HB approach become difficult to use. In this cases, the problem can be avoided by using the so-called *High Dimensional Harmonic Balance* HDHB method.

4.2.2 High dimensional harmonic balance

The HDHB approach can be easily used for all the models that present more complex nonlinearities, like RANS equations augmented with PDEs of turbulence models. The main reason for using the HDHB procedure is to avoid the derivation of the nonlinear terms. Considering the System (4.1), the simplification introduced by the HDHB method is to replace the $(2N_H + 1)\widehat{\mathbf{Q}}_x$, $(2N_H + 1)\widehat{\mathbf{Q}}_y$ and $(2N_H + 1)\widehat{\mathbf{Q}}_z$ unknowns corresponding to the mean value, the real and imaginary parts of the retained complex N_H Fourier harmonics with $(2N_H + 1)$ equally spaced time-domain snapshots of the sought periodic solution. This change simplifies the derivation of the HB equations to be solved. The HDHB procedure for the System (4.1) is outlined in the following.

The $(2N_H + 1)$ harmonic balance Fourier coefficient of the solution variables of $\widehat{\mathbf{Q}}_x$, $\widehat{\mathbf{Q}}_y$ and $\widehat{\mathbf{Q}}_z$ are related to the time-domain solution at $(2N_H + 1)$ equally spaced sub-time levels $\tilde{\mathbf{Q}}_x$, $\tilde{\mathbf{Q}}_y$ and $\tilde{\mathbf{Q}}_z$ over a period of oscillation via a constant Fourier transformation matrix E.

$$\widehat{\mathbf{Q}}_x = E\tilde{\mathbf{Q}}_x \tag{4.13}$$

$$\widehat{\mathbf{Q}}_y = E\tilde{\mathbf{Q}}_y \tag{4.14}$$

$$\widehat{\mathbf{Q}}_z = E\tilde{\mathbf{Q}}_z \tag{4.15}$$

where

$$\tilde{\mathbf{Q}}_x = \begin{bmatrix} x(t_0) \\ x(t_1) \\ x(t_2) \\ \vdots \\ x(t_{2N_H}) \end{bmatrix}, \qquad \tilde{\mathbf{Q}}_y = \begin{bmatrix} y(t_0) \\ y(t_1) \\ y(t_2) \\ \vdots \\ y(t_{2N_H}) \end{bmatrix}, \qquad \tilde{\mathbf{Q}}_z = \begin{bmatrix} z(t_0) \\ z(t_1) \\ z(t_2) \\ \vdots \\ z(t_{2N_H}) \end{bmatrix}$$

$$\widehat{\mathbf{Q}}_x = \begin{bmatrix} \widehat{x}_0 \\ \widehat{x}_1 \\ \widehat{x}_2 \\ \vdots \\ \widehat{x}_{2N_H} \end{bmatrix}, \quad \widehat{\mathbf{Q}}_y = \begin{bmatrix} \widehat{y}_0 \\ \widehat{y}_1 \\ \widehat{y}_2 \\ \vdots \\ \widehat{y}_{2N_H} \end{bmatrix}, \quad \widehat{\mathbf{Q}}_z = \begin{bmatrix} \widehat{z}_0 \\ \widehat{z}_1 \\ \widehat{z}_2 \\ \vdots \\ \widehat{z}_{2N_H} \end{bmatrix}$$

with t_i defined as:

$$t_i = \frac{i}{(2N_H+1)}\frac{2\pi}{\omega}, \qquad i = 0, 1, \cdots, 2N_H \tag{4.16}$$

and the transformation matrix E expressed as:

$$E = \frac{2}{2N_H+1}\begin{bmatrix} 1/2 & 1/2 & \cdots & 1/2 \\ \cos t_0 & \cos t_1 & \cdots & \cos t_{2N_H} \\ \sin t_0 & \sin t_1 & \cdots & \sin t_{2N_H} \\ \cos 2t_0 & \cos 2t_1 & \cdots & \cos 2t_{2N_H} \\ \sin 2t_0 & \sin 2t_1 & \cdots & \sin 2t_{2N_H} \\ \vdots & \vdots & & \vdots \\ \cos N_H t_0 & \cos N_H t_1 & \cdots & \cos N_H t_{2N_H} \\ \sin N_H t_0 & \sin N_H t_1 & \cdots & \sin N_H t_{2N_H} \end{bmatrix}$$

Furthermore, the time-domain solutions at $(2N_H+1)$ equally spaced sub-time levels can be expressed in term of the harmonic balance Fourier coefficients solution using the inverse of the Fourier transformation matrix as:

$$\tilde{\mathbf{Q}}_x = E^{-1}\widehat{\mathbf{Q}}_x \tag{4.17}$$

$$\tilde{\mathbf{Q}}_y = E^{-1}\widehat{\mathbf{Q}}_y \tag{4.18}$$

$$\tilde{\mathbf{Q}}_z = E^{-1}\widehat{\mathbf{Q}}_z \tag{4.19}$$

where the inverse of matrix E is defined as:

$$E^{-1} = \begin{bmatrix} 1 & \cos t_0 & \sin t_0 & \cdots & \cos N_H t_0 & \sin N_H t_0 \\ 1 & \cos t_1 & \sin t_1 & \cdots & \cos N_H t_1 & \sin N_H t_1 \\ \vdots & \vdots & \vdots & & \vdots & \vdots \\ 1 & \cos t_{2N_H} & \sin t_{2N_H} & \cdots & \cos N_H t_{2N_H} & \sin N_H t_{2N_H} \end{bmatrix}$$

Similarly to what done for the unknowns variables, for the arrays $\widehat{\mathbf{R}}_{z^3}$, $\widehat{\mathbf{R}}_{yz}$, $\widehat{\mathbf{R}}_{z^2}$, $\widehat{\mathbf{H}}$ and $\widehat{\mathbf{C}}$ one has:

$$\widehat{\mathbf{R}}_{z^3} = E\tilde{\mathbf{R}}_{z^3} \tag{4.20}$$

$$\widehat{\mathbf{R}}_{yz} = E\tilde{\mathbf{R}}_{yz} \tag{4.21}$$

$$\widehat{\mathbf{R}}_{z^2} = E\tilde{\mathbf{R}}_{z^2} \tag{4.22}$$

$$\widehat{\mathbf{H}} = E\tilde{\mathbf{H}} \tag{4.23}$$

$$\widehat{\mathbf{C}} = E\tilde{\mathbf{C}} \tag{4.24}$$

where

$$\tilde{\mathbf{R}}_{z^3} = \begin{bmatrix} z(t_0)^3 \\ z(t_1)^3 \\ \vdots \\ z(t_{2N_H})^3 \end{bmatrix}, \quad \tilde{\mathbf{R}}_{yz} = \begin{bmatrix} yz(t_0) \\ yz(t_1) \\ \vdots \\ yz(t_{2N_H}) \end{bmatrix}, \quad \tilde{\mathbf{R}}_{z^2} = \begin{bmatrix} z(t_0)^2 \\ z(t_1)^2 \\ \vdots \\ z(t_{2N_H})^2 \end{bmatrix}$$

$$\tilde{\mathbf{H}} = \begin{bmatrix} \sin t_0 \\ \sin t_1 \\ \vdots \\ \sin t_{2N_H} \end{bmatrix}, \quad \tilde{\mathbf{C}} = \begin{bmatrix} 1 \\ 1 \\ \vdots \\ 1 \end{bmatrix}$$

Inserting Eqs. (4.13), (4.14), (4.15), (4.20), (4.21) (4.22), (4.23) and (4.24) into the classical HB formulation of the System (4.1), System (4.12) can be rewritten as:

$$\begin{cases} (\omega A)E\tilde{\mathbf{Q}}_x - E\tilde{\mathbf{Q}}_y + E\tilde{\mathbf{R}}_{z^3} = E\tilde{\mathbf{C}} + FE\tilde{\mathbf{H}} \\ (\omega A)E\tilde{\mathbf{Q}}_y - 0.1E\tilde{\mathbf{Q}}_z + E\tilde{\mathbf{R}}_{yz} = E\tilde{\mathbf{C}} \\ (\omega A)E\tilde{\mathbf{Q}}_z - 2E\tilde{\mathbf{Q}}_x + E\tilde{\mathbf{R}}_{z^2} = 0.5E\tilde{\mathbf{C}} \end{cases} \tag{4.25}$$

Multiplying both sides of each equation of System (4.25) by E^{-1} gives:

$$\begin{cases} (\omega D)\tilde{\mathbf{Q}}_x - \tilde{\mathbf{Q}}_y + \tilde{\mathbf{R}}_{z^3} = \tilde{\mathbf{C}} + F\tilde{\mathbf{H}} \\ (\omega D)\tilde{\mathbf{Q}}_y - 0.1\tilde{\mathbf{Q}}_z + \tilde{\mathbf{R}}_{yz} = \tilde{\mathbf{C}} \\ (\omega D)\tilde{\mathbf{Q}}_z - 2\tilde{\mathbf{Q}}_x + \tilde{\mathbf{R}}_{z^2} = 0.5\tilde{\mathbf{C}} \end{cases} \tag{4.26}$$

where $D = E^{-1}AE$. The System (4.26) is referred to as the HDHB solution system. It does not require complicated analytical transformations such as those needed for the construction of $\widehat{\mathbf{r}}_{i_{z^3}}$, $\widehat{\mathbf{r}}_{i_{yz}}$ and $\widehat{\mathbf{r}}_{i_{z^2}}$ terms of System (4.12) and it is relatively easy to implement into an existing time marching code. This feature is very important when applying the HB approach to solve complex system of equations such as those obtained from the discretisation of the RANS equations and the PDEs of differential turbulence model. For the linear terms, the HDHB method produces the same result as the HB method does. Therefore, the source of any difference is related to the nonlinear terms. As can be seen by the System (4.26), the nonlinear term of the first $(2N_H+1)$ equations is:

$$\tilde{\mathbf{R}}_{z^3} = \begin{bmatrix} \left(\mid E^{-1}\widehat{\mathbf{Q}}_z \mid_1\right)^3 \\ \left(\mid E^{-1}\widehat{\mathbf{Q}}_z \mid_2\right)^3 \\ \vdots \\ \left(\mid E^{-1}\widehat{\mathbf{Q}}_z \mid_{2N_H+1}\right)^3 \end{bmatrix} \equiv \left(E^{-1}\widehat{\mathbf{Q}}_z\right)^3 \tag{4.27}$$

Here a vector's cubic power is defined as the vector of the cubic power of each component. With Eqs. (4.27), (4.17) and (4.18), the first $(2N_H+1)$ equations of System (4.26) becomes:

$$(\omega D)E^{-1}\widehat{\mathbf{Q}}_x - E^{-1}\widehat{\mathbf{Q}}_y + (E^{-1}\widehat{\mathbf{Q}}_z)^3 = E^{-1}\widehat{\mathbf{C}} + FE^{-1}\widehat{\mathbf{H}} \tag{4.28}$$

Multiplying both sides of Eq. (4.28) by E yields the equivalent of the first $(2N_H+1)$ equations of System (4.26) in the frequency-domain:

$$(\omega A)\widehat{\mathbf{Q}}_x - \widehat{\mathbf{Q}}_y + E(E^{-1}\widehat{\mathbf{Q}}_z)^3 = \widehat{\mathbf{C}} + F\widehat{\mathbf{H}} \tag{4.29}$$

From (4.12) and (4.29), the difference between the HB and HDHB system is really the difference between $\widehat{\mathbf{R}}_{z^3}$, whose elements are defined by Eq. (4.9), (4.10) and (4.11) for the HB approach, and $E(E^{-1}\widehat{\mathbf{Q}}_z)^3$ for the HDHB approach. The same behaviour can be shown for the other two nonlinear terms.

However, when N_H approaches to infinity, the solutions are essentially identical, therefore, HB and HDHB methods are asymptotically equivalent [90]. A further example on the difference between these two approaches is reported in [90] where the Duffing's oscillator is used.

4.3 HDHB formulation of turbulent Navier-Stokes equations

The space discretisation of time-dependent RANS and SST turbulence equations leads to a system of ODEs with size equal to the number of cells of the physical domain times the number of partial differential equations ($N_{cell} \times N_{pde}$). The application of the HB approach gives a system of nonlinear algebraic equations of size $[N_{pde} \times N_{cell} \times (2N_H + 1)]$ where the number of harmonics N_H is a user-given parameter. Denoting by $\widehat{\mathbf{u}}$ and $\widehat{\mathbf{h}}$ the volume and surface integral of Eq. (3.36) respectively, it is possible to define both variables by means of the following truncated Fourier series:

$$\widehat{\mathbf{u}}(t) = \widehat{\mathbf{u}}_0 + \sum_{l=1}^{N_H} \left(\widehat{\mathbf{u}}_{2l-1} \cos(l\omega t) + \widehat{\mathbf{u}}_{2l} \sin(l\omega t)\right) \tag{4.30}$$

$$\widehat{\mathbf{h}}(t) = \widehat{\mathbf{h}}_0 + \sum_{l=1}^{N_H} \left(\widehat{\mathbf{h}}_{2l-1} \cos(l\omega t) + \widehat{\mathbf{h}}_{2l} \sin(l\omega t)\right) \tag{4.31}$$

All arrays in Eq. (4.30) and (4.31) have length $N_{pde} = 6$. Inserting both equations into Eq. (3.36) and balancing harmonics with the same order, give a system of $[N_{pde} \times (2N_H + 1)]$ equations, defined as:

$$\omega A \widehat{\mathbf{u}} + \widehat{\mathbf{h}} = 0 \tag{4.32}$$

where ω is the fundamental frequency of the sought periodic flow field. The matrix A and the arrays $\widehat{\mathbf{u}}$ and $\widehat{\mathbf{h}}$ are defined as:

$$A = \begin{bmatrix} 0 & 0 & 0 & \cdots & 0 \\ 0 & J_1 & 0 & \cdots & 0 \\ 0 & 0 & J_2 & \cdots & 0 \\ \cdots & \cdots & \cdots & \cdots & \cdots \\ 0 & 0 & 0 & \cdots & J_{N_H} \end{bmatrix} \qquad J_l = I_{N_{eqs}} \otimes l \begin{bmatrix} 0 & 1 \\ -1 & 0 \end{bmatrix}$$

$$\widehat{\mathbf{u}} = \begin{bmatrix} \widehat{\mathbf{u}}'_0 \\ \widehat{\mathbf{u}}'_1 \\ \cdots \\ \widehat{\mathbf{u}}'_{2N_H} \end{bmatrix}, \qquad \widehat{\mathbf{h}} = \begin{bmatrix} \widehat{\mathbf{h}}'_0 \\ \widehat{\mathbf{h}}'_1 \\ \cdots \\ \widehat{\mathbf{h}}'_{2N_H} \end{bmatrix}$$

where $l = 1, 2, ..., N_H$, the symbol $\otimes$ denotes the Kronecker tensor product, $I_{N_{eqs}}$ denotes the identity matrix of size $(N_{pde})^2$ and blocks J_l have size $(2N_{pde})^2$. As shown for the system example reported in the preceding subsections, the analytical derivation of the equations of the system in Eq. (4.32) can become extremely complex. For this reason the HDHB formulation has been applied and it was obtained by reconstructing the Fourier coefficients of the volume integral $\widehat{\mathbf{u}}$ of the conservation variables and the surface integral $\widehat{\mathbf{h}}$ of the fluxes, from the knowledge of the temporal behaviour of $\mathbf{u}(t)$ and $\mathbf{h}(t)$ at $(2N_H + 1)$ equally spaced snapshots over one period.

Defining the arrays $\tilde{\mathbf{u}}$ and $\tilde{\mathbf{h}}$ as:

$$\tilde{\mathbf{u}} = \begin{bmatrix} \mathbf{u}(t_0)' \\ \mathbf{u}(t_1)' \\ \cdots \\ \mathbf{u}(t_{2N_H})' \end{bmatrix} \qquad \tilde{\mathbf{h}} = \begin{bmatrix} \mathbf{h}(t_0)' \\ \mathbf{h}(t_1)' \\ \cdots \\ \mathbf{h}(t_{2N_H})' \end{bmatrix}$$

and using the Fourier transformation matrix E, one can easily obtain the system:

$$\omega D\tilde{\mathbf{u}} + \tilde{\mathbf{h}} = 0 \tag{4.33}$$

where $D = E^{-1}AE$ is the $[N_{eqs} \times N_{eqs}]$ matrix with $[N_{eqs} = N_{pde} \times (2N_H + 1)]$.

The integral definition of $\tilde{\mathbf{u}}$ and $\tilde{\mathbf{h}}$ can be substituted into Eq. (4.33) to obtain the HDHB formulation of the RANS and SST equations used by COSA:

$$\omega D \left(\int_{V(t)} \widehat{\mathbf{U}}_H dV \right) + \oint_{S_t} (\widehat{\mathbf{\Phi}}_{c_H} - \widehat{\mathbf{\Phi}}_{d_H}) \cdot dS = \int_{V_t} \widehat{\mathbf{S}}_H dV \tag{4.34}$$

The symbol $\widehat{\mathbf{U}}_H$ denotes the unknown array made up of $(2N_H + 1)$ equally spaced flow field snapshots and it is defined as:

$$\widehat{\mathbf{U}}_H = \begin{bmatrix} \widehat{\mathbf{U}}(t_0)' \\ \widehat{\mathbf{U}}(t_1)' \\ \cdots \\ \widehat{\mathbf{U}}(t_{2N_H})' \end{bmatrix}$$

The subarray structure of $\widehat{\mathbf{\Phi}}_{c_H}$, $\widehat{\mathbf{\Phi}}_{d_H}$ and $\widehat{\mathbf{S}}_H$ is similar to that of $\widehat{\mathbf{U}}_H$. From now on, the acronym HB to refer to the HDHB implementation adopted by COSA will be used.

4.4 Semi-implicit integration based on LU factorisation

At the differential level, the only difference between System (3.36) and System (4.34) is that the physical time-derivative of the former system is replaced by a volumetric source term proportional to ω in the latter. The set of nonlinear algebraic equations resulting from the space discretisation of the harmonic balance RANS and SST equations (System (4.34)) can thus be solved with the same four-stage RK smoother used for steady problems described in *Chapter 3*. A fictitious time-derivative $\frac{d\widehat{\mathbf{Q}}_H}{d\tau}$ pre-multiplied by the cell volumes is added to the system giving a system of ODEs defined as:

$$\frac{d\widehat{\mathbf{Q}}_H}{d\tau} + V_H^{-1}\widehat{\mathbf{R}}_{gH}(\widehat{\mathbf{Q}}_H) = 0 \tag{4.35}$$

where

$$\widehat{\mathbf{R}}_{gH}(\widehat{\mathbf{Q}}_H) = \omega V_H D_H \widehat{\mathbf{Q}}_H + \widehat{\mathbf{R}}_{\Phi H}(\widehat{\mathbf{Q}}_H) \tag{4.36}$$

The flow solution array $\widehat{\mathbf{Q}}_H$ is made up of N_{cell} sets of $(2N_H + 1)$ flow states, with each state referring to the physical times defined by Eq. (4.16). Therefore, $\widehat{\mathbf{Q}}_H = [\widehat{\mathbf{Q}}_1' \ \widehat{\mathbf{Q}}_2' \ \cdots \ \widehat{\mathbf{Q}}_{N_{cell}}']'$, where $\widehat{\mathbf{Q}}_i$, with $i = 1, N_{cell}$, is an array of length $[N_{pde} \times (2N_H + 1)]$. The first N_{pde} elements of $\widehat{\mathbf{Q}}_i$ contain the flow state at $t = t_0$, the next N_{pde} elements contain the flow state at $t = t_1$, and the last N_{pde} elements contain the flow state at $t = t_{2N_H+1}$. The arrays $\widehat{\mathbf{R}}_{gH}$ and $\widehat{\mathbf{R}}_{\Phi H}$ have the same structure of $\widehat{\mathbf{Q}}_H$. The $(2N_H + 1)$ states of a subarray $(\widehat{\mathbf{R}}_{\Phi})_i$ contain the cell residuals associated with the convective fluxes, the diffusive fluxes and the turbulent source terms at the physical times defined by Eq. (4.16). The residual subarray $(\widehat{\mathbf{R}}_g)_i$ is the sum of the residuals $\widehat{\mathbf{R}}_{\Phi H}$ and the source term $\omega V_i D\widehat{\mathbf{Q}}_i$, where V_i is the product of the volume of the i^{th} grid cell and $I_{N_{eqs}}$, the identity matrix of size $(N_{eqs} \times N_{eqs})$ with $N_{eqs} = [N_{pde} \times (2N_H + 1)]$. The diagonal matrix V_H is a block-diagonal matrix with blocks given by the matrices V_i defined above, and the block-diagonal matrix D_H is defined as $D_H = I_{N_{cell}} \otimes D$.

It has been verified that the use of the nonturbulent counterpart of the smoother (3.51) for solving the HB equations describing some periodic Euler and laminar flows results in numerical instabilities of the solver that prevent its convergence, unless very low CFL numbers are used. It has been found that the fully explicit Runge-Kutta (FERK) HB solver may become unstable also for solving some turbulent unsteady problems. Therefore, a stabilised point-implicit HB smoother adopted in [34] was extended to the turbulent case, and used to improve the numerical stability of the turbulent HB MG solver. The fundamental step of the stabilisation process requires treating implicitly the source term of Eq. (4.36) and requires to treat implicitly some negative source terms of the turbulence equations within each RK stage. This approach, said to be based a point-implicit Runge-Kutta integration, has been applied for the HB solver and it is similar to that adopted by Liu and Zheng [89] for solving the standard $k - \omega$ equations.

The HB semi-discrete form of k and ω equations can be written as:

$$\frac{\partial}{\partial t}(\rho k)_H + \omega D_H(\rho k)_H + R_k((\rho k)_H, (\rho\omega)_H) = 0 \tag{4.37}$$

$$\frac{\partial}{\partial t}(\rho\omega)_H + \omega D_H(\rho\omega)_H + R_\omega((\rho k)_H, (\rho\omega)_H) = 0 \tag{4.38}$$

The symbol R_k denotes the residual of the k equation, defined as:

$$R_k((\rho k)_H, (\rho\omega)_H) = \frac{1}{V_H}(C_{k_H} - D_{k_H}) - S_{k_H} \tag{4.39}$$

where C_{k_H}, D_{k_H} and S_{k_H} are the discrete forms of the convective flux term, diffusive term and source term of the k equation, respectively. Their expression is:

$$C_{k_H} = \sum_{i_s=1}^{4} \left[(\rho k u_n) \cdot \Delta S\right]_{i_s} \tag{4.40}$$

$$D_{k_H} = \sum_{i_s=1}^{4} \left[(\mu + \sigma_k \mu_T)\nabla k \cdot \Delta S\right]_{i_s} \tag{4.41}$$

$$S_{k_H} = \mu_t P_d - \frac{2}{3}(\nabla \cdot u)(\rho k)_H - \frac{\beta^*}{\rho}(\rho\omega)_H(\rho k)_H \tag{4.42}$$

In Eq. (4.42), the term $\mu_t P_d$ is the major contributor to the production of k and it is always positive, the term $-\frac{2}{3}(\nabla \cdot u)(\rho k)_H$ gives a minor contribution to production and can be either positive or negative, and $-\frac{\beta^*}{\rho}(\rho\omega)_H(\rho k)_H$ is the dissipation term and it is always negative.

The residual for the ω equation is instead defined as:

$$R_\omega((\rho k)_H, (\rho\omega)_H) = \frac{1}{V_H}(C_{\omega_H} - D_{\omega_H}) - S_{\omega_H} \tag{4.43}$$

and C_{ω_H}, D_{ω_H} and S_{ω_H} denote, respectively, the discrete forms of the convective flux, diffusive flux and the source term of the ω equation. They can be expressed as:

$$C_{\omega_H} = \sum_{i_s=1}^{4} \left[(\rho\omega u_n) \cdot \Delta S\right]_{i_s} \tag{4.44}$$

$$D_{\omega_H}=\sum_{i_s=1}^{4}\left[(\mu+\sigma_\omega\mu_T)\nabla\omega\cdot\Delta S\right]_{i_s} \tag{4.45}$$

$$S_{\omega_H}=\gamma\rho P_d-\gamma\frac{2}{3}(\nabla\cdot u)(\rho\omega)_H-\frac{\beta}{\rho}(\rho\omega)^2_H \tag{4.46}$$

As explained for Eq. (4.42), in Eq. (4.46) there is the term $\gamma\rho P_d$ which is the major contributor to the production of ω and it is always positive, the term $-\gamma\frac{2}{3}(\nabla\cdot u)(\rho\omega)_H$ that can be positive or negative and provides minor contribution to the production of ω and $-\frac{\beta}{\rho}(\rho\omega)^2_H$ which is the dissipation term and it is always negative. The two negative terms which appear in the source terms of k and ω annihilate the two turbulent variables. Larger are these terms and faster is the decay of k and ω. The explicit formulation for the k and ω equations used at each stage of the RK scheme can be modified to treat part of S_{k_H} and S_{ω_H} implicitly, improving the convergence rate of the turbulent equations. Defining:

$$\Delta^+=\max\left(0,\frac{2}{3}\nabla\cdot u\right) \tag{4.47}$$

the negative contributions of the source terms in the k and ω equations can be moved to the LHS of Eq. (4.37) and (4.38) to form a semi-implicit formulation. So Eq. (4.37) can be written as:

$$\begin{gathered}\frac{\partial}{\partial t}(\rho k)_H+\omega D_H(\rho k)_H+\frac{1}{V_H}(C_{k_H}-D_{k_H})-\mu_t P_d+\\ \Delta^+(\rho k)_H+\Delta^-(\rho k)_H+\frac{\beta^*}{\rho}(\rho\omega)_H(\rho k)_H=0\end{gathered} \tag{4.48}$$

where $\Delta^-=\frac{2}{3}\nabla\cdot u-\Delta^+$. The general RK step with implicit treatment can be defined as:

$$\begin{gathered}\frac{(\rho k)^m_H-(\rho k)^0_H}{\alpha_m\Delta\tau_H}+\omega D_H(\rho k)^m_H+\frac{1}{V_H}(C_{k_H}-D_{k_H})^{m-1}-(\mu_t P_d)^{m-1}+(\Delta^+(\rho k)_H)^m\\ +(\Delta^+(\rho k)_H)^{m-1}-(\Delta^+(\rho k)_H)^{m-1}+(\Delta^-(\rho k)_H)^{m-1}\\ +\left[\frac{\beta^*}{\rho}(\rho\omega)_H(\rho k)_H\right]^m+\left[\frac{\beta^*}{\rho}(\rho\omega)_H(\rho k)_H\right]^{m-1}-\left[\frac{\beta^*}{\rho}(\rho\omega)_H(\rho k)_H\right]^{m-1}=0\end{gathered} \tag{4.49}$$

where the superscript m is the RK stage. Equation (4.49) can be written as:

$$\begin{gathered}\left(\frac{1}{\alpha_m\Delta\tau_H}+\Delta^++\omega D_H\right)(\rho k)^m_H-\frac{(\rho k)^0_H}{\alpha_m\Delta\tau_H}-(\Delta^+(\rho k)_H)^{m-1})\\ +\frac{\beta^*}{\rho}\left[(\rho\omega)^m_H(\rho k)^m_H-(\rho\omega)^{m-1}_H(\rho k)^{m-1}_H\right]=-R^{m-1}_k\end{gathered} \tag{4.50}$$

The term R^{m-1}_k denote the complete cell residual array of $(\rho k)_H$. Equation (4.50) the approximations $(\Delta^+)^m\approx(\Delta^+)^{m-1}$ and $1/\rho^m\approx 1/\rho^{m-1}$ have been used. Equation (4.50) can now be linearised by setting:

$$(\delta\rho k)_H=(\rho k)^m_H-(\rho k)^{m-1}_H \tag{4.51}$$

$$(\delta\rho\omega)_H = (\rho\omega)^m_H - (\rho\omega)^{m-1}_H \tag{4.52}$$

then:

$$\begin{aligned}(\rho\omega)^m_H(\rho k)^m_H &\approx \left[(\rho\omega)^{m-1}_H + (\delta\rho\omega)_H\right]\left[(\rho k)^{m-1}_H + (\delta\rho k)_H\right]\\ &\approx (\rho\omega)^{m-1}_H(\rho k)^{m-1}_H + (\rho\omega)^{m-1}_H(\delta\rho k)_H + (\rho k)^{m-1}_H(\delta\rho\omega)_H\end{aligned} \tag{4.53}$$

Inserting the expression (4.53) into Eq. (4.50), the update equation for ρk is:

$$\begin{gathered}\left[\tfrac{1}{\alpha_m\Delta\tau_H} + \Delta^+ + \tfrac{\beta^*}{\rho}(\rho\omega)^{m-1}_H + \omega D_H\right](\rho k)^m_H - \tfrac{(\rho k)^0_H}{\alpha_m\Delta\tau_H} - (\Delta^+(\rho k)_H)^{m-1})\\ -\tfrac{\beta^*}{\rho}(\rho\omega)^{m-1}_H(\rho k)^{m-1}_H + \tfrac{\beta^*}{\rho}(\rho k)^{m-1}_H(\delta\rho\omega)_H = -R^{m-1}_k\end{gathered} \tag{4.54}$$

which can be written as:

$$\begin{gathered}\left[1 + (\Delta^+ + \beta^*(\omega)^{m-1}_H)\alpha_m\Delta\tau_H + \alpha_m\omega\Delta\tau_H D_H\right](\rho k)^m_H =\\ \alpha_m\Delta\tau_H\left[-\beta^*(k)^{m-1}_H(\delta\rho\omega)_H + \beta^*(\omega)^{m-1}_H(\rho k)^{m-1}_H + (\Delta^+(\rho k)_H)^{m-1}\right]\\ +(\rho k)^0_H - \alpha_m\Delta\tau_H R^{m-1}_k\end{gathered} \tag{4.55}$$

Note that the LHS of Eq. (4.55) is made up of the sum of two matrices, the first one is a diagonal matrix $I + \alpha_m\Delta\tau_H(\Delta^+ + \beta^*(\omega)^{m-1}_H)$ of size $(2N_H+1)^2$ and an antisymmetric matrix $\alpha_m\omega\Delta\tau_H D_H$ with the same size.

Using the same procedure for ω, Eq. (4.38) can be written as:

$$\begin{gathered}\tfrac{\partial}{\partial t}(\rho\omega)_H + \omega D_H(\rho\omega)_H + \tfrac{1}{V_H}(C_{\omega_H} - D_{\omega_H}) - \gamma\alpha^*\rho P_d\\ +\gamma\Delta^+(\rho\omega)_H + \gamma\Delta^-(\rho\omega)_H + \tfrac{\beta}{\rho}(\rho\omega)^2_H = 0\end{gathered} \tag{4.56}$$

The general RK step with implicit treatment for updating ω can be defined as:

$$\begin{gathered}\tfrac{(\rho\omega)^m_H - (\rho\omega)^0_H}{\alpha_m\Delta\tau_H} + \omega D_H(\rho\omega)^m_H + \tfrac{1}{V_H}(C_{\omega_H} - D_{\omega_H})^{m-1} - \gamma\alpha^*(\rho P_d)^{m-1}\\ +\gamma(\Delta^+(\rho\omega)_H)^m + \gamma(\Delta^+(\rho\omega)_H)^{m-1} - \gamma(\Delta^+(\rho\omega)_H)^{m-1}\\ +\gamma(\Delta^-(\rho\omega)_H)^{m-1} + \left[\tfrac{\beta}{\rho}(\rho\omega)^2_H\right]^m + \left[\tfrac{\beta}{\rho}(\rho\omega)^2_H\right]^{m-1} - \left[\tfrac{\beta}{\rho}(\rho\omega)^2_H\right]^{m-1} = 0\end{gathered} \tag{4.57}$$

Equation (4.57) can be written as:

$$\begin{gathered}\left(\tfrac{1}{\alpha_m\Delta\tau_H} + \gamma\Delta^+ + \omega D_H\right)(\rho\omega)^m_H - \tfrac{(\rho\omega)^0_H}{\alpha_m\Delta\tau_H} - \gamma(\Delta^+(\rho\omega)_H)^{m-1})\\ +\tfrac{\beta}{\rho}\left[((\rho\omega)^2_H)^m - ((\rho\omega)^2_H)^{m-1}\right] = -R^{m-1}_\omega\end{gathered} \tag{4.58}$$

where R^{m-1}_ω denotes the complete cell residual array of $(\rho\omega)_H$.

Using the same approximation used for k, to linearise the Eq. (4.58) one needs to define:

$$(\delta\rho\omega)_H = (\rho\omega)^m_H - (\rho\omega)^{m-1}_H \tag{4.59}$$

then:

$$\begin{aligned}(\rho\omega)_H^m(\rho\omega)_H^m &\approx \left[(\rho\omega)_H^{m-1} + (\delta\rho\omega)_H\right]\left[(\rho\omega)_H^{m-1} + (\delta\rho\omega)_H\right] \\ &\approx (\rho\omega)_H^{m-1}(\rho\omega)_H^{m-1} + 2(\rho\omega)_H^{m-1}(\delta\rho\omega)_H\end{aligned} \tag{4.60}$$

Inserting expression (4.60) into Eq. (4.58), yields:

$$\begin{gathered}\left(\tfrac{1}{\alpha_m\Delta\tau_H} + \gamma\Delta^+ + 2\beta(\omega)_H^{m-1} + \omega D_H\right)(\rho\omega)_H^m - \tfrac{(\rho\omega)_H^0}{\alpha_m\Delta\tau_H} \\ -\gamma(\Delta^+(\rho\omega)_H)^{m-1} - 2\beta(\omega)_H^{m-1}(\rho\omega)_H^{m-1} = -R_\omega^{m-1}\end{gathered} \tag{4.61}$$

which can be written as:

$$\begin{gathered}\left[1 + \alpha_m\Delta\tau_H(\gamma\Delta^+ + 2\beta(\omega)_H^{m-1}) + \alpha_m\omega\Delta\tau_H D_H\right](\rho\omega)_H^m = \\ \alpha_m\Delta\tau_H\left[\gamma(\Delta^+(\rho\omega)_H)^{m-1} + 2\beta(\omega)_H^{m-1}(\rho\omega)_H^{m-1}\right] + (\rho\omega)_H^0 - \alpha_m\Delta\tau_H R_\omega^{m-1}\end{gathered} \tag{4.62}$$

Using the semi-implicit integration for $(\rho k)_H$ and $(\rho\omega)_H$, the update of $(\rho k)_H$ depends on the new value of $(\rho\omega)_H$. So, one needs to update $(\rho\omega)_H$ first and $(\rho k)_H$ thereafter. By doing so, one obtains the following HB-counterpart of the turbulent TD smoother (3.56):

$$\begin{aligned}&\widehat{\mathbf{W}}_H^0 = (\widehat{\mathbf{Q}}_H)_l \\ &[I + \alpha_m(\beta_H D_H + \Delta\tau_H A_H)]\,\widehat{\mathbf{W}}_H^m = \widehat{\mathbf{W}}_H^0 + \\ &\qquad \alpha_m(\beta_H D_H + \Delta\tau_H A_H)\widehat{\mathbf{W}}_H^{m-1} - \alpha_m\Delta\tau_H V_H^{-1} L_{IRS,H}[\widehat{\mathbf{R}}_{gH}(\widehat{\mathbf{W}}_H^{m-1}) + f_{MG,H}] \\ &(\widehat{\mathbf{Q}}_H)_{l+1} = \widehat{\mathbf{W}}_H^m\end{aligned} \tag{4.63}$$

where the N_{cell} subarrays of $\Delta\tau_H$ have length $(2N_H+1)$. Each subarray contain the local time-steps for the $(2N_H+1)$ flow states. One also has $\beta_H = \omega\Delta\tau_H$. The array of the HB MG forcing term has the same structure of $\widehat{\mathbf{Q}}_H$. The matrix A_H can be viewed as a $(N_{cell} \times N_{cell})$ block-diagonal matrix. Each block $A_{H,i}$, of size $[N_{eqs} \times N_{eqs}]$ with $N_{eqs} = [N_{pde} \times (2N_H+1)]$, also has a block-diagonal structure. Its $(2N_H+1)$ nonzero $[N_{pde} \times N_{pde}]$-blocks provide the matrices A_i's for the flow states referring to the times defined by Eq. (4.16). This formulation include the acceleration techniques IRS and MG adopted by COSA. The HB IRS operator has the same block structure of A_H. The use of the turbulent PIRK HB smoother (4.63) enables the use of significantly larger CFL numbers than the use of its FERK counterpart. For test cases affected by the aforementioned numerical instability, the stabilised smoother can use CFL numbers of up to 4, whereas CFL numbers have to be limited to values very low when using the standard non-stabilised smoother. Moreover, the higher stability of this PIRK relative to that of the FERK iteration increases significantly with N_H.

Using the approximation provided by Eq. (3.53) for updating $(\rho k)_H$ and $(\rho\omega)_H$, the structure of the matrix premultiplying $\widehat{\mathbf{W}}_H^m$ at the second line of Algorithm (4.63) is such that, for each grid cell, the update of the $[N_{pde} \times (2N_H+1)]$ unknowns requires the inversion of a single $[(2N_H+1) \times (2N_H+1)]$-sub-block of $[I + \alpha_m(\beta_H D_H + \Delta\tau_H A_H)]$. Such overhead results in the computational cost of the HB analysis growing linearly with N_H. Despite this feature, the computational cost of the HB analysis remains competitive with that of the TD counterpart. If the exact update of the turbulent variables provided by Eq. (3.52) was used, the computational cost of the turbulent PIRK smoother would be higher than the cost incurred by using Eq. (3.53). In the former case, in fact, the update of the four RANS cell variables would require the inversion of a $[(2N_H+1) \times (2N_H+1)]$-matrix as in latter case, but the update of the two SST variables would require the additional inversion of a $[2(2N_H+1) \times 2(2N_H+1)]$-matrix, because of the equation coupling due to all entries of A_{SST} being not zero. However, numerical experiments showed that the results computed with either approach presented no differences for low speed flow problems. For this reason, for updating the harmonics of the SST turbulence variables with the turbulent PIRK HB smoother, Eq. (3.53) has been used. In addition using Eq. (3.53) it yields a significant reduction of the computational cost.

The update of the $[N_{pde} \times (2N_H+1)]$ unknowns, for each grid cell, requires the inversion of a single $[(2N_H+1) \times (2N_H+1)]$-sub-block of $[I + \alpha_m(\beta_H D_H + \Delta\tau_H A_H)]$. After that, the inverted matrix $[I + \alpha_m(\beta_H D_H + \Delta\tau_H A_H)]^{-1}$ must be multiplied by the RHS of the equation at the second line of Algorithm (4.63). To solve the system in an efficient way, LAPACK libraries integration has been successfully implemented to massively improve the computational efficiency of the PIRK approach to the integration of the HB RANS equations and the turbulence model of Menter [38]. LAPACK (Linear Algebra PACKage) [3] is a software library for numerical linear algebra. It provides routines for solving systems of equations, eigenvalue problems, and singular value decomposition. It also includes routines to implement the associated matrix factorizations such as LU, QR, Cholesky and Schur decomposition. Denoting by $\mathbf{B}$ the matrix

$[I + \alpha_m(\beta_H D_H + \Delta\tau_H A_H)]$ and by $\mathbf{C}$ the RHS of the second line of Algorithm (4.63), the latter can be simplified as:

$$\mathbf{B} \cdot \mathbf{W} = \mathbf{C} \tag{4.64}$$

The System (4.64) needs to be solved in two steps:

- *LU* factorisation of the matrix to be inverted, **B**. It is based on the algorithm of Gaussian elimination and performed by a specific LAPACK library.

$$\mathbf{B} = \mathbf{L} \cdot \mathbf{U} \tag{4.65}$$

- a second LAPACK library uses the LU factorisation to solve easily the system:

$$\mathbf{L} \cdot \mathbf{U} \cdot \mathbf{W} = \mathbf{C} \tag{4.66}$$

The overhead due to the inverted matrix results in the computational cost of the HB analysis growing linearly with N_H. Despite this feature, the computational cost of the HB analysis remains competitive with that of the TD approach (see *Appendix D* for LAPACK routines details).

4.5 Hybrid parallelisation

For complex problems, computational resources used by a CFD simulations can be very large, particularly when the user uses meshes with millions of cells. To reduce the run-times of each simulation, it is possible to make use of parallel computing. The research code COSA has been parallelised by EPCC Centre during the last years [74, 72, 73] and now it can run simulations in a faster way, using thousands of cores. The parallelisation approach adopted in COSA is the so-called *hybrid* or *mixed-mode* parallelisation, which combines a distributed parallel computing using Message Passaging Interface (MPI) libraries [4] and shared memory parallelisations using the OpenMP shared memory libraries [5], allowing the access to a large number of processors and large amount of memory than the one available using either approaches separately. The general structure of COSA HB solver can be defined as:

```
for i_b = 1:N_block
  for i_h = 1:(2N_H+1)
    for j_cell = 1:N_cell,j
```

```
         for i_cell = 1:N_cell,i
           Instructions to perform
         end
       end
     end
   end
```

where N_{block} is the number of blocks in the computational domain, N_H is the user-given number of harmonics, and $N_{cell,i}$ and $N_{cell,j}$ are the number of cells in the i and j directions of the current block, respectively.

There are many other works which demonstrates parallel implementations of NS solvers [105, 56]. The key feature of the MPI parallelisation is the computational domain decomposition into two or more discrete blocks as the computation performed on a particular block is independent from those performed on all other blocks, and therefore can be processed in parallel. Thus, the MPI parallelisation is explicitly linked to the loop over blocks, so, during the code execution it distributes one or more blocks to a single processor. This approach cannot provide much benefits for simulations with small number of blocks. Regarding the OpenMP parallelisation, it takes independent instructions of a loop and distribute them to a group of threads that perform these sets of operations in parallel. Since each of the threads can access shared data, it is possible to parallelise any loop with no structural change to the code. However, this approach imposes an overhead for each loop because some operations are needed to set up the threads that will execute the parallelisation. The OpenMP parallelisation has been set-up over the harmonic loop. So, the hybrid code aims to combine the flexibility of the OpenMP solutions with the performance of the MPI solution. Since the OpenMP parallelisation is performed on the harmonic loop, the HB solver can further reduce the run-time of each simulation because it can use more computational resources (cores) in compared to TD technology which uses only the MPI parallelisation over the blocks. In the TD approach, the harmonics loop is not execute ($N_H = 0$) so it can not parallelise over the harmonics (OpenMP is not used in this case).

4.6 Conclusion

A frequency-domain CFD method suitable to solve periodic flow problems has been presented. The aim of using a frequency-domain approach is to reduce the computational cost with respect to time-marching method. The classical HB and HDHB methods have been considered and the differences between these approaches are reported in this chapter. Due to the strong nonlinearity of the governing equations and thanks to the relatively simpler implementation of the HDHB formulation in an existing CFD code, the HDHB approach has been implemented in COSA and the formulation of the NS equations and SST turbulence model has been shown. In addition a semi-implicit variant of the HDHB MG solver has been implemented and discussed. In strongly nonlinear problems requiring the use of many complex harmonics for an adequate resolution of the periodic flow field, this variant enables the use of substantially higher CFL numbers, leading to a further significant reductions of the run-time of the turbulent harmonic balance analysis.

Chapter 5

Time-domain analysis of vertical axis wind turbines

The operating conditions of VAWTs are intrinsically highly unsteady at all wind speeds, due to the periodic variation (every rotor revolution) of the modulus and the direction of the relative velocity perceived by the blades [110, 29], and also the interactions between the wakes shed by the blades travelling in the upwind region of the rotor and the blades crossing the downwind region of the rotor. These complex unsteady flow patterns are further complicated by the occurrence of dynamic stall [52, 133] over a significant portion of the entire turbine operating range [134]. For all these reasons, the aerodynamic design of these machines is a challenging task, since reliable quantitative estimates and sound understanding of the aforementioned unsteady aerodynamic phenomena is required to obtain the power output as a function of the wind and turbine speeds. The use of experimental testing to support VAWT design is still a costly route, and its outcomes can also be affected by uncertainty, due to both finite error margins of the adopted measurement techniques and possibly inaccurate wind tunnel measured data correction, and also the difficulty of reproducing in wind tunnels all the (non-dimensional) parameters characterising open air operation. Navier-Stokes CFD analyses offers an additional cost-effective, versatile and accurate means to improve the understanding of VAWT unsteady aerodynamics and thus achieve higher-performance and more cost effective Darrieus turbine design. In this chapter it has been presented a complete flow analysis of a Darrieus rotor presented in [117]. An accurate sensitivity analysis to the mesh refinement, temporal refinement and distance of the farfield boundaries from the rotor has been performed to better understand the physical and numerical uncertainties of the RANS simulations of Darrieus rotor. For validation purpose, the comparison between the results obtained by the density-based structured multi-block COSA research code and the results obtained by the pressure-based unstructured solver of FLUENT has been shown. Experimental measurements of the three dimensional (3D) model of the reference Darrieus turbine with a slightly different configuration, have been compared with a new 2D model of FLUENT consistent with the 3D model and a new comparison has been reported. In addition, a detailed aerodynamic analyses for low and high λ are presented to explain the operating behaviour of a Darrieus wind turbine.

5.1 Darrieus rotor

The turbine rotor selected for the analyses is a 3-blade H-Darrieus (see Fig. 5.1) and its main characteristics are reported in Table 5.1. The rotor characteristics match the wind turbine proposed by Raciti Castelli et al. [116, 117]. In the 2D CFD simulations the rotor shaft has been neglected.

Blades number (N_b)	3
Blades shape	Straight
Blades aerofoil	NACA0021
Radius (R) [m]	0.5150
Chord (c) [m]	0.0858
c/R ratio	0.166
Solidity (σ)	0.249
Blade connections	0.25 c

Table 5.1: Main features of the H-rotor Darrieus turbine analysed.

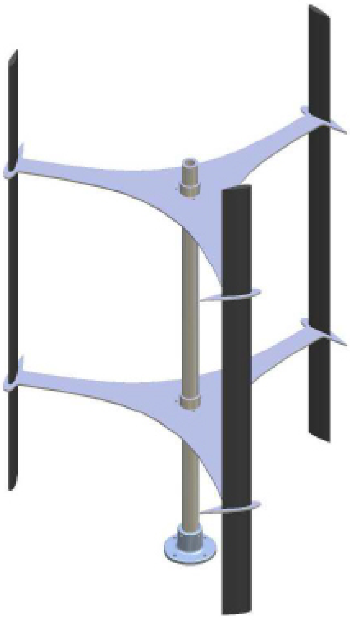

Figure 5.1: Darrieus rotor model layout [116]

5.2 Computational set-up

The numerical simulations performed refer to a turbine operating in open field conditions. The freestream wind speed (V_∞) is 9 m/s in all simulations. The Reynolds number used to perform these simulations is defined by Eq. (5.1)

$$Re = \frac{\rho \cdot (\Omega R) \cdot c}{\mu} \tag{5.1}$$

where:

- ρ is the air density
- Ω is the rotational speed
- R is the rotor radius
- c is the chord
- μ is the dynamic viscosity

The λ has been varied from 2.40 to 4.04 (revolution speed that goes from 400 RPM to 675 RPM). For these two values of λ ($\lambda = \Omega \cdot R/V_\infty$), the relative angular velocity and Reynolds numbers are reported in the Table 5.2. For λ = 2.88 is obtained the maximum power extraction.

	min	max
tip speed ratio (λ)	2.40	4.04
Angular velocity (Ω)	41.9 rad/s	70.7 rad/s
Reynolds (Re)	126,746	213,866

Table 5.2: Computational set-up Darrieus rotor

For unsteady problems with moving bodies, COSA solves the governing equations in the absolute frame of reference using an arbitrary Lagrangian-Eulerian formulation and body-fitted grids. In the case of Darrieus rotors this implies that the entire computational grid, from the rotor center to the farfield boundary, rotates with the rotor. All structured multi-block grids used for the COSA TD analyses of the selected Darrieus rotor have a circular farfield boundary centred at the rotor axis, and they extend from the rotor center to the farfield boundary, featuring a high clustering level in the region around and between the blades.

5.3 Sensitivity analyses

A series of parametric analyses aiming at assessing the sensitivity of the computed solution to:

- the distance of the farfield boundary from the rotor center,
- the level of mesh refinement,
- the size of the physical time-step,
- wall boundary condition and freestream turbulent data.

have been carried out for several tip speed ratios, and their outcomes are reported in the following subsections. To conduct all the analyses, three sets of grids have been used. The three sets are characterised by different farfield distance from the centre of rotation. The first set is composed by two grids with farfield placed at 40 diameters D from the rotational axis, the second one by two grids with farfield placed at 80 D, and the third sets is composed by two grids with farfield placed at 120 D. All grids are made up of two subdomains: the circular region of radius 3.5 D containing the three blades and the annular region with inner radius of 3.5 D and outer radius depending from the farfield distance (see Fig. 5.2). The identification of two distinct sub-domains is irrelevant for the COSA analyses since the entire grid moves with the rotor, but it is introduced in view of the cross-comparison between COSA results and FLUENT results in the section *Validation*. The two grids of each sets, characterised by different number of quadrilateral cells, are denoted by M and C to indicate medium and coarse cells density, respectively. These two grids in each sets have been taken into account to demonstrate the independence from the space refinement. The Table 5.3 shows the density of each mesh.

	40 D	80 D	120 D
Medium mesh (M)	2,457,600	2,734,080	2,918,400
Coarse mesh (C)	614,400	683,520	729,600

Table 5.3: Number of cells of each computational grids.

The grids with farfield at 80 D and 40 D were obtained by removing from grid with farfield at 120 D all cells at radii larger than 80 D and 40 D, respectively. For each sets of grids, the coarse mesh has been generated removing every second line in both directions from the respective medium mesh. Furthermore, the region with radius 3.5 D of all medium meshes has the same cells density, the same nodes distribution around the aerofoils and nodes distribution in the normal direction to the aerofoils. As a consequence, also all the coarse meshes have the same inner regions but the cells density is reduced by a factor of 4. A schematic view of the COSA physical domain is depicted in Fig. 5.2. The number of mesh intervals along the aerofoils in the medium meshes is equal to 896 and in the coarse grid it was obtained dividing the number of mesh intervals of medium grid by a factor of 2. The distance d_w of the first grid points off the aerofoil surface from the surface itself is about 5 $\times 10^{-5} c$ in the medium grids.

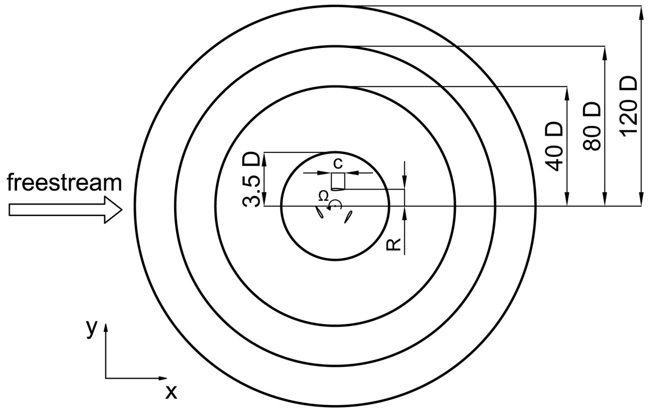

Figure 5.2: Physical domain of the COSA simulations.

To obtain the distance d_w in coarse grids, one needs to multiply 5 $\times 10^{-5}c$ by a factor of 2. The nondimensional minimum distance from the wall is defined as:

$$y^+ = \frac{(u_\tau d_w)}{\nu_w} \tag{5.2}$$

where u_τ is the friction velocity and ν_w is the kinematic viscosity at the wall. In all the simulations reported below, the maximum value of y^+ was always smaller than 1. Fig. 5.3 (a) shows a view of the grid around the rotor and Fig. 5.3 (b) shows an enlarged view of the grid around the aerofoil adopted.

Many comparisons presented in the next subsections have been performed in term of torque coefficient (C_T). Its expression is:

$$C_T = \frac{T}{\frac{1}{2}\rho_\infty R A V_\infty^2} \tag{5.3}$$

where T is the shaft torque, R is the rotor radius and $A = D \cdot h$ is the rotor swept area (in 2D simulations $h = 1$). Similarly to what done in many research works [15, 122], the global convergence of each simulation was monitored by considering the difference between the mean values of C_T over two subsequent revolutions normalised by the mean value over the second period of the pair. In all simulations, the periodicity error threshold was set to 0.1%. The required number of revolutions is not a priori known, and it depends on the rotating speed of the turbine: in all the analyses, it varied between 20 and 30 revolutions, depending on the λ.

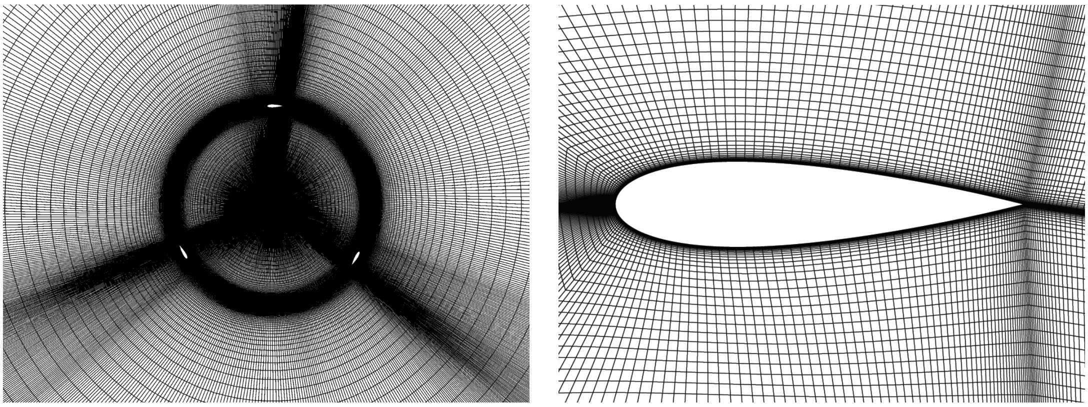
(a) (b)

Figure 5.3: Computational grid M120 around the rotor (a) and an enlarged view of grid M120 in the aerofoil area (b). (Every forth grid line in both directions is plotted for clarity)

5.3.1 Distance to the farfield boundary analysis

To assess the solution sensitivity to the distance of the farfield boundary from the rotor center, the three coarse grids were considered. The calculations were performed for λ 2.88 and 3.30 using 720 time steps per revolution. The curves of the periodic torque coefficient of a single blade obtained with grids C-40D, C-80D and C-120D are reported in Fig. 5.4 and highlight some differences between C-40D and C-80D results, whereas C-80D and C-120D are superimposed. Nevertheless it has been decided to use the grids with farfield at 120 D for all the simulations reported below because for smaller λ a farfield at 80 rotor diameters may be insufficient to avoid solution accuracy losses due to spurious reflections from the farfield boundary.

5.3.2 Space-refinement analysis

To assess the solution sensitivity to mesh refinement, some analyses for λ equal to 2.40, 2.64 and 2.88 using medium and coarse grids with farfield at 120 D have been conducted. The curves of the periodic torque coefficient of a single blade over one revolution computed with the two grids and using a physical time step equal to 0.25 degrees (i.e. performing 1440 physical time steps per revolution) are reported in Fig. 5.5.

The angular position $\theta = 0^o$ corresponds to the aerofoil chord being parallel to the freestream wind and the aerofoil moving against the wind, whereas $\theta = 180^o$ corresponds to the chord being parallel to the wind but the aerofoil travelling in the same direction

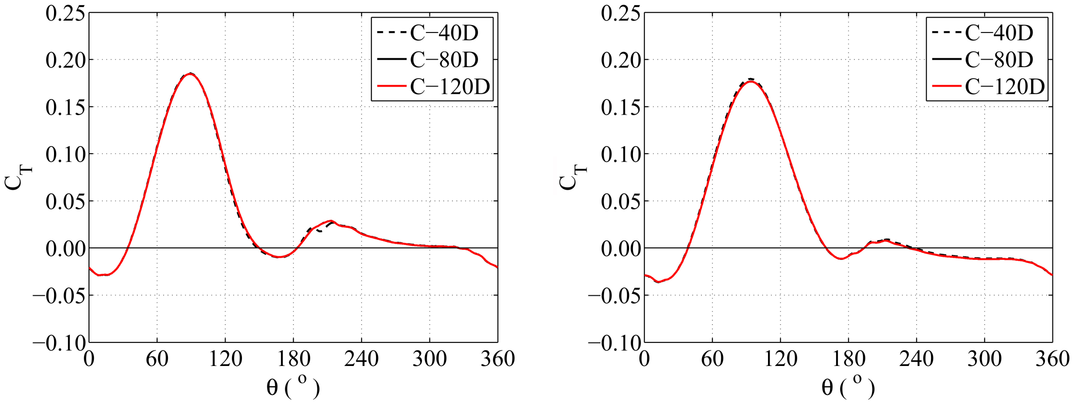

(a) $\lambda = 2.88$ **(b)** $\lambda = 3.30$

Figure 5.4: Solution sensitivity to the distance of farfield boundary (N=720).

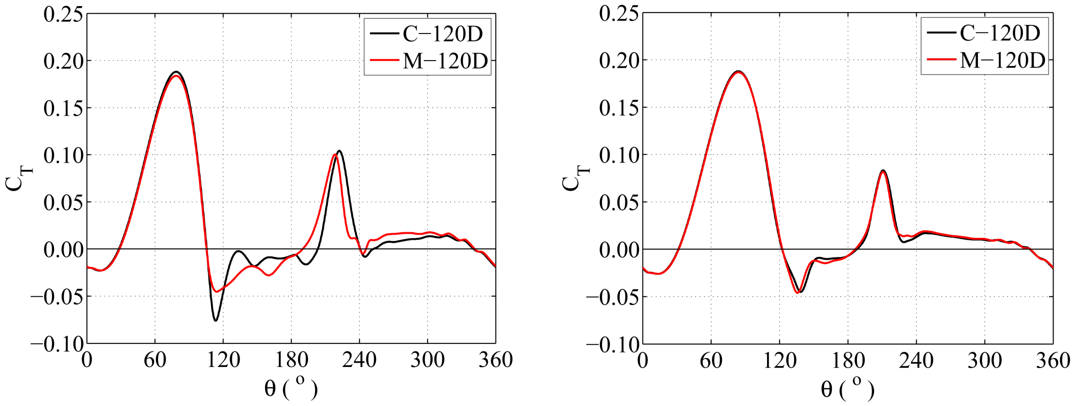

(a) $\lambda = 2.40$ **(b)** $\lambda = 2.64$

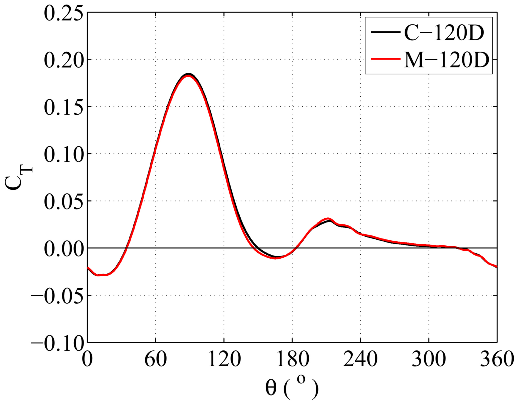

(c) $\lambda = 2.88$

Figure 5.5: Solution sensitivity to mesh refinement.

of the wind. Negligible differences are observed between C-120D and M-120D solutions for $\lambda = 2.64$ and $\lambda = 2.88$ demonstrating that mesh C-120D is grid independent for these two λ. Fig. 5.5 highlights that with the increase of the λ the differences between coarse and medium results decrease because the flow past the rotor presents lower complexity like vortices and wake/blade interactions. So, mesh C-120D, featuring 729,600 cells has been used for the following analyses for $\lambda \geq 2.64$. Relatively larger differences are observed for $\lambda = 2.40$. For this λ, it would be useful compared mesh M-120D solution with a solution obtained by a finer mesh with farfield at 120 D (F-120D), but four times more dense. Due to the higher computational resources required, F-120D has not been run. Thus, for $\lambda = 2.40$, mesh M-120D has been selected for the following analysis.

5.3.3 Time-refinement analysis

The solution sensitivity to the step size was assessed by computing the torque profile using the grid C-120D for λ equal to 2.64, 2.88 and 3.30. The time step size, Δt, has been defined according to the following equation:

$$\Delta t = \frac{1}{N} \frac{2\pi}{\Omega} \tag{5.4}$$

where N is the number of physical time steps per revolution. The results of Fig. 5.6 highlight that for $\lambda = 2.88$ a time step corresponding to 0.5 degree ($N = 720$) rotation is sufficient to obtain a solution independent of further reductions of the time step. The same behaviour has been found for $\lambda = 3.30$, so for $\lambda \geq 2.88$, all simulations have been performed using 720 time steps per revolution. For $\lambda = 2.64$ one can see that a time step of 0.5^o is not sufficient, so a time step equal to 0.25^o ($N = 1440$) rotation has been considered to obtain a solution fairly independent of further reductions of the time step. For this reason, for $\lambda \leq 2.64$ all simulations have been done using 1440 time steps per period.

The temporal refinement analysis was also performed in terms of pressure coefficient c_p and skin friction coefficient c_f. These coefficients are defined by Eq. (5.5) and (5.6) respectively.

$$c_p = \frac{p_w - p_\infty}{\frac{1}{2}\rho_\infty V_\infty^2} \tag{5.5}$$

$$c_f = \left| \frac{\tau_w}{\frac{1}{2}\rho_\infty V_\infty^2} \right| \tag{5.6}$$

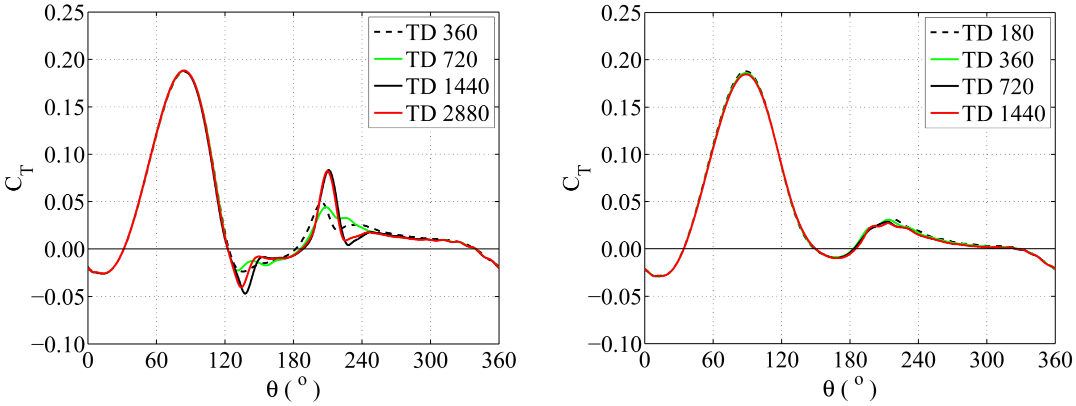

(a) $\lambda = 2.64$ **(b)** $\lambda = 2.88$

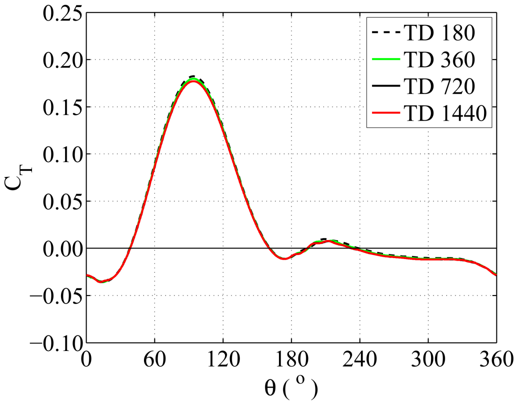

(c) $\lambda = 3.30$

Figure 5.6: Torque coefficient sensitivity to temporal refinement (grid C-120D).

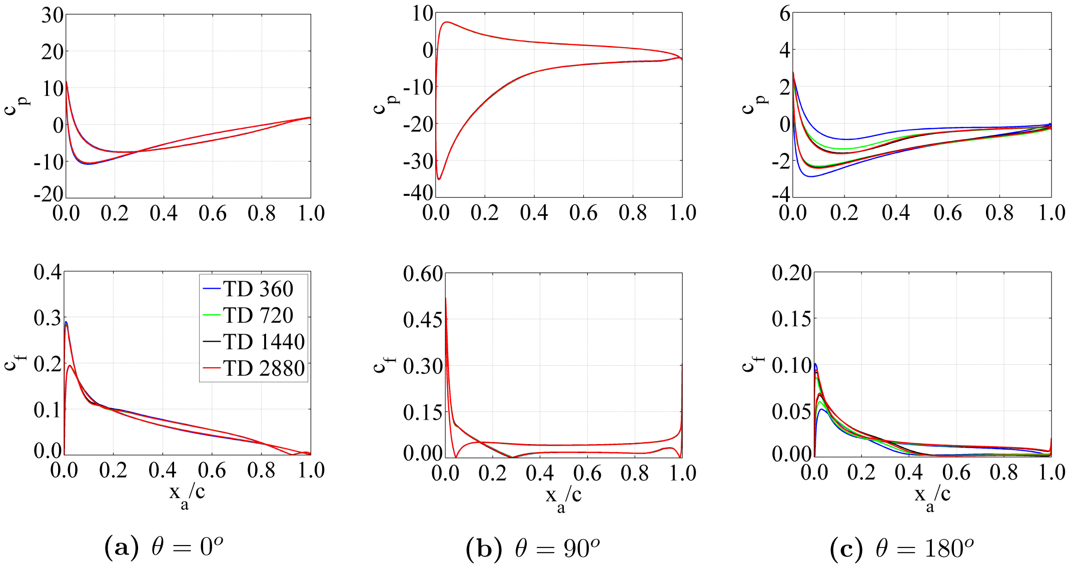

(a) $\theta = 0^o$ **(b)** $\theta = 90^o$ **(c)** $\theta = 180^o$

Figure 5.7: c_p and c_f sensitivity to temporal refinement, for $\lambda = 2.64$.

Fig. 5.7 and Fig. 5.8 show the comparisons of c_p and c_f for $\lambda = 2.64$ and $\lambda = 2.88$ in three different positions over the period. The variable x_a/c along the x-axis of all plots is the axial position along the aerofoil normalised by the chord. The analyses were performed also for more λ. All the results confirm that for $\lambda = 2.64$, a time step equal to 0.25^o rotation ($N = 1440$) has been necessary to obtain a solution fairly independent of further reductions of the time step, whereas for $\lambda = 2.88$ is sufficient a time step equal to 0.5^o rotation ($N = 720$).

The relatively high values of c_p and c_f are related to the absolute wind velocity V_∞ which appears at the denominator of Eq. (5.5) and (5.6). Smaller c_p and c_f values would be obtained if the relative wind velocity perceived by the blade had been used. Relative wind velocity depends from the λ and from θ and it is bigger than V_∞ for all azimuth angles and for all λ analysed (see Fig. 5.24).

5.3.4 Wall BC and freestream turbulent data

When using the SST model of Menter [101] (similarly to using the $k-\omega$ model of Wilcox [155]), one has the option of using two alternative wall boundary conditions (BCs) for the specific dissipation rate ω: either Wilcox's rough wall BC, which is based on the actual viscous stress at the wall [155], or Menter's approximation to Wilcox's rough

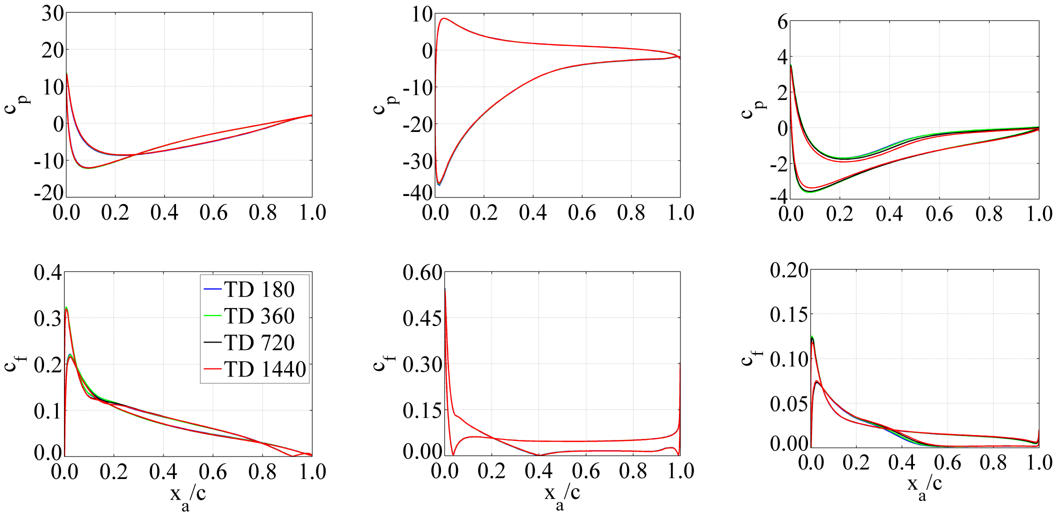

(a) $\theta = 0^o$ **(b)** $\theta = 90^o$ **(c)** $\theta = 180^o$

Figure 5.8: c_p and c_f sensitivity to temporal refinement, for $\lambda = 2.88$.

wall BC for the case of a smooth wall, which does not use the actual viscous stress at the wall. All results of previous subsections have used Menter's BC. In order to confirm the equivalence of Menter's BC and Wilcox's BC a C-120D analysis for $\lambda = 2.88$ was repeated using Wilcox's wall BC and 720 steps per revolution. The torque coefficient obtained with Menter's and Wilcox's BC were compared and it confirms the equivalence of these two conditions, given the no differences between the two curves. Menter's BC was used for all COSA analyses reported in the remainder of this research, as this resulted in slightly higher numerical stability of the simulations.

Regarding the set-up of farfield turbulent data to simulate the Darrieus wind turbine in open field conditions, the characteristic turbulence intensity (I) and turbulence length scale (l_T) have been considered. The turbulence intensity is defined as:

$$I = \frac{u'}{u_{avg}} \tag{5.7}$$

where u' is the root-mean-square of the velocity fluctuations, and u_{avg} is the mean flow velocity. A turbulence intensity of 1% or less is generally considered low and turbulence intensities greater than 10% are considered high [16]. In this research, $I =$ 5% has been used to simulate the open field condition. The turbulence length scale is instead a physical quantity related to the size of the large eddies that contain the energy in turbulent flows. An approximate relationship between l_T and the physical size of the obstacle is $l_T = 0.07 \cdot L$, where L is the characteristic length of the obstacle. In this case, the Darrieus rotor diameter is ≈ 1 m, so the turbulent length scale was set to 0.07 m. In COSA, I and l_T are not given directly, but the user needs to give I^2 and the turbulent viscosity ratio (μ_T/μ). The turbulent viscosity ratio is defined as:

$$\mu_T/\mu = \frac{\rho \cdot k}{\omega \cdot \mu} \tag{5.8}$$

where $k = \frac{3}{2} I^2 V_\infty^2$ is the turbulent kinetic energy and ω is the specific dissipation rate. The equation which provides the relationship between ω and the characteristic length l_T is defined as $\omega = \frac{k^{1/2}}{C_\mu^{1/4} l_T}$ where $C_\mu = 0.09$ is a constant. A disadvantage of the two-equations turbulence ω based models is the excessive generation of turbulent energy. For this reason, COSA allows the users to apply some production limiters to avoid non-physical values of turbulent kinetic energy and specific dissipation rate. A calculation has been performed to analyse the production limiters effect. The result has been analysed in term of torque coefficient. The analysis for $\lambda = 2.88$ with grid C-120D and 720 time steps per period is shown in Fig. 5.9. The figure shows that using the production limiters, the C_T solution is changed significantly. The C_T without using limiters is lower for most of the period highlighting an higher level of turbulent intensity with respect to the case with limiters. The higher level of turbulence is related to wind that fluctuates rapidly and in this situation the turbine is subjected to larger loads on the blades and minor performance. In this VAWT analysis, production limiters have been used in all simulations.

5.4 Integral performance parameters

The results presented in this section aim at defining the Darrieus rotor performance in terms of C_T and power coefficient (C_p) at different λ, starting from $\lambda = 2.40$ up to $\lambda = 4.04$, and constant freestream velocity $V_\infty = 9$ m/s. In order to explain the torque coefficient behaviour, it is possible to consider the azimuthal variation of the torque contribution exerted by blade 1 for all the λ analysed (Fig. 5.10). Starting from $\theta = 0^o$, for all λ the torque contribution is negative: in this condition the actual angle of attack (α) is almost equal to zero (the blade velocity is about parallel to the absolute wind velocity) so that lift is negligible and drag dominates. In order to estimate the

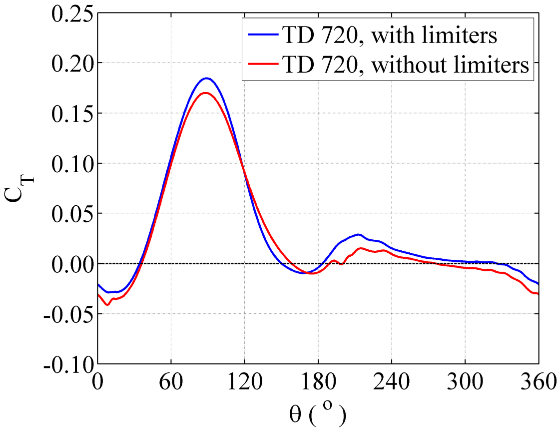

Figure 5.9: Torque coefficient sensitivity to the application of limiters (λ=2.88, C-120D).

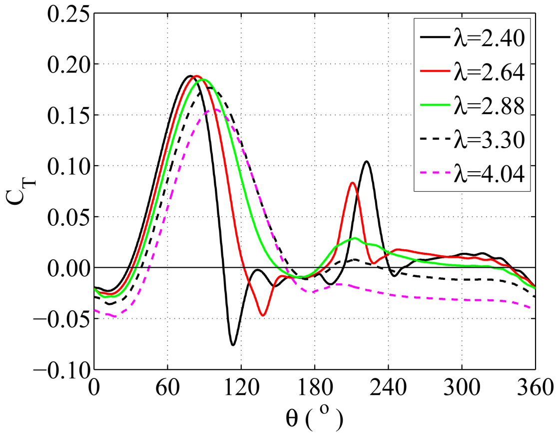

Figure 5.10: Torque contribution exerted by blade 1 vs. azimuth position.

variation of α with respect to the azimuth angle θ, the following simplified relation (without the velocity induction) can be used:

$$\alpha = \tan^{-1}\left(\frac{\sin(\theta)}{\cos(\theta)+\lambda}\right) \tag{5.9}$$

The variation of α with θ during the rotation causes an inherent unsteady aerodynamic behaviour which characterises the Darrieus rotor. The variation of α along the entire rotor revolution for different λ is shown in Fig. 5.11. One can see that for $\theta = 0^o$, $\alpha = 0^o$. The angle of attack increases until its maximum value for $\theta = 110^o$. After that, α decreases to reach again 0^o at $\theta = 180^o$. In the second half of the period, the behaviour of α is identical but with opposite signs. In addition, α decrease passing from lower to higher λ values, because of the raising influence of blade entrainment speed (ΩR). Fig. 5.10 shows that the higher contribution of torque is observed when the blade is upstream. Indeed, the peak of the C_T occurs for θ between 0^o and 180^o. When the blade is downstream (θ between 180^o and 360^o), it interacts with wakes produced by the blade upwind. $\lambda = 2.88$ gives the maximum power coefficient as a result of a balance between a high positive torque contribution on the upstream side and a minor negative torque contribution on the downwind. For $\lambda < 2.88$, the positive C_T area between $\theta = 0^o$ and 180^o become smaller due to the higher angle of attack that falls the aerofoil in stall condition. For $\lambda = 3.30$ the dynamic stall decreases and, as shown in the section *Aerodynamic analysis*, only a small pocket of stalled flow is observed near the trailing edge for θ between 90^o and 150^o. For $\lambda = 4.04$, the flow is mainly attached to the blade during the rotation, but the torque contribution decreases because lower α produces a lower lift.

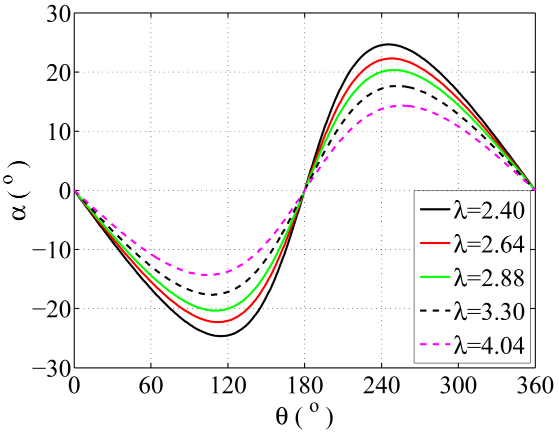

Figure 5.11: Angle of attack vs. azimuth angle.

The total torque computed by all the rotor blades is plotted versus θ for all λ in Fig. 5.12. Since the Darrieus rotor analysed in this research is composed of three blades, the torque coefficient should have a periodicity equal to 120^o. Actually, this expected behaviour is satisfied at all tip speed ratios except for $\lambda = 2.40$ where one can see some differences in the three peaks region. This behaviour is due to the higher interactions between the vortices and the blades, that happens for this λ. Moreover, the behaviour

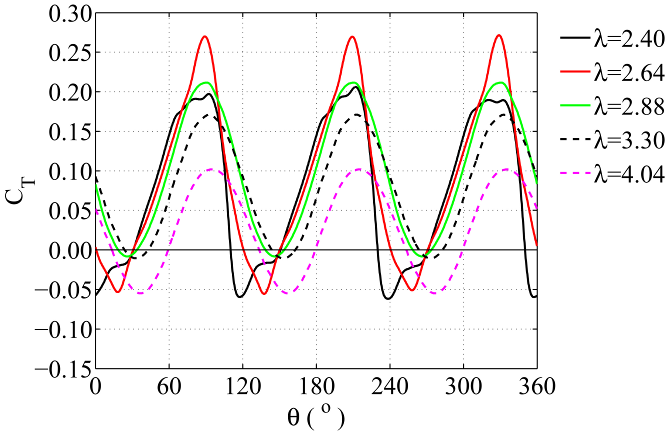

Figure 5.12: Rotor torque contribution vs. azimuth position.

of the pressure and viscous component of the torque has been analysed and two separate plots for $\lambda = 2.64$ and $\lambda = 2.88$ have been presented in the Fig. 5.13. The two plots show a similar behaviour, the pressure component of the torque is higher than the total torque. It decreases when one adds the viscous contribution that is negative for all the period.

Another important parameter considered in this thesis is the power coefficient C_p. It is expressed as the ratio of power extracted by the turbine to the total available in the wind stream. The C_p is defined as:

$$C_p = \frac{P}{\frac{1}{2}\rho_\infty A V_\infty^3} \tag{5.10}$$

where $P = T \cdot \Omega$ is the shaft power, T is the torque and Ω is the angular velocity. The power curve for all the λ analysed using the time-domain approach of COSA is shown in Fig. 5.14. It shows the peak of the curve for $\lambda = 2.88$. In the next section *Validation*, the power curve, will be compared with the CFD solution obtained by FLUENT.

5.5 Validation

In this thesis, a comparison between the results obtained by COSA and by the commercial code ANSYS FLUENT [16] has been conducted.

The commercial code FLUENT was used in a two-dimensional form to solve the time dependent URANS equations in pressure-based formulation. Some researchers

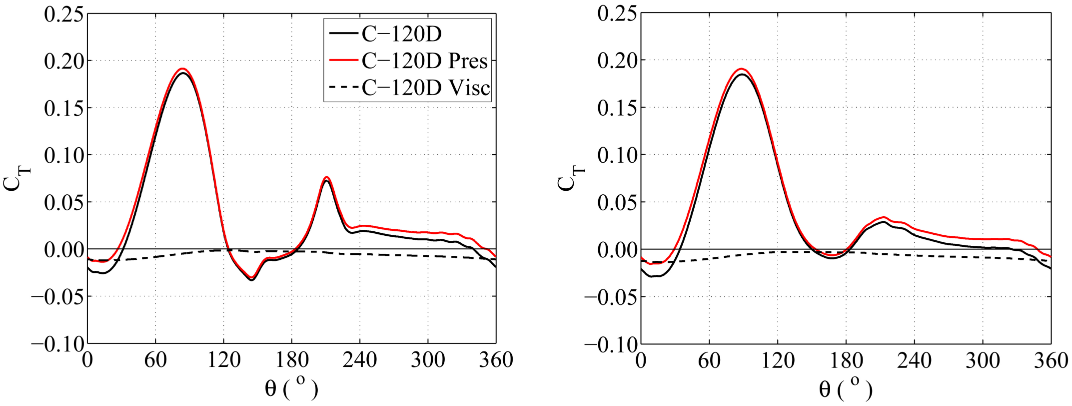

(a) λ = 2.64

(b) λ = 2.88

Figure 5.13: Pressure and viscous contribution of the torque.

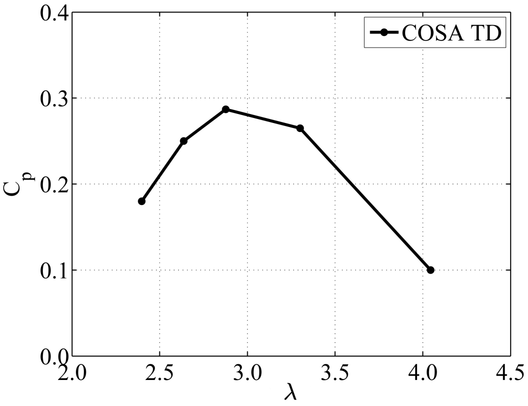

Figure 5.14: Power coefficient vs λ.

have recently presented [20] the assessment and validation of the main settings for the CFD simulation of Darrieus wind turbines using FLUENT, and have verified them by means of experimental data [20] of a rotor very similar to that investigated in the present case study. On this basis, the same numerical settings were used also in the present study, although a proper checks on the domain size, the spatial and the temporal discretisation have been done. Turbulence closure is achieved by means of Menter's shear stress transport (SST) model derived from the $k-\omega$ two-equation formulation [101]. The second order upwind scheme was used for the spatial discretisation of the whole set of RANS and turbulence equations, as well as the bounded second order for time differencing to obtain a good resolution [15, 71]. The physical domain used in FLUENT is split into two subdomains:

- a circular zone containing the turbine, rotating with the same angular velocity of the rotor,
- a rectangular fixed outer zone, determining the overall domain extent

The two regions communicate by means of a sliding interface. This solution is a common practice in this type of unsteady simulations [15, 122]. The domain was here extended in the downstream direction for a complete development of the wake. For the definition of the rotor geometry, only the three blades were taken into account, neglecting the presence of supporting spokes and the shaft. Fig. 5.15 shows the simulation domain, where all the boundary distances are given as a function of the rotor diameter (D). An unstructured mesh made up of triangular elements was used for the discretisation of the core flow region, except for the blade boundary layer region where a structured O-grid was generated to accurately resolve the entire boundary layer. The rotating domain, containing the three blades, is characterised by a periodical repetition of a 120^o mesh sector, where elements are progressively coarsened with the distance from the blade. The mesh is refined in the wake region of each blade due to the higher complexity of the flow field downstream the trailing edge. The sliding interface (red

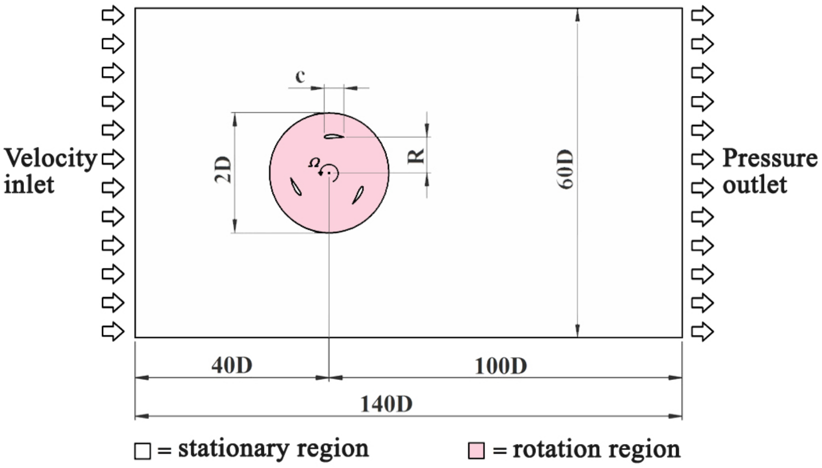

Figure 5.15: Physical domain of FLUENT simulations.

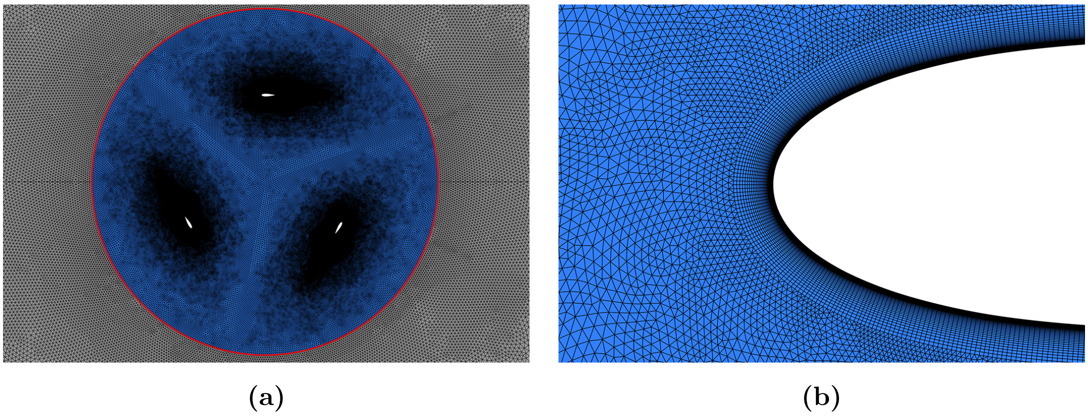
(a)
(b)

Figure 5.16: Computational rotating domain adopted by FLUENT simulations (a) and an enlarged view in the aerofoil leading edge area (b).

colored in Fig. 5.16 (a)) guarantees the conservation of conservative variables all of the quantities between the stationary and the rotating domains. The extrusion of quadrilateral elements for the discretisation of the boundary layer is clearly distinguishable in Fig. 5.16 (b) for the blade leading edge. The chosen mesh topology requires a grid-clustering ensuring a smaller spacing between the nodes in the area around the leading and trailing edges, i.e. the regions experiencing the highest gradients.

To assess the solution sensitivity to mesh refinement, two different levels of refinement of the mesh focusing on the number of grid nodes on the aerofoil and the cells density in the rotation subdomain have been conducted. This is a crucial requirement for the determination of both the angle of attack of the incoming flow on the blade and the boundary layer evolution from the leading edge to the trailing edge. The sensitivity analyses were performed for λ equal to 2.64, 2.88 and 3.30. The coarse C_{FLUENT} grid is characterised by 760 nodes around the aerofoil surface, a rotating subdomain consisting of about 6.5×10^5 elements and a stationary subdomain consisting of about 2.0×10^5 elements. A velocity-inlet boundary condition is imposed at the inlet section, which is placed 40 rotor diameters upwind of the rotating axis. The ambient pressure condition is imposed at the outlet boundary, 100 rotor diameters downwind, while a symmetry condition is defined for the lateral boundaries at a distance of 30 rotor diameters. The fine F_{FLUENT} grid, instead, has an aerofoil resolution increased to about 1400 nodes, a rotating subdomain of about 1.2×10^6 elements and a computational domain width was extended by placing the lateral boundaries at a distance of 50 rotor diameters from the rotating axis in order to avoid spurious reflections at the boundaries. The dimensions of the domains were selected on the basis of sensitivity analyses reported in [20]. The first element height was chosen so as to guarantee that the y^+ values at the grid nodes of the first grid line off the blade surface, for both grids, did not exceed the limit of the SST turbulence model, i.e. $y^+ \approx 1$.

Fig. 5.17 highlights that for λ equal to 2.88 and 3.30, coarse and fine meshes give identical solutions. For this reason, C_{FLUENT} grid has been used to conduct all the simulations for $\lambda \geq 2.88$. For λ equal to 2.64, F_{FLUENT} solution is fairly different from C_{FLUENT} and in according with the sensitivity analyses reported in [20], F_{FLUENT} is independent from further mesh refinement. Thus, for $\lambda \leq 2.64$, F_{FLUENT} has been used for the following analyses.

The sensitivity to the temporal refinement settings was assessed through a specific combined time step sensitivity on a similar case study [20]. From FLUENT calculations, to obtain a solution independent from further reductions of time steps, 0.25 degrees and 0.125 degrees rotation have been used for C_{FLUENT} and F_{FLUENT} respectively.

The subplots of Fig. 5.18 show the comparison between the torque coefficient computed by COSA and FLUENT for λ equal to 2.64, 2.88, 3.30 and 4.04. Fig. 5.18 highlights a good agreement for all λ considered. As written above, COSA results are obtained using medium grid for $\lambda = 2.40$ and coarse grid for $\lambda \geq 2.64$, while FLUENT results are obtained using coarse grid for $\lambda \geq 2.88$ and fine grid for $\lambda \leq 2.64$. Inspection of COSA and FLUENT profiles highlight that larger differences are shown for $\lambda = 2.64$. These differences between the two predictions occur from 90 degrees (aerofoil approach to its maximum α) to 240 degrees of the period (aerofoil just outside the wake interaction region). Similar behaviour was verified for $\lambda = 2.40$. Increasing the λ, the differences become smaller and can be neglected for the highest λ. For $\lambda = 2.64$ and 3.30, Fig. 5.18 shows another curve which refers to the FLUENT simulation using the circular grid generated for COSA analyses with farfield placed at 120 D. In this case, the region with radius of 3.5 D from the centre has been used as rotating circular subdomain. These simulations have been performed to check if the small differences observed between COSA and FLUENT were dependent on the grid. However the fact that FLUENT using the rectangular domain (labeled FLUENT) and FLUENT using the circular domain (labeled FLUENT 120D) show very similar profiles enables one to

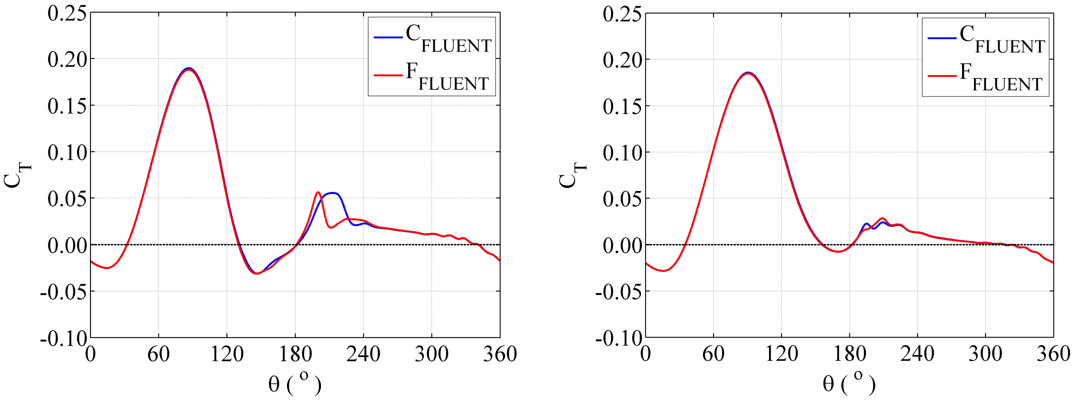

(a) $\lambda = 2.64$

(b) $\lambda = 2.88$

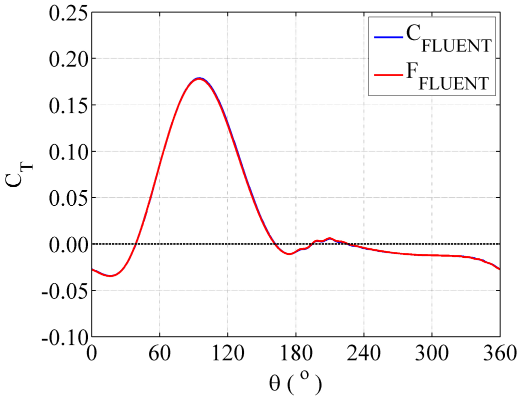

(c) $\lambda = 3.30$

Figure 5.17: FLUENT solution sensitivity to mesh refinement (C and F indicate coarse and fine mesh, respectively).

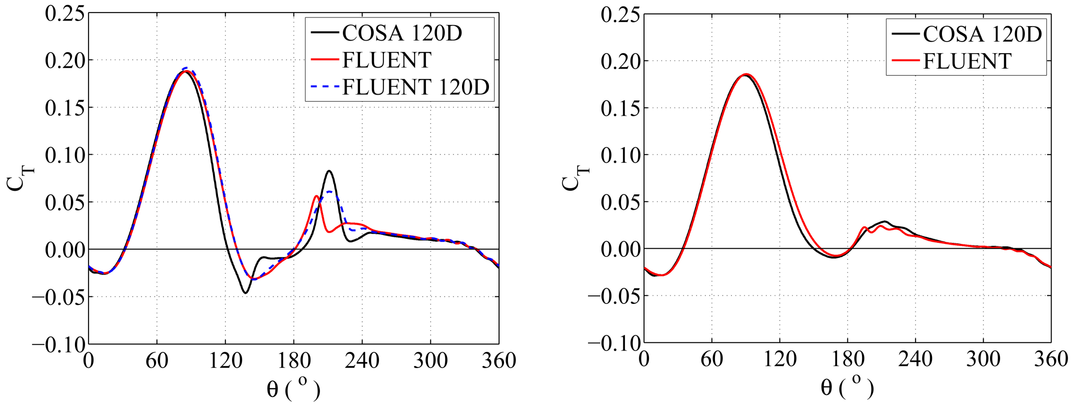

(a) λ = 2.64 **(b)** λ = 2.88

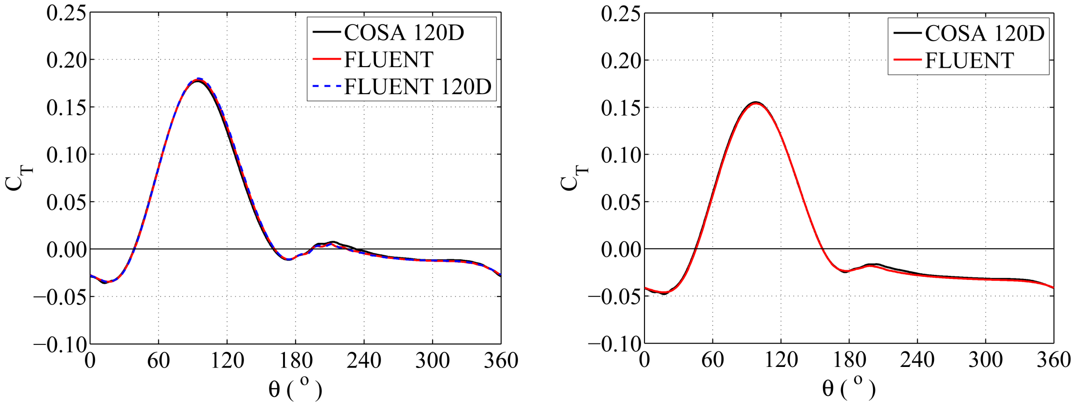

(c) λ = 3.30 **(d)** λ = 4.04

Figure 5.18: Comparison COSA - FLUENT for several λ.

rule out that the small differences between COSA and FLUENT profiles are caused by the use of different grids.

In this research, also the comparison between COSA and FLUENT c_p and c_f profiles at the rotor angular positions and of 0^o, 33^o, 66^o, 99^o, 186^o and 240^o have been analysed. Fig. 5.19 and 5.20 report the c_p and c_f profiles for $\lambda = 3.30$. The agreement between the two sets of results is good in all cases. The c_p subplots at the first four angular positions highlight the expected increment of the blade load due to the increment of the angle of attack from 0^o to 99^o. After 99^o the c_p decreases as the blade load decreases. The same behaviour is observed for all tip speed ratios analysed. Concurrently, the separation on the blade side facing the rotor axis grows significantly, as indicated by the forward motion of the c_f cusp from about 90% of the chord at $\theta = 0^o$ to about 50%

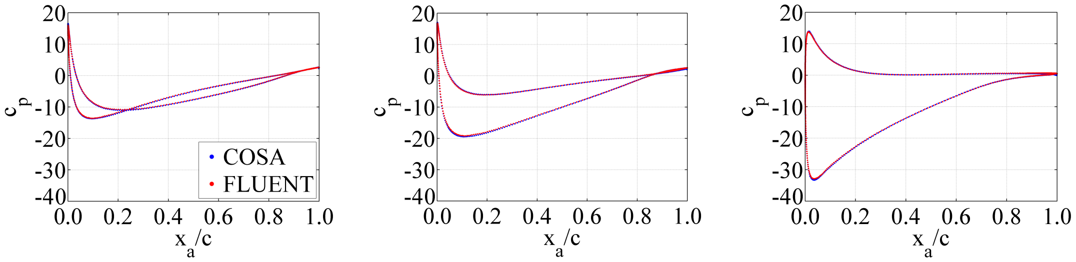

(a) $\theta = 0^o$ **(b)** $\theta = 33^o$ **(c)** $\theta = 66^o$

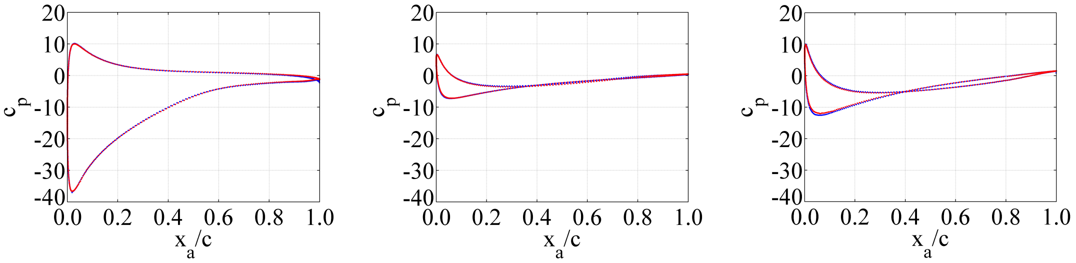

(d) $\theta = 99^o$ **(e)** $\theta = 186^o$ **(f)** $\theta = 240^o$

Figure 5.19: Blade pressure coefficient predicted by the COSA and FLUENT simulations for several angular positions ($\lambda = 3.30$).

of the chord at $\theta = 99^o$. All c_f subplots also show a secondary cusp very close to the trailing edge, which corresponds to the reattachment point of the flow.

In terms of power coefficient it is possible to compare the estimates of the 2D simulations performed by COSA and FLUENT. The comparison is reported in Fig. 5.21 and it highlights a very good agreement for all λ. The Darrieus wind turbine analysed in this research was also tested in Bovisa's low turbulence wind tunnel (Milan) [1]. The main features of the 3D turbine tested in the wind tunnel are those reported in Table 5.1 except for the blade connections to the radial arms which is different from the CFD models and it is equal to 0.50 c. In this case, new computational grids with the same characteristics of C_{FLUENT} and F_{FLUENT} have been generated. The grids are suitable to the new blades connection point and new simulations have been run using the solver of FLUENT. The results have been compared with experimental measurements reported in [117] in terms of C_p. The comparison between 2D and 3D configurations is plotted in Fig. 5.22. The data are comparable as expressed by Eq. (5.10). The swept area A at the denominator is equal to the product of h (turbine height) and D (turbine diameter). For the 3D case, the output torque is related to the finite length h of the

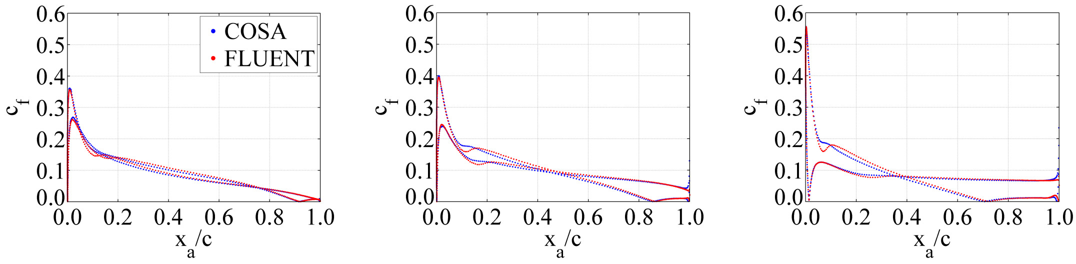

(a) $\theta = 0^o$ **(b)** $\theta = 33^o$ **(c)** $\theta = 66^o$

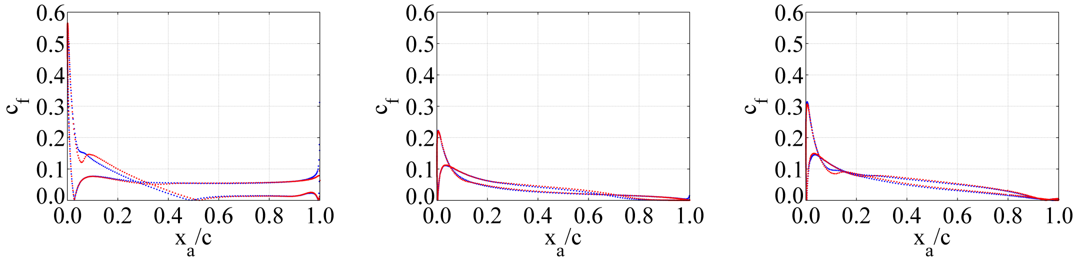

(d) $\theta = 99^o$ **(e)** $\theta = 186^o$ **(f)** $\theta = 240^o$

Figure 5.20: Blade skin friction coefficient predicted by the COSA and FLUENT simulations for several angular positions ($\lambda = 3.30$).

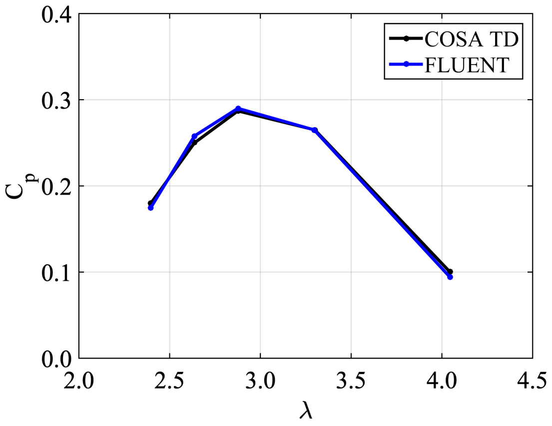

Figure 5.21: Comparison of power coefficients between COSA (2D) and FLUENT (2D) (wind turbine geometry with blades connections at 0.25 c).

blade, so one needs to divide the power by turbine length. For the 2D case, instead, the output power is related to a fictitious length of 1 so a division for $h = 1$ is required. The 2D CFD estimates by FLUENT are in good agreement with the experimental data for all λ.

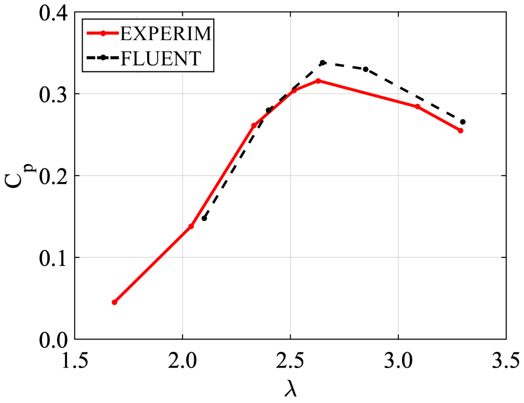

Figure 5.22: Comparison of power coefficients between FLUENT (2D) and experimental measurements (3D) (wind turbine geometry with blades connections at 0.50 c).

5.6 Aerodynamic analysis

As written previously, the Darrieus rotor is characterised by an unsteady aerodynamic behaviour due to the variation of the angle of attack with the angular position. Fig. 5.23 shows a sketch of all forces acting on the rotor. The velocity triangles show how the

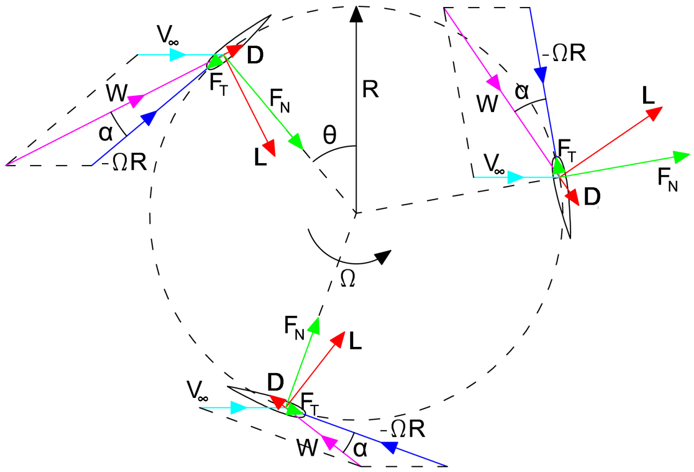

Figure 5.23: Aerodynamic forces acting on a Darrieus rotor.

direction and the amplitude of the relative wind speed W vary with the angular position of the blades. In Fig. 5.24, the W non-dimensionalised with respect to V_∞, is plotted against θ.

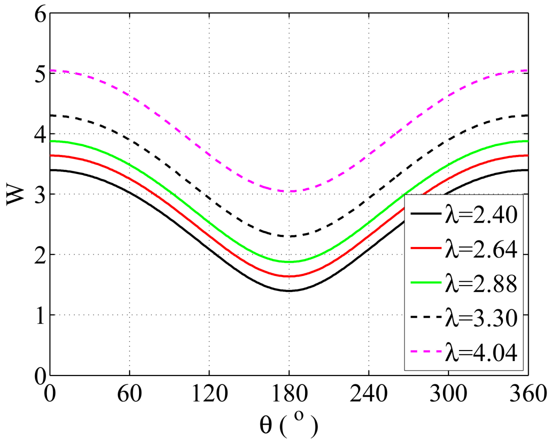

Figure 5.24: Relative velocity vs. azimuth angle.

The normal force (F_N) and tangential force (F_T) to the aerofoil chord can be expressed as:

$$F_N = L \cdot \cos(\alpha) + D \cdot \sin(\alpha) \tag{5.11}$$

$$F_T = L \cdot \sin(\alpha) - D \cdot \cos(\alpha) \tag{5.12}$$

L and D are, respectively, lift and drag forces on the aerofoil. The tangential force is considered positive when directed forward along the turbine rotate direction. The normal and tangential forces acting on a blade can be written in terms of the sectional non-dimensional normal force (C_{F_N}) and sectional non-dimensional tangential force (C_{F_T}) defined by Eq. (5.13).

$$C_{F_N} = \frac{F_N}{\frac{1}{2}\rho A V_\infty^2}, \qquad C_{F_T} = \frac{F_T}{\frac{1}{2}\rho A V_\infty^2} \tag{5.13}$$

Fig. 5.25 shows the behaviour of the C_{F_T} (subplot (a)) and the C_{F_N} (subplot (b)) over the period. Fig. 5.25 (a) highlights a very similar behaviour of the C_{F_T} with respect to the torque coefficient C_T plotted in Fig. 5.10. For all λ, C_{F_N} starts from values close to zero and reaches its maximum value with negative sign when the blade passing on the upstream side (about at $\theta = 90^o$). In this position the blade is perpendicular to

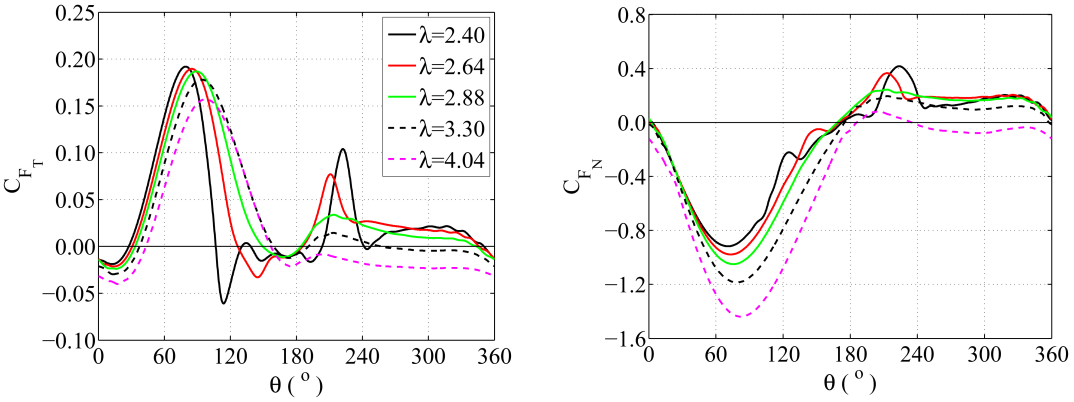

(a) C_{F_T} **(b)** C_{F_N}

Figure 5.25: Tangential and normal force contributions exerted by blade 1 vs. azimuth position.

the absolute wind direction. After 90^o it reaches values close to zero for the angular position of 180^o. Between 180^o and 240^o some oscillations are observed also in C_{F_N} curves, especially for lower tip speed ratios, that represent the downwind region affected by wake/blade interactions.

In order to investigate the unsteady aerodynamics of the considered Darrieus rotor, a detailed analysis of the flow field for several λ has been carried out. The entire range of turbine operation has been divided in two regions denoting with low λ the operating conditions lower than 2.88 (λ which gives the maximum C_p) and with high λ the operating conditions greater or equal than 2.88.

5.6.1 Low tip speed ratio aerodynamics

In the preceding section, a full analysis of the Darrieus wind turbine in term of torque and power coefficient has been presented. In order to have a visualisation of the flow field in and around the rotor for low λ, the normalised vorticity ($\widehat{\Omega}$) contours for $\lambda = 2.40$ and $\lambda = 2.64$ have been used and reported in Fig. 5.26. The vorticity is a vector field $\widehat{\Omega}$ defined as the curl of the velocity vector $\widehat{v}$. The vorticity of a two-dimensional flow is always perpendicular to the plane of the flow, so $\widehat{\Omega}$ vector is parallel to the z axis, and can be expressed as:

$$\widehat{\Omega} = \left(\frac{\partial}{\partial x}, \frac{\partial}{\partial y}, \frac{\partial}{\partial z}\right) \times (v_x, v_y, 0) = \left(\frac{\partial v_y}{\partial x} - \frac{\partial v_x}{\partial y}\right) \widehat{z} \tag{5.14}$$

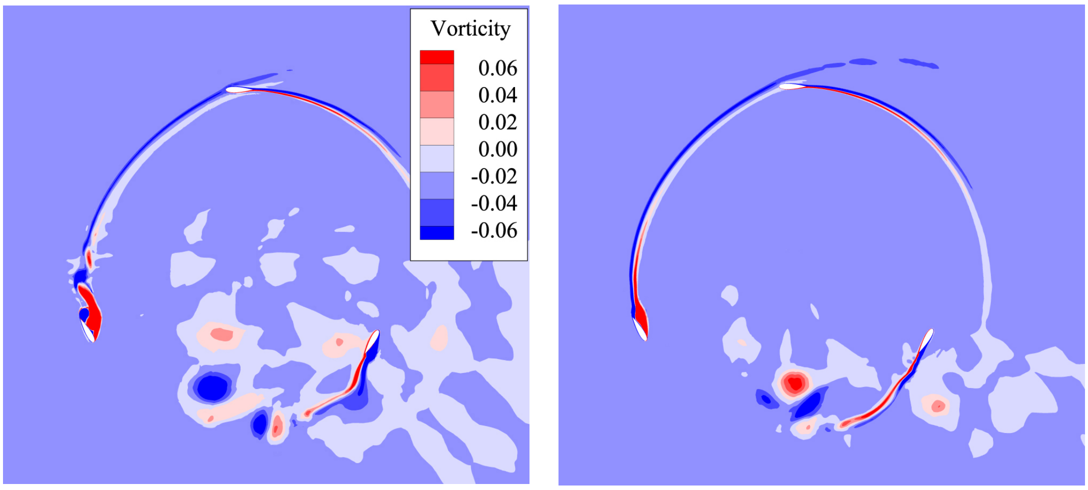

(a) $\lambda = 2.40$ **(b)** $\lambda = 2.64$

Figure 5.26: Normalized vorticity contours past the rotor predicted by COSA simulations.

The normalised vorticity plotted in the figures has been obtained normalising the dimensional vorticity by the ratio between the freestream sound speed and the aerofoil chord.

For $\lambda = 2.40$ (Fig. 5.26 (a)) and $\lambda = 2.64$ (Fig. 5.26 (b)) one can see the flow separation near the blade on upwind side ($\theta = 120^o$) and vortices which are generated as a consequence of the stalled flow. These blades vortex shedding, crossing the rotor, interact with the blade itself on the returning side (from $\theta = 180^o$ to $\theta = 270^o$). The vorticity of $\lambda = 2.40$ highlights a larger flow complexity than $\lambda = 2.64$ due to the stalled condition of the aerofoil induced by the higher angle of attack.

Stall condition and flow separation of blade 1 (which is the blade that start the rotor revolution on the top and goes against the wind), are emphasised in Fig. 5.27 for $\lambda = 2.40$, for several angular positions. It depicts the COSA flow streamlines and Mach contours in the aerofoil region. One can see that the separation starts when $\theta = 60^o$ ($\alpha \approx -17^o$) and increases going to $\theta = 90^o$. In this angular position, there is a secondary smaller recirculation very close to the trailing edge which rotates in the opposite direction comparing with the first one. Fig. 5.27 (e) demonstrate the presence of the stall which appears to be even stronger than $\theta = 90^o$ and the secondary recirculation has a comparable size with the first one. After $\theta = 120^o$, the relative angle of attack starts to decrease and it approaches to $\theta = 150^o$ where the recirculations move near the trailing edge of the aerofoil and they leave the blade. The vortex shedding will cross the rotor and it will impact on the blade itself on the downstream. The low wind speed is mainly characterised by the development of vortices that will interact with the blades. The generation of those vortices can generate other problems such as vibrations, noise and reduction of fatigue life of the blades.

5.6.2 High tip speed ratio aerodynamics

Going from $\lambda = 2.88$ to $\lambda = 4.04$ (Fig. 5.28), there appears to be a gradual reduction of the vortex shedding. For $\lambda = 4.04$ the flow appears to be completely attached to the blade during the entire rotation and only very long wakes are present around the rotor. The wakes/blade interactions still occur as shown by Fig. 5.28 (c).

As done for $\lambda = 2.40$ in *Low tip speed ratio aerodynamics* subsection, Fig. 5.29 shows the streamlines and Mach contours for $\lambda = 3.30$ and θ equal to 0^o, 30^o, 60^o, 90^o, 120^o and 150^o. One can see that the level of the stalled flow is lower than $\lambda = 2.40$ and the recirculation that appears at 60^o increases its size going to 90^o and 120^o. The secondary vortex on the trailing edge that rotates in opposite direction with respect to the first vortex, is even smaller than that occurs for $\lambda = 2.40$ case. Approaching to 150^o the circulation, that appears near the trailing edge, starts to decrease and no vortex shedding occurs since the main trailing edge vortex is still attached to the aerofoil, and thereafter the amount of stall decreases as a result of the rapid reduction of the angle of attack.

5.7 Conclusion

A detailed time-domain CFD analysis of a Darrieus wind turbine has been presented. On the modelling side, the chapter reports some important parametric analysis on the numerical set-up like the sensibility to the farfield boundary distance, sensibility to mesh and temporal refinement and sensibility to the characteristic turbulent variables of the SST turbulence model. The analysis also showed a comparison with results obtained by a commercial CFD code. In addition, the aerodynamics analyses of the considered wind turbine highlighted an higher level of flow nonlinearity, particularly for lower λ, characterised by stalled flow near the blades, vortices that pass through the rotor and interactions between vortices and blades. Mach contour plots, vorticity

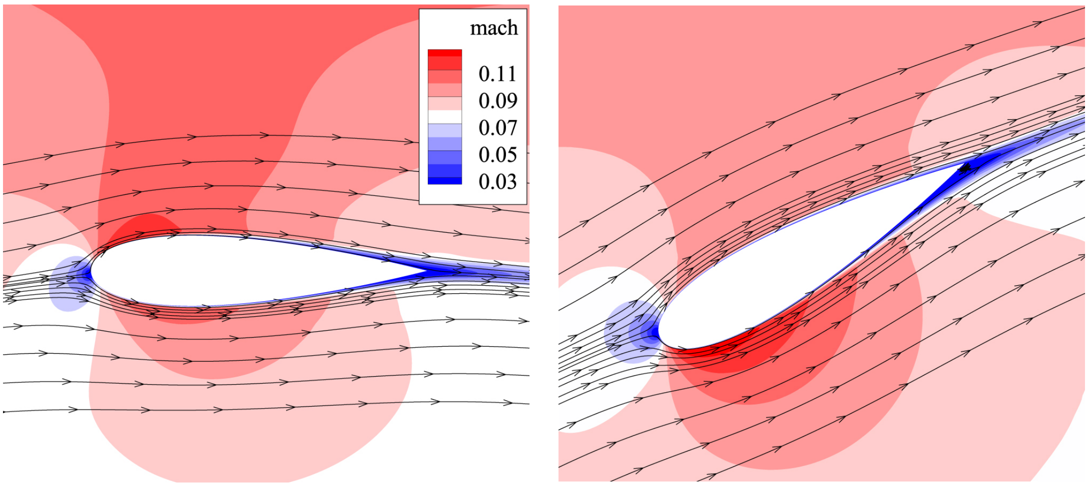

(a) $\theta = 0^o$, $\alpha = 0^o$ **(b)** $\theta = 30^o$, $\alpha = -8^o$

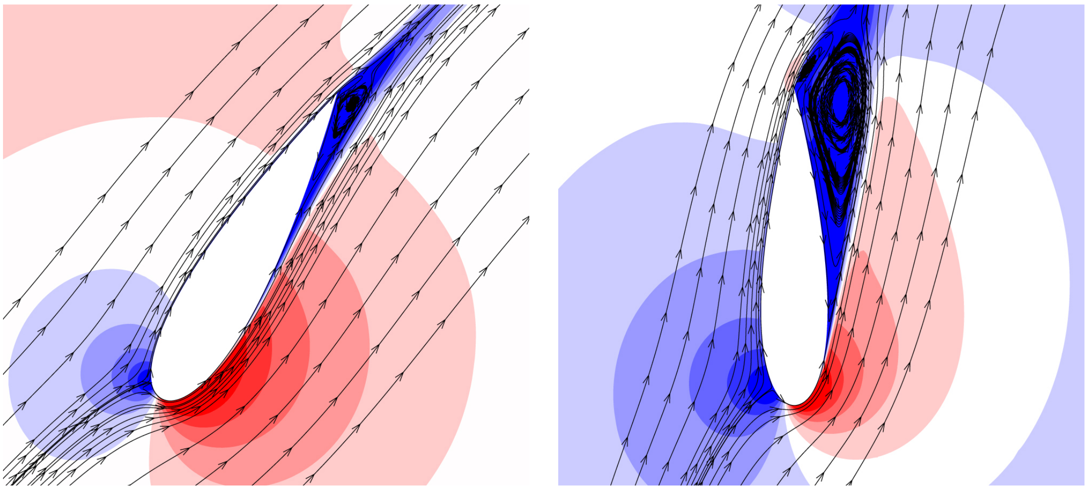

(c) $\theta = 60^o$, $\alpha = -17^o$ **(d)** $\theta = 90^o$, $\alpha = -23^o$

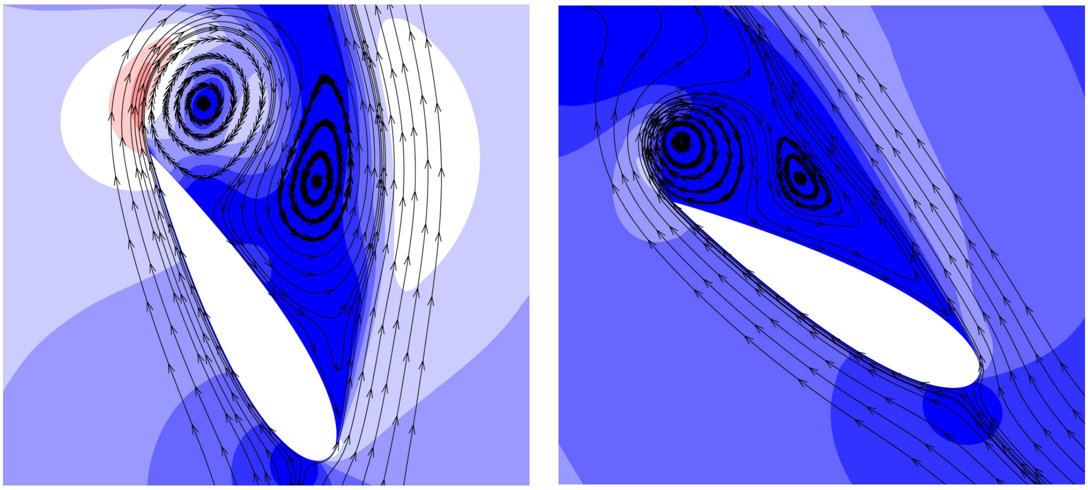

(e) $\theta = 120^o$, $\alpha = -25^o$ **(f)** $\theta = 150^o$, $\alpha = -19^o$

Figure 5.27: Streamlines and Mach contours in the aerofoil region obtained with COSA simulations ($\lambda = 2.40$).

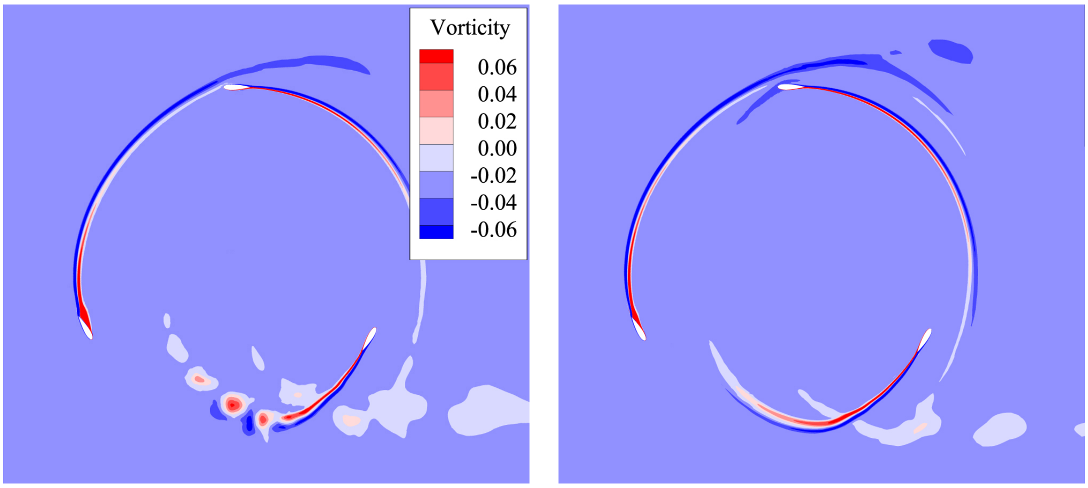

(a) $\lambda = 2.88$ **(b)** $\lambda = 3.30$

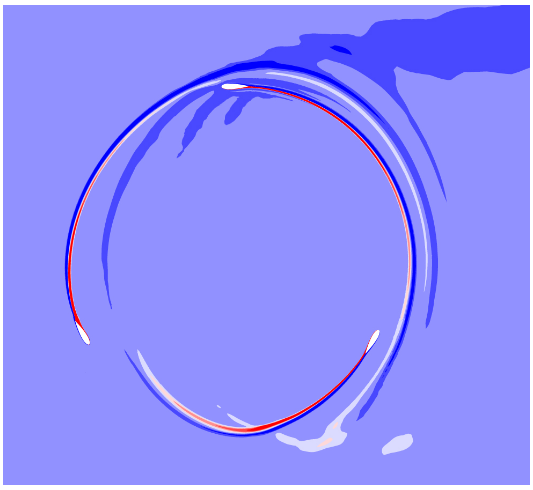

(c) $\lambda = 4.04$

Figure 5.28: Normalized vorticity contours past the rotor predicted by COSA simulations.

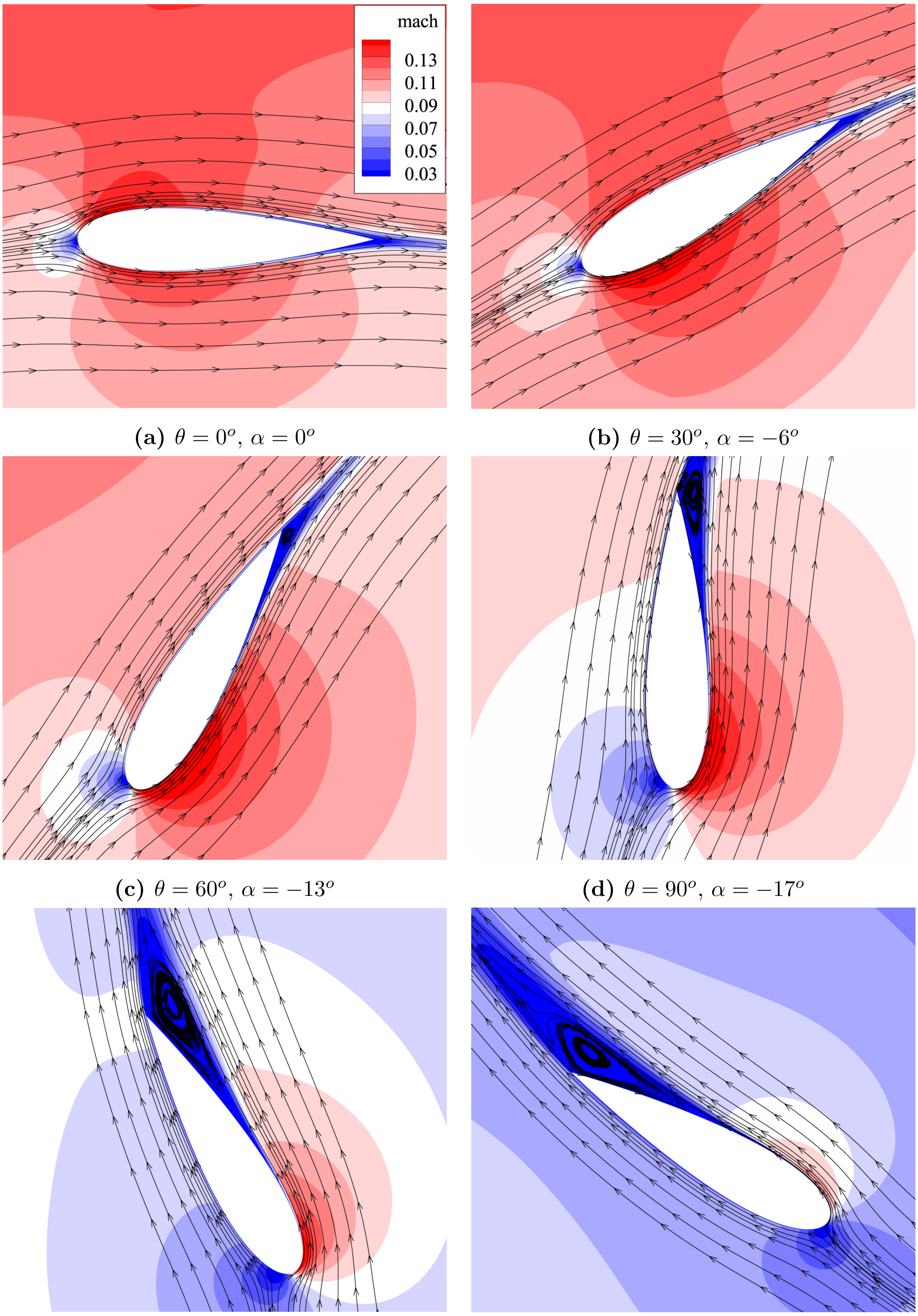

(a) $\theta = 0^o$, $\alpha = 0^o$

(b) $\theta = 30^o$, $\alpha = -6^o$

(c) $\theta = 60^o$, $\alpha = -13^o$

(d) $\theta = 90^o$, $\alpha = -17^o$

(e) $\theta = 120^o$, $\alpha = -17^o$

(f) $\theta = 150^o$, $\alpha = -11^o$

Figure 5.29: Streamlines and Mach contours in the aerofoil region obtained with COSA simulations ($\lambda = 3.30$).

contour plots and streamlines showed these unsteady effects which occur during normal VAWT working condition.

Chapter 6

Time-domain analysis of horizontal axis wind turbines

The aeromechanical design of HAWTs is a complex multidisciplinary task that requires consideration of a large number of operating regimes due to the extreme variability of the environmental conditions on time scales ranging from seconds (i.e. wind gusts) to months (i.e. seasonal wind variations). As seen for VAWTs analysis, also for HAWT, the use of high-fidelity computational aerodynamics tools such as NS solvers in an integrated aeromechanical analysis and design system has the potential to accurately predict the behaviour of new HAWT configurations and their extreme off-design operating conditions. Several outstanding examples of the predictive capabilities of NS solvers for HAWT aerodynamics have been published [61, 84, 137]. Yawed wind regime which occurs when the freestream wind velocity is not orthogonal to the turbine rotor, is one for which the underlying assumptions of BEMT-based systems are particularly weak, and a more reliable analysis of which would therefore benefit from the use of unsteady NS solvers. A complete 2D TD NS analysis of yawed flow past the blades of a 8 MW HAWT rotor is presented in this chapter. The blade sections at 30% and 85% have been considered to study the forces acting on the blade and the flow details during the entire rotor revolution.

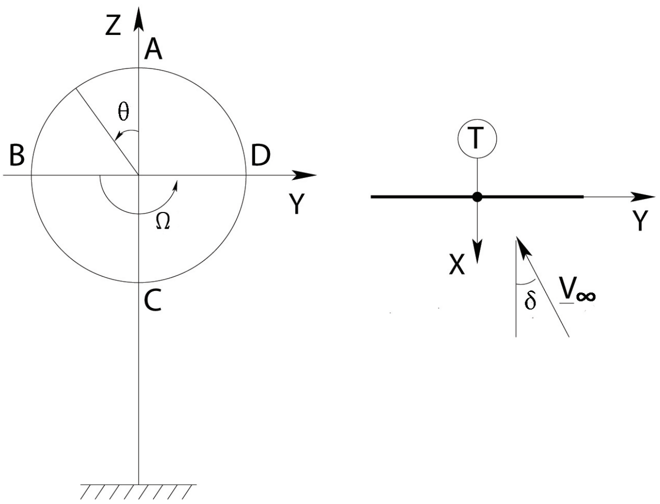

(a) front view **(b)** top view

Figure 6.1: Schematic views of HAWT in yawed wind.

6.1 Yawed wind modelling

The details of the HAWT analyses and the kinematic model are reported below. The periodic flow regime experienced by the aerofoils of a HAWT blade in yawed wind depends on the freestream wind speed V_∞, the turbine rotational speed Ω, the angle δ between V_∞ and the normal to the rotor plane (*yaw angle*), the chord c of the aerofoil and its distance R from the rotational axis. Fig. 6.1 respectively depicts the front and top views of a HAWT in yawed wind, and highlight some of the aforementioned parameters. The circumferential position of a blade is defined by the angle $\theta = \Omega t$, which is taken to be zero when the blade is vertical and descending (position A).

Fig. 6.2 reports the velocity triangles associated with a blade aerofoil at distance R from the rotational axis for the positions labeled A to D in the Fig. 6.1 (a). The modulus of the axial velocity component, $|\underline{V}_\infty \cos(\delta)|$, and that of the entrainment velocity, $|\underline{\Omega} \times \underline{R}|$, are the same in all four triangles. The velocity $\underline{W}_i$ and the angle ϕ_i ($i = A, B, C, D$) denote respectively the wind velocity and *inflow angle* observed by the considered blade section, and both parameters vary with θ. Each velocity triangle is contained in the plane tangent to the cylinder of radius R centred on the rotational axis, and it therefore neglects radial (i.e. along the blade axis) velocity components. The magnitude of the discarded radial component varies with θ: no component is discarded

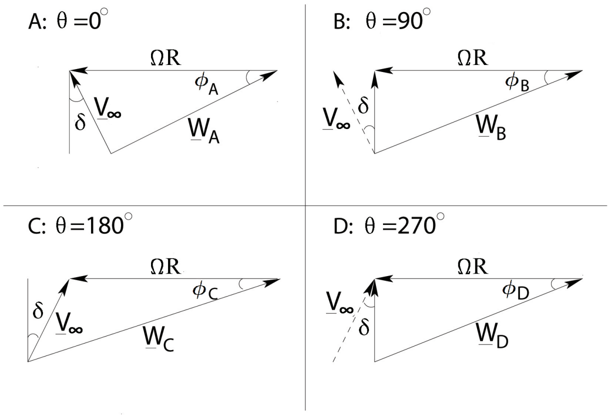

Figure 6.2: Velocity triangles of HAWT blade section for position labeled A to D.

when the blade is vertical (positions A and C), as the entire vector $\underline{V}_\infty$ is contained in the tangent plane; the entire radial component $\underline{V}_\infty \sin(\delta)$ is instead neglected when the blade is horizontal (positions B and D), as the radial component of $\underline{V}_\infty$ is orthogonal to the tangent plane.

Given the above, the axial and circumferential components of the farfield wind velocity perceived by a blade section are respectively:

$$W_X = V_\infty \cos(\delta), \qquad W_\theta = \Omega R - V_\infty \sin(\delta)\cos(\Omega t) \tag{6.1}$$

which define a time-dependent velocity vector $\underline{W}$. The angle formed by $\underline{W}$ and the rotor plane is:

$$\phi = \arctan(W_X / W_\theta) \tag{6.2}$$

The 2D simulation of the unsteady flow past the blade aerofoil of the HAWT in yawed wind could be performed by using a motionless domain and enforcing the time-dependent farfield velocity defined by Eq. (6.1). To simplify the code development work associated with designing, testing and implementing reliable time-dependent farfield boundary conditions, however, the alternative choice of using a moving-domain simulation with steady farfield conditions and suitably defined grid motion has been made. The modulus W_∞ and the orientation ϕ_∞ of the time-independent freestream are obtained by discarding the time-dependent term of W_θ, and their expressions are respectively:

$$W_\infty = \sqrt{(V_\infty \cos\delta)^2 + (\Omega R)^2} \tag{6.3}$$

$$\phi_\infty = \arctan\left[(V_\infty \cos\delta)/(\Omega R)\right] \tag{6.4}$$

In the moving-domain simulations, the aerofoil and the grid experience a horizontal sinusoidal motion with time-dependent displacement $h(t)$ defined by:

$$h(t) = h_0 \sin(\Omega t), \qquad h_0 = V_\infty \sin\delta/\Omega \tag{6.5}$$

A typical HAWT aerofoil twisted by an angle γ_p is depicted in the left sketch of Fig. 6.3 along with an indication of the harmonic motion. The right plot provides a representation of Eq. (6.5), and the four positions A to D correspond to those labeled with the same symbols in Fig. 6.1 and 6.2.

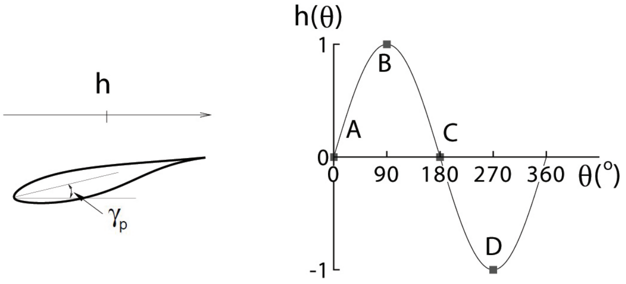

Figure 6.3: Harmonic motion of HAWT blade section corresponding to yawed inflow.

6.2 Computational set-up

The selected turbine is a 8 MW HAWT for off-shore application and the main characteristics are reported in Table 6.1. The rotor speed of 12 RPM corresponds to a value

Blades number (N_b)	3
Rotor radius (R) [m]	82
Rotor speed [RPM]	12.0
Swept area (A) [m^2]	21,124
Max. chord (c) [m]	5.4

Table 6.1: Main features of the analysed rotor.

of Ω of about 1.26 rad/s. The freestream wind velocity V_∞ is 13 m/s, and a yaw angle δ of 45^o is assumed. In this research, the blade sections at 30% rotor radius (inboard blade) and at 85% rotor radius (outboard blade) have been simulated. The details of each blade section are summarised in the Table 6.2 (a) and (b). The Reynolds number used to perform these two simulations is defined by Eq. (6.6)

radius (R) [m]	24.6
chord (c) [m]	5.225
twist angle (γ_p)	10.44^o
aerofoil type	DU-W-350LM

(a) section 30%

radius (R) [m]	69.7
chord (c) [m]	2.822
twist angle (γ_p)	1.36^o
aerofoil type	NACA64-618

(b) section 85%

Table 6.2: Rotor details in the two blade sections considered.

$$Re = \frac{\rho \cdot W_\infty \cdot c}{\mu} \tag{6.6}$$

where:

- ρ is the standard density of 1.22 kg/m^3
- W_∞ is the relative freestream velocity
- c is the chord
- μ is the dynamic viscosity at standard temperature of 288 K

The reduced frequency $K = \Omega c/W_\infty$ has been computed using the rotational speed Ω, the chord and the relative freestream velocity W_∞ defined by Eq. (6.3). The freestream Mach number M_∞ has been computed by the ratio between W_∞ and the speed of sound. The value of α_∞ between the relative freestream and the chord is obtained by subtracting the twist γ_p to the inflow angle ϕ_∞ obtained from Eq. (6.4). The computational parameters adopted in the 2D simulations at section 30% and 85% of the blade radius are summarised in Table 6.3. In the unsteady simulations, the whole grid undergoes a sinusoidal motion defined by Eq. (6.5), with amplitude h_0 defined in Table 6.3. All TD simulations have been performed using the MG solver with 3 grid levels and CFL ramping with final CFL number equal to 4.

Reynolds (Re)	$1.15 \cdot 10^7$
Mach number (M_∞)	0.095
reduced freq. (K)	0.203
inflow angle (ϕ_∞)	16.56^o
relative AoA (α_∞)	6.12^o
motion amplitude (h_0)	$1.4\ c$

(a) section 30%

Reynolds (Re)	$1.70 \cdot 10^7$
Mach number (M_∞)	0.259
reduced freq. (K)	0.040
inflow angle (ϕ_∞)	5.99^o
relative AoA (α_∞)	4.63^o
motion amplitude (h_0)	$2.59\ c$

(b) section 85%

Table 6.3: Computational parameters adopted to simulate the two blade sections considered.

6.3 Sensitivity analysis

A parametric analysis aiming at assessing the sensitivity of the computed solution to the size of the physical time-step has been carried. To conduct all the analyses for both blade sections, two reference grids have been used. They are characterised by different aerofoils to simulate. Both meshes are C-grids type (Fig. 6.4) with farfield boundary placed at about 50 chords from the aerofoil. The grids are identical in terms of number of cells, mesh intervals along the aerofoil, intervals in the grid cut and in the normal-like direction. The details of both grids are summarised in the Table 6.4

grid type	n. of cells	int. along the airf.	int. grid cut	int. normal-like dir.
C-grid	524,288	512	256	512

Table 6.4: Details of grids used to simulate 30% and 85% blade sections of an 8 MW HAWT.

The distance d_w of the first grid points off the aerofoil surface from the surface itself was set about $1 \cdot 10^{-6}c$. The nondimensional minimum distance from the wall y^+ was smaller than 1 in all simulations. All TD simulations have been run until the maximum C_x, C_y and C'_m differences over two consecutive oscillation cycles became less than 0.1% of their maxima over the latter cycle of the cycle pair. These coefficients

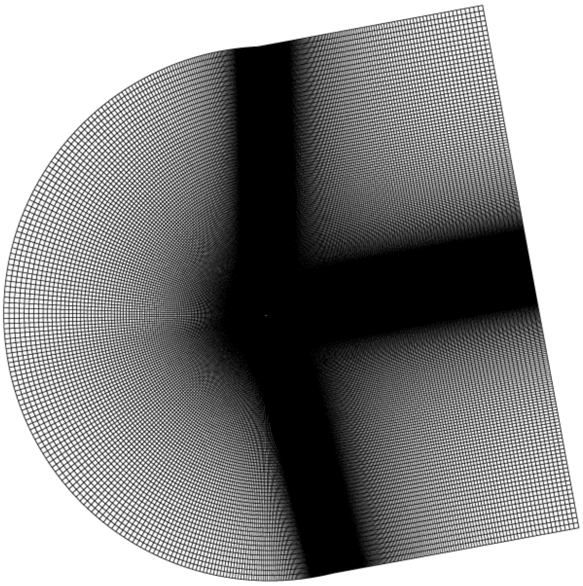

Figure 6.4: C-grid type adopted for the analyses of both HAWT blade sections. For visual clarity, only every second line of both grid line sets is plotted.

are defined respectively as:

$$C_x = \frac{F_x}{0.5\rho_\infty W_\infty^2 c}, \quad C_y = \frac{F_y}{0.5\rho_\infty W_\infty^2 c}, \quad C'_m = \frac{M}{0.5\rho_\infty W_\infty^2 c^2} \tag{6.7}$$

where the horizontal force per unit blade length F_x is the tangential force component that results in useful torque; the vertical force per unit blade length F_y is the axial force component that results in rotor thrust; the pitching moment M per unit blade length results in a torsional load on the blade.

In all simulations, the aerofoils and the whole grids are inclined by the respective twist angle γ_p on the horizontal direction. Fig. 6.5 provides an enlarged view of the coarse grids in the aerofoil region.

6.3.1 Time-refinement analysis

The temporal refinement analysis has been conducted for both blade sections. The results are compared in terms of conventional lift C_l, drag C_d and pitching moment C_m coefficients. This second set of forces is defined as:

$$C_l = \frac{L}{0.5\rho_\infty W^2 c}, \quad C_d = \frac{D}{0.5\rho_\infty W^2 c}, \quad C_m = \frac{M}{0.5\rho_\infty W^2 c^2} \tag{6.8}$$

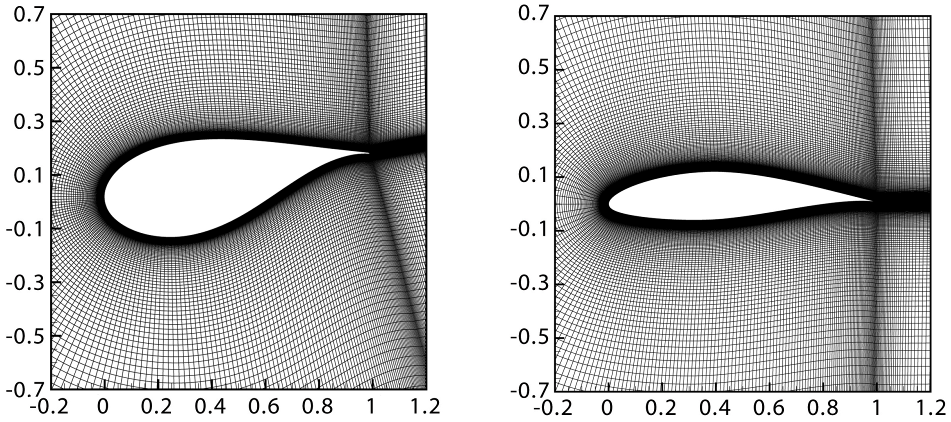

(a) section 30% **(b)** section 85%

Figure 6.5: Grids view in the aerofoil region.

where $W^2 = W_X^2 + W_\theta^2$ is the time-dependent dynamic head. The direction of the lift force per unit blade length L, and that of the drag force per unit blade length D also vary during the rotor revolution, as they depend on the inclination of the vector $\underline{W}$ on the rotor plane. The curves of the C_l, C_d and C_m force coefficients over one rotor revolution computed by the reference grids have been analysed. A time-step study was performed for the section at 30%, to determine the minimal time-resolution of the TD analysis required to obtain a solution independent of further reductions of the physical time-step. Four TD simulations have been performed using 256, 128, 64, and 32 physical time-steps per period and they are denoted by TD 256, TD 128, TD 64 and TD 32, respectively. The C_l, C_d and C_m force coefficients over one rotor revolution are depicted in the three subplots of Fig. 6.6. The variable along the x-axis of these subplots is the percentage time of a period T.

These results show that at least 64 intervals per period are required to achieve lift and drag predictions independent of further increments of the time resolution, whereas at least 128 intervals per period are required for a time-grid independent estimate of the pitching moment. Thus, TD 128 simulation is therefore taken as the reference TD result for the blade section 30%.

The minimal time-resolution of the TD analysis for section at 85% has been performed using four TD simulations with the same number of time steps per period used for section 30%. The C_l, C_d and C_m force coefficients are shown in Fig. 6.7. These results show that for lift, drag and pitching moment there are negligible differences

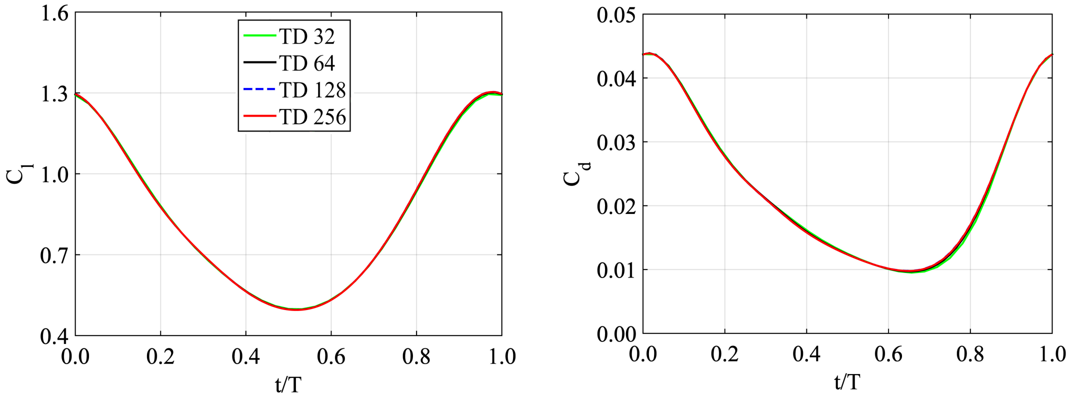

(a) C_l **(b)** C_d

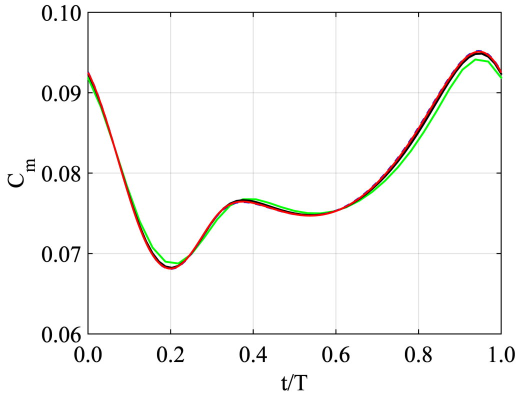

(c) C_m

Figure 6.6: Sensitivity to temporal refinement for section 30%. The x-axis indicates the percentage time of a period T.

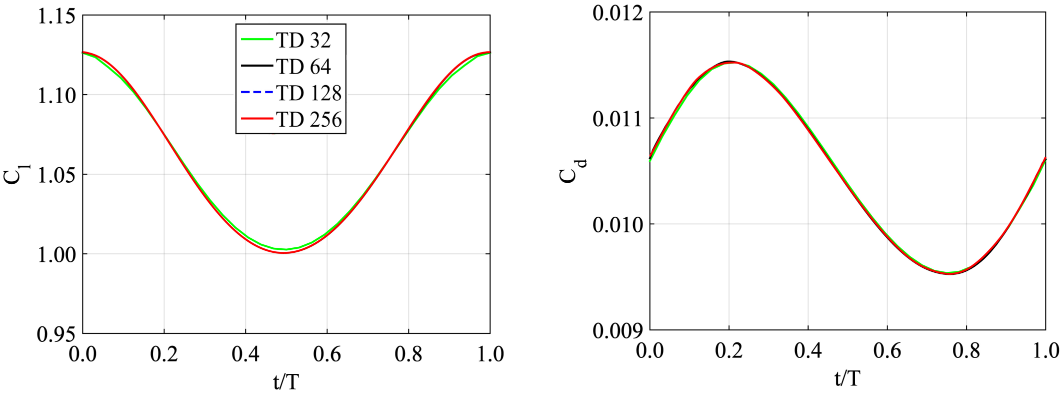

(a) C_l

(b) C_d

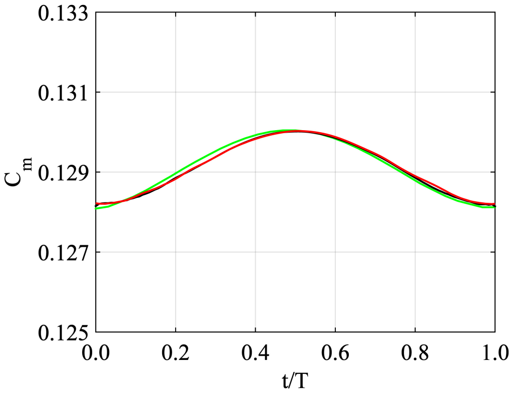

(c) C_m

Figure 6.7: Sensitivity to temporal refinement for section 85%. The x-axis indicates the percentage time of a period T.

between TD 64, 128 and 256, whereas some relatively larger differences are shown between TD 32 and the other TD results. Thus, TD 64 is taken as reference TD result for the following analysis of section 85%.

6.4 Aerodynamic analysis

Detailed aerodynamic analyses of the blade aerofoil at section 30% and 85%, of the rotating 8 MW HAWT blade in yawed wind are considered in this section. The results are presented in terms of conventional lift, drag and pitching moment coefficients. In addition, vorticity contours are presented to highlight flow details past the aerofoil at position 0%, 25%, 50% and 75% of the rotor revolution.

6.4.1 Inboard blade

Fig. 6.8 reports the C_l, C_d and C_m solutions for section 30% obtained with the reference grid and 128 time steps per period and the value of the angle α_∞ between the time-dependent freestream velocity $\underline{W}$ defined by Eq. (6.1) and the chord over one period. In general, the angle $\alpha = \phi - \gamma_p$, which is determined by the yawed flow conditions upstream of the turbine, differs from the local AoA, which defines the flow direction close to the blade, due to the blade-bound vorticity. The analyses do not take into account this difference, but this omission is believed not to alter the main conclusions of the analyses below. The local AoA could be easily determined by postprocessing the computed velocity field as proposed in [129]. Moreover, the three subplots of Fig. 6.8 shows that α has its maximum at the beginning of the period, when $h(0) = 0$ and the blade is at $\theta = 0^o$ (position A in the sketch of Fig. 6.1 (a)), and it decreases to its minimum at 50% of the period. When $h(0.5T) = 0$ again and the blade is at $\theta = 180^o$ (position C in the sketch of Fig. 6.1 (a)). In the first half of the period, the blade sweeps a 180^o-sector starting from the vertical position above the hub and moving in the counterclockwise direction indicated in the sketch of Fig. 6.1 (a). As the blade moves from its lowest to its highest vertical position in the second half of the period, the angle α increases from its minimum to its maximum.

Fig. 6.8 (a) highlights that the lift force coefficient is fairly non-hysteretic whereas Fig. 6.8 (b) shows a peak of C_d shortly before the end of the period. This occurrence breaks the symmetry of the C_d curve with respect to the $t/T = 0.5$ axis, and denotes

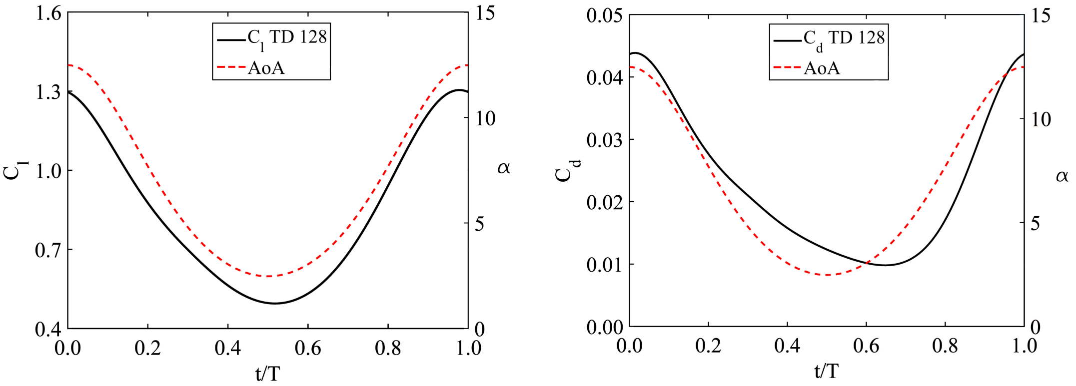

(a) C_l **(b)** C_d

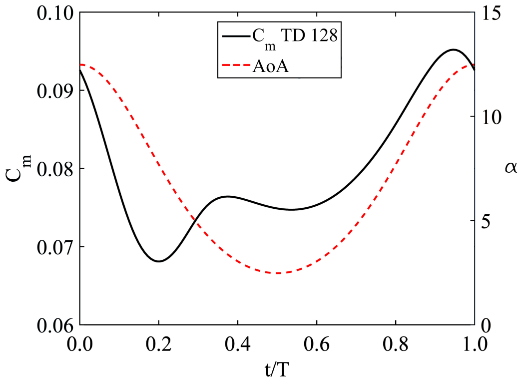

(c) C_m

Figure 6.8: Time-evolution of force coefficients of 30% blade section.

the existence of a hysteretic loop, quite pronounced for the highest values of α. The existence of the C_d hysteresis loop denotes a significant level of flow nonlinearity. This is likely to be due to a flow reversal at the trailing edge (TE) on the suction side (SS) when the blade approaches its highest vertical position, and the relatively high value of the reduced frequency at the considered radius. Also the pitching moment coefficient curve highlights a pronounced hysteretic loop like the drag coefficient. It should be noted that the dynamic head and the relative flow direction used to compute the C_l, C_d and C_m coefficients vary during the period, and therefore they do not provide a direct measure of the sectional aerodynamic loads.

The four subplots of Fig. 6.9 depict the TD 128 contours of the flow vorticity $\widehat{\Omega}$ and the streamlines past the blade section when the aerofoil is at 0, 25, 50 and 75 percent of the revolution cycle. The subplots referring to the 0% position confirms the existence of a pocket of stalled flow in the trailing edge region when the blade is at its highest position. Inspection of the four subplots also reveals that the 0% position is also that in which the section experiences the thickest SS boundary layer, as highlighted by the large amount of vorticity on the SS relative to the other three positions. It is also noted that the variation of the direction of the oncoming flow visible in the four subplots is consistent with the variation of the direction of the velocity vector $\underline{W}$ observed in the four velocity triangles of Fig. 6.2.

6.4.2 Outboard blade

The outboard blade section analysed highlights that lift, drag and pitching moment coefficient are fairly non-hysteretic. This behaviour shows a very small level of flow nonlinearity with respect to the inboard blade case. Fig. 6.10 (a), (b) and (c) report the curves of C_l, C_d, C_m and the value of the angle α_∞. The angle α has its maximum at the beginning of the period, when $\theta = 0^o$ and it decreases to its minimum at 50% of the period as it has shown for the previous blade section analysed. For section 85%, the variation of the amplitude of α is quite smaller in comparison to the 30% section. The lift coefficient (Fig. 6.10 (a)) shows a peak at the beginning of the period and it appears to be symmetric about the axis $t/T = 0.5$. The variation between its minimum and maximum values is about 6 times smaller with respect to the C_l value obtained at section 30% counterpart. Also the drag coefficient and the pitching moment coefficient curves (Fig. 6.10 (b) and (c)) report the same symmetric behaviour which does not denote the existence of a hysteretic loop. The reduction of the level of nonlinear flow at section 85% is linked to value of the reduced frequency K reported in the section *Computational set-up*. K is a parameter that defines the degree of unsteadiness of the problem, and one can see that it decreases going from the inboard to the outboard section of the blade. At section 85%, $K = 0.04$ is about 5 times smaller than the value at section 30% and as expected the aerofoil does not present complicate phenomena like stall and separation.

The four subplots of Fig. 6.11 depict the TD 64 contours of the flow vorticity and the streamlines past the blade section when the aerofoil is at 0, 25, 50 and 75 percent of the revolution cycle. All subplots show no stalled flow in the TE region of the aerofoil.

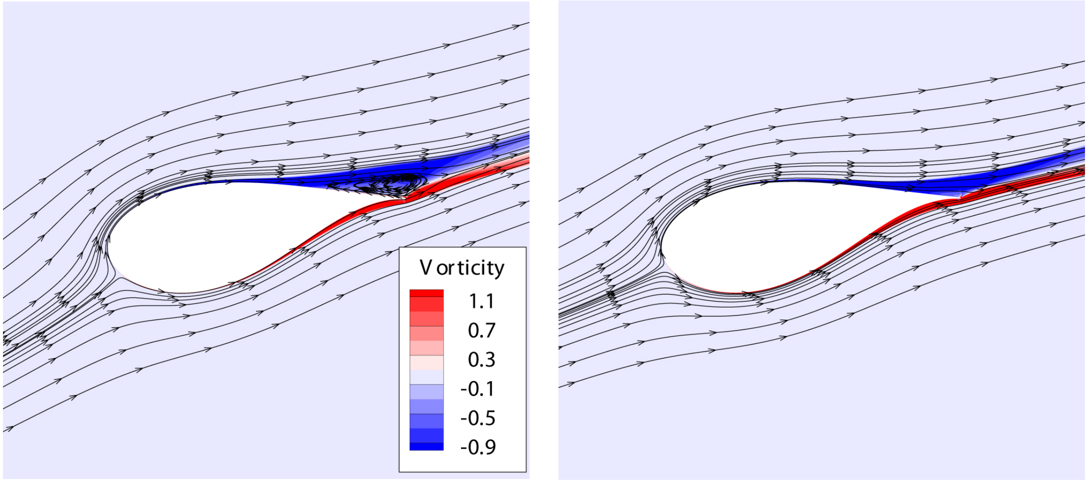

(a) A: 0% **(b)** B: 25%

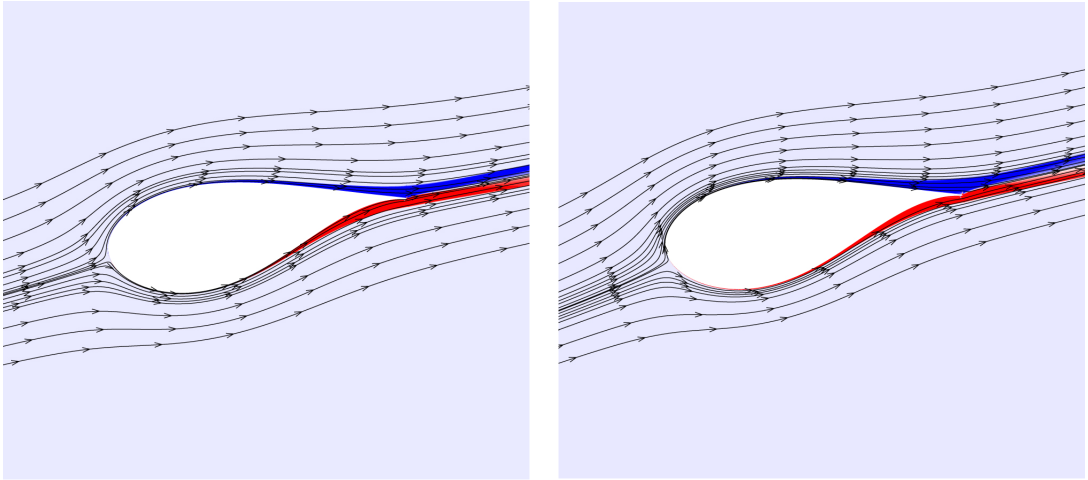

(c) C: 50% **(d)** D: 75%

Figure 6.9: Strealines and vorticity contours at four positions of the revolution cycle (section 30%).

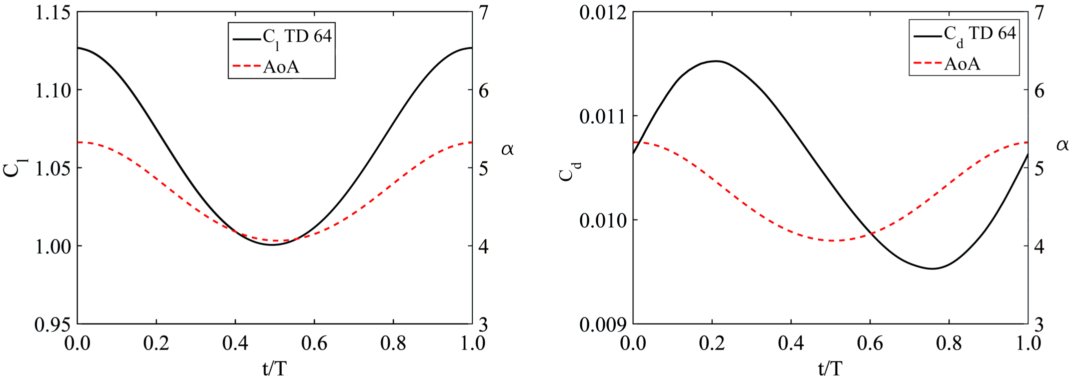

(a) C_l **(b)** C_d

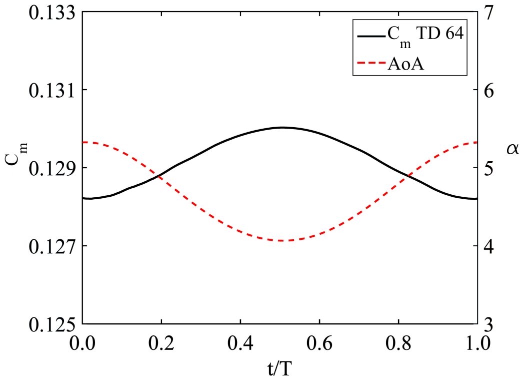

(c) C_m

Figure 6.10: Time-evolution of force coefficients of 85% blade section.

Also when the blade is at its highest position (A in Fig. 6.1), α is not too high to induce the stall and the flow appears to be completely attached to the blade.

6.5 Conclusion

The chapter reports a 2D time-domain analysis of two blade sections of an off-shore multi-megawatt horizontal axis wind turbine working in yawed wind condition. The forces acting on the blade sections at 30% (inboard blade) and 85% (outboard blade), and the flow details during the entire rotor revolution have been studied. An aerodynamic analysis in terms of conventional lift, drag and pitching moment coefficients has highlighted, for the inboard blade, the existence of hysteretic loops of drag and pitching moment coefficient which denotes a significant level of flow nonlinearity. It is confirmed from the vorticity analysis, where a pocket of stalled flow near the trailing edge for the highest values of α is visible. Conversely, the flow analysis at outboard blade section shows that forces coefficients are non-hysteretic and no stalled flow occurs during the blades rotation.

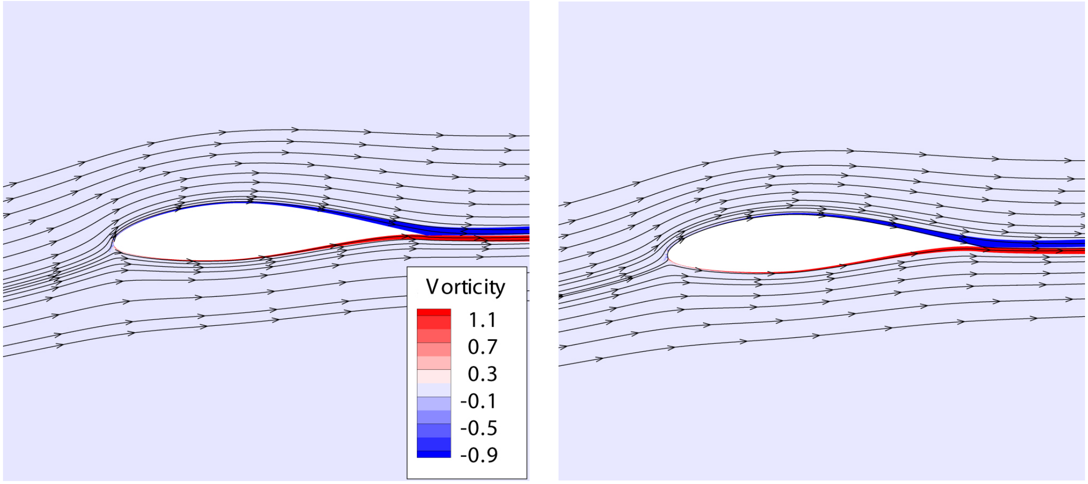

(a) A: 0%

(b) B: 25%

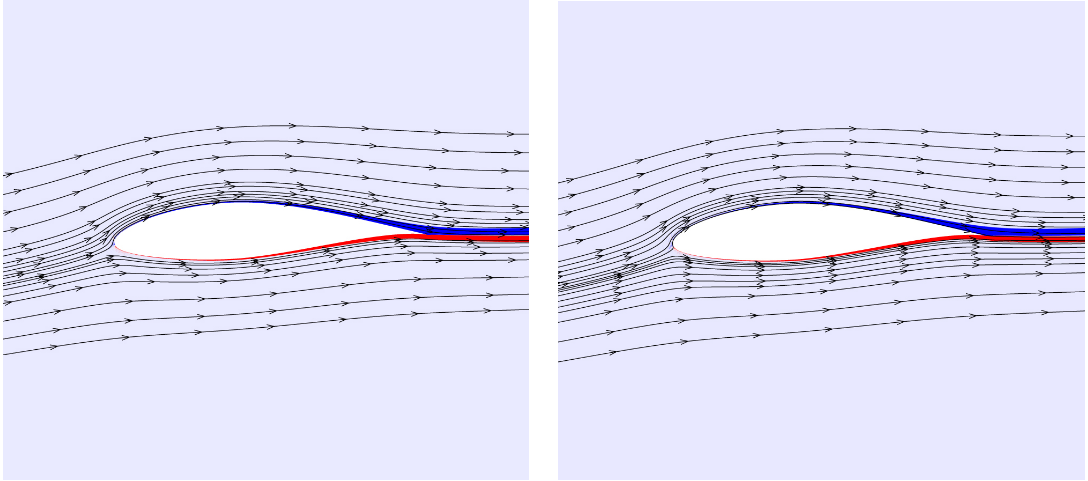

(c) C: 50%

(d) D: 75%

Figure 6.11: Strealines and vorticity contours at four positions of the revolution cycle (section 85%).

Chapter 7

Harmonic Balance acceleration of wind turbine unsteady flow analysis

This chapter presents the turbulent results of COSA HB solver to predict the yawed wind periodic loads acting on multimegawatt HAWT blade section geometries and to predict the flow past the rotor of a Darrieus wind turbine for several operating conditions. Several spectral refinement analyses have been conducted for each test case to find the correct number of complex harmonics which reproduces accurately the respective TD solutions. HB speed-ups and MG overheads will highlight the advantage of using COSA HB solver to study engineering problems more than 10 times faster than its TD counterpart.

7.1 HB analysis of HAWT

The HB analysis of the HAWT has been performed at 30% and 85% blade sections as done for the TD analysis counterpart and it has been conducted to determine the minimum number of harmonics to reproduce the TD solutions in terms of horizontal force coefficient, vertical force coefficient and constant-head pitching moment coefficient defined by Eq. (6.7). In addition, to assess in greater detail the differences between the TD and HB analyses, the blade static pressure c_p and the blade skin friction coefficient c_f have also been compared. The analysis of each blade section is followed by the HB speed-ups calculations which highlight the HB efficiency with respect to the traditional TD approach.

7.1.1 Spectral refinement of inboard blade

The spectral refinement analysis has been performed first for the blade section at 30%. To determine the minimum number of harmonics required to resolve the time-dependent problem at hand with the HB solver achieving a time-resolution comparable to that of the TD, five HB calculations have been performed. These five simulations use values of N_H of 1, 2, 3, 4 and 5 and they are denoted by the acronym HB followed by the value of N_H.

The hysteresis cycles of C_x, C_y and C'_m force coefficients computed by the five HB analyses are compared with the TD 128 results obtained from the refinement assessment of the respective section and are plotted against α in the three subplots of Fig. 7.1. These results show that at least 5 complex harmonics are required to achieve a resolution of the force coefficients comparable to that of the TD 128 simulation, since the HB 5 force loops is superimposed to the TD curves of all three force coefficients, whereas HB 4 shows little discrepancies for highest values of α. Lower number of harmonics present discrepancies more evident for the entire range of the angle α. The noticeable size of the hysteresis loops of Fig. 7.1 also highlights that the level of nonlinearity of the periodic flow field caused by the yawed wind condition requires the use of nonlinear frequency-domain CFD. The use of linear CFD is likely to yield insufficiently accurate estimates of the time-dependent loads required for reliable fatigue and aeroelastic analysis and design of the HAWT blades. It is also observed that C_x, C_y and C'_m coefficients point to periodic variations of the contribution of this section, to the rotor thrust, torque and blade torsional loads of about ± 22%, ± 15% and ± 40% respectively. The variation of the coefficients is computed with respect to their mean value and one can see that C'_m points to a significant contribution of this section to the blade torsional loads caused by the yawed wind regime.

The real and imaginary parts of the first harmonic component of pressure coefficient c_p computed by the TD and the five HB analyses are plotted in Fig. 7.2. In both cases, the x-axis reports the axial position along the aerofoil normalized by the chord. The imaginary part of c_p confirms that 5 harmonics are necessary to resolve the flow unsteadiness with the HB analysis, whereas the real part of c_p does not show large

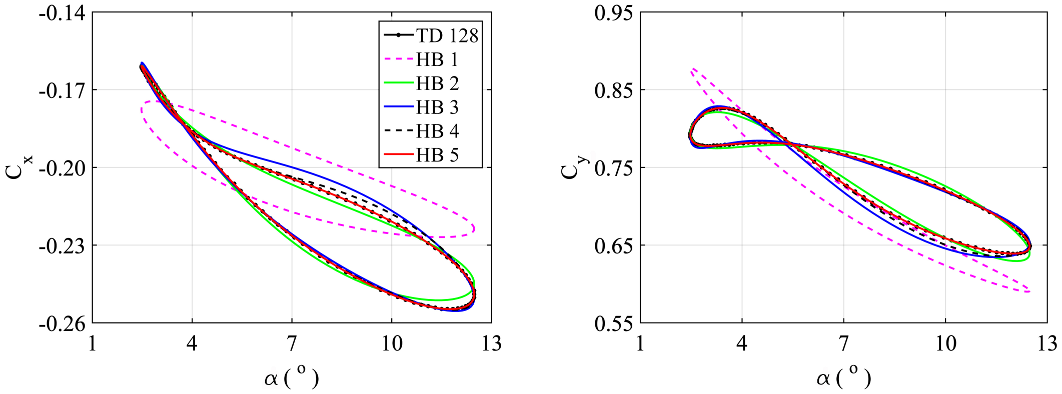

(a) C_x **(b)** C_y

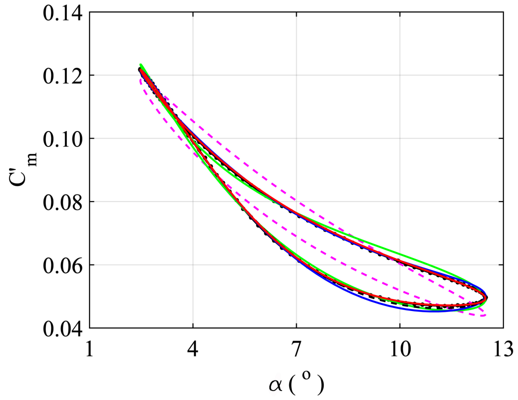

(c) C'_m

Figure 7.1: Hysteresis force loops of 30% blade section.

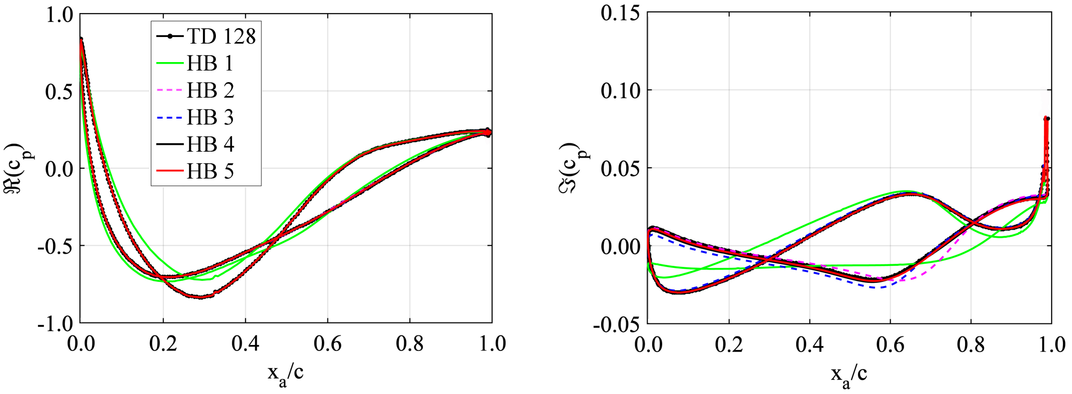

(a) c_p real part **(b)** c_p imaginary part

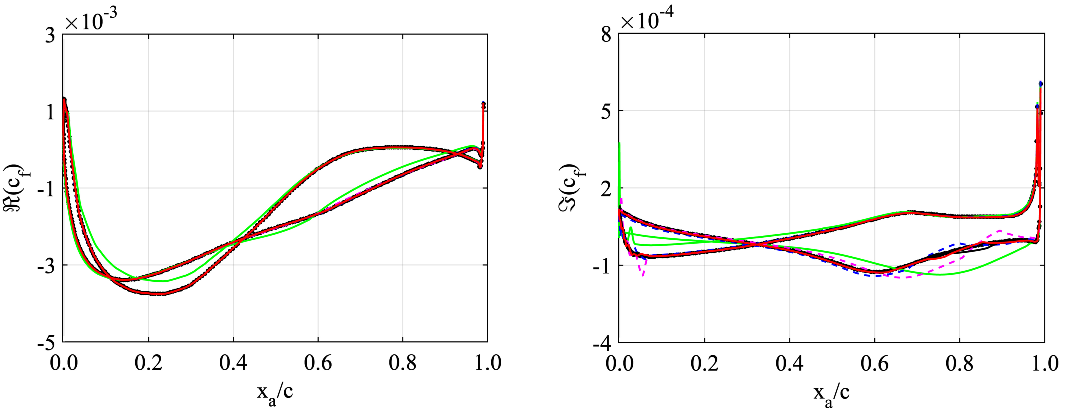

(c) c_f real part **(d)** c_f imaginary part

Figure 7.2: Pressure coefficient (c_p) and skin friction coefficient (c_f) of 30% blade section.

differences, showing that HB 2 result is sufficient to achieve the TD accuracy. The real and imaginary part of the first harmonic component of skin-friction coefficient c_f computed by the TD and the five HB analyses are reported in the subplot (c) and (d) of Fig. 7.2. One can see the same behaviour observed for the c_p results. An adequate HB resolution of the imaginary part of c_f requires $N_H = 5$, while the resolution on the real part of c_f needs at least 2 harmonics. For both c_p and c_f, only the comparison of the first harmonic components are shown because they give the biggest contribution.

7.1.2 Spectral refinement of outboard blade

The spectral refinement analysis performed at section 30%, has been done also for section 85%. Five HB simulations have been run to determine the minimum number of harmonics required to resolve the flow problem using the HB solver. These five simulations used values of N_H of 1, 2, 3, 4 and 5.

The hysteresis cycles of C_x, C_y and C'_m force coefficients computed by the five HB analyses are compared with the TD 64 results obtained from the refinement assessment of section 85% and are plotted against α in the three subplots of Fig. 7.3. These results show that at least 3 complex harmonics are required to achieve a resolution of the force coefficients comparable to that of the TD 64 simulation, since HB 3, 4 and 5 force loops are superimposed to the TD curves of C_x and C'_m, whereas HB 2 and 1 differ very little. The C_y plot highlights that HB 2 is sufficient to reproduce the TD result, but HB 3 was selected as reference for this blade section analysis since 3 harmonics are required to accurately reproduce C_x and C'_m force coefficients. The size of the hysteresis loops of Fig. 7.3 highlight that the level of nonlinearity of the periodic flow field is decreased with the decreasing of the reduced frequency, consistently with the conclusions deducted form the TD analysis in *Chapter 6*. It is also observed that the C_x, C_y and C'_m loops, point to periodic variations of the coefficients, computed with respect to their mean value of about ± 3%, ± 15% and ± 20% respectively, highlighting a smaller hysteresis cycles of thrust and blade torsional loads caused by the yawed wind regime on this blade section.

The real and imaginary part of the c_p computed by the TD analysis and the five HB analyses are plotted in Fig. 7.4. The real and imaginary part of c_p confirm that 3 harmonics are sufficient to resolve the flow unsteadiness with the HB solver even if HB 2 solution does not show large differences. The real and imaginary part of the c_f reported in the subplot (c) and (d) of Fig. 7.4 show the same behaviour observed for the c_p results. An adequate HB resolution of the real and imaginary part of c_f requires $N_H = 3$.

7.1.3 HB speed-ups and MG overheads

The HB analyses performed for blade section at 30% have been run for 15,000 MG iterations, since this was the minimum value required for the convergence of all harmonics of all force components for all five HB analyses. Each physical time-step of the TD 128 analysis has instead used 2,000 MG iterations, as this value has been sufficient for the convergence of all force components. In order to reduce the periodicity error below the

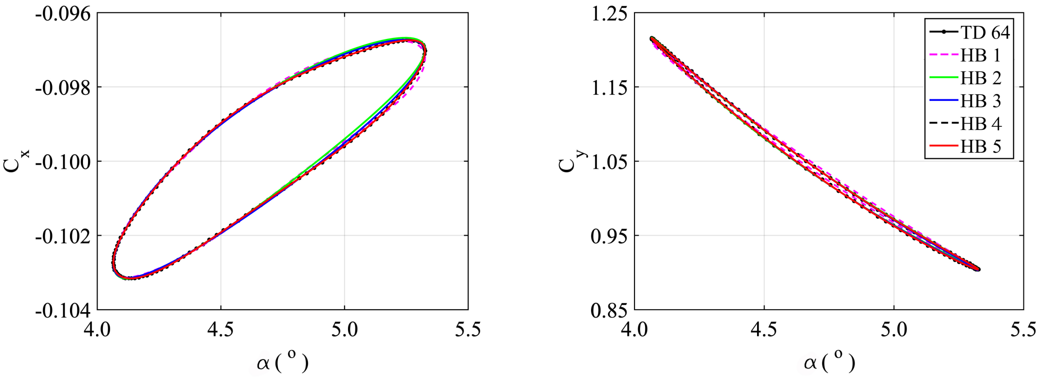

(a) C_x **(b)** C_y

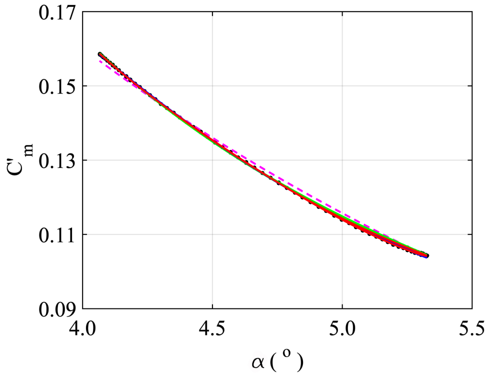

(c) C'_m

Figure 7.3: Hysteresis force loops of 85% blade section.

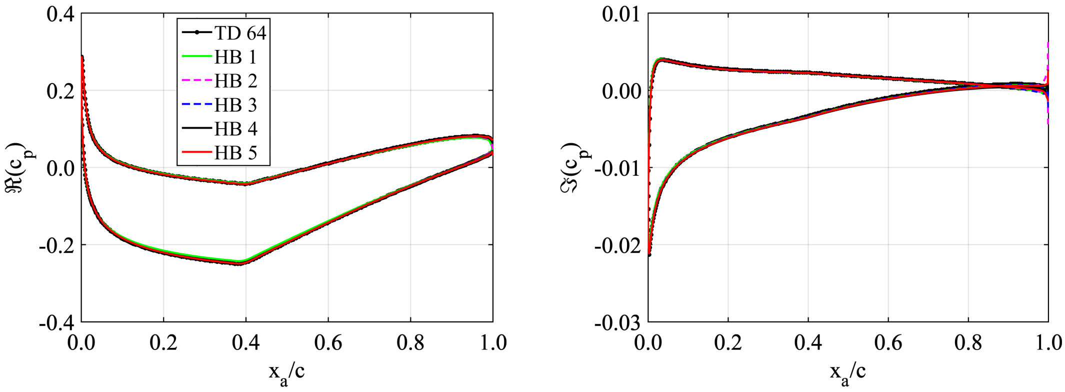

(a) c_p real part

(b) c_p imaginary part

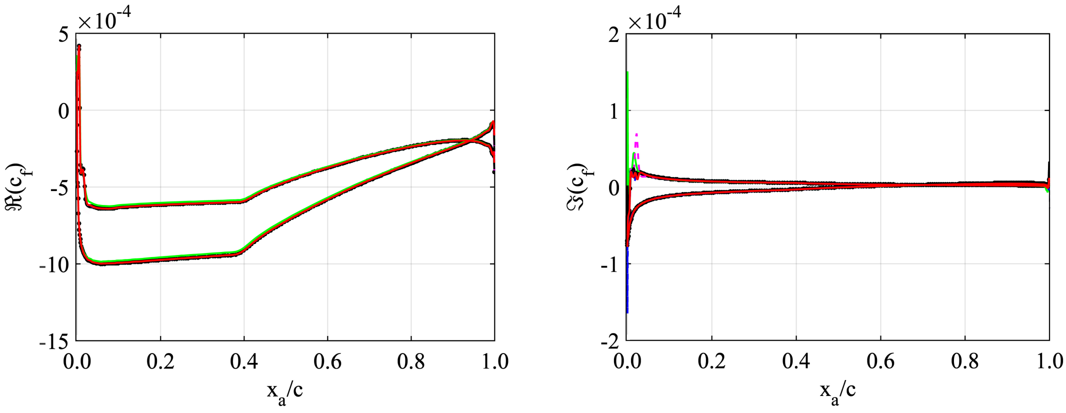

(c) c_f real part

(d) c_f imaginary part

Figure 7.4: Pressure coefficient (c_p) and skin friction coefficient (c_f) of 85% blade section.

0.1% threshold, eight revolutions had to be simulated starting from a freestream initial condition.

The convergence histories of the five HB analyses and that of the TD 128 simulation are reported in Fig. 7.5. The variable on the x-axis is the number of MG iterations. For the HB analyses, the variable Δl_r on the y-axis is the logarithm in base 10 of the normalised RMS of all cell-residuals of the four RANS equations of the $2N_H + 1$ snapshots. Each RMS curve is normalised by the RMS value at the first MG iteration. For the TD 128 analysis, the variable Δl_r on the y-axis is instead the logarithm in base 10 of the RMS of all cell-residuals of the four RANS equations of the 128 physical times of the last period. An interesting feature is that the convergence histories of all HB analyses are fairly close to each other. Some differences are only observed between HB 1 curve on one hand, and the other four HB curves on the other. This occurrence appears to confirm that the periodic flow nonlinearity is dominated by the first two harmonics: the contribution of the progressively smaller higher-frequency harmonics of the HB 3, HB 4 and HB 5 analyses does not affect significantly the spectrum of the linearised operator associated with the integration of these HB set-ups with respect to that associated with the HB 2 set-up. Fig. 7.5 also reports the convergence history of the steady problem obtained from the HB set-up by only turning-off the grid motion. The curve of the steady residual history does not differ substantially from those of the HB analyses, and this points to the fact that the level of flow unsteadiness in the problem at hand is not very high.

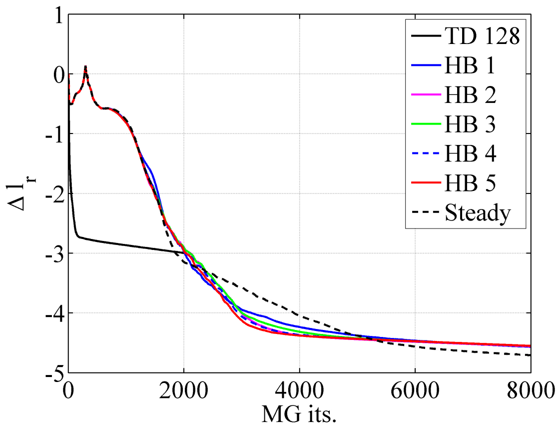

Figure 7.5: Convergence hystories of TD, HB and steady analyses for 30% blade section.

When one solves the HB equations, the CPU-time of one HB MG iteration increases superlinearly with N_H. This implies that the cost of a HB N_H simulation with a given number of MG cycles is higher than $(2N_H + 1)$ times the cost of the steady simulation using the same number of MG cycles. This overhead is due to the calculation of the HB source term $\omega V_H D_H Q_H$ appearing in Eq. (4.36), and is proportional to $(2N_H + 1)^2$. Such an overhead can be quantified by taking the ratio of the measured CPU-time of one MG iteration of the HB N_H analysis and that of one MG cycle of the steady analysis, and dividing such a ratio by $(2N_H + 1)$. The variable C_{MG} thus obtained is reported in the second row of Table 7.1. It is seen that the overhead for the calculation of the HB source term with the HB 5 analysis makes the average CPU-time of the portion of one HB MG cycle for calculating one HB snapshot about 74% higher than that of one steady MG cycle. The sixth column of Table 7.1 reports C_{MG} for the TD simulation. The small overhead of 2% is that required for the calculation of the source term $1.5Q^{n+1}/\Delta t$ appearing in Eq. (3.55). The HB speed-up parameter, defined as the ratio of the wallclock time of the TD 128 simulation and the HB analysis for the five values of N_H is reported in the third row of Table 7.1. It is seen that the HB 5 analysis allows a very accurate estimate of the time-dependent loads associated with the considered yawed condition to be obtained more than 7 times faster than TD 128 analysis.

Table 7.1: Acceleration factors of HB analyses with respect to TD analysis for the 30% blade section.

	HB 1	HB 2	HB 3	HB 4	HB 5	TD 128	steady
C_{MG}	1.21	1.38	1.52	1.60	1.74	1.02	1.00
speed-up	38.4	20.3	13.1	9.7	7.3	1.00	

For section 85%, 12,000 MG iterations was the minimum value required for the convergence of all harmonics of all force components for all five HB analyses. For the TD 64 analysis counterpart has instead used 3,000 MG iterations for each physical time-step. In order to reduce the periodicity error below the 0.1% threshold, seven revolutions had to be simulated starting from a freestream initial condition. The convergence histories of the five HB analyses and that of the TD 64 simulation have a similar behaviour like that observed for section 30%. Table 7.2 reports the C_{MG} (second row) and the HB speed-up (third row) obtained from the section 85% simulations. In this case the C_{MG} for the TD analysis refers to TD 64 simulation. The overhead for the calculation of the HB source term with the HB 3 analysis (which is taken as reference for this section), makes the average CPU-time of the portion of one HB MG cycle for calculating one HB snapshot about 38% higher than that of one steady MG cycle. It is seen that the HB 3 analysis gives an accurate estimate of the TD resolutions more than 10 times faster than the TD 64 analysis.

Table 7.2: Acceleration factors of HB analyses with respect to time-domain analysis for the 30% blade section.

	HB 1	HB 2	HB 3	HB 4	HB 5	TD 64	steady
C_{MG}	1.22	1.38	1.51	1.63	1.73	1.02	1.00
speed-up	31.2	16.6	10.8	7.8	6.00	1.00	

In the Table 7.1 and 7.2 can be viewed that the cells of the speed-ups corresponding to the steady calculations are empty because the speed-ups are measured between two approaches which allow to get a periodic solution. The steady calculations do not allow it and for this reason they do not represent a term of comparison with respect to HB and TD approaches.

7.2 HB analysis of VAWT

The HB analysis of the VAWT problem has been performed for two different λ. Several HB simulations have been done to find the minimum number of harmonics to reproduce the TD solutions in term of tangential force, normal force and torque coefficients defined by Eq. (7.11). Moreover, a comparison of c_p and c_f has been performed to study in greater detail the differences between the TD and HB analyses and it is shown in the next subsection. The HB VAWT analyses for each λ is followed by the HB speed-ups calculations which highlight the efficiency of the HB approach with respect to TD counterpart, also for strongly non-linear problems.

7.2.1 Spectral refinement

The spectral refinement analysis of the VAWT problem, has been performed for two operating conditions. $\lambda = 2.88$ and $\lambda = 3.30$ have been selected. To determine the minimum number of harmonics to achieve a solution comparable to that of the TD, for $\lambda = 2.88$, four HB simulations have been performed. These four simulations use values of N_H of 8, 16, 32 and 64. The tangential force coefficient C_{F_T}, normal force coefficient C_{F_N} and the torque coefficient C_T of an entire rotor revolution computed by the four HB analyses, are plotted against θ and are compared with the TD 720 solution. The HB results are denoted by the acronym HB followed by the value of N_H. The results of C_{F_T}, C_{F_N} and C_T reported in the subplots of Fig. 7.6 show that the solutions using 32 complex harmonics are not exactly superimposed to the TD result but they can be chosen as reference because they achieve a similar resolution to the TD 720 simulation during the entire upwind area and HB 64 results does not improve too much the accuracy. In the downwind region the interaction with wakes increases and achieving the same TD accuracy is more difficult because the periodic flow has the highest nonlinearity. HB 8 and the HB 16 results present large discrepancies and they are not sufficient to achieve a good solution.

One can see several oscillations in the HB 32 and HB 64 solutions of all force coefficients. They appear in the upwind region, between the peak and $\theta = 180^o$, where the blade is going to move in the same direction of the wind freestream and the relative wind velocity to the blade decreases until to reach its minimum value at $\theta = 180^o$. The convergence histories of the four HB analyses for $\lambda = 2.88$ are reported in Fig. 7.7. The variable on the x-axis is the number of MG iterations and the variable Δl_r on the y-axis is the logarithm in base 10 of the normalised RMS of all cell-residuals of the four RANS equations of the $(2N_H + 1)$ snapshots. Each RMS curve is normalised by the RMS value at the first MG iteration. Fig. 7.7 shows a small convergence rate for all HB analyses. The residuals convergence decreases only two order of magnitude. The difference between the level of the residuals convergence between VAWT and HAWT highlights the different flow complexity. For higher nonlinear problems like VAWT, the HB approach can become unstable as in this case. As a consequence, also the convergence of forces does not achieve a constant solution, even if a large number of MG iterations is used. Taking as reference the calculation HB 32, the convergence of

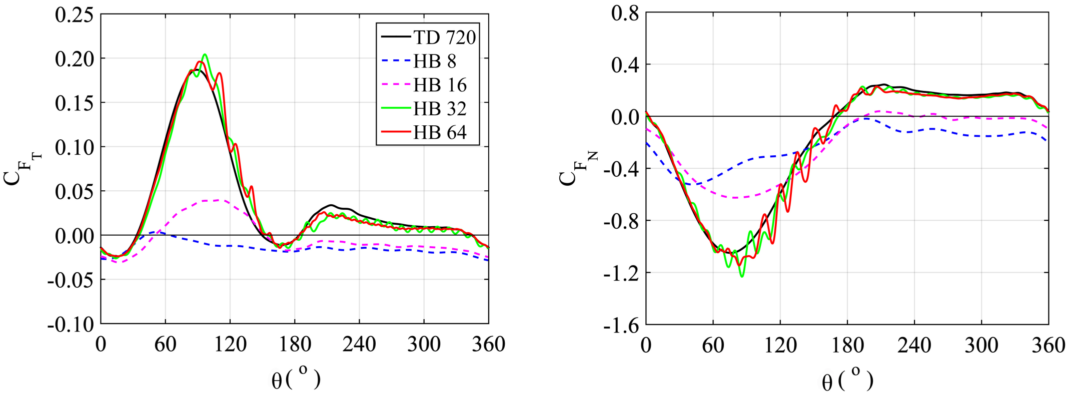

(a) C_{F_T} **(b)** C_{F_N}

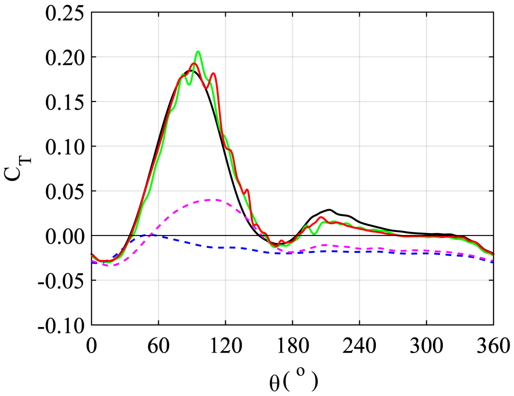

(c) C_T

Figure 7.6: Spectral refinement analysis of blade 1 for $\lambda = 2.88$.

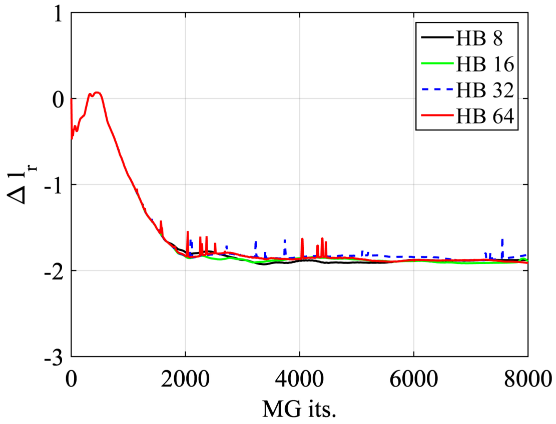

Figure 7.7: Convergence hystories of HB analyses for $\lambda = 2.88$.

C_T in a few snapshots has been plotted in Fig. 7.8. It shows that several oscillations affect the complete C_T convergence. Very similar behaviour has been found for the convergences of tangential and normal force coefficients. The snapshots reported in Fig. 7.8 correspond to θ equal to 30^o, 90^o, 150^o and 240^o, respectively. Has been verified that similar oscillations occur also in the forces convergence obtained for different λ for the same reason.

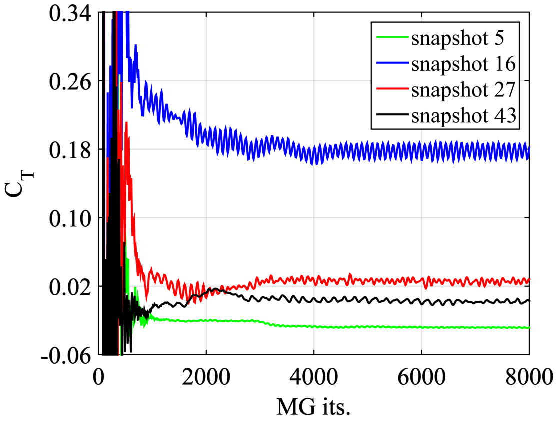

Figure 7.8: C_T convergence in four different snapshots of HB 32 analyses for $\lambda = 2.88$.

The spectral refinement analysis for $\lambda = 3.30$ have been performed in the same way. Using the same set of N_H, the simulation with 32 complex harmonics has been selected

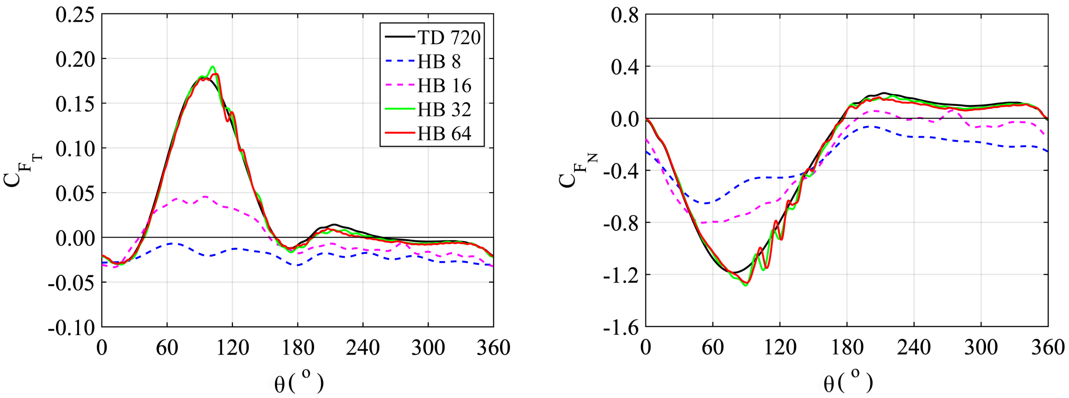

(a) C_{F_T} **(b)** C_{F_N}

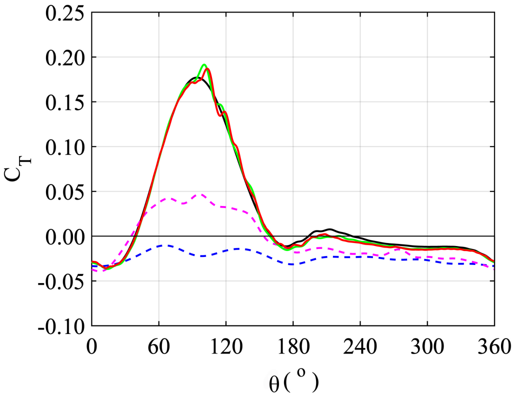

(c) C_T

Figure 7.9: Spectral refinement analysis of blade 1 for $\lambda = 3.30$.

as reference for the same reasons explained for $\lambda = 2.88$. The C_{F_T}, C_{F_N} and C_T defined by Eq. (5.13) and Eq. (5.3), have been used for the comparison with the TD 720 results obtained from the sensitivity analysis of the respective λ. The force coefficients of an entire rotor revolution computed by the four HB analyses and one TD solution are reported in the subplots of Fig. 7.9. Also in this case, the results of C_{F_T}, C_{F_N} and C_T show that the solutions using 32 complex harmonics is not exactly superimposed to the TD solution but the HB 64 does not improve the accuracy, so HB 32 can be chosen as reference. HB 8 and HB 16 results are too far from the TD solution so they cannot be considered as the optimal results. Also for $\lambda = 3.30$, the HB solutions present several oscillations in the region between $\theta = 90^o$ and $\theta = 180^o$.

The real and imaginary parts of c_p and c_f were computed for both λ analysed,

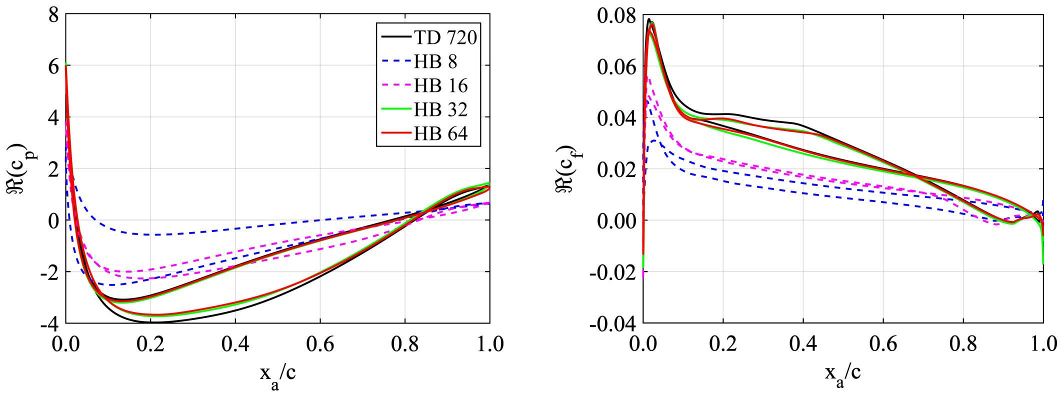

(a) c_p real part **(b)** c_p imaginary part

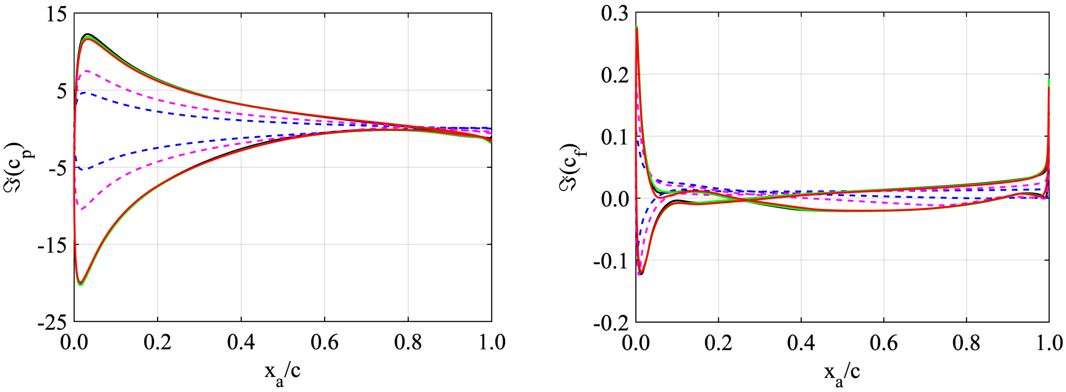

(c) c_f real part **(d)** c_f imaginary part

Figure 7.10: Pressure coefficient (c_p) and skin friction coefficient (c_f) for $\lambda = 3.30$.

but only the solutions for $\lambda = 3.30$ are reported in Fig. 7.10 because the results of $\lambda = 2.88$ present a similar behaviour. The subplots in Fig. 7.10 confirm that 32 complex harmonics are necessary to have a sufficient accuracy to reproduce the c_p and c_f coefficients obtained with the TD solver.

However a further comparison between TD and HB analyses has been done in terms of power coefficient C_p. After the choice of HB 32 as a reference number of complex harmonics to reproduce the TD results, one HB 32 simulation for each VAWT operating condition analysed has been performed. In this way, it is possible to reproduce the entire power curve and compare that with the TD power curve which has been validated with experimental data and compared with FLUENT solution in *Chapter 5*. Fig. 7.11 reports the comparison between HB and TD power curves for all operating conditions of the Darrieus wind turbine chosen. The comparison shows little differences between the two curves so the HB solver can be used successfully also for strong non-linear problem like VAWT.

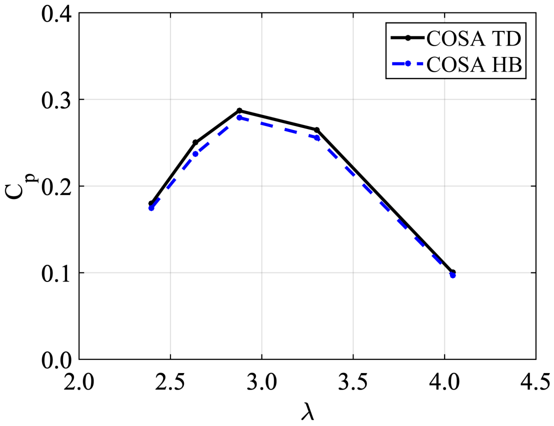

Figure 7.11: Comparison between HB and TD power curves.

7.2.2 HB speed-ups and MG overheads

All HB analyses for $\lambda = 2.88$ and $\lambda = 3.30$ have been run for 8,000 MG iterations, since this was the minimum value required for the convergence of all harmonics of all force components. For each physical time-step of both TD 720 calculations, it has been used 200 MG iterations as this value has been sufficient for the convergence of all forces and residuals. In order to reduce the periodicity error below the 0.1%, for the two λ analysed, COSA required approximately thirty revolutions starting from a freestream initial condition. The number of periods required to achieve a periodic solution using the TD solver depends on the λ. For lower tip speed ratios about forty revolutions are required to achieve a periodicity error close to 0.1%. The HB overhead and the HB speed-ups parameter computed with respect to the wallclock time of the TD 720 simulations, for λ equal to 2.88 and 3.30 for all N_H values are reported in Table 7.3 and Table 7.4.

It is seen that the HB 32 analysis allows an estimate of the time-dependent solution 4.5 times faster than TD counterpart. Also in the Table 7.3 and 7.4 the speed-ups

Table 7.3: Acceleration factors of HB analyses with respect to TD analysis for $\lambda = 2.88$.

	HB 8	HB 16	HB 32	HB 64	TD 720	steady
C_{MG}	1.41	1.70	1.89	2.16	1.02	1.00
speed-up	22.92	9.88	4.50	1.97	1.00	

Table 7.4: Acceleration factors of HB analyses with respect to TD analysis for $\lambda = 3.30$.

	HB 8	HB 16	HB 32	HB 64	TD 720	steady
C_{MG}	1.41	1.69	1.88	2.15	1.02	1.00
speed-up	22.91	9.86	4.51	1.97	1.00	

corresponding to the steady calculations are empty because the steady calculations do not represent a term of comparison for the HB and TD approaches.

7.3 Conclusion

As shown in the preceding sections, COSA HB approach was applied to two different non linear periodic flow problems and for the first time to study VAWT rotors. The results reported in this chapter have shown that COSA HB solver can lead to a substantial reduction of the computational cost with respect to the TD counterpart. In particular, the effectiveness of the developed technology has been demonstrated by using the 2D HB to determine the periodic aerodynamic loads acting on two blade sections of a 164 m-diameter HAWT rotor in yawed wind conditions. Presented results highlight that the turbulent HB solver can compute the calculation 10 times faster with respect to its TD counterpart. The HB approach was also used for strong non linear problems like VAWT. In this case, the HB speed-ups is lower than that obtained for HAWT case, but it can be increased again to one order of magnitude using the hybrid parallelisation implemented in COSA and presented in *Chapter 4*, which allows the CFD code to use more computational resources with respect to TD technology which use only the MPI parallelisation. From the point of view of the accuracy, the HB solutions of the HAWT application does not show differences between the reference HB and TD results, highlighting a very good agreement also in terms of pressure coefficient and skin friction coefficient. The HB results of the VAWT test case, instead, show larger discrepancies in term of tangential force, normal force and torque coefficients, even using a large number of complex harmonics. But, for engineering applications the HB solution is still acceptable because it follows the trend of the TD result and the power coefficient computed considering the mean value of the torque coefficient presents negligible differences compared with the power coefficient obtained by the TD approach.

Chapter 8

Conclusions

The numerical models underlying the implementation of a novel turbulent HB compressible solver of the RANS equations coupled to Menter's SST turbulence model have been presented. The computational benefits achievable by using the Harmonic Balance solver have been successfully demonstrated analysing the complex flow behaviour of wind energy devices like horizontal and vertical axis wind turbines.

8.1 HAWT conclusions

An accurate flow analysis of typical inboard and outboard blade sections of a 8 MW HAWT in yawed wind regime has been presented. The comparative assessment of the turbulent HB and TD MG solvers in terms of time-accuracy and computational performance highlights that the former solver yields the sought periodic flow with an accuracy comparable to that of the time-grid independent solution of the latter solver. The comparative assessment is based on the analysis of the unsteady flow field past the 30% and 85% blade sections of a 164 m-diameter HAWT rotor in a 45^o 13 m/s yawed wind. Significant hysteresis cycles of all forces acting on the blade section at 30% are observed, with variations of the axial, tangential force and blade torsional load coefficients of about 22%, 15% and 40% of their mean values, respectively. For the section at 85% blade length, it is also observed that the variations of the axial force, tangential force and blade torsional load loops point to periodic variations of about 3%, 15% and 20% of their mean values, respectively, highlighting a smaller hysteresis cycles of thrust and blade torsional loads caused by the yawed wind regime on this blade section. Due to the use of 2D simulations, these estimates do not account for aerodynamic effects associated with the omitted radial velocity components. This may affect the estimates above, but it is unlikely to significantly modify the physical findings of this study. The HB solutions at section 30% show that the HB approach provides a solution comparable to that obtained by the TD counterparts, using 5 complex harmonics. In this case the HB solver is more than 7 times faster than TD. On the other side, the results of section 85%, needs only 3 complex harmonics requiring 1/10 of the run-time of the corresponding TD simulation. These results demonstrate the HB efficiency for solving the turbulent periodic flow past the HAWT blades.

8.2 VAWT conclusions

The capabilities of the compressible density-based RANS/SST COSA have been also applied to predict the turbulent unsteady flow past the rotor of a vertical axis wind turbine rotor. The results of a 2D unsteady flow analyses were proposed for a classical NACA0021 three-bladed Darrieus rotor. Solution sensitivity analyses to crucial parameters, such as spatial and temporal grid refinement and distance of the farfield boundary from the rotor have been presented. Flow field characteristics were investigated for a wide range of operating conditions allowing a comparison between rotor operation at design and off-design tip speed ratios. Vorticity magnitude contours have been used as an effective means for depicting the flow structures generated during the turbine operating conditions and to investigate the wakes interactions between rotor blades. The 2D turbulent solutions have also been validated by comparing torque profile, power coefficients and small-scale flow detail (blade pressure and viscous stress) with numerical solutions obtained by the state-of-the-art TD FLUENT showing an excellent agreement for all λ analysed. This is a remarkable outcome, given the substantial differences of the COSA and FLUENT approaches, such as a significantly different formulation of the governing equations (pressure based in FLUENT and density-based in COSA) and the use of a sliding surface approach with stationary and rotating subdomains in FLUENT, and the use of the arbitrary Lagrangian-Eulerian approach over the entire physical domain in COSA. In addition, experimental measurements of the 3D model of the reference Darrieus turbine with blades connections at 0.5 c, have been compared with a consistent 2D model of FLUENT showing a good agreement also in this case.

The use of the HB method for VAWT has been innovative since it was the first application on this type of renewable energy device characterised by a strong nonlinearity. It has been shown that the COSA HB solver needs 32 or more complex harmonics to reach a solution comparable to the TD. The accuracy of the HB 32 solution in terms of torque coefficient is not accurate as for the HAWT test case, but from the point of view of engineering problems it is acceptable since it does not give large differences in terms of power coefficient. Furthermore, the speed-ups computed accounting the computational costs of HB 32 and TD simulations, is about 4.5 which is not very high, but it can be increased by means of hybrid parallelisation to about 8 using two OpenMP threads for each MPI process.

8.3 Future work

Future extensions of this work include the demonstration of the 2D turbulent flow capabilities of COSA HB solver for more applications like helicopter rotor flows, propfan engines open rotor flows, vibrating aircraft wings, etc. On the computational side, a further improvement of the HB performances, can be achieved using the fast Fourier transforms to compute the harmonic balance source term. In addition, the three dimensional extension of COSA has been developed in the recent months, so the demonstration of the 3D turbulent flow capabilities is another future task. A substantially larger reduction of computational times is expected also for the 3D turbulent flows. In these circumstances the benefits of using the HB technology could be even higher.

Chapter 9

Appendices

9.1 A) Betz's law

The Betz model used to calculate the maximum power that can be extracted from the wind assumes a control volume in which the control volume boundaries are the surface of a stream tube and two cross-sections of the stream tube. The turbine is represented by a uniform "actuator disc" which creates a discontinuity of pressure in the stream tube of air flowing through it. A schematic view of the actuator disc model can be seen in the Fig. 9.1. Applying the conservation of linear momentum to the control volume enclosing the whole system, one can find the net force on the contents of the control volume. That force is equal and opposite to the thrust, T, which is the force exerted by the wind on the turbine. From the conservation of linear momentum for a

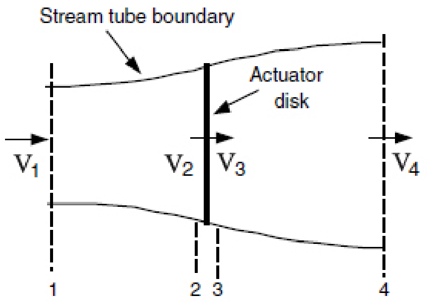

Figure 9.1: Actuator disc model of a wind turbine; V, mean air velocity; 1, 2, 3, and 4 indicate locations

one-dimensional, incompressible, time-invariant flow, the thrust is equal and opposite to the rate of change of momentum of the air stream:

$$T = V_1(\rho AV)_1 - V_4(\rho AV)_4 \tag{9.1}$$

where ρ is the air density, A is the cross-sectional area, V is the air velocity, and the subscripts indicate values at numbered cross-sections in Fig. 9.1. For steady state flow, $(\rho AV)_1 = (\rho AV)_4 = \dot{m}$, where $\dot{m}$ is the mass flow rate. Therefore:

$$T = \dot{m}(V_1 - V_4) \tag{9.2}$$

The thrust is positive so the velocity behind the rotor, V_4, is less than the free stream velocity, V_1. No work is done on either side of the turbine rotor. Thus the Bernoulli's equation, which expresses the conservation of energy for an incompressible fluid, can be used in the two control volumes on either side of the actuator disc. In the stream tube upstream of the disc:

$$p_1 + \frac{1}{2}\rho V_1^2 = p_2 + \frac{1}{2}\rho V_2^2 \tag{9.3}$$

In the stream tube downstream of the disc:

$$p_3 + \frac{1}{2}\rho V_3^2 = p_4 + \frac{1}{2}\rho V_4^2 \tag{9.4}$$

where it is assumed that the far upstream and far downstream pressures are equal ($p_1 = p_4$) and that the velocity across the disc remains the same ($V_2 = V_3$). The thrust can also be expressed as the net sum of the forces on each side of the actuator disc:

$$T = A_2(p_2 - p_3) \tag{9.5}$$

If one solves for $(p_2 - p_3)$ using Eq. (9.3) and (9.4) and substitutes that into Eq. (9.5), one obtains:

$$T = \frac{1}{2}\rho A_2(V_1^2 - V_4^2) \tag{9.6}$$

Equating the thrust values from Eq. (9.2) and (9.6) and recognizing that the mass flow rate is also $\rho A_2 V_2$, one obtains:

$$V_2 = \frac{V_1 + V_4}{2} \tag{9.7}$$

Thus, the wind velocity at the rotor plane, using this simple model, is the average of the upstream and downstream wind speeds. If one defines the axial induction factor,

a, as the fractional decrease in wind velocity between the free stream and the rotor plane, then

$$a = \frac{V_1 - V_2}{V_1} \tag{9.8}$$

$$V_2 = V_1(1 - a) \tag{9.9}$$

$$V_4 = V_1(1 - 2a) \tag{9.10}$$

The quantity $V_1 a$ is often referred to as the induced velocity at the rotor, in which case the velocity of the wind at the rotor is a combination of the free stream velocity and the induced wind velocity. As the axial induction factor increases from 0, the wind speed behind the rotor slows more and more. If $a = 1/2$, the wind has slowed to zero velocity behind the rotor and this simple theory is no longer applicable. The output power P, is equal to the thrust times the velocity at the disc:

$$P = \frac{1}{2}\rho A_2(V_1^2 - V_4^2)V_2 = \frac{1}{2}\rho A_2 V_2(V_1 + V_4)(V_1 - V_4) \tag{9.11}$$

Substituting for V_2 and V_4 from Eq. (9.9) and (9.10) gives:

$$P = \frac{1}{2}\rho A V^3 4a(1 - a)^2 \tag{9.12}$$

where the control volume area at the rotor, A_2, is replaced by A, the rotor area, and the free stream velocity V_1 is replaced by V. Wind turbine rotor performance is usually characterised by its power coefficient, C_p:

$$C_p = \frac{P}{1/2\rho V^3 A} = \frac{\textit{Rotor power}}{\textit{Power in the wind}} \tag{9.13}$$

The non-dimensional power coefficient represents the fraction of the power in the wind that is extracted by the rotor. For Eq. (9.12), the power coefficient is:

$$C_p = 4a(1 - a)^2 \tag{9.14}$$

The maximum theoretically possible rotor power coefficient C_p is determined by taking the derivative of the power coefficient (Eq. (9.14)) with respect to a and setting it equal to zero, yielding $a = 1/3$. Thus:

$$C_{p,max} = 16/27 = 0.5926 \tag{9.15}$$

when a=1/3. For this case, the flow through the disc corresponds to a stream tube with an upstream cross-sectional area of 2/3 the disc area that expands to twice the disc area downstream. This result indicates that, if an ideal rotor were designed and operated such that the wind speed at the rotor were 2/3 of the free stream wind speed, then it would be operating at the point of maximum power production. Furthermore, given the basic laws of physics, this is the maximum power possible. In practice, some effects like rotation of the wake behind the rotor, non-zero aerodynamic drag and tip losses, lead to a decrease in the maximum achievable C_p. From Eq. (9.6), (9.9) and (9.10), the axial thrust on the disc is:

$$T = \frac{1}{2}\rho A V^2 \left[4a(1-a)\right] \tag{9.16}$$

Similarly to the power, the thrust on a wind turbine can be characterised by a non-dimensional thrust coefficient:

$$C_T = \frac{T}{1/2\rho V^2 A} = \frac{\textit{Thrust force}}{\textit{Dynamic force}} \tag{9.17}$$

From Eq. (9.16), the thrust coefficient for an ideal wind turbine is equal to $4a(1-a)$. C_T has a maximum of 1.0 when $a = 0.5$ and the downstream velocity is zero. At maximum power output ($a = 1/3$), C_T has a value of 8/9. A graph of the power and thrust coefficients for an ideal Betz turbine and the non-dimensionalised downstream wind speed are illustrated in Fig. 9.2. V is the velocity of undisturbed air, V_4 is the air velocity behind the rotor, C_p is the power coefficient and C_T is the thrust coefficient.

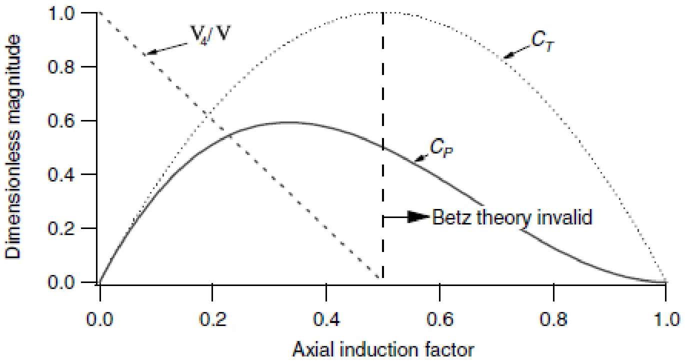

Figure 9.2: Operating parameters for a Betz turbine

9.2 B) $k - \omega$ turbulence model of Wilcox

The $k - \omega$ model is one of the most commonly used turbulence models. It is a two equations model, that means, it includes two extra transport equations to represent the turbulent properties of the flow. This allows to account for history effects like convection and diffusion of turbulent energy. The first transported variable is turbulent kinetic energy, k, that determines the energy in the turbulence. The second is the specific dissipation, ω that is the variable that determines the scale of the turbulence. The basic equations of the version of the $k - \omega$ turbulence model reported by Wilcox [155], are:

$$\frac{\partial}{\partial t}(\rho k) + \frac{\partial}{\partial x_j}(\rho u_j k) = \tau_{ij}^F \frac{\partial u_i}{\partial x_j} - \beta^* \rho \omega k + \frac{\partial}{\partial x_j}\left[(\mu + \sigma_k \mu_T)\frac{\partial k}{\partial x_j}\right] \tag{9.18}$$

$$\frac{\partial}{\partial t}(\rho \omega) + \frac{\partial}{\partial x_j}(\rho u_j \omega) = \frac{\gamma \rho}{\mu_T}\tau_{ij}^F \frac{\partial u_i}{\partial x_j} - \beta \rho \omega^2 + \frac{\partial}{\partial x_j}\left[(\mu + \sigma_\omega \mu_T)\frac{\partial \omega}{\partial x_j}\right] \tag{9.19}$$

and the turbulent eddy viscosity is computed from:

$$\mu_T = \frac{\rho k}{\omega} \tag{9.20}$$

In the Eq. (9.18) and (9.19), one can see the production terms of k and ω:

$$P_k = \tau_{ij}^F \frac{\partial u_i}{\partial x_j}, \qquad P_\omega = \frac{\gamma \rho}{\mu_T}\tau_{ij}^F \frac{\partial u_i}{\partial x_j} \tag{9.21}$$

and the destruction terms of the k and ω:

$$D_k = \beta^* \rho \omega k, \qquad D_\omega = \beta \rho \omega^2 \tag{9.22}$$

The production terms can be also written in the form:

$$P_k = \mu_T P_d - \frac{2}{3}(\nabla \cdot u)\rho k \tag{9.23}$$

$$P_\omega = \gamma \rho P_d - \frac{\gamma \rho}{\mu_T}\frac{2}{3}(\nabla \cdot u)\rho k \tag{9.24}$$

where $P_d = 2\left(S^* - \frac{1}{3}\nabla \cdot u\right)\nabla u$ and $S^* = \frac{1}{2}(\nabla \cdot u + \nabla \cdot u')$.

The production and the destruction terms of each variable are the so called *source terms*. So the *source terms* of k has a production term $\mu_T P_d$ that is always positive, a term which depends from $\nabla \cdot u$ that can be positive or negative depending on the sign of $\nabla \cdot u$ and a destruction term D_k which is always negative. The source term of ω-equation also has a term which is always positive (production term proportional to P_d), a term which is positive or negative depending on the sign of $\nabla \cdot u$ and a destruction term D_ω which is always negative. The identification of positive and negative source terms is very important, due to the different numerical treatment that can be adopted for positive and negative source terms that improve the convergence rate of the solution. The value of the constant appearing in the $k - \omega$ equations are:

$$set_1 : [\beta \quad \beta^* \quad \gamma \quad \sigma_k \quad \sigma_\omega] = [0.075 \quad 0.090 \quad 0.555 \quad 0.500 \quad 0.500] \tag{9.25}$$

9.3 C) Integration methods

Several integration methods as Runge-Kutta, Matlab function FSOLVE, COSA FERK and COSA SIRK, have been implemented in a Matlab code to solve the system of nonlinear ODEs (9.26) presented in *Chapter 4* and used to demonstrate the differences between the classical HB integration and the HDHB integration.

$$\begin{cases} \dot{x} = y - z^3 + 1 + Fsin(\omega t) \\ \dot{y} = 0.1z + 1 - y \cdot z \\ \dot{z} = 2x - z^2 + 0.5 \end{cases} \tag{9.26}$$

The main script is defined as follow. The variable *nharms* define the number of complex harmonics to be used to solve accurately the problem with HB methods.

```
%———————————————————————————————————————————————————————————————
%   Integration methods
%———————————————————————————————————————————————————————————————

    [f0,omega,T,npde] = getprop_mysys;

    toler = 1d-14;
    nharms = 8;

%   TD Runge-Kutta integration
    hist='no'; nperiod = 20; int_per_period = 128;
    t_start = 0; t_end = nperiod*T;
    ntime = nperiod*int_per_period;
    deltat = (t_end-t_start)/ntime;
    y0(1)=0; y0(2)=0; y0(3)=0;
    [t_rk,y_rk] = urk(f0,omega,t_start, ...
                      t_end,y0,hist,deltat,ntime);
```

```
%   HB integration with COSA FERK solver
    uH0 = zeros(npde*(1+2*nharms),1);
    ncycle=1500;
    [uH_ferk,rms_hb_ferk] = hb_ferk(nharms, ...
                   npde,f0,omega,uH0,deltat,ncycle);

%   HB integration with COSA SIRK solver
    uH0 = zeros(npde*(1+2*nharms),1);
    ncycle=1500;
    [uH_sirk,rms_hb_sirk] = hb_sirk(nharms, ...
                   npde,f0,omega,uH0,deltat,ncycle);

%   HB integration with FSOLVE
    uH0 = uH_ferk;
    [uH,fun,exflag] = fsolve(@(uH)mysys_hdhb(uH,omega, ...
    f0,nharms),uH0,optimset('TolFun',toler, ...
    'MaxFunEvals',1e10));
```

The RK function is defined as:

```
%-------------------------------------------------------------
%   Performs ncycle iterations of 4-step RK integration
%-------------------------------------------------------------

    function[t,y] = urk(f0,omega,t_start,t_end,y0, ...
                                        hist,delta,ncycle)
    nstep = 4;
    alfa = [1/2 1/2 1 1];
    beta = [1/6 1/3 1/3 1/6];
    gamma = [0 1/2 1/2 1];
    t(1)   = t_start;
    y(1,:) = y0;

    for ic=1:ncycle
      t(ic+1) = t_start + ic*delta;
      y_old = y(ic,:)';
      y_new = y(ic,:)';
      res2 = zeros(size(y,2),1);
      for ns=1:nstep
        tloc = t(ic) + delta*gamma(ns);
        res1 = mysys_res(tloc,y_new,f0,omega);
        res2 =res2 + beta(ns)*res1 ;
        if ns==nstep; res1=res2; end;
```

```
      y_new = y_old + delta*alfa(ns)*res1;
    end
    y(ic+1,:) = y_new';
    rms = norm([res1])/sqrt(length(y));
    if strcmp(hist,'yes')
      fprintf(fid,'%4.0f   %13.10f\n',ic,log10(rms));
      if rms < toler; break; end;
    end
  end

  t = t';
```

The function HB SIRK represent the semi-implict RK method described in the *Chapter 4* of this thesis.

```
%---------------------------------------------------------------------------
%   function HB SIRK
%---------------------------------------------------------------------------

  function [y_hb_rk,rms_hb] = ...
          hb_sirk(nh,npde,f0,omega,y0,deltat,ncycle)
  nstage = 4;
  alfa = [1/4 1/3 1/2 1];
  y = y0;

  D = d_HB(npde,nh,omega);

  for ic=1:ncycle
    y_old = y;
    for ns=1:nstage
      res1 = mysys_hdhb(y,omega,f0,nh);

      rhs3(1:2*nh+1,1) = (y_old(3:npde:npde*(2*nh+1)))+ ...
       deltat*alfa(ns)*(omega*D*y(3:npde:npde*(2*nh+1))- ...
       res1(3:npde:npde*(2*nh+1)));
       hbstb(1:2*nh+1,1:2*nh+1) = (eye(2*nh+1) + ...
       deltat*alfa(ns)*omega*D);
      ome(1:2*nh+1) = hbstb \ rhs3;
       y(3:npde:npde*(2*nh+1)) = ome;

      rhs2(1:2*nh+1,1) = (y_old(2:npde:npde*(2*nh+1)))+ ...
       deltat*alfa(ns)*(omega*D*y(2:npde:npde*(2*nh+1))- ...
       res1(2:npde:npde*(2*nh+1)));
       hbstb(1:2*nh+1,1:2*nh+1) = (eye(2*nh+1) + ...
```

```
         deltat*alfa(ns)*omega*D);
         k(1:2*nh+1) = hbstb \ rhs2;
         y(2:npde:npde*(2*nh+1)) = k;

        rhs1(1:2*nh+1,1) = (y_old(1:npde:npde*(2*nh+1)))+ ...
         deltat*alfa(ns)*(omega*D*y(1:npde:npde*(2*nh+1))- ...
         res1(1:npde:npde*(2*nh+1)));
         hbstb(1:2*nh+1,1:2*nh+1) = (eye(2*nh+1) + ...
         deltat*alfa(ns)*omega*D);
         u1(1:2*nh+1) = hbstb \ rhs1;
         y(1:npde:npde*(2*nh+1)) = u1;

      end
      rms_hb(ic) = norm([res1])/sqrt((2*nh+1)*npde);
    end

    y_hb_rk = y;
```

In the HB SIRK function is called another function $d_H B$ that compute the matrix D which appears in the HDHB approach.

```
%---------------------------------------------------------------------------
%     Matrix D
%---------------------------------------------------------------------------

     function D = d_HB(npde,nh,omega)

     dt                     = 2*pi/omega/(2*nh+1);
     t                      = (0:dt:2*nh*dt);
     harms                  = (1:nh)';
     E(1,1:2*nh+1)          = 0.5*ones(1,2*nh+1);
     E(2:2:2*nh,1:2*nh+1)   = cos(omega*kron(harms,t));
     E(3:2:2*nh+1,1:2*nh+1) = sin(omega*kron(harms,t));
     E                      = 2/(2*nh+1)*E;

     Ei(1:2*nh+1,1)         = ones(1,2*nh+1)';
     Ei(1:2*nh+1,2:2:2*nh)  = cos(omega*kron(harms,t))';
     Ei(1:2*nh+1,3:2:2*nh+1)= sin(omega*kron(harms,t))';

     A(2:2*nh+1,2:2*nh+1)   = kron(diag(1:nh),[0 1; -1 0]);
     D                      = Ei*A*E;
     end
```

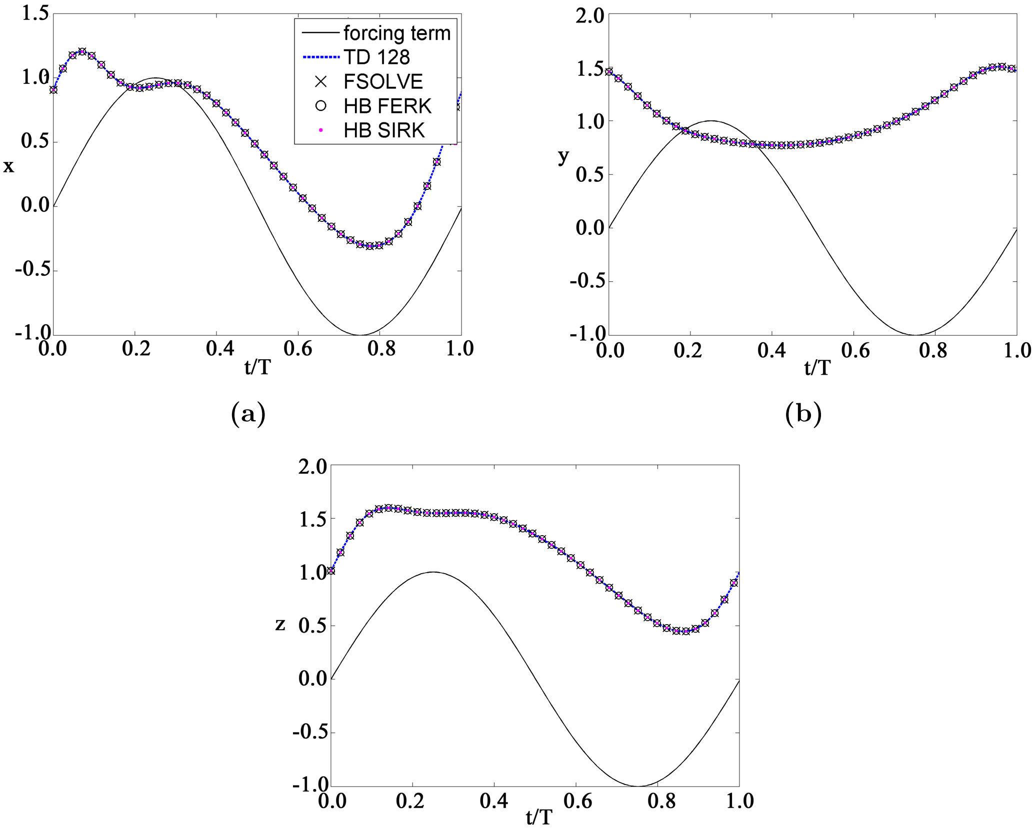

(a) **(b)**

(c)

Figure 9.3: Solutions of the system.

The solutions of System (9.26) are shown in the subplots of Fig. 9.3 (a), (b) and (c). The subplots report a sinusoidal curve that is the forcing term which appears in the first equation of the system. The others four curves are superimposed. They represent the solutions using the Runge-Kutta time marching, the Matlab function FSOLVE, COSA FERK and COSA SIRK methods. The figures highlight that 8 complex harmonics are needed to achieve an accurate solution.

9.4 D) LAPACK routines speed-up

LAPACK (Linear Algebra PACKage) [3] is a software library for numerical linear algebra. It provides routines for solving systems of linear equations and linear least squares, eigenvalue problems, and singular value decomposition. It also includes routines to implement the associated matrix factorisations such as LU, QR, Cholesky and Schur decomposition. LAPACK was originally written in FORTRAN 77, but moved to Fortran 90. Subroutines in LAPACK have a characteristic naming convention which makes the identifiers short but rather obscure. This was necessary as the first Fortran standards only supported identifiers up to six characters long, so the names had to be shortened to fit into this limit. A LAPACK subroutine name is in the form *pmmaaa*, where:

- *p* is a one-letter code denoting the type of numerical constants used. S, D stand for real floating point arithmetic respectively in single and double precision, while C and Z stand for complex arithmetic with respectively single and double precision. The newer version LAPACK95 use generic subroutines in order to overcome the need to explicitly specify the data type.
- *mm* is a two-letter code denoting the kind of matrix expected by the algorithm. The codes for the different kind of matrices are reported below; the actual data are stored in a different format depending on the specific kind; e.g., when the code DI is given, the subroutine expects a vector of length n containing the elements on the diagonal, while when the code GE is given, the subroutine expects an nn array containing the entries of the matrix.
- *aaa* is a one- to three-letter code describing the actual algorithm implemented in the subroutine, e.g. SV denotes a subroutine to solve linear system, while R denotes a rank-1 update.

For example, the subroutine to solve a linear system with a general (non-structured) matrix using real double-precision arithmetic is called DGESV.

The LAPACK routines that were used in the CFD code, are:

- DGETRF that computes an LU factorization of a general M-by-N matrix A using partial pivoting with row interchanges. The factorization has the form:

  $$A = P \cdot L \cdot U \tag{9.27}$$

  where P is a permutation matrix, L is lower triangular with unit diagonal elements and U is upper triangular matrix.

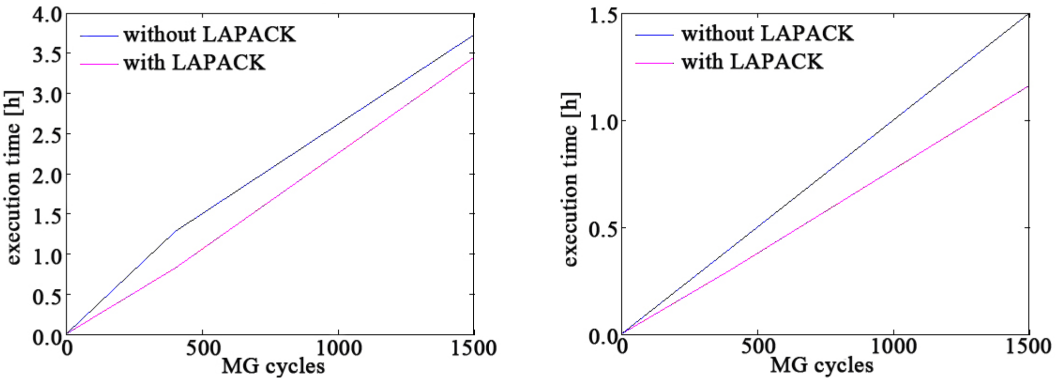

(a) serial code **(b)** parallel code

Figure 9.4: CPU-time comparison using COSA HB solver with $N_H = 7$.

- DGETRS that solves a system of linear equations

$$A \cdot X = B \tag{9.28}$$

with a general N-by-N matrix A using the LU factorization computed by DGETRF.

With the integration of the subroutines LAPACK inside COSA HB solver, was observed a significant speed-up. The reduction of the computational cost, varies between 35% and 70%. The figures show the CPU time of the HB solver with $N_H = 7$, to compute 1500 MG cycles using a test case characterised by inviscid flow over a single steady aerofoil NACA0012, with angle of attack equal to 5^o and Mach $= 0.1$ (Fig. 9.4 (a) and (b)) and the CPU time of the HB solver with $N_H = 5$, to compute 400 MG cycles using a different test case characterised by turbulent flow over a single steady aerofoil NACA0012, with angle of attack equal to 9^o, Mach $= 0.22$ and Reynolds $=$ 50,000 (Fig. 9.5 (a) and (b)). For the first test case, serial and parallel version of COSA using 2 MPI processes have been run. For the second case serial and parallel version of COSA using 16 MPI processes have been performed. All cases highlight a significant reduction of the computational cost when LAPACK routines are used.

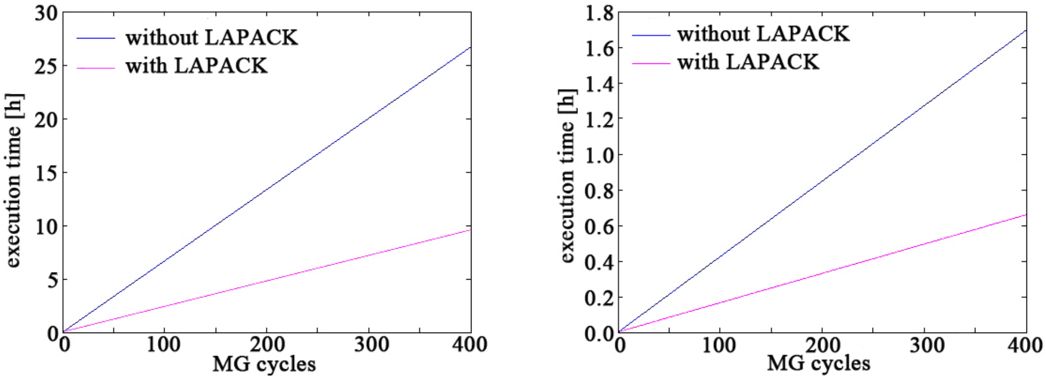

(a) serial code **(b)** parallel code

Figure 9.5: CPU-time comparison using COSA HB solver with $N_H = 5$.

References

[1] "Galleria del Vento Politecnico di Milano". URL `http://www.windtunnel.polimi.it`. 113

[2] "EPSRC". URL `http://gow.epsrc.ac.uk`. 57

[3] "LAPACK Linear Algebra PACKage". URL `http://www.netlib.org/lapack`. 87, 171

[4] "MPI Forum, MPI a message-passing interface standard.". URL `http://www.mpi-forum.org`. 88

[5] "MPI Forum, OpenMP architecture review board. OpenMP Fortran application program interface.". URL `http://www.openmp.org`. 88

[6] "Union of Concerned Scientists.". URL `http://www.ucsusa.org`. 4, 6

[7] "Where is the real innovation in wind energy?". URL `http://cleantechnica.com`. vi, 13

[8] "Renewable generation". URL `http://www.energy-uk.org.uk`. 2

[9] "Renewables 2015, Global Status Report". URL `http://www.ren21.net`. vi, 1, 2, 3

[10] "The Renewable Energy Website". URL `http://www.reuk.co.uk`. vi, 18

[11] "Wind Farm Realities". URL `http://www.windfarmrealities.org`. vi, 37

[12] Adaramola M.S. and Per-Age Krogstad. "Model test of a horizontal axis wind turbine in yawed condition". *European Offshore Wind 2009 Conference and Exhibition*, Stockholm, Sweden, 2009. 36

[13] Agren O., Berg M. and Leijon M. “A time-dependent potential flow theory for the aerodynamics of vertical axis wind turbines.”. *Journal of Applied Physics*, 97 (1049):13, 2005. 20

[14] Allet A., Hall .S. and Paraschivoiu I. “Numerical Simulation of Dynamic Stall Around an Airfoil in Darrieus Motion”. *ASME Journal Solar Energy Eng.*, 121: 69–76, 1999. 42

[15] Amet E., Matre T., Pellone C. and Achard J.L. “2D numerical simulations of blade-vortex interaction in a Darrieus turbine”. *Journal of Fluids Engineering*, 131(11):115, 2009. 96, 108

[16] Ansys, Inc. *“Fluent Theory Guide”*, 2013. 41, 102, 106

[17] Aprille T.J. and Trick T.N. “Steady-state analysis of nonlinear circuits with periodic inputs”. *Proc IEEE*, 60(1):108, 1972. 71

[18] Arnone A., Liou M.S. and Povinelli L.A. “Multigrid Time-Accurate Integration of Navier-Stokes Equations”. Technical Memorandum NASA TM 106373, ICOMP-93-37, Lewis Research Center, Cleveland, OH, USA, November 1993. 66

[19] Attar P.J., Dowell E.H., White J.R. and Thomas J.P. “Reduced Order Nonlinear System Identification Methodology”. *AIAA Journal*, 44(8):1895–1904, 2006. 71

[20] Balduzzi F., Bianchini A., Maleci R., Ferrara G. and Ferrari L. “Blade Design Criteria to Compensate the Flow Curvature Effects in H-Darrieus Wind Turbines”. *Journal of Turbomachinery*, 137(1), 2014. 107, 110

[21] Baldwin B.S. and Lomax H. “Thin Layer Approximation and Algebraic Model for Separated Turbulent Flows”. *AIAA Pap. 78-257*, 1978. 63

[22] Bauer P., de Haan S.W.H. and Dubois M.R. “Windenergy and offshore windparks: state of the art and trends.”. *10th International power electronics and motion control conference EPE-PEMC*, Cavtat and Dubrovnik, Croatia, 2002. 19

[23] Beran P. and Petit C. “A direct method for quantifying limit cycle oscillation response characteristics in the presence of uncertainties.”. *AIAA paper*, 2004. 71

[24] Biswas A. and Gupta R. “Unsteady aerodynamics of a twist bladed H-Darrieus rotor in low Reynolds number flow”. *Journal of Renewable and Sustainable Energy*, page 110, 2014. 38

[25] Blazek J. *“Computational Fluid Dynamics: Principles and Applications”*. Elsevier, 2001. 51

[26] Blazek J., Kroll N., Radespiel R. and Rossow C.C. “Upwind Implicit Residual Smoothing Method for Multi-Stage Schemes”. *AIAA*, pages 70–80, 1991. 63

[27] Blazek J., Rossow C.C., Kroll N. and Swanson R.C. “A Comparison of Several Implicit Residual Smoothing Methods in Combination with Multigrid”. *13th International Conference on Numerical Methods in Fluid Dynamics*, 414:386–390, 1993. 64

[28] Blevins R.D. *“Flow-Induced Vibrations”*. Van Nostrand Reinhold, 1990. 33

[29] Brahimi M., Allet A. and Paraschivoiu I. “Aerodynamic analysis models for vertical-axis wind turbines”. *International Journal of Rotating Machinery*, 2(1): 15–21, 1995. 91

[30] Brothers C. “Vertical axis wind turbines for cold climate applications.”. *Renewable Energy Technologies in Cold Climates*, Montreal, 1998. 19, 20

[31] Brown R.E. “Rotor wake modelling for flight dynamic simulation of helicopters.”. *AIAA Journal*, 38:57–63, 2000. 43

[32] Burton T., Jenkins N., Sharpe D. and Bossanyi E. *“Wind Energy Handbook, 2nd ed.”*. Wiley, 2011. vi, 9, 22

[33] Campobasso M.S. and Baba-Ahmadi M.H. “Ad-hoc Boundary Bonditions for CFD Analyses of Turbomachinery Problems with Strong Flow Gradients at Farfield Boundaries”. *ASME Journal of Turbomachinery*, 133(4), 2011. 57

[34] Campobasso M.S. and Baba-Ahmadi M.H. “Analysis of unsteady flows past horizontal axis wind turbine airfoils based on harmonic balance compressible Navier-Stokes equations with low-speed preconditioning”. *Journal of Turbomachinery*, 134(6), 2012. 57, 60, 72, 82

[35] Campobasso M.S. and Drofelnik J. "Compressible Navier-Stokes analysis of an oscillating wing in a powerextraction regime using efficient low-speed preconditioning". *Computers and Fluids*, 67:26–40, 2012. 60

[36] Campobasso M.S., Gigante F.A. and Drofelnik J. "Turbulent Unsteady Flow Analysis of Horizontal Axis Wind Turbine Airfoil Aerodynamics Based on the Harmonic Balance Reynolds-Averaged Navier-Stokes Equations". *Proc. of the ASME Turbo Expo*, Dusseldorf, Germany, June 16-20, 2014. 27, 57, 72

[37] Campobasso M.S., Piskopakis A. and Yan M. "Analysis of an Oscillating Wing in a Power-Extraction Regime Based on the Compressible Reynolds-Averaged Navier-Stokes Equations and the $k-\omega$ SST Turbulence Model". *in ASME Turbo Expo*, San Antonio, Texas, USA, 2013. 66

[38] Campobasso M.S., Piskopakis A., Drofelnik J. and Jackson A. "Turbulent Navier-Stokes Analysis of an Oscillating Wing in a Power-Extraction Regime using the Shear Stress Transport Turbulent Model". *Computers and Fluids*, 88:136–155, 2013. 57, 60, 67, 87

[39] Campobasso M.S., Yan M., Drofelnik J., Piskopakis A. and Caboni M. "Compressible Reynolds-Averaged Navier-Stokes Analysis of Wind Turbine Turbulent Flows Using a Fully Coupled Low-speed Preconditioned Multigrid Solver". *Proc. of the ASME Turbo Expo*, Dusseldorf, Germany, June 16-20, 2014. 57

[40] Cao L., Wang H., Ji Y., Wang Z. and Yuan W. "Analysis on the influence of rotational speed to aerodynamic performance of vertical axis wind turbine". *International Conference on Advances in Computational Modeling and Simulation*, 31:245–250, 2012. vi, 38, 39

[41] Carlin P.W., Laxson A.S. and Muljadi E.B. "The history and state of the art of variable-speed wind turbine technology.". *National Renewable Energy Laboratory, Technical report: NREL/TP-28607*, 2001. 17

[42] Chiras D. *"Wind Power Basics"*. New Society Publisher, Canada, 2010. 17

[43] Choudhry A., Arjomandi M. and Kelso R. "Horizontal axis wind turbine dynamic stall predictions based on wind speed and direction variability". *Journal of Power and Energy*, 227(3):338–351, 2013. 34

[44] Da Ronch A., McCracken A., Badcock K., Widhalm M. and Campobasso M.S. "Linear Frequency Domain and Harmonic Balance Predictions of Dynamic Derivatives". *Journal of Aircraft*, 50(3):694–707, 2013. 27, 71

[45] Danao L.A., Edwards J., Eboibi O. and Howell R. "The Performance of a Vertical Axis Wind Turbine in Fluctuating Wind - A Numerical Study". *Proceedings of the World Congress on Engineering*, London, UK, 2013. 38

[46] Darrieus G.J.M. "Turbine having its rotating shaft transverse to the flow of the current.". *US Patent no. 1.835.018*, 1931. 17

[47] de Vries O. *"Fluid Dynamic Aspects of Wind Energy Conversion."*. Advisory Group for Aerospace Research and Development, North Atlantic Treaty Organization, 1979. 21

[48] Del Campo V., Ragni D., Micallef D., Diez F.J. and Simo Ferreira J.C. "Estimation of loads on a horizontal axis wind turbine operating in yawed flow conditions". *Wind Energy*, 2014. 35

[49] DNV/Riso. *"Guidelines for Design of Wind Turbines, 2nd Edition"*. Det Norske Veritas and Ris National Laboratory, Denmark, 2002. 14

[50] Douglas C.C. "Multigrid Methods in Science and Engineering". *IEEE Computational Science and Engineering*, pages 55–68, 1996. 64

[51] Edenhofer O., Pichs-Madruga R., Sokona Y., Seyboth K., Kadner S., Zwickel T., Eickemeier P., Hansen G., Schlmer S., Von Stechow C. and Matschoss P. *"Renewable Energy Sources and Climate Change Mitigation"*. Cambridge University Press, 2012. 4, 7

[52] Ekaterinaris J.A. and Platzer M.F. "Computational prediction of airfoil dynamic stall". *Progress in Aerospace Sciences*, 33(11), 1998. 91

[53] Ekici K. and Hall K.C. "Nonlinear analysis of unsteady flows in multistage turbomachines using harmonic balance.". *AIAA Journal*, 45(5):1047–1057, 2007. 71

[54] Eliasson P. and Wallin S. “A Positive Multigrid Scheme for Computations with Two-Equation Turbulence Models”. *in ECCOMAS, Barcelona*, 2000. 63

[55] Elliott D.L. and Cadogan J.B. “Effects of wind shear and turbulence on wind turbine power curves”. *Proceedings of the European Community Wind Energy Conference and Exhibition*, 1990. 37

[56] Elman H., Howle V.E., Shadid J. and Tuminaro R. “A parallel block multi-level preconditioner for the 3D incompressible Navier-Stokes equations.”. *Journal of Computational Physics*, 187:504–523, 2003. 89

[57] Eriksson S., Bernhoff H. and Leijon M. “Evaluation of different turbine concepts for wind power”. *Renewable and Sustainable Energy Reviews*, 12:14191434, 2006. 19

[58] German J. “The end of an era: Sandias 17-meter vertical axis wind turbine comes down after two decades.”. *Sandia Lab News*, 1997. 17

[59] Glasgow J.C., Miller D.R. and Corrigan R.D. “Comparison of Upwind and Downwind Rotor Operations of the DOE/MASA 100-kW Mod-0 Wind Turbine”. *Proceedings of the 2nd DOE/NASA Wind Turbine Dynamics Workshop*, Cleveland, Ohio, 1981. 30

[60] Glauert H. *“Airplane Propellers”*. Aerodynamic Theory (Ed. W. F. Durand), Berlin, 1935. 21

[61] Gomez-Iradi S., Steijl R. and Barakos G.N. “Development and Validation of a CFD Technique for the Aerodynamic Analysis of HAWT”. *Journal of Solar Energy Engineering*, 31(8), 2009. 124

[62] Gopinath A.K. and Jameson A. “Time Spactral Method for Periodic Unsteady Computations over Two- and Three- Dimentional Bodies”. *in AIAA Aerospace Meeting*, Reno, Nevada, 2005. 71

[63] Gopinath A.K., Beran P.S., Jameson A. “Comparative analysis of computational methods for limit-cycle oscillations.”. *AIAA Journal*, 2006. 71

[64] Hagen T.R., Reiso M. and Muskulus M. "Numerical Analysis of Turbulent Flow Past a Truss Tower for Offshore Downwind Turbines". *Proceedings of the 21st International Offshore (Ocean) and Polar Engineering Conference, Maui, HI*, 7: 319–326, 2011. 30, 33

[65] Hall K.C., Thomas J.P. and Clark W.S. "Computation of Unsteady Nonlinear Flows in Cascades Using a Harmonic Balance Technique". *AIAA Journal*, 40(5): 879–886, 2002. 27, 69, 71

[66] Hassan D. and Sicot F. "A Time-Domain Harmonic Balance Method for Dynamic Derivatives Predictions". *in AIAA Aerospace Meeting*, Orlando, Florida, 2011. 71

[67] Hau E. *"Wind Turbines: Fundamentals, Technologies, Application, Economics. 2-nd Ed."*. Springer, 2005, . 36, 37

[68] Hau E. *"Wind Turbines: Fundamentals, Technologies, Application, Economics. Edition 2."*. Springer Science and Business Media, 2005, . 6

[69] Hirsch C. *"Numerical Computation of Internal and External Flows"*. John Wiley and Sons, Brussels, Belgium, 1994. 46

[70] Honrubia A., Vigueras-Rodrguez A., Gomez Lazaro E. and Rodrguez-Sanchez D. "The influence of wind shear in wind turbine power estimation.". *European Wind Energy Conference*, 2010. 37

[71] Howell R., Qin N., Edwards J. and Durrani N. "Wind Tunnel and Numerical Study of a Small Vertical Axis Wind Turbine". *Renewable Energy*, 35(2):412–422, 2010. 108

[72] Jackson A. and Campobasso M.S. "Shared-memory, Distributed-memory and Mixed-mode Parallelization of a CFD Simulation Code". *Computer Science Research and Development*, 26(3), 2011. 88

[73] Jackson A. and Campobasso M.S. "Optimised Hybrid Parallelisation of a CFD code on Many Core architectures". *15th International Symposium on Symbolic and Numeric Algorithms for Scientific Computing*, Timisoara, Romania, 2013. 88

[74] Jackson A., Campobasso M.S. and Baba-Ahmadi M.H. “On the Parallelization of a Harmonic Balance Compressible Navier-Stokes Solver for Wind Turbine Aerodynamics”. *ASME paper GT2011-45306*, Vancouver, British Columbia, Canada, 2011. 60, 88

[75] Jameson A. “Time Dependent Calculations Using Multigrid, with Applications to Unsteady Flows Past Airfoils and Wings”. *AIAA paper*, 1991, Honolulu, Hawaii. 66

[76] Jameson A. and Baker T.J. “Solution of the Euler Equations for Complex Configurations”. *in 6-th AIAA computational fluid*, Danvers, Massachusetts, 1983. 63

[77] Jameson A., Schmidt W. and Turkel E. “Numerical Solution of the Euler Equations by Finite Volume Methods Using Runge-Kutta Time-Stepping Schemes”. *in AIAA 14th Fluid and Plasma Dynamics*, Palo Alto, 1981. 63

[78] Johnson G.L. *“Wind Energy System”*. Prentice Hall, Manhattan, KS, 2001. 22, 23

[79] Jones W. and Launder B. “The Calculation of Low-Reynolds-Number Phenomena with a Two-Equation Model for Turbulence”. *International Journal of Heat and Mass Transfer*, 16:1119–1130, 1973. 52, 53

[80] Jonkman J., Butterfield S., Musial W. and Scott G. “Definition of a 5-MW Reference Wind Turbine for Offshore System Development, Tech. Rep. NREL/TP-500-38060”. *National Renewable Energy Laboratory, Golden, CO, 2009*, 2009. 32

[81] Kim Y., Noah S. and Choi Y. “Periodic response of multi-disk rotors with bearing clearances.”. *Journal of Sound and Vibration*, 144(3):381, 1991. 71

[82] Knupp P. and Steinberg S. *“Fundamentals of Grid Generation”*. 1993. 59

[83] Kryloff N. and Bogoliuboff N. “Introduction to nonlinear mechanics”. *Princeton University Press*, Princeton, NJ, 1947. 71

[84] Le Pape A. and Gleize V. "Improved Navier-Stokes Computations of a Stall-regulated Wind Turbine Using Low Mach Number Preconditioning". AIAA paper 2006-1502, 2006. 44th AIAA Aerospace Sciences Meeting and Exhibit, Reno, Nevada. 124

[85] Lee S. and Choi D.W. "On Coupling the Reynolds-Averaged NavierStokes Equations with Two-Equation Turbulence Model Equations". *J. for Numerical Methods in Fluids*, 50(2):165–197, 2006. 63

[86] Leer B.V. "Towards the Ultimate Conservative Difference Scheme. A new Approach to Numerican Convection". *Journal of Computational Physics*, 23:276–299, 1977. 61

[87] Lin F.B. and Sotiropoulos F. "Strongly-Coupled Multigrid Method for 3-D incompressible Flows Using Near-Wall Turbulence Closures". *Journal of Fluids Engineering*, 119:314–324, 1997. 54, 63

[88] Liu F. and Zheng X. "Staggered Finite Volume Scheme for Solving Cascade Flow with a $k-\omega$ Turbulence Model". *AIAA Journal*, 32(8):1589–1597, 1994. 63

[89] Liu F. and Zheng X. "A Strongly Coupled Time-Marching Method for Solving the Navier-Stokes $k-\omega$ Turbulence Model Equations with Multigrid". *Journal of Computational Physics*, 1996. 54, 63, 64, 83

[90] Liu L., Thomas J., Dowell E., Attar P. and Hall K. "A comparison of classical and high dimensional harmonic balance approaches for a Duffing oscillator". *Journal of Computational Physics*, 215(1):298–320, 2006. 79

[91] Loland K.M. "Wind Turbine in Yawed Operation". *Master thesis of Science in Energy and Environment, Norwegian University of Science and Technology,*, 2011. vi, 35

[92] Long H. and Moe G. "Truss Type Towers in Offshore Wind Turbines". *Proceedings of European Offshore Wind Conference (EOW 2007)*, Berlin, 2007. 30, 33

[93] Mahmoud N.H., El-Haroun A.A., Wahba E. and Nasef M.H. "An experimental study on improvement of Savonius rotor performance". *Alexandria Engineering Journal*, 51:19–25, 2012. 40

[94] Malael I., Dumitrescu H. and Cardos V. "Numerical Simulation of Vertical Axis Wind Turbine at Low Speed Ratios". *Global Journal of Researches in Engineering: Numerical Methods*, 14(1):920, 2014. 38

[95] Manwell J.F., McGowan J.G. and Rogers A.L. *"Wind energy explained: Theory, Design and Application, 2nd Edition"*. Wiley, Chichester, West Sussex (UK), 2009. vi, 9, 13, 23, 24, 36

[96] Marsh G. and Peace S. "Tilting at windmills: utility-scale VAWTs: towards 10MW and beyond?". *Refocus*, 6(5):3742, 2005. 20

[97] Mays I.D. and Morgan C.A. "The 500kW VAWT 850 demonstration project.". *Proceedings 1989 European wind energy conference*, Glasgow, Scotland, 1989. 18

[98] McMullen M., Jameson A. and Alonso J. "Acceleration of convergence to a periodic steady state in turbomachinery flows.". *AIAA Journal*, 2001. 71

[99] Melson N.D., Sanetrik M.D. and Atkins H.L. "Time-Accurate Navier-Stokes Calculations with Multigrid Acceleration". *Proc. 6th Copper Mountain Conference on Multigrid Methods*, Orlando, France, 1993. 65, 66

[100] Menter F.R. "Zonal Two Equation $k - \omega$ Turbulence Models for Aerodynamic Flows". *AIAA Journal*, 93(2906), 1993. 54, 55

[101] Menter F.R. "Two-Equation Turbulence-Models for Engineering Applications". *AIAA Journal*, 32(8):1598–1605, 1994. 26, 52, 57, 101, 107

[102] Morcos V.H. and Abdel-Hafez O.M.E. "Testing of an arrow-head vertical axis wind turbine model.". *Renewable Energy*, 7(3):223–31, 1996. 20

[103] Morgan C.A., Gardner P., Mays I.D. and Anderson M.B. "The demonstration of a stall regulated 100kW vertical axis wind turbine.". *Proceedings 1989 European wind energy conference*, Glasgow, Scotland, 1989. 18

[104] Morrison J. "Flux Difference Split Scheme for Turbulent Transport Equations". *AIAA Second Intrernational Aerospace Planes Conference*, Orlando, 1990. 62

[105] Mulas M., Beeri Z., Golby D., Surridge M. and Talice M. "A parallel Navier-Stokes code for large industrial flow simulations.". *Fifteenth international conference on numerical methods in fluid dynamics*, 490:450–455, 1997. 89

[106] Muljadi E. and Butterfield C.P. "Pitch-controlled Variable-speed Wind Turbine Generation". *National Renewable Energy Laboratory*, Colorado, 2000. 15

[107] Musgrove P.J. "Wind energy conversion: recent progress and future prospects.". *Sol Wind Technol*, 4(1):37–49, 1987. 18, 20

[108] Nastov O. "Spectral methods for circuit analysis.". *PhD thesis*, Massachusetts Institute of Technology, 1999. 71

[109] Nobile R., Vahdati M., Barlow J. and Mewburn-Crook A. "Dynamic stall for a Vertical Axis Wind Turbine in a two-dimensional study". *World Renewable Energy Congress*, Sweden, 2011. vii, 41, 42

[110] Paraschivoiu I. *"Wind turbine design with emphasis on Darrieus concept, 1st ed."*. Canada: Polytechnic International Press, 2002. 91

[111] Peace S. "Why not vertical axis?". *Refocus*, 4(3):30, 2003. 17, 20

[112] Peace S. "Another approach to wind". *Journal of Mechanical Engineering*, 126 (6):28–31, 2004. 17, 18

[113] Powles S.R.J. "The effect of tower shadow in the dynamics of a horizontal-axis wind turbine". *Wind Engineering*, 7:26–42, 1983. 33

[114] Pramod J. *"Wind Energy Engineering"*. Mc Graw Hill, 2011. vi, 10, 11, 12

[115] Raciti Castelli M., De Betta S. and Benini E. "Effect of Blade Number on a Straight-Bladed Vertical-Axis Darreius Wind Turbine". *World Academy of Science, Engineering and Technology*, 6, 2012. 39, 40

[116] Raciti Castelli M., Englaro A. and Benini E. "The Darrieus wind turbine: Proposal for a new performance prediction model based on CFD". *Journal of Energy*, 36:4919–4934, 2011. vii, 92, 93

[117] Raciti Castelli M., Pavesi G., Battisti L., Benini E. and Ardizzon G. “Modeling strategy and numerical validation for a Darrieus vertical axis micro-wind turbine”. *Proc. of the ASME 2010 International Mechanical Engineering Congress and Exposition (IMECE)*, Vancouver, British Columbia, Canada, 2010. 91, 92, 113

[118] Reiso M., Muskulus M. and Moe G. “Tower Shadow - Experiment Comparing Wake Behind Tubular and Truss Towers”. *Proceedings of the Twenty-first International Offshore and Polar Engineering Conference*, 2011. vi, 30, 32, 33

[119] Reuter R.C. and Worstell M.H. “Torque ripple in a vertical axis wind turbine.”. *Sandia National Laboratories, Sandia report SAND78-0577*, 1978. 20

[120] Riegler H. “HAWT versus VAWT: small VAWTs find a clear niche.”. *Refocus*, 4 (4), 2003. 20

[121] Robinson M.C., Simms D.A., Hand M.M. and Schreck S.J. “Horizontal axis wind turbine aerodynamics: three-dimensional, unsteady and separated flow influences”. *3rd ASME/JSME Joint Fluids Engineering Conference*, San Francisco, CA, 1999. 34

[122] Rossetti A. and Pavesi G. “Comparison of Different Numerical Approaches to the Study of the H-Darrieus Turbines Start-Up”. *Renewable Energy*, 50:719, 2013. 38, 96, 108

[123] Roynarin W., Leung P.S. and Datta P.K. “The performances of a vertical Darrieus machine with modern high lift airfoils.”. *Proceedings from IMAREST conference MAREC*, Newcastle, UK, 2002. 19

[124] Schaffarczyk A.P. *“Introduction to Wind Turbine Aerodynamics”*. Springer. vi, 19

[125] Scheurich F., Fletcher T.M. and Brown R.E. “Simulating the aerodynamic performance and wake dynamics of a vertical-axis wind turbine”. *Wind Energy*, 14: 159–177, 2011. 43

[126] Schlichting H. and Gersten K. *“Boundary-Layer Theory”*. Springer. 33

[127] Schreck S.J., Robinson M.C. and Hand M.M. “Blade dynamic stall vortex kinematics for a horizontal axis wind turbine in yawed conditions.”. *Journal of Solar Energy Engineering*, 123:272, 2001. 34

[128] Schubel P.J. and Crossley R.J. “Wind Turbine Blade Design”. *Journal of Energies*, 5:3425–3449, 2012. 20

[129] Shen W., Hansen M. and Sorensen J. “Determination of the Angle of Attack on Rotor Blades”. *Wind Energy*, 12:91–98, 2009. 134

[130] Sicot F., Puigt G. and Montagnac M. “Block-Jacobi Implicit Algorithms for the Time Spectral Method”. *AIAA Journal*, 46(12):3080–3089, 2008. 27, 71

[131] Simao Ferreira C.J., Bijl H., van Bussel G. and van Kuik G. “Simulating Dynamic Stall in a 2D VAWT: Modeling strategy, verification and validation with Particle Image Velocimetry data”. *Journal of Physics*, 75, 2007. 40, 41

[132] Simao Ferreira C.J., van Bussel G. and van Kuik G. “2D PIV visualization of dynamic stall on a vertical axis wind turbine”. *45th AIAA Aerospace Sciences Meeting and Exhibit / ASME Wind Energy Symposium*, 2007. 40

[133] Simao Ferreira C.J., van Bussel G., Scarano F. and van Kuik G. “Visualization by PIV of dynamic stall on a vertical axis wind turbine”. *Experiments in Fluids*, 46(1):97–108, 2009. 91

[134] Simao Ferreira C.J., van Zuijlen A., Bijl H., van Bussel G. and van Kuik G. “Simulating dynamic stall in a two-dimensional vertical-axis wind turbine: verification and validation with particle image velocimetry data”. *Wind Energy*, 13(1):1–17, 2010. 41, 91

[135] Singh J.P. “An Improved Navier-Stokes flow computation of AGARD case-10 Flow over RAE2822 airfoil using Baldwin-Lomax Model”. *ACTA Mechanica*, 151:255–263, 2001. 63

[136] Smith D.R. “The wind farms at Altamont Pass area.”. *Annual Review of Energy and Environment*, 12(145):83, 1987. 17

[137] Sorensen N.N., Michelsen J.A. and Schreck S. "Navier-Stokes Predictions of the NREL Phase VI Rotor in the NASA Aimes 80 ft. x 120 ft. Wind Tunnel". *Wind Energy*, 5:151–169, 2002. 124

[138] Spalart P.R. and Allmaras S.R. "A one-equation turbulence model for aerodynamic flows". *La Recherche Aerospatiale*, 1:521, 1994. 26, 40

[139] Strickland J.H., Smith T. and Sun K. "A vortex model of the Darrieus turbine: an analytical and experimental study". *Sandia Technical Report SAND81-7017*, 1981. 43

[140] Su X. and Yuan X. "Implicit Solution of Time-Spectral Method for Periodic Unsteady Flows". *International Journal for Numerical Methods in Fluids*, 63(7): 860876, 2010. 27, 72

[141] Sumner J. and Masson C. "Influence of Atmospheric Stability on Wind Turbine power Performance Curves". *Journal of Solar Energy Engineering*, 128:531–538, 2006. 37

[142] Swanson R.C. "An Efficient Flow Solver with a Transport Equation for Modelling Turbulence". *in 19th AIAA Computational Fluid Dynamics*, San Antonio, Texas, 2009. 64

[143] Thomas J.P., Dowell E.H. and Hall K.C. "Nonlinear inviscid aerodynamic effects on transonic divergence, flutter, and limit-cycle oscillations". *AIAA Journal*, 40 (4):638, 2002. 71

[144] Thomas J.P., Dowell E.H. and Hall K.C. "Modeling Viscous Transonic Limit-Cycle Oscillation Befavior Using a Harmonic Balance Approach". *Journal of Aircraft*, 41(6):1266–1274, 2004. 71

[145] Thompson J.E., Warsi Z.U.A. and Wayne Mastin C. *"Numerical Grid Generation, Foundations and Applications"*. Elsevier Science Publishing, 1997. 59

[146] Thompson J.F., Soni B.K. and Weatherill N.P. *"Handbook of Grid Generation"*. CRC Press LLC, 1999. 59

[147] Tongchitpakdee C., Benjanirat S. and Sankar L.N. “Numerical Simulation of the Aerodynamics of Horizontal Axis Wind Turbines under Yawed Flow Conditions”. *Journal of Solar Energy Engineering*, 127(4):464–474, 2005. 36

[148] Van Beek J. “Keeping Antarctica pollution free.”. *Windpower Monthly*, 1990. 18

[149] Van der Weide E., Gopinath A. and Jameson A. “Turbomachinery Applications with the Time Spectral Method”. *17th AIAA Computational Fluid Dynamics Conference, paper 2005-4905*, Toronto, Ontario, Canada, 2005. 27, 72

[150] Wagner H.J. and Mathur J. *“Introduction to Wind Energy System. Basics, Technology and Operation. 2nd ed.”*. Springer, 2013. 15

[151] Wang S., Ingham D.B., Ma L., Pourkashanian M. and Tao Z. “Numerical investigations on dynamic stall of low Reynolds number flow around oscillating airfoils”. *Computers and Fluids*, 39(9):1529–1541, 2010. 41

[152] Warschauer K.A. and Leene J.A. “Experiments on mean and fluctuating pressures of circular cylinders at cross flow at very high Reynolds numbers”. *Proc. Int. Conference Wind Effects Buildings Structures, Tokyo*, pages 305–315, 2009. 33

[153] Wesseling P. *“An Introduction to Multigrid Methods”*. John Wiley and Sons, New York, 1992. 64

[154] Wilcox D.C. *“Turbulence Modeling for CFD. Second Ed.”*. 1998. 40

[155] Wilcox D.C. “Reassessment of the Scale-Determining Equation for Advanced Turbulence Models”. *AIAA Journal*, 26(11):1299–1310, 1988. 52, 53, 101, 166

[156] Wilson R.E. and Lissaman P.B.S. *“Applied Aerodynamics of Wind Power Machine.”*. Oregon State University, 1974. 21

[157] Wilson R.E., Lissaman P.B.S. and Walker S.N. “Aerodynamic Performance of Wind Turbines.”. *Energy Research and Development Administration*, page 1, 1976. 21

[158] Woodgate M.A. and Badcock K.J. “Implicit Harmonic Balance Solver for Transonic Flows with Forced Motions”. *AIAA Journal*, 47(4):893–901, 2009. 27, 72